BOTTOM-UP AND TOP-DOWN: MOLECULES AND CIRCUITS THAT UNDERLIE CHEMOSENSORY BEHAVIORS

EDITED BY: Markus Rothermel, Pablo Chamero, Shaina M. Short, Jeremy C. McIntyre and Julian P. Meeks

PUBLISHED IN: Frontiers in Cellular Neuroscience

frontiers Research Topics

frontiers

ISSN 1664-8714
ISBN 978-2-88971-442-1
DOI 10.3389/978-2-88971-442-1

About Frontiers

Frontiers is more than just an open-access publisher of scholarly articles: it is a pioneering approach to the world of academia, radically improving the way scholarly research is managed. The grand vision of Frontiers is a world where all people have an equal opportunity to seek, share and generate knowledge. Frontiers provides immediate and permanent online open access to all its publications, but this alone is not enough to realize our grand goals.

Frontiers Journal Series

The Frontiers Journal Series is a multi-tier and interdisciplinary set of open-access, online journals, promising a paradigm shift from the current review, selection and dissemination processes in academic publishing. All Frontiers journals are driven by researchers for researchers; therefore, they constitute a service to the scholarly community. At the same time, the Frontiers Journal Series operates on a revolutionary invention, the tiered publishing system, initially addressing specific communities of scholars, and gradually climbing up to broader public understanding, thus serving the interests of the lay society, too.

Dedication to Quality

Each Frontiers article is a landmark of the highest quality, thanks to genuinely collaborative interactions between authors and review editors, who include some of the world's best academicians. Research must be certified by peers before entering a stream of knowledge that may eventually reach the public - and shape society; therefore, Frontiers only applies the most rigorous and unbiased reviews.
Frontiers revolutionizes research publishing by freely delivering the most outstanding research, evaluated with no bias from both the academic and social point of view. By applying the most advanced information technologies, Frontiers is catapulting scholarly publishing into a new generation.

What are Frontiers Research Topics?

Frontiers Research Topics are very popular trademarks of the Frontiers Journals Series: they are collections of at least ten articles, all centered on a particular subject. With their unique mix of varied contributions from Original Research to Review Articles, Frontiers Research Topics unify the most influential researchers, the latest key findings and historical advances in a hot research area! Find out more on how to host your own Frontiers Research Topic or contribute to one as an author by contacting the Frontiers Editorial Office: frontiersin.org/about/contact

BOTTOM-UP AND TOP-DOWN: MOLECULES AND CIRCUITS THAT UNDERLIE CHEMOSENSORY BEHAVIORS

Topic Editors:
Markus Rothermel, University of Veterinary Medicine Hannover, Germany
Pablo Chamero, INRA Centre Val de Loire, France
Shaina M. Short, The University of Utah, United States
Jeremy C. McIntyre, University of Florida, United States
Julian P. Meeks, University of Texas Southwestern Medical Center, United States

Citation: Rothermel, M., Chamero, P., Short, S. M., McIntyre, J. C., Meeks, J. P., eds. (2022). Bottom-up and Top-down: Molecules and Circuits that Underlie Chemosensory Behaviors. Lausanne: Frontiers Media SA.
doi: 10.3389/978-2-88971-442-1

Table of Contents

frontiers in Cellular Neuroscience

EDITORIAL
published: 13 August 2021
doi: 10.3389/fncel.2021.729791

Editorial: Bottom-Up and Top-Down: Molecules and Circuits That Underlie Chemosensory Behaviors

Pablo Chamero[1], *Shaina M. Short*[2], *Jeremy C. McIntyre*[3], *Julian P. Meeks*[4] *and Markus Rothermel*[5]*

[1] CNRS, IFCE, INRAE, Université de Tours, Nouzilly, France, [2] Neurobiology Department, University of Utah School of Medicine, Salt Lake City, UT, United States, [3] Department of Neuroscience, Center for Smell and Taste, University of Florida, Gainesville, FL, United States, [4] University of Rochester School of Medicine and Dentistry, Rochester, NY, United States, [5] Institute for Physiology and Cell Biology, University of Veterinary Medicine Hannover, Foundation, Hanover, Germany

Keywords: neuromodulation, behavior, physiology, social cues, chemosensation

Editorial on the Research Topic

Bottom-Up and Top-Down: Molecules and Circuits That Underlie Chemosensory Behaviors

This Research Topic highlights recent advancements in our understanding of how genes and neural circuits in the brain shape complex natural behaviors that are evolutionary conserved and essential for survival across species. Like any cortical area, including visual and somatosensory cortices, the chemosensory brain is strongly affected by attention, expectation, and perceptual tasks mainly mediated by so-called "top-down" inputs (Gilbert and Sigman, 2007; McIntyre et al., 2017). "Bottom-up" and "top-down" networks converge in early sensory areas and higher brain regions. Top-down systems signal risk, reward, novelty, effort, and social cooperation (Richardson and DeLong, 1986; Krichmar, 2008; Rutledge et al., 2015; Schultz, 2015). These systems provide the basis for higher cognitive functions like attention (Thiele and Bellgrove, 2018), decision-making (Rutledge et al., 2015), emotion (Wang and Pereira, 2016), and goal-directed behavior (Hirayama et al., 2014), which are thought to result from the interaction between top-down and higher brain areas (Mesulam, 1998). Through top-down processes, factors like experience, motivation and expectation, i.e., the general "brain state," affect sensory input analysis and, thereby, our internal representation of the world (Manita et al., 2015).

How the brain balances critical extrinsic, bottom up and intrinsic, top-down information to enable adaptive behaviors is currently a major topic in neurobiology. All organisms rely on chemosensory systems to seek food, communicate, and avoid hazards and predators. In turn, internal brain states modulate the detection of external chemosensory stimuli and chemosensation is shaped by hunger, the drive to procreate, hormones, stress and fear. This requires neural circuits to adapt depending on the behavioral needs (wakefulness/sleep state, arousal, learning, metabolic demands, reproduction state, etc.). Therefore, chemosensation represents an excellent model system to investigate how the brain processes extrinsic and intrinsic information (Lizbinski and Dacks, 2017; Brunert and Rothermel, 2021). Since chemosensory information can reach cortical areas without thalamic involvement, the organization of these bottom-up pathways is at least partially different compared to other sensory systems. On the other hand, the vast majority of its top-down projections are not chemosensory brain-specific and innervate a broad range of sensory

OPEN ACCESS

Edited and reviewed by:
Arianna Maffei,
Stony Brook University, United States

***Correspondence:**
Markus Rothermel
markus.rothermel@tiho-hannover.de

Specialty section:
This article was submitted to Cellular Neurophysiology, a section of the journal Frontiers in Cellular Neuroscience

Received: *23 June 2021*
Accepted: *19 July 2021*
Published: *13 August 2021*

Citation:
Chamero P, Short SM, McIntyre JC, Meeks JP and Rothermel M (2021) Editorial: Bottom-Up and Top-Down: Molecules and Circuits That Underlie Chemosensory Behaviors. Front. Cell. Neurosci. 15:729791. doi: 10.3389/fncel.2021.729791

cortical and subcortical areas. The link between chemosensory processing and behavior has been investigated in great detail in both vertebrates and invertebrates. By making use of an advanced genetic toolset, mechanisms adapting chemosensory processing and perception to internal states such as hunger and reproductive state have been investigated in great detail in invertebrates (Sayin et al., 2018). In mice, olfactory cues such as pheromones have been shown to elicit specific social forms of behavior (Stowers and Liberles, 2016) and hippocampal top-down projections to sensory centers have been shown to match place information to odor memory, thereby linking internal brain state, top-down activity, and memory processes (Aqrabawi and Kim, 2018).

Work from many labs has demonstrated that the activity of neurons at any stage of chemosensory information can be modulated to optimize stimulus processing and behavioral outputs. This Research Topic captures the current progress on our understanding of how changes in chemosensory neural circuits can have significant behavioral consequences.

This Research Topic comprises a wide variety of articles contributing to current views and understanding of different bottom-up and top-down systems: pioneering researchers in the field use state-of-the-art tools such as, genetically encoded neurotransmitter indicators and odor plume concentrations measurments and cover a wide spectrum of methods that range from genetics to behavioral analysis. The reader will find several articles related to the architecture and function of neural circuits involved in social signal processing. Transgenic approaches that partially eliminate sensory function in the vomeronasal organ are used to show that social behavior in female mice results from interactions between intrinsic mechanisms in the vomeronasal system and experience-dependent plasticity (Trouillet et al.). In order to explore whether motherhood alters sensory processing of pup-derived chemosignals (Navarro-Moreno et al.) analyzed the expression of immediate early genes in the vomeronasal organ and centers of the olfactory and vomeronasal brain pathways in virgin and late-pregnant females. They found changes in sensory processing with pregnancy in both the main as well as the accessory olfactory system. Finally, Chu et al. used mass staining, calcium imaging, and intracellular recordings to characterize the morphological and physiological properties of the male-specific macroglomerular complex (MGC) neurons of the lateral tract in the moth antennal lobe. These pheromone-sensitive projections neurons could mediate fast control of hard-wired behavior like e.g., odor tracking.

In behavioral studies, odor tracking in mammals and odor plumes were investigated in a publication from David Gire's lab. In order to investigate how plume dynamics impact early odor representation in the mouse olfactory system (Lewis et al.) measured wide-field GCaMP6f signaling from the dendrites of mitral and tufted cells in head-fixed animals in response to naturally fluctuating odor plumes. They found that across flow conditions odor dynamics are a major driver of activity in many glomerular networks. In another study, activation of the dopamine receptor D1 was found to potentiate feedforward excitation in the olfactory bulb, enhancing mitral tufted cell output and sensitivity to odor stimuli (Liu). The results provide a mechanistic basis for the functional roles of dopamine in modulating odor detection and discrimination. In order to determine how local cholinergic signaling impacts basal forebrain output pathways that participate in top-down regulation (Hanson et al.) utilized fiber photometry and the genetically encoded acetylcholine indicator GAChR2.0 to define temporal patterns of cholinergic signaling in the basal forebrain during olfactory-guided, motivated behaviors, and learning. Their results suggest that cholinergic tone in the basal forebrain changes rapidly to reflect reward-seeking behavior and positive reinforcement and may impact downstream circuitry that modulates olfaction. The role of neuromodulators was also investigated in non-neuronal cell types. Confocal calcium imaging and immunohistochemistry in mouse olfactory bulb slices provide insight into calcium signaling evoked by norepinephrine in astrocytes (Fischer et al.). At the periphery, genetic control of chemosensory receptors is critical for the intial detection of odors, yet the choice of odorant receptors is still not fully known. The role of genetic background itself on olfactory receptor expression was investigated by Leme Silva et al.. This study analyzed the expression of the OR gene Olfr17 (also named P2) in different genomic contexts and show that genetic variations in *cis* regulatory regions can lead to differential DNA methylation frequencies in these OR gene alleles. Expression of the *OR* alleles is largely affected by the genetic background as well as epigenetic modifications.

All together, this Research Topic highlights data from different model organisms, neuronal as well as glia cells and incorporates genetic, physiological, and behavioral approaches to offer new perspectives about the complex interaction of bottom-up and top-down systems.

AUTHOR CONTRIBUTIONS

MR wrote the first draft of the manuscript. All authors contributed to manuscript revision, read, and approved the submitted version.

FUNDING

This work was supported by the DFG (German Research Foundation; RO 4046/2-1 /2-2, Research Training Group 368482240/GRK2416) [MR], IZFK, RWTH Aachen University (IZKF TN1-7 532007) [MR] a common ANR-DFG grant (The French National Research Agency (ANR); ANR-20-CE92-0003 [PC] and DFG RO 4046/5-1 [MR]) and the National Institute on Deafness and Other Communication Disorders of the USA National Institutes of Health (Grants R01DC015784 [JPM], R01DC017985 [JPM], R21DC018904 [SMS], and R01DC019379 [JCM]).

REFERENCES

Aqrabawi, A. J., and Kim, J. C. (2018). Hippocampal projections to the anterior olfactory nucleus differentially convey spatiotemporal information during episodic odour memory. *Nat. Commun.* 9:2735. doi: 10.1038/s41467-018-05131-6

Brunert, D., and Rothermel, M. (2021). Extrinsic neuromodulation in the rodent olfactory bulb. *Cell Tissue Res.* 383, 507–524. doi: 10.1007/s00441-020-03365-9

Gilbert, C. D., and Sigman, M. (2007). Brain states: top-down influences in sensory processing. *Neuron* 54, 677–696. doi: 10.1016/j.neuron.2007.05.019

Hirayama, K., Moroz, L. L., Hatcher, N. G., and Gillette, R. (2014). Neuromodulatory control of a goal-directed decision. *PLoS ONE* 9:e102240. doi: 10.1371/journal.pone.0102240

Krichmar, J. L. (2008). the neuromodulatory system: a framework for survival and adaptive behavior in a challenging world. *Adapt. Behav.* 16, 385–399. doi: 10.1177/1059712308095775

Lizbinski, K. M., and Dacks, A. M. (2017). Intrinsic and extrinsic neuromodulation of olfactory processing. *Front. Cell. Neurosci.* 11:424. doi: 10.3389/fncel.2017.00424

Manita, S., Suzuki, T., Homma, C., Matsumoto, T., Odagawa, M., Yamada, K., et al. (2015). A top-down cortical circuit for accurate sensory perception. *Neuron* 86, 1304–1316. doi: 10.1016/j.neuron.2015.05.006

McIntyre, J. C., Thiebaud, N., McGann, J. P., Komiyama, T., and Rothermel, M. (2017). Neuromodulation in chemosensory pathways. *Chem. Senses* 42, 375–379. doi: 10.1093/chemse/bjx014

Mesulam, M. M. (1998). From sensation to cognition. *Brain* 121 (Pt 6), 1013–1052. doi: 10.1093/brain/121.6.1013

Richardson, R. T., and DeLong, M. R. (1986). Nucleus basalis of Meynert neuronal activity during a delayed response task in monkey. *Brain Res.* 399, 364–368. doi: 10.1016/0006-8993(86)91529-5

Rutledge, R. B., Skandali, N., Dayan, P., and Dolan, R. J. (2015). Dopaminergic modulation of decision making and subjective well-being. *J. Neurosci.* 35, 9811–9822. doi: 10.1523/JNEUROSCI.0702-15.2015

Sayin, S., Boehm, A. C., Kobler, J. M., De Backer, J. F., and Grunwald Kadow, I. C. (2018). Internal state dependent odor processing and perception-the role of neuromodulation in the fly olfactory system. *Front. Cell. Neurosci.* 12:11. doi: 10.3389/fncel.2018.00011

Schultz, W. (2015). Neuronal reward and decision signals: from theories to data. *Physiol. Rev.* 95, 853–951. doi: 10.1152/physrev.00023.2014

Stowers, L., and Liberles, S. D. (2016). State-dependent responses to sex pheromones in mouse. *Curr. Opin. Neurobiol.* 38, 74–79. doi: 10.1016/j.conb.2016.04.001

Thiele, A., and Bellgrove, M. A. (2018). Neuromodulation of attention. *Neuron* 97, 769–785. doi: 10.1016/j.neuron.2018.01.008

Wang, F., and Pereira, A. (2016). Neuromodulation, emotional feelings and affective disorders. *Mens Sana Monogr.* 14, 5–29. doi: 10.4103/0973-1229.154533

Conflict of Interest: The authors declare that the research was conducted in the absence of any commercial or financial relationships that could be construed as a potential conflict of interest.

Publisher's Note: All claims expressed in this article are solely those of the authors and do not necessarily represent those of their affiliated organizations, or those of the publisher, the editors and the reviewers. Any product that may be evaluated in this article, or claim that may be made by its manufacturer, is not guaranteed or endorsed by the publisher.

frontiers in Cellular Neuroscience

ORIGINAL RESEARCH
published: 08 June 2020
doi: 10.3389/fncel.2020.00147

A Novel Major Output Target for Pheromone-Sensitive Projection Neurons in Male Moths

Xi Chu[1]*, *Stanley Heinze*[2], *Elena Ian*[1] and *Bente G. Berg*[1]

[1]Chemosensory Laboratory, Department of Psychology, Norwegian University of Science and Technology, Trondheim, Norway, [2]Lund Vision Group, Department of Biology, Lund University, Lund, Sweden

Even though insects have comparably small brains, they achieve astoundingly complex behaviors. One example is flying moths tracking minute amounts of pheromones using olfactory circuits. The tracking distance can be up to 1 km, which makes it essential that male moths respond efficiently and reliably to very few pheromone molecules. The male-specific macroglomerular complex (MGC) in the moth antennal lobe contains circuitry dedicated to pheromone processing. Output neurons from this region project along three parallel pathways, the medial, mediolateral, and lateral tracts. The MGC-neurons of the lateral tract are least described and their functional significance is mainly unknown. We used mass staining, calcium imaging, and intracellular recording/staining to characterize the morphological and physiological properties of these neurons in the noctuid moth, *Helicoverpa armigera*. All lateral-tract MGC neurons targeted the column, a small region within the superior intermediate neuropil. We identified this region as a unique converging site for MGC lateral-tract neurons responsive to pheromones, as well as a dense congregating site for plant odor information since a substantial number of lateral-tract neurons from ordinary glomeruli (OG) also terminates in this region. The lateral-tract MGC-neurons responded with a shorter peak latency than the well-described neurons in the medial tract. Different from the medial-tract MGC neurons encoding odor quality important for species-specific signal identification, those in the lateral tract convey a more robust and rapid signal—potentially important for fast control of hard-wired behavior.

Keywords: pheromone system, insect olfaction, parallel processing, intracellular recording/staining, calcium imaging

OPEN ACCESS

Edited by:
Julian P. Meeks, University of Texas Southwestern Medical Center, United States

Reviewed by:
Monika Stengl, University of Kassel, Germany
Nicolás Pírez, Molecular Biology and Neurosciences (IFIBYNE), Argentina

***Correspondence:**
Xi Chu
xi.chu@ntnu.no

Specialty section:
This article was submitted to Cellular Neurophysiology, a section of the journal Frontiers in Cellular Neuroscience

Received: *05 March 2020*
Accepted: *04 May 2020*
Published: *08 June 2020*

Citation:
Chu X, Heinze S, Ian E and Berg BG (2020) A Novel Major Output Target for Pheromone-Sensitive Projection Neurons in Male Moths. Front. Cell. Neurosci. 14:147. doi: 10.3389/fncel.2020.00147

INTRODUCTION

Pheromones are chemical signals serving in social and sexual communication between individuals of the same species throughout the animal kingdom. While the peripheral mechanisms for pheromone detection are well described in many species, knowledge about central processing principles of these key sensory stimuli remains incomplete. Noctuid moths contain numerous prime examples of species with highly specific pheromone communication combined with exquisite sensitivity. Among the most intensively investigated are several species of the subfamily

Heliothinae (Lepidoptera: Noctuidae; Fitt, 1989; Cho et al., 2008), including some of the world's most detrimental crop pests. In contrast to the also intensively studied, domesticated silk moth, *Bombyx mori*, heliothinae moths are *flying* species utilizing pheromones to communicate over long distances. The males recognize minute amounts of the female produced pheromones *via* highly sensitive sensory neurons housed in specialized sensilla on the antennae.

In most moths, the male-specific sensory neurons project directly to a distinct region in the antennal lobe, the macroglomerular complex (MGC). This pathway is dedicated to processing input about female produced compounds and is present in addition to the general olfactory circuit involving the usually more numerous ordinary glomeruli (OG). The species used in this study, *Helicoverpa armigera*, utilizes two pheromone components: *cis*-11-hexadecenal (Z11-16:Al) as the primary component and *cis*-9-hexadecenal (Z9-16:Al) as secondary component (Kehat and Dunkelblum, 1990). The MGC of this species contains three glomeruli, named cumulus, dorsomedial anterior (dma), and dorsomedial posterior (dmp; Skiri et al., 2005; Zhao et al., 2016a). Originating from the sensory neurons in specific antennal sensillae, signals resulting from the two pheromone components as well as one behavioral antagonist, *cis*-9 tetradecenal (Z9-14:Al), are received by the cumulus, dmp, and dma, respectively (see Figure 7 in Wu et al., 2015).

In the antennal lobe, all sensory axons make synaptic contacts with local interneurons and projection neurons. The latter cells carry odor information to higher integration centers in the protocerebrum *via* several parallel antennal-lobe tracts (ALTs). The three main ALTs, the medial ALT, the mediolateral ALT, and the lateral ALT, connect the antennal lobe with the calyces of the mushroom bodies (MB) and the lateral protocerebrum, which constitute the two most prominent higher-order olfactory projection areas across insects (Homberg et al., 1988; Seki et al., 2005; Rø et al., 2007; Ito et al., 2014). A third area is targeted by a significant proportion of lateral-tract projection neurons and is embedded in the superior intermediate protocerebrum (SIP, see Ito et al., 2014), occupying the space in between the anterior optic tubercle (AOTU) and the MB vertical lobe. Although this area was discovered in the hawkmoth *Manduca sexta* (Homberg et al., 1988), its prominence as a major projection region was pointed out in the heliothinae moth, where it was termed the *column* (Ian et al., 2016).

Similar to insects, an arrangement of parallel olfactory tracts and projection areas is also found in vertebrates, such as fish (Hamdani and Døving, 2007) and mammals (Kauer, 1991; Mori, 2016). In fish, each of three tracts carries a different category of olfactory information, i.e., social cues, pheromones, and food odors (Hamdani and Døving, 2007). Contrary, in insects, particularly in moths, each of the three main ALTs is formed by axons of projection neurons originating from both the MGC and the OG (Homberg et al., 1988; Kanzaki et al., 2003; Zhao et al., 2014). Thus, different categories of olfactory cues are processed by neurons confined to each ALT. Rather than encoding different stimulus categories, the parallel tracts in insects are likely to transmit information about different features (e.g., concentrations) of the same odor (reviewed by Galizia and Rössler, 2010). Due to the limited number of involved odorants and their high relevance to behavior, examining pheromone processing provides a low-dimensional model to illuminate the functional differences across parallel pathways.

To reveal these differences, functional and anatomical work on neurons in all ALTs is required. However, studies on individual MGC projection neurons in moths have focused almost exclusively on uni-glomerular medial-tract neurons. These previous reports include studies of heliothinae moths, e.g., *Heliothis virescens*, *Helicoverpa zea*, and *Helicoverpa assulta* (Christensen et al., 1991, 1995; Vickers et al., 1998; Zhao and Berg, 2010; Zhao et al., 2014), as well as *Manduca sexta* (Christensen and Hildebrand, 1987; Kanzaki et al., 1989; Hansson et al., 1991), *Agrotis ipsilon* (Jarriault et al., 2009), and *Bombyx mori* (Kanzaki et al., 2003; Seki et al., 2005). Only a recent publication on two heliothinae species focused on pheromone neurons passing along ALTs other than the medial (Lee et al., 2019). However, complete and unequivocal projection patterns of individual lateral-tract MGC neurons were mainly absent. We, therefore, investigated morphological and physiological properties of male-specific projection neurons confined to the second prominent ALT, the lateral tract. By using intracellular recordings combined with staining, calcium imaging, and mass labeling of neurons, we found that all identified lateral-tract MGC neurons projected to the column. This convergence of lateral-tract axons within a single, restricted region was distinct from the more widespread medial tract MGC terminals in the superior lateral protocerebrum, which have been suggested to form patterns according to behavioral significance (Zhao et al., 2014). Also, temporal dynamics and tuning characteristics of the lateral-tract MGC neurons were distinct from those confined to the medial tract. Finally, a substantial proportion of lateral-tract projection neurons originating from the OG also terminated in the column, exposing this region as a site for convergence for sensory information from the pheromone and plant odor subsystems. Taken together, the results presented here suggest that the morphologically distinct types of MGC lateral-tract neurons play other roles than the corresponding neurons in the medial tract, possibly ensuring fast initiation of stereotypical plume tracking flight behavior.

MATERIALS AND METHODS

Insects

Male and female moths (2–3 days) of *H. armigera* (Lepidoptera: Noctuidae; Heliothinae) were used in this study. Pupae were supplied by Keyun Bio-pesticides (Henan, China). After emergence, the moths were kept at 25°C and 67% humidity on a 14:10 h light/dark cycle (lights on at 18:00), with 10% sucrose solution available *ad libitum*. According to the Norwegian law of animal welfare, there are no restrictions regarding the experimental use of Lepidoptera.

Experimental Design and Statistical Analyses

Intracellular Recording and Staining

The preparation of the insect has been described in detail elsewhere (see Rø et al., 2007; Zhao et al., 2014). Briefly, the moth was restrained inside a plastic tube with the head exposed and then immobilized with dental wax (Kerr Corporation, Romulus, MI, USA). The brain was exposed by opening the head capsule and removing the muscle tissue. The procedure of intracellular recording/staining of antennal-lobe projection neurons was performed as previously described (Zhao et al., 2014; Ian et al., 2016). Sharp glass electrodes were made by pulling borosilicate glass capillaries (OD: 1 mm, ID: 0.5 mm, with filament 0.13 mm; Hilgenberg GmbH, Germany) on a horizontal puller (P97; Sutter Instruments, Novarto, CA, USA). The tip of the micropipette was filled with a fluorescent dye, i.e., 4% biotinylated dextran-conjugated tetramethylrhodamine (3,000 mw, micro-ruby, Molecular Probes) in 0.2 M potassium acetate (KAc). The glass capillary was back-filled with 0.2 M KAc. To facilitate microelectrode insertion into the tissue, the sheath of the antennal lobe was gently removed by using fine forceps. The exposed brain was continuously supplied with Ringer's solution (in mM: 150 NaCl, 3 $CaCl_2$, 3 KCl, 25 sucrose, and 10 N-tris (hydroxymethyl)-methyl-2-amino-ethane sulfonic acid, pH 6.9). A chloridized silver wire inserted into the muscle in the mouthpart served as a reference electrode. The recording electrode, having a resistance of 70–150 MΩ, was carefully inserted into the dorsolateral region of the AL *via* a micromanipulator (Leica). Neuronal spike activity was amplified (AxoClamp 2B, Axon Instruments, Union, CA, USA) and monitored continuously by oscilloscope and loudspeaker. Data were digitized with CED1401 micro using Spike2 6.02 (Cambridge Electronic Design, Cambridge, England) as acquisition software. During recording, the moth was ventilated constantly with a steady stream of fresh air. Spontaneous activity in the pre-test window was recorded for a period of 25–40 s. During odor stimulation, a pulse of air from the continuous airstream was diverted *via* a solenoid-activated valve (General Valve Corp.) through a glass cartridge bearing the odorant on a piece of filter paper. Six odors were tested in each recording experiment. The stimulation period was 400 ms, and the application of each odor was repeated at least two times. After testing all odor stimuli, the neuron was iontophoretically stained by applying 2–3 nA pulses with 200 ms duration at 1 Hz for about 5–10 min (no recording was conducted after staining). To allow neuronal transportation of the dye, the preparation was kept overnight at 4 °C. The brain was then dissected from the head capsule and fixed in 4% paraformaldehyde for 1 h at room temperature before it was dehydrated in an ascending ethanol series (50%, 70%, 90%, 96%, 2 × 100%; 10 min each). Finally, the brain was cleared and mounted in methyl salicylate.

Mass Staining

Three types of mass staining experiments were performed. In the first, we achieved an overview of pheromone projection neurons vs. non-pheromone projection neurons in male moths *via* double dye injection experiments. Two fluorescent dyes were applied to the same preparation—one to the MGC and the other to the OG. A focal injection was achieved by inserting a sharp electrode filled with a 4% micro-ruby solution to the MGC region, using our intracellular electrophysiology setup and applying depolarizing current pulses of 7–8 nA at 1 Hz for 15 min. To label non-MGC projection neurons, the antennal lobe region including OG was manually perforated with a fine needle containing crystals of Alexa Fluor 488 dextran (10,000 mw, Molecular Probes). To visualize input and output areas of the male column region, micro-ruby was applied to this neuropil in the second experiment *via* pulsed current injection. To compare the antennal-lobe output projections in males and females, a third mass staining experiment was conducted by applying micro-ruby to the female antennal lobe. In all mass staining experiments, the brains were kept for 2 h at room temperature for transportation of the dyes. The subsequent procedure included dissection, fixation, dehydration, and mounting in methyl salicylate as described above.

Calcium Imaging

Sixteen males (age: 2–3 days) were used to measure pheromone-evoked responses from the MGC using calcium imaging. Selective staining of projection neurons in *H. armigera* was described elsewhere (Ian et al., 2017). Briefly, the head capsule was opened after the moth was immobilized in a small plastic tube. Membranes and trachea covering the brain were gently removed. Glass electrodes loaded with calcium-sensitive dye, Fura-2 dextran (potassium salt, 10,000 mw, Molecular Probes) was inserted into the column in eight of the individuals and into the calyces in the eight remaining, to stain (via retrograde transport) lateral-tract neurons and medial-tract neurons, respectively. To determine whether the retrograde staining was successful, Fura-2 was mixed with a fluorescent dye, Alexa 488 dextran, having the same molecular weight as the calcium indicator. Then the insect was kept in the dark at 4°C overnight.

In vivo calcium imaging recordings were obtained from the dorsal region of the antennal lobe with an epifluorescent microscope (Olympus BX51WI) equipped with 20 × 1.00 water immersion objective (OlympusXLUMPlanFLN). Images were acquired by a 1,344 × 1,224 pixel CMOS camera (Hamamatsu ORCA-Flash4.0 V2 C11440–22CU). The preparation was excited with monochromatic light of 340 nm and 380 nm, respectively (TILL Photonics Polychrome V). Data were acquired ratiometrically. A dichroic mirror (420 nm) and an emission filter (490–530 nm) were used to separate the excitation and emission light. Each recording consisted of 100 double frames at a sampling frequency of 10 Hz, with 43 ms and 14 ms exposure times for the 340 nm and 380 nm lights, respectively. The duration of one recording trial was 10 s, including 4 s with spontaneous activity, 2 s odor stimulation, and a 4 s post-stimulus period. The odor stimulation was carried out by a stimulus controller (SYNTECH CS-55), *via* which humidified charcoal-filtered air was delivered through a 150 mm glass Pasteur-pipette with the stimulus on a piece of filter paper inside. Each odor stimulus was applied twice. To avoid possible

adaptation the interval between trials was 60 s. To confirm that the obtained calcium imaging corresponded to neurons confined to the medial and lateral tract, respectively, we dissected 50% of the brains afterward to visualize the traces of Alexa 488 dextran.

Odor Stimulation

During intracellular recordings, the following stimuli were tested: (i) the primary sex pheromone of *H. armigera*, Z11–16: Al; (ii) the secondary sex pheromone, Z9–16: Al; (iii) the binary mixture of Z11–16: Al and Z9–16: Al; (iv) the behavioral antagonist of *H. armigera*, Z9 14:Al; (v) the headspace of a host plant (sunflower leaves); and (vi) hexane as vehicle control. The three insect-produced components were obtained from Pherobank, Wijk Bij Duurstede, Netherlands. The mixture of Z11–16: Al and Z9–16: Al was in a 95:5 proportion to resemble the natural blend emitted by conspecific females (Piccardi et al., 1977; Kehat et al., 1980; Wu et al., 1997). Stimuli i-iv were diluted in 99% hexane (Sigma) with a final concentration of 500 ng/ml. Twenty microliter of each stimulus was applied to a filter paper placed inside a 120 mm glass cartridge. For the female produced compounds, this meant that each filter paper contained 10 ng of the relevant stimulus. The same odor stimuli as listed above were used during the calcium imaging experiment, but at a higher concentration (required to evoke a response in this technique), i.e., 10 μg at the filter paper. An additional stimulus containing a 50:50 mixture of the host plant (20 μl) and pheromone mix (20 μl) was added in the calcium imaging measurements.

Immunohistochemistry

A total number of nine brains were synapsin stained to generate representative data of the brain of the *H. armigera* male. The moth brain was dissected and immediately transferred into a Zinc-Formaldehyde fixative (Ott, 2008) at room temperature overnight. The brain was then washed in HEPES-buffered saline (HBS, 8 × 30 min; Ott, 2008), and subjected to a permeabilization step (60 min incubation with a fresh mixture of 20% DMSO and 80% methanol) before being washed 3 × 10 min in Tris-HCL buffer (0.1 M, pH 7.4). After pre-incubation in 5% normal goat serum (NGS, Sigma–Adrich, St. Louis, MO, USA) in 0.1 M phosphate-buffered saline (PBS, pH 7.2) containing 0.3% Triton X-100 (PBT), the brain was incubated for 5–6 days at 4°C in the primary antibody, SYNORF1 (dilution 1:25 in PBT containing 1% NGS). Following rinsing in PBT 8 × 30 min, the brain was incubated for 4–5 days at 4°C with Alexa Flour plus 647 conjugated goat-anti-mouse secondary antibody solution (Invitrogen, Eugene, OR; dilution 1:300 in PBT with 1% NGS). After washing 4 × 30 in PBT and 2 × 30 min in PBS, the brain was dehydrated in increasing ethanol series (50%, 70%, 90%, 95%, and 100% (2×), 15 min each). Then, the brain was transferred to the mixture of methyl salicylate and ethanol (1:1) for 15 min and after that cleared completely in methyl salicylate for at least 1 h. Finally, the brains were mounted in Permount between two coverslips, separated by spacers.

Confocal Microscopy

Whole brains containing injected neurons were imaged dorso-frontally by using a confocal laser scanning microscope (LSM 800 Zeiss, Jena, Germany) equipped with a Plan-Neofluar 20×/0.5 objective. Micro-ruby staining was excited with a HeNe laser at 553 nm and the fluorescent emission passed through a 560 nm long-pass filter. The staining of Alexa Fluor 488 was excited with an argon laser at 493 nm and a 505–550 nm bandpass filter. In addition to the fluorescent dyes, the autofluorescence of endogenous fluorophores in the neural tissue was imaged to visualize relevant structures in the brain containing the stained neurons. Since many auto-fluorescent molecules in the tissue are excited at 493 nm, images were obtained using the 493 nm argon laser in combination with a 505–550 nm bandpass filter. Serial optical sections with a resolution of 1,024 × 1,024 pixels were obtained at 2 μm intervals through the entire depth of the brain. The confocal images shown in this study were edited in ZEN 2.3 (blue edition, Carl Zeiss Microscopy GmbH, Jana, Germany).

The immunostained brains were imaged using a Leica SP8 confocal microscope equipped with a 20× multi-immersion objective (HC PL APO CS2 20 × 0.75 IMM). The samples were excited with a 638 nm laser. Images (8 bit) were obtained *via* the Hybrid detector (standard mode) at a voxel size of 0.76 × 0.76 × 1 μm. Multiple Scans were carried out from both the anterior and posterior sides to cover the entire brain.

Spike Data Analyses

The electrophysiological data were analyzed in Spike 2.8. When stable neuronal contact was established, we measured the pre-test activity for 25–40 s to determine the basic firing properties of each recorded neuron before applying stimuli. The spike-trains were abstracted from voltage waveform traces when there was a good signal-to-noise ratio that fitted to a single wave-mark. The pre-test activity pattern of each neuron was described by mean interspike interval (ISI), mean firing rate, coefficient of variation (*Cv*) of ISI, ISI distribution, and joint-ISI scatter plot. Each odor application trial comprised a total period of 2.4 s, including 1 s baseline activity before the stimulus onset, 0.4 s stimulation period, and 1 s post-stimulation period. For describing neural activity during repeated trials of the same stimulus, mean odor traces showing the neuron's firing rates (FR) of every 50 ms were generated. To characterize the temporal responding pattern, we also calculated the binned instantaneous firing rate (BIFR) of every 10 ms for each trial.

To measure responses of individual projection neurons, the odor-evoked response properties were analyzed in two steps. (i) For determining significant responses of individual trials, the upper threshold (T_U) and lower threshold (T_L) was calculated according to the BIFR in the 1 s pre-stimulus (1 s baseline activity) window ($BIFR_{PS}$) at a 5% significance level:

$$T_U \textit{ of individual trial } = \overline{BIFR_{\mathrm{PS}}} + 1.96\sigma_{BIFR_{\mathrm{PS}}} \quad (1)$$

$$T_L \textit{ of individual trial } = \overline{BIFR_{\mathrm{PS}}} - 1.96\sigma_{BIFR_{\mathrm{PS}}} \quad (2)$$

If there was an individual BIFR in the stimulation window higher than the value of T_U or lower than T_L, the trial was determined as an excitatory or inhibitory response, respectively. If the "Lower Threshold" was less than zero, zero was used as the "Lower Threshold."

(ii) For determining responses of repetitive trials, we calculated an upper and lower threshold (TT_U and TT_L) around the mean firing rate in the pre-stimulus window (FR_{PS}) for each mean odor trace at a 5% significance level when there was at least one trial with excitatory/inhibitory response:

$$TT_U \, of \, repetitive \, trial \; = \; \overline{FR_{PS}} + 1.96\sigma_{FR_{PS}} \quad (3)$$

$$TT_L \, of \, repetitive \, trial \; = \; \overline{FR_{PS}} - 1.96\sigma_{FR_{PS}} \quad (4)$$

When the mean firing rate in the stimulation window was higher than the value of TT_U or lower (equal included) than TT_L, the neuron was determined to display a significant excitatory or inhibitory response, respectively. If the TT_L was less than zero, zero was used as the "Lower Threshold."

For displaying the response amplitude, we first standardized the baseline activity by setting the firing rate before stimulation onset to zero. Then, we calculated the spike frequency, i.e., Δ firing rate, averaged over the 400 ms stimulation window. For comparing the odor-evoked response to the same stimulus across individual trials, pairwise Pearson correlations were conducted on the binned instantaneous firing rate histograms of every two trials. The ISI, the firing rate of individual neurons, and the response onset and peak all failed to follow a normal distribution, thus nonparametric analyses (Mann–Whitney *U* test and Wilcoxon test) were conducted among medial-tract and lateral-tract neurons. All probabilities given are two-tailed. For statistical analysis, SPSS, version 24, was used.

Calcium Imaging Data Analyses

In this study, neural activities of projection neurons innervating the cumulus of the MGC were analyzed. Recordings were acquired with Live Acquisition V2.3.0.18 (TILL Photonics) and imported in KNIME Analytics Platform 2.12.2 (KNIME GmbH, Konstanz, Germany). Here, ImageBee neuro plugin (Strauch et al., 2013) was used to construct AL maps and glomerular time series. To determine an average baseline activity, the Fura signal representing the ratio between 340 and 380 nm excitation light (F_{340}/F_{380}) from 0.5 to 0.25 s (within 4 s spontaneous activity) was selected and set to zero. Responses were illustrated as changes in fluorescent level being different from that corresponding to the average baseline activity, specified as $\Delta F_{340}/F_{380}$.

Nomenclature

For naming the neuropil structures of the brain, we used the nomenclature established by Ito et al. (2014). However, with respect to the lateral horn (LH), we have restricted this region to include the area targeted by the non-MGC uni-glomerular projection neurons passing in the medial ALT. The definition of the LH as the target region of all antennal-lobe projection neurons, as stated in Ito et al. (2014), is not applicable to moths, as a prominent branch of the lateral ALT projects to a region located in the SIP. The orientation of all brain structures is indicated relative to the body axis of the insect, as in Homberg et al. (1988).

3D Brain Reconstruction and Single Neuron Tracing

The criteria for selecting suitable preparations for 3D reconstruction were the least damage in regions of interest and sufficient contrast through the entire stack. Out of totally nine immuno-stained male brains, three were selected to construct either full brains or all neuropils of the central brain. Raw confocal stacks were aligned and stitched together using FIJI (Preibisch et al., 2009) and resampled to 1.5 × 1.5 × 1.5 μm voxel size in Amira (Amira 5.3; Thermo Fisher, Visualization Science Group). These complete image stacks were then utilized to carry out image segmentation in Amira. We manually labeled key cross sections of each neuropil of interest in all three spatial planes and then used the wrap-tool in Amira to obtain full neuropil volumes. This process yielded segmented image stacks containing all major neuropils of the moth brain. A surface model of the segmented image stacks was produced in Amira. These were either visualized in Amira or exported as obj-files and uploaded to the Insect Brain Database[1] for visualization.

Five stained neurons from three preparations were traced manually using the *SkeletonTree* plugin in Amira (Schmitt et al., 2004; Evers et al., 2005). Based on background fluorescence of the neuron channel, neuropils close to the traced neurons were segmented in each brain preparations as described above.

RESULTS

Outline of the Male *Helicoverpa armigera* Brain

To provide a general anatomical framework for interpreting the functional and morphological information from odor processing neurons we have generated 3D reconstructions of three representative male *H. armigera* brains. Based on synapsin-labeled whole-mount preparations, we segmented all identifiable major neuropils (**Figure 1**). This 3D brain atlas includes 25 separate neuropils (23 paired and two unpaired) and is thus the most detailed representations of any moth brain to date (interactive viewing and download at: www.insectbrain.org; https://hdl.handle.net/20.500.12158/SIN-0000020.2). While particular attention was paid to the reconstruction of olfactory brain regions, such as the antennal lobes (AL) and the components of the mushroom body, we also reconstructed all optic lobe neuropils (lamina, medulla, lobula, lobula plate and accessory medulla), as well as the sub-compartments of the anterior optic tubercle (upper unit, lower unit and nodular unit), the lateral complex (lateral accessory lobe (LAL), bulb and gall), and the central complex (fan-shaped body, ellipsoid body, protocerebral bridge (PB), noduli, and posterior optic tubercle). Given the unclear boundaries within the remaining major parts of the brain (superior, inferior, ventrolateral, ventromedial, supraesophageal, and subesophageal neuropils, as well as the LH), we did not segment these regions separately,

[1] www.insectbraindb.org

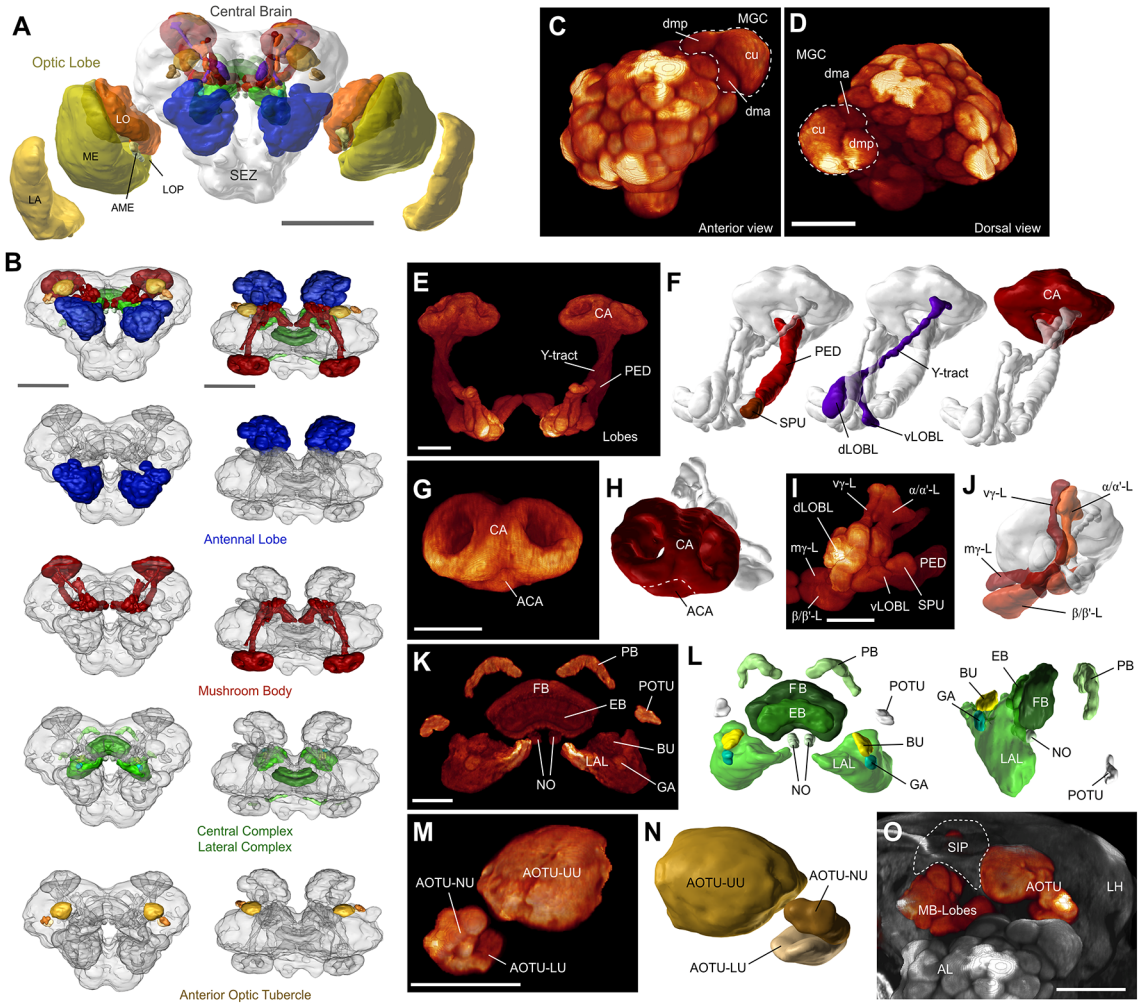

FIGURE 1 | The layout of the *Helicoverpa armigera* brain. **(A)** Three-dimensional reconstruction of an anti-synapsin labeled male brain. Shown are polygonal surface models based on segmented confocal image stacks. LA, lamina; ME, medulla; LO, lobula; LOP, lobula plate; AME, accessory medulla; SEZ, subesophageal zone. Scale bar: 500 μm. **(B)** The main defined neuropils of the central brain. *From top to bottom*: All defined central brain neuropils (colored) shown together with the continuous mass of undefined regions (gray); antennal lobes (AL); mushroom bodies (MB); central and lateral complex; anterior optic tubercle. Scale bar: 300 μm **(C,D)** Volume rendering of one male antennal lobe (anti-synapsin labeling), highlighting the location and composition of the macroglomerular complex (MGC); anterior view **(C)**, and dorsal view **(D)**. Scale bar: 100 μm. **(E)** Volume rendering of the MB. All remaining neuropils were masked. **(F)** Principal components of the mushroom body besides the main lobe system: Calyx (CA), pedunculus (PED) with spur (SPU), and Y-tract with dorsal and ventral lobelets (dLOBL, vLOBL). **(G)** Volume rendering of the calyx, highlighting the accessory calyx (ACA), and the two fused rings of the main calyx. **(H)** Surface reconstruction of the calyx. **(I,J)** Volume rendering **(I)** and reconstruction **(J)** of the main lobe systems of the mushroom body. Vertical gamma lobe (vγ-L), medial gamma lobe (mγ-L), alpha/alpha'-lobes (α/α'-L), and beta/beta'-lobes (β/β'-L). **(K,L)** Volume rendering **(K)** and reconstruction **(L)** of the central complex and lateral complexes. *Left panel* in **(L)**: anterodorsal view; *right panel*: lateral view. PB, protocerebral bridge; FB, fan-shaped body; EB, ellipsoid body; NO, noduli; POTU, posterior optic tubercle; BU, bulbs; GA, gall; LAL, lateral accessory lobe. **(M,N)** Volume rendering **(M)** and reconstruction **(N)** of the anterior optic tubercle (AOTU) and its three compartments; upper unit (UU), lower unit (LU), and nodular unit (NU). **(O)** Volume rendering of the frontal portion of the central brain, highlighting the relative location of the AOTU, the mushroom body lobes, the AL, and the approximate locations of the superior intermediate protocerebrum (SIP, dashed line) and the lateral horn (LH). AOTU and mushroom body lobes were rendered separately, using a different colormap. Scalebar **(E–O)**: 50 μm. Panels A, F, H, J, L, and N obtained from insectbraindb.org.

but rather used the below described dye fills to highlight relevant compartments in these "unstructured" parts of the brain.

Overall, the *H. armigera* brain is a typical lepidopteran brain and resembles the general outline of previously described butterflies (Heinze and Reppert, 2012; Montgomery and Ott, 2015; Montgomery et al., 2016) and hawkmoths (El Jundi et al., 2009; Stöckl et al., 2016). Whereas these species rely heavily on vision and therefore possess large regions dedicated to early visual processing, our nocturnal moth has much smaller optic lobes, in line with its olfactory ecology. Additionally, the first processing station for visual information in the central brain, the anterior optic tubercle, is also smaller compared to the day active butterflies.

With respect to olfactory brain areas, a pronounced sexual dimorphism is represented by a three-unit MGC in

H. armigera males (Skiri et al., 2005; Zhao et al., 2016b). Accordingly, we also identified these three male-specific glomeruli in the individuals examined in the current study. The main second-order olfactory brain region, the mushroom body, was much smaller in our noctuid moths compared to butterflies and hawkmoths, but nevertheless consists of equally elaborate subdivisions.

Finally, the central and lateral complexes appear largely identical to all other lepidopteran insects studied and in fact comprise the same subdivisions as all insects examined to date. With respect to shape and relative size, these regions most closely reflected the layout of the corresponding areas in the Bogong moth (*Agrotis infusa*, Adden et al., 2020) and the Turnip moth (*Agrotis segetum*, de Vries et al., 2017), underlining the high degree of conservation of these central brain centers.

The Column Is a Major Site of Convergence for Pheromone and General Odor Processing

To obtain an anatomical overview of the pheromone and the plant-odor pathways in the moth brain, we applied two different fluorescent dyes into the male antennal lobe (n = 5). Micro-ruby was injected into the MGC and Alexa 488 into the OG (**Figures 2A,B**). These injections confirmed previous findings reporting that projection fields of medial-tract neurons that originate in the MGC are not overlapping with those originating from the OG (Homberg et al., 1988; Seki et al., 2005; Zhao et al., 2014). While medial-tract neurons from OG targeted large areas of the mushroom body calyx before terminating in the LH, the MGC projections sent collaterals to a restricted area in the inner layer of the calycal cups and ended in the superior lateral protocerebrum, located dorso-medially of the LH.

In contrast, the target regions of the two projection neuron types in the lateral ALT overlapped substantially (**Figure 2C**). Strikingly, all MGC projection neurons in this tract projected to the column, the small, pillar-like region located in the superior inter-mediate protocerebrum (SIP), tucked between the anterior optic tubercle (AOTU) and the mushroom body vertical lobe (**Figure 2D**). This structure also received projections from lateral-tract projection neurons originating from OG (**Figure 2E**). The column is therefore a site of convergence for pheromone and general odor information. However, only a subset of non-MGC projection neurons in the lateral tract terminate in the column. Approximately half of these axons continue along a lateral trajectory to terminate in the LH (**Figures 2E,H**). While the majority of projections remained on the ipsilateral side of the brain, a few commissural fibers (CFs) originating from the MGC were also observed in these preparations.

Corresponding injections into the female antennal lobe visualized the same ALTs as in males (n = 7), including lateral-tract projection neurons targeting the column and the LH. The CF bundle found in male (**Figures 2C,D**) was not stained in females (**Supplementary Figure S1**).

As the column was the only site in the brain that showed substantial overlap in pheromone and plant odor processing neurons, we aimed at obtaining more precise information about the neurons serving as input to this region. We injected a small amount of fluorescent dye to the column region using the intracellular-staining setup (n = 2). These injections resulted in labeling of projection neurons only in the lateral ALT, with no axons marked in the medial or mediolateral ALT (**Figure 3A**). This finding confirmed that neurons in the lateral tract provide the sole antennal-lobe input to the column. Furthermore, a belt-like CF bundle passing posteriorly of the fan-shaped body connected the columns in both hemispheres (**Figure 3B**). In addition to the contralateral column, the calyces and the antennal lobe in the contralateral hemisphere were labeled as well (**Figure 3B**). In the contralateral antennal lobe, the staining was most pronounced in the cumulus of the MGC, but traces of fluorescent dye were also visible in the two smaller MGC units, as well as in one ordinary glomerulus (**Figures 3C,D**). In the preparation with the most numerously labeled neurons, a group of eight cell bodies in the lateral soma cluster of the contralateral antennal lobe were strongly stained (**Figure 3B**, red dashed circle), suggesting that at least eight MGC-projection neurons provide input to both columns.

Neurons Projecting to the Column Functionally Differ From Those Projecting to the Calyces

After we established that the column receives exclusive input from the lateral ALT and serves as a likely major site for pheromone processing, we aimed at identifying functional correlates of these anatomical findings. We therefore performed calcium imaging on neurons originating in the main glomerulus of the MGC, the cumulus. We specifically compared the response patterns of cumulus-neuron populations within the lateral tract (projecting to the column) to those of the medial-tract (projecting to the calyx). For this purpose, we applied a calcium-sensitive dye (Fura 2) together with Alexa 488 in either one of the two target sites (**Figure 3E**). As expected, injection from the calyces selectively labeled medial tract neurons, while injections from the column region only labeled neurons confined to the lateral tract (**Supplementary Figure S2**). The imaging data were obtained from the dorsal region of the antennal lobe, i.e., the input sites for both sets of neurons (**Figures 3F,G**).

Cumulus lateral tract neurons responded to all insect-produced compounds, including the primary pheromone, secondary pheromone, behavioral antagonist, and the natural pheromone blend (**Figure 3H**). These responses were similar across all stimulus conditions and showed a consistently tonic temporal profile with a moderate response amplitude. In contrast, the medial-tract neurons projecting to the calyces were activated mainly by stimuli containing the primary pheromone. These responses were stronger and showed a phasic component that decayed over the course of the stimulation period. Interestingly, despite the fact that both MGC neuron populations

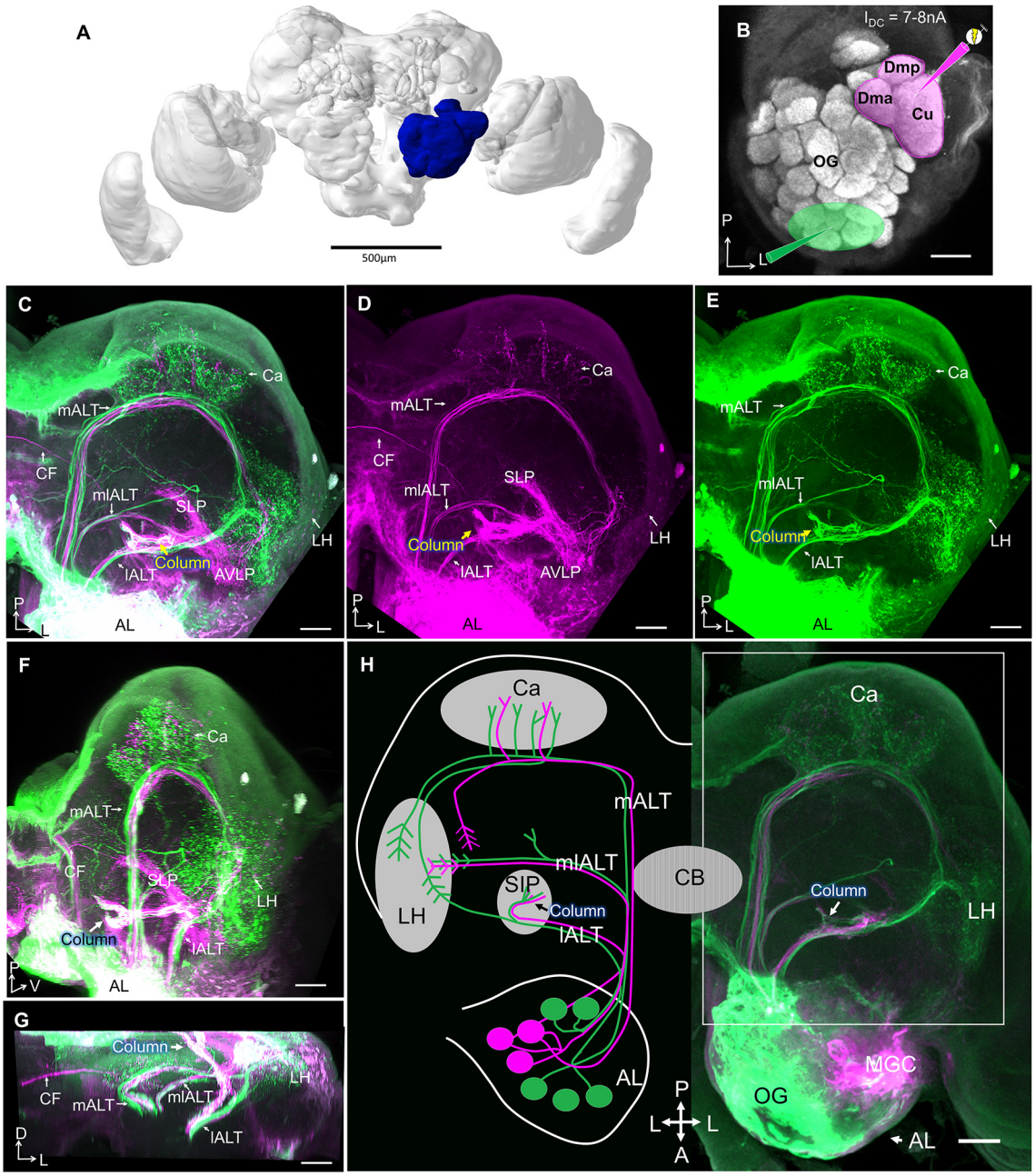

FIGURE 2 | Projection profiles of pheromone and non-pheromone antennal-lobe output neurons in males. **(A)** Brain reconstruction with highlighted left antennal lobe (AL, *blue*). Scale bar, 500 µm. **(B)** Confocal image of the left AL illustrating two "anterograde labeling" sites, the MGC in *magenta*, and the ordinary glomeruli (OG) in *green*. **(C)** Confocal image of a mass-stained preparation showing the three main AL tracts (ALTs), including staining MGC (*magenta*) and the OG (*green*). *White* indicates target regions receiving overlapping input from MGC and OG. Both MGC and OG lateral-tract projection neurons innervate the column (arrow). **(D,E)** Single-channel confocal images of **(C)** showing distinct projection patterns of MGC output neurons **(D)** vs. OG output neurons **(E)** in the protocerebrum. **(F,G)** Target areas of lateral ALT (lALT) neurons originating from the MGC (*magenta*) and the OG (*green*) in sagittal **(F)** and frontal **(G)** view. *White* indicates an overlap of projections from MGC and OG. **(H)** Schematic overview of pheromone (*magenta*) and non-pheromone (*green*) AL output neurons in males and a corresponding confocal image. All sections except **(F,G)** in dorsal view. (l/m/ml)ALT, (lateral/medial/mediolateral) antennal lobe tract; Ca, Calyces of the mushroom body; LH, lateral horn; PC, protocerebrum; SIP, superior intermediate protocerebrum; SLP, superior lateral protocerebrum; AVLP, anterior ventro-lateral protocerebrum; CF, commissural fiber; CB, central body. A, anterior; L, lateral; M, medial; P, posterior; V, ventral. Scale bars **(B–H)**, 50 µm.

received input from the same glomerulus, i.e., the cumulus, there were clear differences in response patterns to the pheromone stimuli. In addition, the mixture of plant odors and pheromone blend elicited a suppression in medial-tract neurons, whereas the lateral-tract neurons showed no such effect (**Figure 3H**, black rectangle).

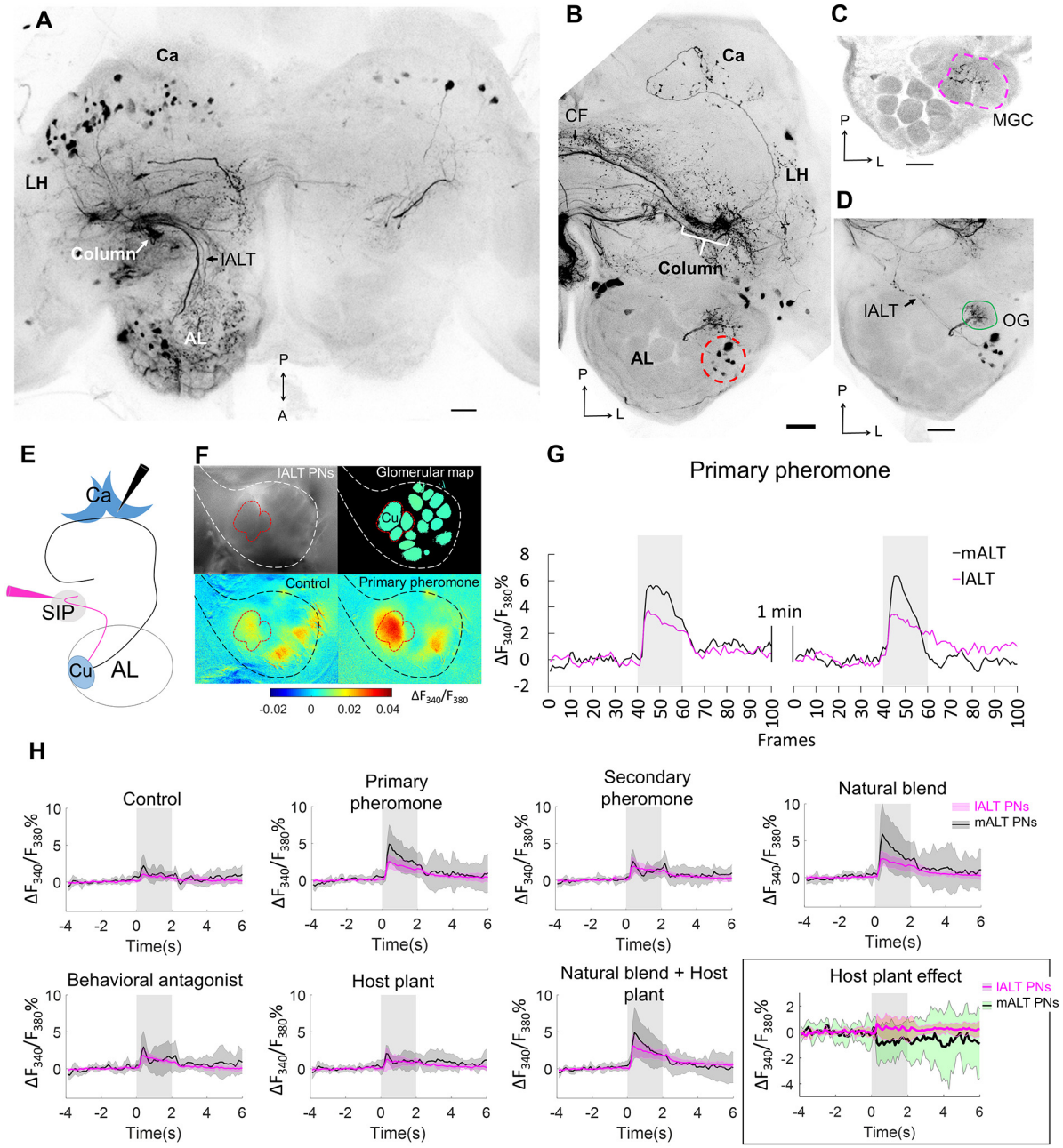

FIGURE 3 | Cumulus neurons confined to the lALT and their odor responses during calcium imaging as compared to mALT neurons. **(A)** Application of dye in the superior inter-mediate protocerebrum (SIP) visualized antennal-lobe projection neurons confined to the lateral AL-tract (lALT) in the ipsilateral hemisphere. These neurons, which originate from both MGC and OG, have somata in the lateral cell cluster and project to the ipsilateral column. **(B)** Dye application in the SIP also labeled a bundle of commissural fibres (CFs) crossing the brain midline and connecting with the contralateral column. Here, in the other hemisphere, eight AL somata (red dash circle) were labeled, demonstrating that these bilateral AL neurons connect the column in both hemispheres. Stained projections in the calyces (Ca) indicate that the bilateral neurons innervate this neuropil as well. **(C,D)** Confocal images showing that the dendrites of the bilateral neurons branch in the MGC **(C)** and one ordinary glomerulus located more ventrally **(D)**. **(E)** Illustration of the two "retrograde labeling" sites used for the application of the calcium indicator. *Black* arrowhead indicates the injection point into the calyx for labeling the mALT neurons. *Magenta* arrowhead indicates the injection point in the column region to label the lALT neurons. **(F)** Pictorial material representing calcium imaging data: *top-left*, raw image of an AL stained with Fura from the column; *top-right*, a processed image showing a map of recognized glomeruli; *down-left* and *down-right*, Heat maps of responses to the control and primary pheromone. *White* and *black* border circumvents the area of AL, *red* border shows the MGC region. **(G)** Example of calcium imaging traces showing response to the primary pheromone from neurons in the mALT (*black*) and lALT (*magenta*). The standardized traces quantify the neuronal activity of two repeated stimulations with 100 ms sampling frequency. The interval between stimulations is 1 min. **(H)** Responding patterns of lALT and mALT neurons to each stimulus. Each neuron group contains 8 moths, data showed as mean ± SD. The host plant effect is illustrated in the *black* rectangle. (l/m)ALT, (lateral/medial) antennal lobe tract; LH, lateral horn; A, anterior; L, lateral; M, medial; P, posterior. Scale bars, 50 μm. *Gray* bar, the duration of the stimulus (2 s).

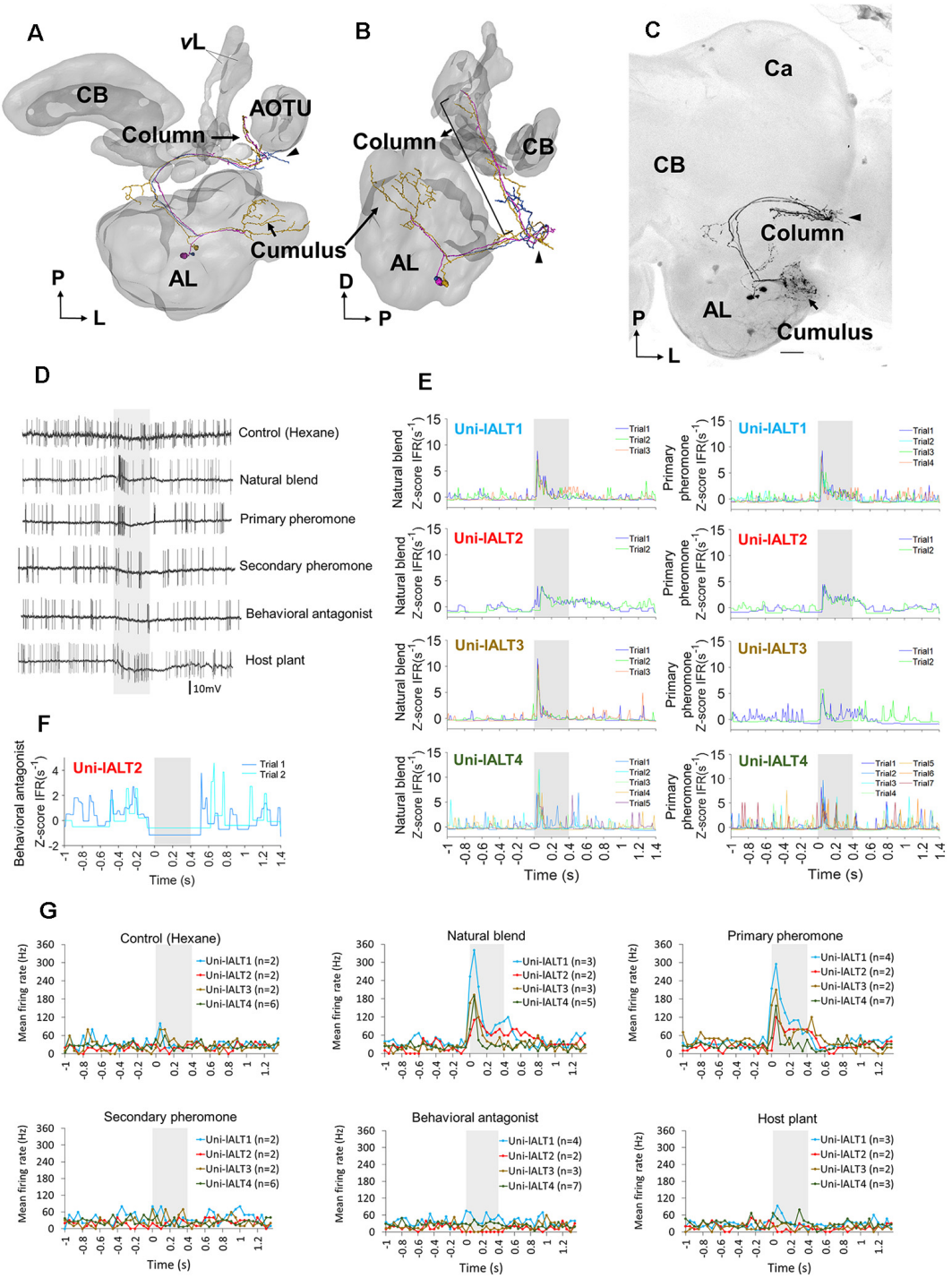

FIGURE 4 | Morphology and electrophysiology of unilateral lateral-tract neurons originating in the cumulus. **(A,B)** 3D reconstruction of three morphologically similar, co-stained neurons (Uni-lALT4) in dorsal frontal view **(A)** and sagittal view **(B)**. The neurons project directly to the column tucked between the vertical lobe (*v*L) and the anterior optic tubercle (AOTU). The arrowhead indicates a short side branch extending from one axon posterior of the antennal lobe (AL). **(C)** Confocal image of the three co-stained lateral-tract cumulus neurons. **(D)** Spiking activity of one of the three co-stained unilateral neurons during the application of odor stimuli. The neuron (Uni-lALT4) showed a phasic activation to the natural blend and the primary pheromone. **(E)** Traces of instantaneous firing rates including responses of four unilateral lALT neurons to the natural blend and the primary pheromone on each trial. **(F)** Traces of instantaneous firing rates of one neuron (Uni-lALT2) showing an inhibitory response to the behavioral antagonist. **(G)** Mean spike frequencies of repeated trials in each neuron (bin-size: 50 ms, n: number of repeated trials). Ca, Calyces of the mushroom body; CB, central body. A anterior; L, lateral; M, medial; P, posterior. Scale bars, 50 μm. *Grey* bar, the duration of the stimulus (400 ms).

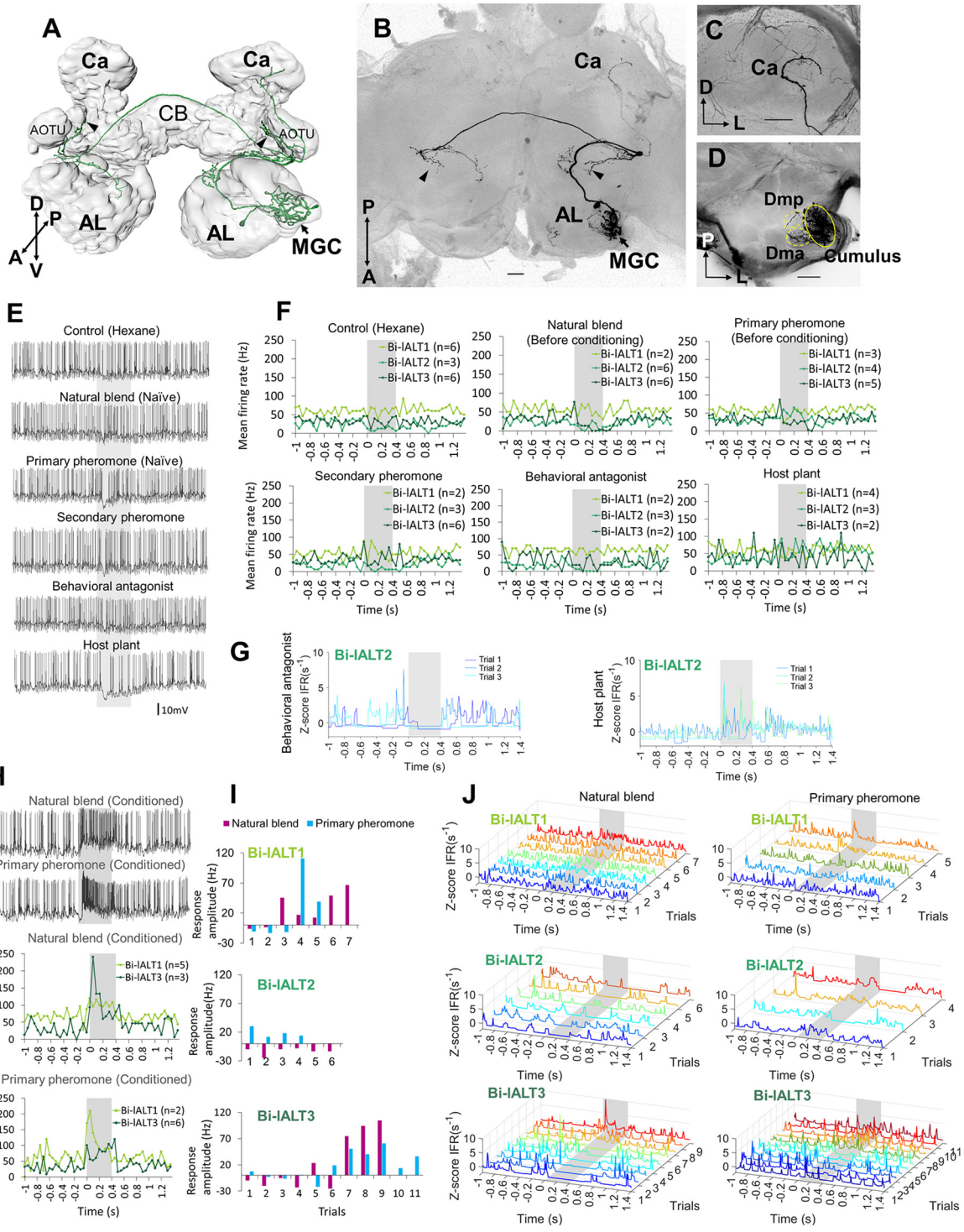

FIGURE 5 | Morphology and electrophysiology of bilateral lateral-tract neurons with restricted projections in the protocerebrum (Sub-type I). **(A)** 3D reconstruction of one neuron (Bi-lALT3) in dorsal-frontal view, demonstrating projections to ipsilateral and contralateral column (arrowheads), and ipsilateral calyx (Ca). **(B–D)** Confocal images of Bi-lALT3. The fiber projecting to the ipsilateral Ca is shown in **(C)**. Arborizations in the antennal lobe (AL) are shown in **(D)**, including dendrites restricted to the MGC, in which the cumulus is considerably stronger innervated than dma and dmp. **(E)** Spiking activity of one neuron (Bi-lALT3) during the first-trial application of each stimulus (i.e., naïve). **(F)** Mean spiking frequencies during repeated trials in the three Sub-type I bilateral neurons before induced response appeared, i.e., first three trials for Bi-lALT1 and first five trials for Bi-lALT3 (bin-size: 50 ms, n: number of repeated trials). **(G)** Traces of instantaneous firing rates of one neuron (Bi-lALT2) showing an inhibitory response to the behavioral antagonist and an excitatory response to the host plant. **(H)** Induced response in neuron Bi-lALT3. *Upper part*: spiking activities of the neuron during the 7th application of natural blend and primary pheromone, respectively. *Lower part*: spiking frequencies to the

FIGURE 5 | Continued
same stimuli during 4th–7th trials in neuron Bi-lALT1 and 7th–11th trial in neurons Bi-lALT3 (bin-size: 50 ms, n: number of repeated trials). **(I)** Induced responses are present in two of the three sub-type I bilateral neurons, i.e., Bi-lALT1 and Bi-lALT3 (no effect in Bi-lALT2). **(J)** Traces of instantaneous firing rates illustrating variable responses to the natural blend and the primary pheromone across repeated trials in the same two Sub-type I bilateral lALT neurons, Bi-lALT1 and Bi-lALT3. AOTU, anterior optic tubercle; CB, central body. A, anterior; L, lateral; M, medial; P, posterior; V, ventral. AL, antennal lobe; Ca, Calyces of the mushroom body; CB, central body. A, anterior; L, lateral; M, medial; P, posterior; V, ventral. Scale bars, 50 μm. *Gray* bar, the duration of the stimulus (400 ms).

MGC Neurons of the Lateral ALT Are Morphologically and Physiologically Heterogeneous

As we found broad differences in the odor response profiles on the population level between neurons of the lateral and the medial ALTs, we next aimed at investigating how these odor responses were reflected on the level of anatomically identified, single neurons. We thus carried out intracellular recordings from the thick dendrites of MGC projection neurons combined with intracellular dye injection. Ten MGC lateral-tract neurons were identified morphologically and physiologically, all having glomerular dendritic arborizations focused in the cumulus of the MGC. The physiological features of these neurons were then compared to nine MGC cumulus neurons confined to the medial tract.

Morphological Features

All ten MGC lateral-tract projection neurons from which complete dye fills were obtained originated in the cumulus and projected to the column in the SIP. Typically, these neurons exited the postero-ventral part of the antennal lobe and projected laterally. Before reaching the LH, they changed direction and continued dorso medially, eventually terminating in the column (located between the AOTU and the MB vertical lobe). Despite all targeting the column and having their somata located in the lateral cell body cluster of the antennal lobe, these projection neurons constituted a relatively heterogeneous population. Four were unilateral neurons targeting exclusively the ipsilateral column, whereas the remaining six cells projected bilaterally.

All unilateral neurons turned off their initial course within the lateral ALT and continued dorsally towards the column. Here they formed a mainly unbranched terminal projection (example in **Figures 4A–C**; all unilateral neuron anatomies shown in **Supplementary Figures S3A–D**). Two of these neurons extended a short side-branch into the lateral protocerebrum before entering the column.

The six bilateral neurons targeted the column in *both* hemispheres. Like their unilateral counterparts, they originated in the cumulus and followed the initial course of the lateral ALT. At the turning point adjacent to the LH, the axons split. One projection targeted the ipsilateral column, whereas the other targeted the contralateral column, with the main axon crossing the brain midline posteriorly of the fan-shaped body. In addition to innervating the column in both hemispheres, all bilateral neurons had some terminal branches in the ipsilateral calyx.

Based on their projection patterns, the six bilateral neurons were classified in two sub-populations (all morphologies shown in **Supplementary Figures S3E–J**). One consisted of three morphologically similar neurons with clearly defined terminals in restricted areas of the protocerebrum (sub-type I), whereas the other included three morphologically similar neurons with more widespread projections (sub-type II). A typical example of sub-type I is shown in **Figure 5**. This neuron possesses three main projection fields covering the ipsilateral column, the ipsilateral calyx (**Figure 5C**), and the contralateral column. An example of sub-type II is shown in **Figure 6**. In addition to innervating the three projection fields mentioned above, this neuron had numerous terminal projections in a relatively large area of the ipsilateral protocerebrum and one or two short side branches extending dorsally from the CF into the SIP, terminating near the medial edge of the MB vertical lobe (**Figure 6D**). Finally, this neuron extended numerous short processes from the main axon on its initial route from the antennal lobe.

Physiological Characteristics Differ Between the Two Main Types of Lateral-Tract Neurons

The two main morphological categories of lateral-tract MGC neurons, i.e., the unilateral and bilateral types, displayed different response patterns during stimulation. Generally, the odor-evoked activation patterns were more homogenous in the unilateral neurons than in the bilateral neurons. All four unilateral neurons displayed significant responses in the form of increased spiking frequencies during stimulation with the primary pheromone and the pheromone mixture (**Figures 4D,E,G**). Three of these neurons (Uni-lALT1, 3, and 4) not only shared consistent responses with respect to odor tuning, but additionally displayed highly similar temporal response profiles. These were characterized by sharp phasic onset responses (lasting 20–30 ms) that gradually faded away towards background activity over the course of the remaining stimulus duration. The fourth neuron (Uni-lALT2) showed a slightly different response pattern. In addition to responding with more phasic-tonic excitation to the primary pheromone and natural blend, it was inhibited by the behavioral antagonist (**Figures 4E,F**). Interestingly, the highly phasic responses seen in the majority of unilateral neurons differ from the population responses of lateral-tract neurons as described by calcium imaging. Whereas those experiments revealed a moderate, tonic increase in activation in response to all insect produced stimuli, the single cell responses of the unilateral neurons appeared to be more similar to the calcium imaging based population responses of neurons in the medial ALT.

In contrast to the relatively consistent response properties of the unilateral MGC neurons in the lateral ALT, the bilateral neurons showed more heterogeneous spiking patterns and less pronounced responses (**Figures 5**, **6**). The three cells with restricted projections (sub-type I) were not strongly excited by any of the stimuli that elicited responses in the unilateral neurons. Only one neuron, Bi-lALT2, showed an immediate response in the form of a mild excitation to the primary pheromone (and the plant odor) and an inhibition to the behavioral antagonist (**Figures 5G,J**). Interestingly,

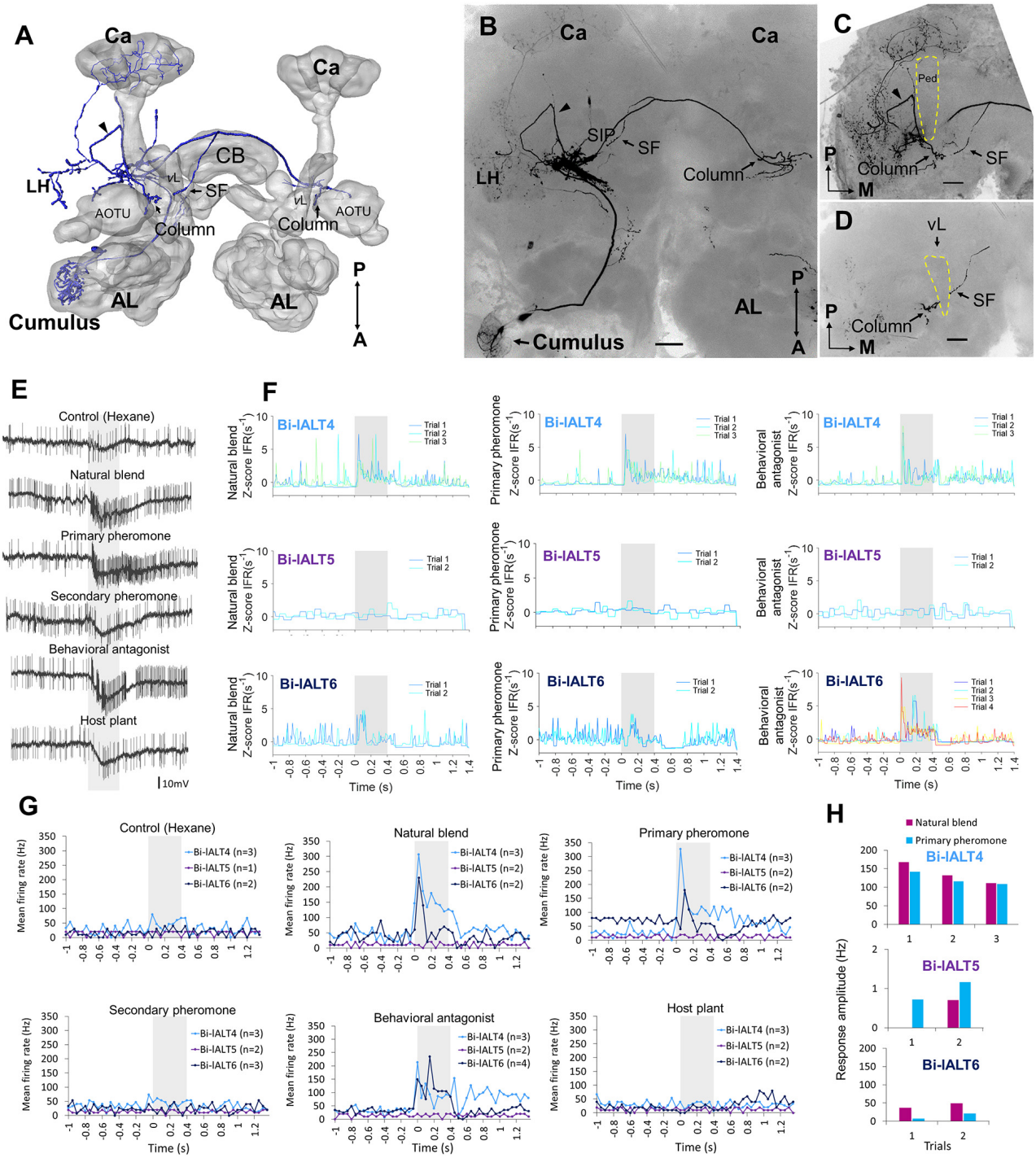

FIGURE 6 | Morphology and electrophysiology of the bilateral lateral-tract neuron type with widespread protocerebral innervations (Sub-type II). **(A–D)** 3D reconstruction **(A)** and confocal images **(B–D)** of one neuron (Bi-IALT6) in dorsal-frontal view. In addition to innervating the column in both hemispheres, the neuron projects to calyces (Ca), LH, and superior inter-mediate protocerebrum (SIP) in the ipsilateral hemisphere. The arrowhead in panel **(C)** indicates one neural branch forming a small loop close to the lateral edge of the peduncle (Ped) before targeting the ipsilateral column. In panel **(D)**, a short side fiber (SF) extending from the CF and projecting dorsally of the vertical lobe (*v*L) to the ipsilateral SIP is visualized. **(E)** Spiking activity of the bilateral neuron, Bi-IALT6, during the application of odor stimuli. The neuron showed a phasic-tonic excitation to the natural blend, the primary pheromone, and the behavioral antagonist. **(F)** Traces of instantaneous firing rates illustrate the responses of the three Sub-type II bilateral IALT neurons to the natural blend, the primary pheromone, and the behavioral antagonist on each trial. **(G)** Mean spike frequencies of repeated trials in each neuron (bin-size: 50 ms, n: number of repeated trials). **(H)** No induced responses appear in any of the three Sub-type II bilateral neurons. AL, antennal lobe; CB, central body. A, anterior; L, lateral; M, medial; P, posterior. Scale bars, 50 μm. *Gray* bar, the duration of the stimulus (400 ms).

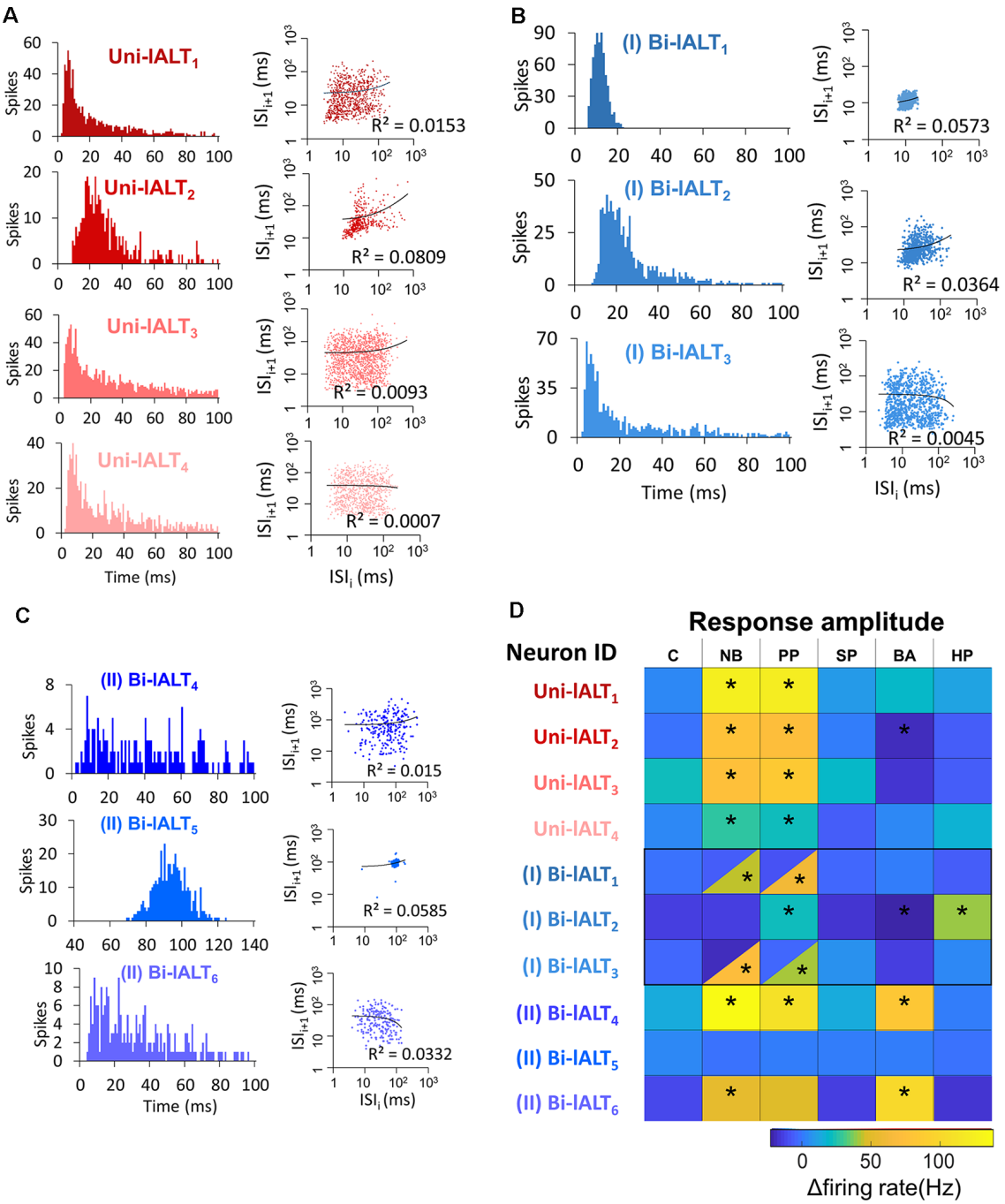

FIGURE 7 | Overview of distinct parameters in all recorded lateral-tract neurons. **(A–C)** Spontaneous firing pattern during pre-test activity, including ISI histograms and Joint ISI scatter plot. **(D)** Heat map of firing rate amplitudes in the 10 lateral-tract neurons. *Indicates significant response, determined according to the threshold of baseline activity of individual neurons (with 95% confidence level). C, control; NB, natural blend; PP, primary pheromone; SP, secondary pheromone; BA, behavioral antagonist; HP, host plant.

the two remaining cells showed a remarkable switch in response characteristics after repeated stimulations. The first one, Bi-lALT1, displayed no response to the primary pheromone in the first three trials (naïve), but did respond on the forth and the fifth trial (**Figures 5E,H,I,J**). An induced response occurred during stimulation with the pheromone blend as well, but less pronounced. The second neuron, Bi-lALT3, also displayed induced responses, but switched from inhibition to excitation. In this case, the sensitization occurred mainly during repeated stimulations with the natural blend. Here, a phasic-tonic excitation appeared after the sixth trial (**Figures 5I,F**). The effect was much weaker during repeated stimulation with

the major pheromone alone. The third bilateral neuron with restricted branching pattern, Bi-lALT2, was not dependent on repeated stimulations for eliciting responses. Generally, the responses of these three bilateral neurons had a phasic tonic temporal profile.

The three sub-type II bilateral neurons exhibited even more heterogeneous response patterns than the sub-type I (**Figure 6E**). Two of these cells, Bi-lALT4 and Bi-lALT6, showed strong excitatory responses to the primary pheromone and/or pheromone mixture, as well as to the behavioral antagonist, while the third neuron, Bi-lALT5, did not respond to any stimulus. Two of three cells responded immediately, thus repeated stimulations were applied only two or three times. They kept a consistent temporal response profile throughout the experiments, characterized by a strong onset burst followed by a lasting tonic response in most stimulus presentations. In some cases, a tonic response (either excitatory or inhibitory) outlasted the stimulus duration. These neurons might therefore account for the tonic responses in the calcium imaging experiments.

Analysis of all neurons' spontaneous firing properties during the 25–40 s pre-test window revealed a moderately high coefficient of variation of inter-spike interval of the uni-lateral neurons (ISI *Cv* = 1.14 ± 0.19, for details see **Supplementary Table S1**). This value and the Poisson-like distributions of ISI histograms indicate that the spontaneous firing properties of the unilateral neurons are relatively bursty (**Figure 7A**). This is in contrast to the recorded bilateral neurons, which displayed more varied firing patterns (**Figures 7B,C**). Taken together, the unilateral neurons are homogeneous with regard to both pre-test activity and odor-evoked responses (**Figure 7D**), while the bilateral neurons are heterogeneous according to these properties.

Lateral-Tract and Medial-Tract Neuron Physiologies Differ in Detailed Response Profiles

So far, our results have shown that the response properties of the lateral tract neurons differ from those of the medial tract in several ways. On a population level (calcium imaging), responses of the lateral-tract cells occurred during stimulation with all insect produced compounds tested and were moderate in strength with a largely tonic temporal profile. In contrast, when medial–tract neurons were investigated in the same way, responses were selective to stimuli containing the primary pheromone and showed a more transient temporal profile. On the level of single neurons, the more tonic responses of lateral-tract neurons were partially reflected by individual bilateral neurons, whereas all unilateral neurons of the lateral tract resembled medial-tract neurons more closely. To more thoroughly differentiate the physiological properties of the MGC neurons in the lateral and medial ALT, we quantitatively compared the electrophysiological data from the ten described lateral-tract cumulus neurons with nine medial-tract cumulus neurons.

A comparison was first conducted between the two most homogeneous neuron types, the medial-tract neurons and unilateral lateral-tract neurons. Since the firing pattern of spontaneous activity is an intrinsic property often used to describe individual cell types, we compared the spiking patterns of the two neuron types during the pre-test window. The unilateral neurons in the lateral ALT, in contrast to the medial-tract neurons, displayed more bursty spiking patterns, demonstrated by the shorter minimum ISI during pre-test activity (Mann–Whitney *U* test, $U = 4$, $p = 0.03$), and at the same time, a comparable mean ISIs ($p > 0.28$, **Figure 8A**). Moreover, the response amplitude during stimulation with the primary pheromone was larger in the unilateral lateral-tract neurons than in the medial-tract neurons ($U = 5$, $p = 0.05$, **Figure 8B**). No other stimuli evoked significantly different firing rate changes between these two neuron types.

To compare the odor-evoked responses across all neuron categories, including the bilateral lateral-tract neurons, we compared the instantaneous firing rate plots (binned every 10 ms) of each trial of single-cell recording to all stimuli (**Supplementary Figure S4**). Stimuli containing the primary pheromone evoked distinct temporal response patterns in each neuron category, i.e., a phasic response in the unilateral lateral–tract neurons, a phasic-tonic response in the bilateral lateral-tract neurons, and a phasic-tonic or phasic-inhibition response in the medial-tract neurons. The response patterns of unilateral neurons to the main pheromone component and to the pheromone mixture were largely consistent across all four neurons. Medial-tract neurons, on the other hand, responded more variably. Only six of nine medial-tract neurons responded to the primary component, of which four responded to the natural blend. During these stimulations, almost all responsive medial-tract neurons had an apparently longer response delay compared to the lateral-tract neurons (**Figure 8C**). To confirm this observation, we quantified these neurons' onset and peak of excitatory responses based on each recorded trial (**Figure 8D**). The onsets were determined at the time point when the instantaneous firing rate (binned every 1 ms) exceeded the response threshold (mean instantaneous firing rate in the 1 s pre-stimulation + 1.96*SD). The response onsets failed to show difference across neuron types Mann–Whitney *U* test, *p*s > 0.08). Comparisons of response peak latency of all recorded neurons showed that the unilateral lateral-tract neurons had an earlier response peak to the natural blend than the bilateral type (54.7 ± 9.8 vs. 134.4 ± 41.4 ms, Mann–Whitney *U* test, $U = 1$, $p = 0.04$, **Figure 8D**). The response peaks of unilateral neurons during stimulation with the primary pheromone also appeared earlier than corresponding peaks in medial-tract neurons (54.7 ± 9.8 vs. 85.0 ± 7.5 ms, Mann–Whitney *U* test, $U = 2$, $p = 0.03$, **Figure 8D**). The response timing pattern illustrated that the unilateral lateral-tract neurons generally responding in a rapid manner compared with the medial-tract neurons as well as the bilateral neurons (**Figure 8E**).

Several physiological features, including response profile, temporal response pattern, and onset delay, as well as peak delay, suggest that the unilateral lateral-tract neurons respond more homogeneously than the medial-tract neurons, whereas the bilateral lateral-tract neurons are the most heterogeneous population. This was confirmed by correlating the binned instantaneous firing rate between every two trials of 19 neurons

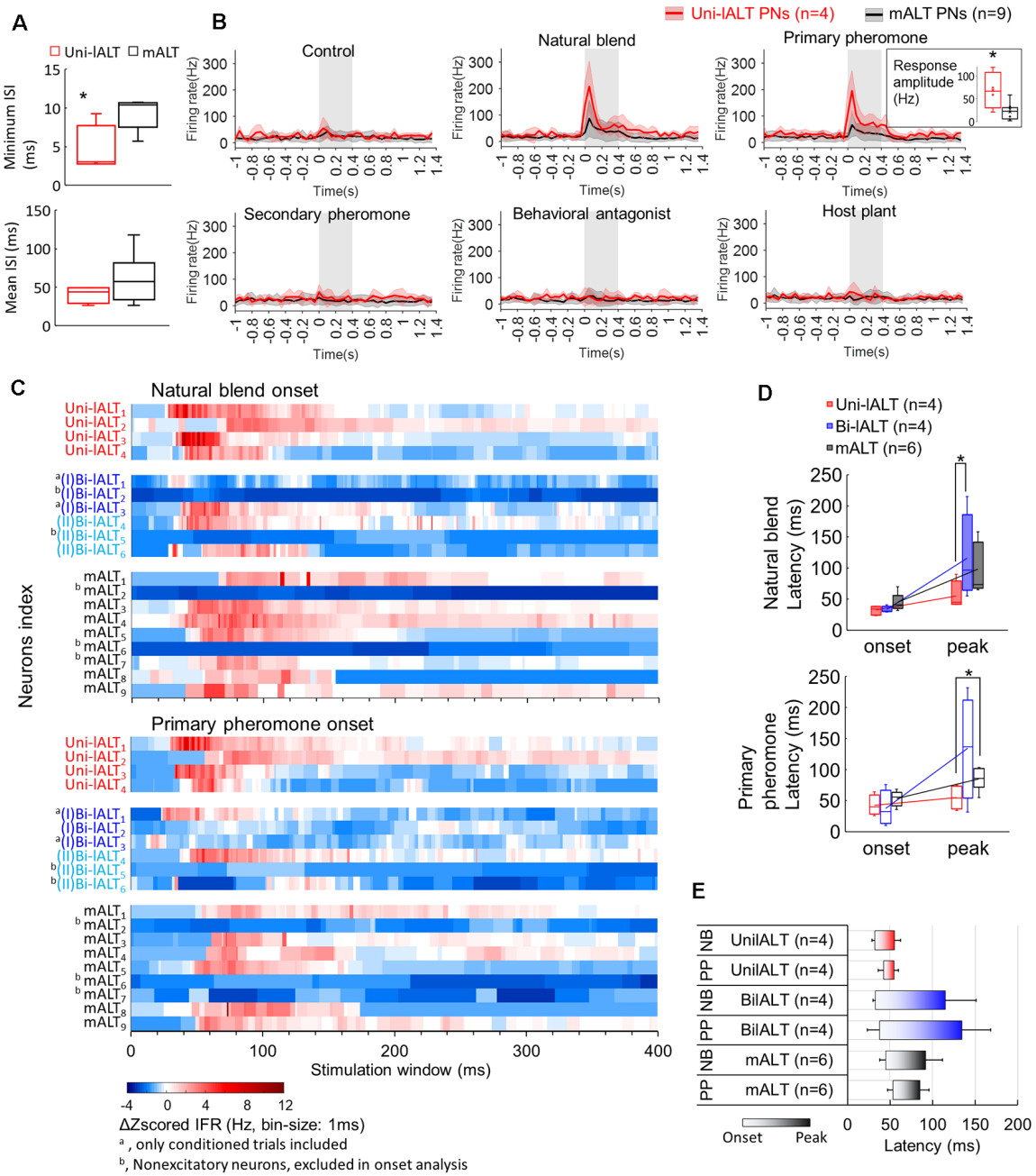

FIGURE 8 | Comparison of spiking activities in lALT neurons and mALT neurons. **(A)** Comparison of minimum and mean ISI in unilateral lALT neurons and mALT neurons before stimulation. **(B)** Average spike frequencies (bin-size: 50 ms) of all unilateral lALT neurons and mALT neurons. *Gray* bar: duration of the stimulus (400 ms). The different response strengths of these two types of neurons are shown in the inset. *$p < 0.05$. **(C)** Heat map of all neurons' responses during stimulus applications. Each row plots the mean of Δz-scored IFR (Instantaneous firing rate) of each neuron to the same repeated stimulus during the 400 ms stimulation window. The Δz-scored IFR was computed by subtracting the response threshold from the z-scored IFR. **(D)** The latency of response onset and response peak in medial-tract vs. the two types of lateral-tract neurons with excitatory responses to the natural blend (*top*) and the primary pheromone (*bottom*). *$p < 0.05$. **(E)** Comparison of response timing patterns (from the onset to the peak) across all excitatory lateral-tract and medial-tract neurons. The lateral-tract neurons illustrated a consistent and rapid timing pattern to both pheromone mixture (NB) and primary pheromone alone (PP; Wilcoxon test, $p > 0.14$).

confined to the lateral and the medial tract, respectively (**Supplementary Figure S5**). The overall response shapes of the unilateral lateral-tract neurons were, on average, more highly correlated with each other than those of the medial-tract neurons when the primary pheromone and the natural blend were used as stimuli. The overall response shapes of the bilateral lateral-tract neurons, on the other hand, had the lowest mean correlation.

DISCUSSION

In this study, we combined anatomical and functional experiments to characterize morphological and physiological properties of male-specific projection neurons confined to the lateral ALTs in the moth brain. Different from classic olfactory projections, our data revealed the SIP—a recently defined neuropil flanked by the AOTU and the mushroom body vertical lobe (Ito et al., 2014)—as the main target of MGC neurons projecting along the lateral ALT. More specifically, all neurons identified here terminated in a small area within the SIP called the column. In addition, double mass staining experiments demonstrated that lateral-tract neurons originating from the MGC as well as the OG provide converging input to the column. The neurons originating in the MGC comprise several morphological types, including unilateral and unusual bilateral neurons. Finally, functional characterization of individual neurons and neuron populations *via* electrophysiological recordings and calcium imaging demonstrated distinct physiological properties of lateral-tract MGC neurons as compared to corresponding neurons in the medial ALT.

Major Targets of Lateral-Tract Neurons Across Moth Species

Among the moth species most intensely studied, there are obvious differences in lateral-tract projection patterns, in particular regarding the male-specific share. In the silk moth, *B. mori*, the MGC lateral-tract projections target the "*delta area*," a pyramid-shaped region in the inferior lateral protocerebrum (Seki et al., 2005). This triangular area is formed by the male specific axons confined to the medial and medio-lateral tract as well. Projections originating from the OG, on the other hand, terminate in the LH, both in males and females. We recently found similar projection patterns of neurons passing along the three main antennal-lobe tracts in the Chinese oak silk moth, *Antheraea pernyi* (**Supplementary Figure S6A**). Notably, these domestic moth species seek the mate by walking or gliding, and are barely capable to fly. In moths performing long-distance flight, however, the lateral tract displays a different projection pattern including a specific target region exclusively for lateral-tract neurons. Our data from both mass staining and individual neuron labeling in male *H. armigera* indicates that all lateral-tract projection neurons from MGC and some from OG target the column within the SIP. In the classical anatomical study of the ALTs in the tobacco hawk moth, *M. sexta*, Homberg et al. (1988) showed that the main sub-category of lateral-tract neurons (named POa) branched off from the lateral path and projected dorsally terminating in the region between the AOTU and MB vertical lobe. The notion that these projections "*seem to branch in several OG or exclusively in the MGC*" is in full agreement with our findings. Previous studies in heliothine moths have identified "dorsally projecting" lateral-tract projection neurons as well. In a recent study of two heliothine species, *Heliothis virescens* and *Heliothis subflexa*, lateral-tract MGC neurons passing along "*the dorsal path*" were reported (Lee et al., 2019). Besides, similarly projecting lateral-tract neurons that originate from several OG were found in *H. virescens* (Rø et al., 2007; Ian et al., 2016). In addition, we have found lateral-tract projections targeting the column in the SIP in two migratory moths, the Silver Y, *Autographa gamma*, and the Bogong moth, *Agrotis infusa* (**Supplementary Figures S6B,C**). Altogether, the data obtained from flying and non-flying moths indicate that the column in the SIP might be involved in odor-evoked flight behavior, aimed at tracking females or other sources of essential odors over comparably large distances. Interestingly, we noted that *B. mori* and *M. sexta*, i.e., phylogenetically related species belonging to the same superfamily (*Bombyciodea)*, exhibit less similar lateral-tract systems than *M. sexta* and the more distantly related heliothine moths and other noctuids. This indicates that functional requirements rather than phylogenetic distance are the main factors driving the evolution of these projection areas.

A comparable target region of antennal-lobe projections close to the MB vertical lobe was also reported in two other well-studied insect species. In *Drosophila*, the most common lateral-tract neurons (AL-LPN2 in Tanaka et al., 2012) mainly terminate at the ventromedial part of the LH and an area surrounding the MB vertical lobe, termed the "ring neuropil." In the honeybee, the mediolateral ALT, i.e., the path likely corresponding to the lateral tract in other insects (Ian et al., 2016), also targets a region called the ring neuropil (Kirschner et al., 2006). While future work will have to show whether all these regions are homologous, it is tempting to speculate that the ring neuropil in the fruit fly and honeybee might be functionally comparable to the column in moths.

Unilateral Lateral-Tract Neurons Could Boost Robust Signal Transmission

Based on the homogenous morphology and physiology of the unilateral MGC lateral-tract neurons, we can conclude that they convey highly consistent information to a specific target area. The signals carried by these cells are even more uniform than those of cumulus-neurons confined to the medial tract. In addition, the lateral-tract neurons have shorter response delays. The encoding of a strong, consistent, and fast signal to a narrow target area, as performed by the unilateral neurons, seem unsuitable to capture fine details of the stimulus. In contrast, this configuration might facilitate robust information transmission with a minimum of ambiguity. While medial-tract neurons are involved in odor identification and establishment of odor memory—functions that require fine-tuning and precision—the uni-lateral lateral-tract neurons could serve a more direct role for fast control of key behaviors, requiring strength and sturdiness. Interestingly, these observations are in line with the robustness–efficiency trade-off hypothesis, stating that neural coding cannot be simultaneously optimized for robustness and efficiency, i.e., information capacity (Pryluk et al., 2019). The observed division of labor between neurons of the medial and lateral ALT might thus be an implementation of this trade-off.

Bilateral MGC Lateral-Tract Neurons Are Suited to Optimize Pheromone Tracking Strategies

A significant proportion of the lateral-tract MGC projection neurons stained in this study (six of 10) were bilateral neurons targeting the column in both brain hemispheres. When adding dye to the column, eight MGC-connected somata in the lateral cell cluster of the contralateral antennal lobe were labeled (**Figure 3B**), indicating the presence of at least eight bilateral projection neurons confined to the lateral tract. Considering the average axonal diameter of the bilateral neurons which is about 1 μm larger than that of the unilateral lateral-tract neurons (Unilateral lALT PNs: 1.92 ± 0.28 μm; Bilateral lALT PNs: 2.80 ± 0.80 μm), it is not surprising that we recorded more bilateral neurons here. The proportion of this neuron type is not known yet.

The bilateral lateral-tract projection neurons identified in *H. armigera* seem to be present exclusively in males. As male-specific lateral-tract neurons with bilateral innervations in the SIP region were also found in three other moth species, *H. virescens* (Ian et al., 2016), *Heliothis subflexa* (Lee et al., 2019), and *Agrotis segetum* (Wu et al., 1996), this neuron category likely plays a role specific to pheromone processing. One putative role is to integrate pheromone input with bilateral signals from other sensory modalities. Male moths seek the calling female not by sensing a chemical gradient of pheromone concentration, but by combining vision and mechano-sensation to fly against the wind as long as the pheromone signal is present. Both the visual and mechano-sensory systems are inseparably linked to space and thus to bilateral coding mechanisms (Jacobs et al., 2008; Homberg et al., 2011; Pfeiffer and Homberg, 2014; Patella and Wilson, 2018). An alternative explanation is that the bilateral projections summate simultaneous bilateral signals (Rodrigues, 1988) and thereby double the input from upstream sensory neurons to enhance signal-to-noise ratio (Raman et al., 2008).

Interestingly, among the bilateral neurons identified here, two of sub-type I enhanced their responses during repeated exposure to pheromone stimuli. These MGC bilateral projections could therefore serve as an arousal system that maintains plume tracking behavior by switching the downstream circuit into a more responsive state once the signal has crossed a reliability threshold. This strategy would prevent continued tracking after the detection of a single pheromone pulse, averting expensive investment into the pursuit of potentially false-positive signals. Only when several odor filaments are detected in close sequence, the neurons would fire and switch the circuit to drive continued seeking of the odor source. Consistent with this hypothesis, behavioral tests in a wind tunnel showed that when a single pheromone pulse was applied, male *H. virescens* followed a shorter distance than when multiple pulses of pheromone were used as stimulus (Vickers and Baker, 1994).

A Potential Role of the Column in Odor Integration and Navigation

Both MGC and non-MGC lateral-tract projection neurons target the column. Whereas the MGC projection neurons are mainly uni-glomerular, those responding to plant odors have been described as multi-glomerular (Homberg et al., 1988; Rø et al., 2007; Ian et al., 2016). Since all lateral-tract MGC-neurons identified here originated in the cumulus, it is not unlikely that this neuron group actually lacks connections with the two smaller MGC units. Such an arrangement would indicate the behavioral relevance of the primary pheromone component alone. The multi-glomerular non-pheromone neurons, on the other hand, would assumingly require a stimulus containing a mixture of the proper odor components (Løfaldli et al., 2012). Thus, this labeled-line arrangement suggests that all lateral-tract neurons projecting to the column are "pre-coded" in the antennal lobe to transmit specific, behaviorally significant information about the key pheromone, distinct plant-odor combinations, or a combination of both. Which information besides pheromones is encoded *via* this labeled-line pathway remains to be shown.

One behavior in which such labeled lines might be of importance is odor-evoked spatial orientation, e.g., to follow a conspecific pheromone plume or to pursue egg-laying sites. While not being directly connected (**Supplementary Figure S7**), the spatial proximity of the column to visual processing neuropils (e.g., the AOTU) is intriguing, as both might share downstream targets. Flying insects rely fundamentally on the visual system when tracing an odor source (reviewed by Baker and Hansson, 2016). Without visual feedback, moths find it very difficult to track airborne pheromone plumes successfully (Willis et al., 2011). Contrary to intuition, no odor-mediated behavior in moths is based on chemotaxis, i.e., there is no direct navigating response to odor concentration gradients. Moths rather steer against the odor source in correspondence with optomotor anemotaxis (anemo: wind, taxis: directed movement), which requires both olfactory and visual feedback (Kennedy and Marsh, 1974). Lateral-tract projection neurons targeting the column may provide olfactory signals optimized for being integrated with visual information and might therefore be directly involved in triggering species-specific, odor-evoked upwind flight behavior. To explore the putative integration of visual and olfactory input in neural networks connected to the column provides an exciting subject for future studies.

In contrast to the lateral-tract projections, converging into a restrict structure, the medial-tract terminals cover a bigger area in the lateral protocerebrum with segregated outputs for MGC and non-MGC neurons (**Figure 2**; also see Homberg et al., 1988; Kanzaki et al., 2003; Zhao et al., 2014). In male moths, these regions are believed to play a role in innate behavioral responses, such as pheromone attraction vs. inhibition of attraction (Zhao et al., 2014). This suggests that the lateral protocerebrum contributes to innate attraction/avoidance based on composite odor input coding, while the column acts as a simple and fast on/off switch to flying behavior based on key stimuli.

DATA AVAILABILITY STATEMENT

All datasets generated for this study are included in the article/**Supplementary Material**.

ETHICS STATEMENT

Ethical review and approval was not required for the animal study because it is in accordance of the Norwegian law of animal welfare and there are no restrictions regarding experimental use of Lepidopteras.

AUTHOR CONTRIBUTIONS

XC and BB designed the research. XC and SH performed the research. XC, SH, EI, and BB analyzed the data. XC, SH, and BB wrote the manuscript.

FUNDING

We are grateful for financial support from the following organizations: the Research Council of Norway (Norges Forskningsråd; project nr. 287052 to BB), the Swedish Research Council (Vetenskapsrådet; 621-2012-2213 to SH), and the European Research Council (ERC) under the European Union's Horizon 2020 research and innovation program (grant agreement no. 714599 to SH).

ACKNOWLEDGMENTS

We thank Jonas H. Kymre (NTNU), Christoffer Nerland Berge (NTNU), and Pramod KC (NTNU) for assistance with data collection. This article has been released as a pre-print at bioRxiv (Chu et al., 2019).

SUPPLEMENTARY MATERIAL

The Supplementary Material for this article can be found online at: https://www.frontiersin.org/articles/10.3389/fncel.2020.00147/full#supplementary-material.

REFERENCES

Adden, A., Wibrand, S., Pfeiffer, K., Warrant, E., and Heinze, S. (2020). The brain of a nocturnal migratory insect, the Australian Bogong moth. *J. Comp. Neurol.* doi: 10.1002/cne.24866 [Epub ahead of print].

Baker, T. C., and Hansson, B. S. (2016). "Moth sex pheromone olfaction," in *Pheromone Communication in Moths: Evolution, Behavior and Application*, eds J. D. Allison and R. T. Carde. (Oakland, CA: University of California Press), 139–172.

Cho, S., Mitchell, A., Mitter, C., Regier, J., Matthews, M., and Robertson, R. (2008). Molecular phylogenetics of heliothine moths (Lepidoptera: Noctuidae: Heliothinae), with comments on the evolution of host range and pest status. *Syst. Entomol.* 33, 581–594. doi: 10.1111/j.1365-3113.2008.00427.x

Christensen, T. A., and Hildebrand, J. G. (1987). Male-specific, sex pheromone-selective projection neurons in the antennal lobes of the moth *Manduca sexta*. *J. Comp. Physiol. A* 160, 553–569. doi: 10.1007/bf00611929

Christensen, T. A., Mustaparta, H., and Hildebrand, J. G. (1991). Chemical communication in heliothine moths. *J. Comp. Physiol. A* 169, 259–274.

Christensen, T. A., Mustaparta, H., and Hildebrand, J. G. (1995). Chemical communication in heliothine moths. *J. Comp. Physiol. A* 177, 545–557.

Chu, X., Heinze, S., Ian, E., and Berg, B. G. (2019). A novel major output target for pheromone-sensitive projection neurons in male moths. *bioRxiv* [Preprint]. doi: 10.1101/804922

de Vries, L., Pfeiffer, K., Trebels, B., Adden, A. K., Green, K., Warrant, E., et al. (2017). Comparison of navigation-related brain regions in migratory versus non-migratory noctuid moths. *Front. Behav. Neurosci.* 11:158. doi: 10.3389/fnbeh.2017.00158

El Jundi, B., Huetteroth, W., Kurylas, A. E., and Schachtner, J. (2009). Anisometric brain dimorphism revisited: implementation of a volumetric 3D standard brain in *Manduca sexta*. *J. Comp. Neurol.* 517, 210–225. doi: 10.1002/cne.22150

Evers, J. F., Schmitt, S., Sibila, M., and Duch, C. (2005). Progress in functional neuroanatomy: precise automatic geometric reconstruction of neuronal morphology from confocal image stacks. *J. Neurophysiol.* 93, 2331–2342. doi: 10.1152/jn.00761.2004

Fitt, G. P. (1989). The ecology of heliothis species in relation to agroecosystems. *Ann. Rev. Entomol.* 34, 17–53. doi: 10.1146/annurev.en.34.010189.000313

Galizia, C. G., and Rössler, W. (2010). Parallel olfactory systems in insects: anatomy and function. *Ann. Rev. Entomol.* 55, 399–420. doi: 10.1146/annurev-ento-112408-085442

Hamdani, E. H., and Døving, K. B. (2007). The functional organization of the fish olfactory system. *Prog. Neurobiol.* 82, 80–86. doi: 10.1016/j.pneurobio.2007.02.007

Hansson, B. S., Christensen, T. A., and Hildebrand, J. G. (1991). Functionally distinct subdivisions of the macroglomerular complex in the antennal lobe of the male sphinx moth *Manduca sexta*. *J. Comp. Neurol.* 312, 264–278. doi: 10.1002/cne.903120209

Heinze, S., and Reppert, S. M. (2012). Anatomical basis of sun compass navigation I: the general layout of the monarch butterfly brain. *J. Comp. Neurol.* 520, 1599–1628. doi: 10.1002/cne.23054

Homberg, U., Montague, R. A., and Hildebrand, J. G. (1988). Anatomy of antenno-cerebral pathways in the brain of the sphinx moth *Manduca sexta*. *Cell Tissue Res.* 254, 255–281. doi: 10.1007/bf00225800

Homberg, U., Heinze, S., Pfeiffer, K., Kinoshita, M., and el Jundi, B. (2011). Central neural coding of sky polarization in insects. *Philos. Trans. R Soc. Lond. B Biol. Sci.* 366, 680–687. doi: 10.1098/rstb.2010.0199

Ian, E., Kirkerud, N. H., Galizia, C. G., and Berg, B. G. (2017). Coincidence of pheromone and plant odor leads to sensory plasticity in the heliothine olfactory system. *PLoS One* 12:e0175513. doi: 10.1371/journal.pone.0175513

Ian, E., Zhao, X. C., Lande, A., and Berg, B. G. (2016). Individual neurons confined to distinct antennal-lobe tracts in the heliothine moth: morphological characteristics and global projection patterns. *Front. Neuroanat.* 10:101. doi: 10.3389/fnana.2016.00101

Ito, K., Shinomiya, K., Ito, M., Armstrong, J. D., Boyan, G., Hartenstein, V., et al. (2014). A systematic nomenclature for the insect brain. *Neuron* 81, 755–765. doi: 10.1016/j.neuron.2013.12.017

Jacobs, G. A., Miller, J. P., and Aldworth, Z. (2008). Computational mechanisms of mechanosensory processing in the cricket. *J. Exp. Biol.* 211, 1819–1828. doi: 10.1242/jeb.016402

Jarriault, D., Gadenne, C., Rospars, J.-P., and Anton, S. (2009). Quantitative analysis of sex-pheromone coding in the antennal lobe of the moth *Agrotis* ipsilon: a tool to study network plasticity. *J. Exp. Biol.* 212, 1191–1201. doi: 10.1242/jeb.024166

Kanzaki, R., Arbas, E. A., Strausfeld, N. J., and Hildebrand, J. G. (1989). Physiology and morphology of projection neurons in the antennal lobe of the male moth*Manduca sexta*. *J. Comp. Physiol. A* 165, 427–453. doi: 10.1007/bf00611233

Kanzaki, R., Soo, K., Seki, Y., and Wada, S. (2003). Projections to higher olfactory centers from subdivisions of the antennal lobe macroglomerular complex of the male silkmoth. *Chem. Senses* 28, 113–130. doi: 10.1093/chemse/28.2.113

Kauer, J. S. (1991). Contributions of topography and parallel processing to odor coding in the vertebrate olfactory pathway. *Trends Neurosci.* 14, 79–85. doi: 10.1016/0166-2236(91)90025-p

Kehat, M., and Dunkelblum, E. (1990). Behavioral responses of male *Heliothis armigera* (Lepidoptera: Noctuidae) moths in a flight tunnel to combinations of components identified from female sex pheromone glands. *J. Insect Behav.* 3, 75–83. doi: 10.1007/bf01049196

Kehat, M., Gothilf, S., Dunkelblum, E., and Greenberg, S. (1980). Field evaluation of female sex pheromone components of the cotton bollworm, *Heliothis*

armigera. *Entomol. Exp. Appl.* 27, 188–193. doi: 10.1111/j.1570-7458.1980.tb02963.x

Kennedy, J. S., and Marsh, D. (1974). Pheromone-regulated anemotaxis in flying moths. *Science* 184, 999–1001. doi: 10.1126/science.184.4140.999

Kirschner, S., Kleineidam, C. J., Zube, C., Rybak, J., Grunewald, B., and Rossler, W. (2006). Dual olfactory pathway in the honeybee, *Apis mellifera*. *J. Comp. Neurol.* 499, 933–952. doi: 10.1002/cne.21158

Lee, S. G., Celestino, C. F., Stagg, J., Kleineidam, C., and Vickers, N. J. (2019). Moth pheromone-selective projection neurons with cell bodies in the antennal lobe lateral cluster exhibit diverse morphological and neurophysiological characteristics. *J. Comp. Neurol.* 527, 1443–1460. doi: 10.1002/cne.24611

Løfaldli, B., Kvello, P., Kirkerud, N., and Mustaparta, H. (2012). Activity in neurons of a putative protocerebral circuit representing information about a 10 component plant odor blend in heliothis virescens. *Front. Syst. Neurosci.* 6:64. doi: 10.3389/fnsys.2012.00064

Montgomery, S. H., Merrill, R. M., and Ott, S. R. (2016). Brain composition in Heliconius butterflies, posteclosion growth and experience-dependent neuropil plasticity. *J. Comp. Neurol.* 524, 1747–1769. doi: 10.1002/cne.23993

Montgomery, S. H., and Ott, S. R. (2015). Brain composition in Godyris zavaleta, a diurnal butterfly, reflects an increased reliance on olfactory information. *J. Comp. Neurol.* 523, 869–891. doi: 10.1002/cne.23711

Mori, K. (2016). "Chapter 1-axonal projection of olfactory bulb tufted and mitral cells to olfactory cortex A2-Rockland, Kathleen S," in *Axons and Brain Architecture*, ed. K. Rockland (San Diego, CA: Academic Press), 3–26.

Ott, S. R. (2008). Confocal microscopy in large insect brains: Zinc-formaldehyde fixation improves synapsin immunostaining and preservation of morphology in whole-mounts. *J. Neurosci. Methods* 172, 220–230. doi: 10.1016/j.jneumeth.2008.04.031

Patella, P., and Wilson, R. I. (2018). Functional maps of mechanosensory features in the *Drosophila* brain. *Curr. Biol.* 28, 1189.e5–1203.e5. doi: 10.1016/j.cub.2018.02.074

Pfeiffer, K., and Homberg, U. (2014). Organization and functional roles of the central complex in the insect brain. *Ann. Rev. Entomol.* 59, 165–184. doi: 10.1146/annurev-ento-011613-162031

Piccardi, P., Capizzi, A., Cassani, G., Spinelli, P., Arsura, E., and Massardo, P. (1977). A sex pheromone component of the old world bollworm *Heliothis armigera*. *J. Insect Physiol.* 23, 1443–1445. doi: 10.1016/0022-1910(77)90170-6

Preibisch, S., Saalfeld, S., and Tomancak, P. (2009). Globally optimal stitching of tiled 3D microscopic image acquisitions. *Bioinformatics* 25, 1463–1465. doi: 10.1093/bioinformatics/btp184

Pryluk, R., Kfir, Y., Gelbard-Sagiv, H., Fried, I., and Paz, R. (2019). A tradeoff in the neural code across regions and species. *Cell* 176, 597.e8–609.e8. doi: 10.1016/j.cell.2018.12.032

Raman, B., Ito, I., and Stopfer, M. (2008). Bilateral olfaction: two is better than one for navigation. *Genome Biol.* 9:212. doi: 10.1186/gb-2008-9-3-212

Rø, H., Müller, D., and Mustaparta, H. (2007). Anatomical organization of antennal lobe projection neurons in the moth *Heliothis virescens*. *J. Comp. Neurol.* 500, 658–675. doi: 10.1002/cne.21194

Rodrigues, V. (1988). Spatial coding of olfactory information in the antennal lobe of *Drosophila* melanogaster. *Brain Res.* 453, 299–307. doi: 10.1016/0006-8993(88)90170-9

Schmitt, S., Evers, J. F., Duch, C., Scholz, M., and Obermayer, K. (2004). New methods for the computer-assisted 3-D reconstruction of neurons from confocal image stacks. *NeuroImage* 23, 1283–1298. doi: 10.1016/j.neuroimage.2004.06.047

Seki, Y., Aonuma, H., and Kanzaki, R. (2005). Pheromone processing center in the protocerebrum of Bombyx mori revealed by nitric oxide-induced anti-cGMP immunocytochemistry. *J. Comp. Neurol.* 481, 340–351. doi: 10.1002/cne.20392

Skiri, H. T., Rø, H., Berg, B. G., and Mustaparta, H. (2005). Consistent organization of glomeruli in the antennal lobes of related species of heliothine moths. *J. Comp. Neurol.* 491, 367–380. doi: 10.1002/cne.20692

Stöckl, A., Heinze, S., Charalabidis, A., el Jundi, B., Warrant, E., and Kelber, A. (2016). Differential investment in visual and olfactory brain areas reflects behavioural choices in hawk moths. *Sci. Rep.* 6:26041. doi: 10.1038/srep26041

Strauch, M., Rein, J., Lutz, C., and Galizia, C. G. (2013). Signal extraction from movies of honeybee brain activity: the ImageBee plugin for KNIME. *BMC Bioinformatics* 14:S4. doi: 10.1186/1471-2105-14-S18-S4

Tanaka, N. K., Endo, K., and Ito, K. (2012). Organization of antennal lobe-associated neurons in adult *Drosophila melanogaster* brain. *J. Comp. Neurol.* 520, 4067–4130. doi: 10.1002/cne.23142

Vickers, N. J., and Baker, T. C. (1994). Reiterative responses to single strands of odor promote sustained upwind flight and odor source location by moths. *Proc. Natl. Acad. Sci. U S A* 91, 5756–5760. doi: 10.1073/pnas.91.13.5756

Vickers, N. J., Christensen, T. A., and Hildebrand, J. G. (1998). Combinatorial odor discrimination in the brain: attractive and antagonist odor blends are represented in distinct combinations of uniquely identifiable glomeruli. *J. Comp. Neurol.* 400, 35–56. doi: 10.1002/(SICI)1096-9861(19981012)400:1<35::AID-CNE3>3.0.CO;2-U

Willis, M. A., Avondet, J. L., and Zheng, E. (2011). The role of vision in odor-plume tracking by walking and flying insects. *J. Exp. Biol.* 214, 4121–4132. doi: 10.1242/jeb.036954

Wu, W., Anton, S., Lofstedt, C., and Hansson, B. S. (1996). Discrimination among pheromone component blends by interneurons in male antennal lobes of two populations of the turnip moth, *Agrotis segetum*. *Proc. Natl. Acad. Sci. U S A* 93, 8022–8027. doi: 10.1073/pnas.93.15.8022

Wu, H., Xu, M., Hou, C., Huang, L.-Q., Dong, J.-F., and Wang, C.-Z. (2015). Specific olfactory neurons and glomeruli are associated to differences in behavioral responses to pheromone components between two Helicoverpa species. *Front. Behav. Neurosci.* 9:206. doi: 10.3389/fnbeh.2015.00206

Wu, D., Yan, Y., and Cui, J. (1997). Sex pheromone components of Helicoverpa armigera:chemical analysis and field tests. *Insect Sci.* 4, 350–356. doi: 10.1111/j.1744-7917.1997.tb00109.x

Zhao, X.-C., and Berg, B. G. (2010). Arrangement of output information from the 3 macroglomerular units in the heliothine moth *Helicoverpa assulta*: morphological and physiological features of male-specific projection neurons. *Chem. Senses* 35, 511–521. doi: 10.1093/chemse/bjq043

Zhao, X. C., Chen, Q. Y., Guo, P., Xie, G. Y., Tang, Q. B., Guo, X. R., et al. (2016a). Glomerular identification in the antennal lobe of the male moth *Helicoverpa armigera*. *J. Comp. Neurol.* 524, 2993–3013. doi: 10.1002/cne.24003

Zhao, X. C., Ma, B. W., Berg, B. G., Xie, G. Y., Tang, Q. B., and Guo, X. R. (2016b). A global-wide search for sexual dimorphism of glomeruli in the antennal lobe of female and male *Helicoverpa armigera*. *Sci. Rep.* 6:35204. doi: 10.1038/srep35204

Zhao, X.-C., Kvello, P., Løfaldli, B. B., Lillevoll, S. C., Mustaparta, H., and Berg, B. G. (2014). Representation of pheromones, interspecific signals and plant odors in higher olfactory centers; mapping physiologically identified antennal-lobe projection neurons in the male Heliothine moth. *Front. Syst. Neurosci.* 8:186. doi: 10.3389/fnsys.2014.00186

Conflict of Interest: The authors declare that the research was conducted in the absence of any commercial or financial relationships that could be construed as a potential conflict of interest.

frontiers in Cellular Neuroscience

ORIGINAL RESEARCH
published: 12 June 2020
doi: 10.3389/fncel.2020.00172

Dopaminergic Modulation of Glomerular Circuits in the Mouse Olfactory Bulb

*Shaolin Liu**

Department of Anatomy, Howard University College of Medicine, Washington, DC, United States

Dopaminergic neurons are located in several brain areas including the olfactory bulb (OB) and involved in many physiological and pathophysiological processes. In the OB, dopamine (DA) is released exclusively by a population of interneurons termed short axon cells (SACs) in the glomerular layer, the initial synaptic integration site of the whole olfactory system. SACs corelease GABA and extend their processes to many glomeruli forming the interglomerular circuit. Two major groups of DA receptors D1-like (D1LRs) and D2-like (D2LRs) types are differentially distributed in the OB, i.e., D1LRs are broadly present except the most superficial olfactory nerve (ON) layer while D2LRs are predominantly confined to the ON and glomerular layers, suggesting that they mediate different physiological functions. In contrast to the well-known D2LR-mediated presynaptic inhibition of ON terminals in the OB, the cellular and circuit targets of the D1LR-mediated DA actions remain unclear even though D1LR activation improves odor detection and discrimination. We recently demonstrated that endogenous DA released from SACs or exogenous DA excites a population of excitatory glomerular neurons termed external tufted cells (ETCs) via D1LRs. But the physiological significance of this D1LR activation is largely unknown. In the present study, we addressed these questions by a systematic examination of exogenous DA actions on synaptic activities and excitabilities in most glomerular neurons and OB output neurons with the following major findings: (1) DA via D1LRs enhances OB output by potentiating the ETC-mediated feedforward excitation to the OB output neurons but suppresses spontaneous excitatory synaptic activities in both types of inhibitory glomerular interneurons periglomerular (PGCs) and SACs; (2) this suppression of excitatory synaptic activities in PGCs and SACs depends on activation of $GABA_B$ receptors; (3) DA via D1LRs augments spontaneous inhibitory synaptic activities in all glomerular neurons and OB output neurons; (4) DA selectively activates SACs via D1LRs. These findings suggest that activation of D1LRs elevates the system's sensitivity to odor stimuli and provide a mechanistic basis for the functional roles of DA in modulating odor detection and discrimination.

Keywords: dopamine, synaptic transmission, interneuron, olfactory bulb, excitation, inhibition

OPEN ACCESS

Edited by:
Julian P. Meeks,
University of Texas Southwestern Medical Center, United States

Reviewed by:
Shin Nagayama,
Texas Medical Center, United States
David Henry Gire,
University of Washington, United States

***Correspondence:**
Shaolin Liu
Shaolin.liu@howard.edu

Specialty section:
This article was submitted to Cellular Neurophysiology, a section of the journal Frontiers in Cellular Neuroscience

Received: *15 April 2020*
Accepted: *20 May 2020*
Published: *12 June 2020*

Citation:
Liu S (2020) Dopaminergic Modulation of Glomerular Circuits in the Mouse Olfactory Bulb. Front. Cell. Neurosci. 14:172. doi: 10.3389/fncel.2020.00172

INTRODUCTION

Dopamine (DA) as a neurotransmitter or neuromodulator plays important roles in many brain functions including motor control, motivation, reward, cognition, maternal and reproductive behaviors (Bjorklund and Dunnett, 2007a; Klein et al., 2019). DA actions are mediated by G protein-coupled receptors, which are classified into two major types based on their gene sequence homology and functions: the excitatory D1-like (D1LRs) and inhibitory D2-like (D2LRs) receptors (Beaulieu and Gainetdinov, 2011). In the mammalian brain DA-containing neurons are located in several distinctive cell groups distributed from the mesencephalon to the olfactory bulb (OB) (Dahlstroem and Fuxe, 1964; Bjorklund and Dunnett, 2007b).

In the OB, DA is exclusively released by a population of interneurons termed short axon cells (SACs), which express glutamic acid decarboxylase (GAD) 67, a key enzyme for biosynthesis of the inhibitory neurotransmitter GABA (Kosaka and Kosaka, 2008; Kiyokage et al., 2010). Both D1LRs and D2LRs are present in the OB with distinct distribution patterns, i.e., D1LRs are broadly present from glomerular to granule cell layers while D2LRs are confined only to the superficial olfactory nerve (ON) and the glomerular layers (Guthrie et al., 1991; Levey et al., 1993; Coronas et al., 1997; Gutierrez-Mecinas et al., 2005; Yu et al., 2019). Pharmacological activation of D2LRs (Nickell et al., 1991; Hsia et al., 1999; Ennis et al., 2001; Maher and Westbrook, 2008; McGann, 2013) or optogenetic activation of SACs inhibits glutamate release from ON terminals to postsynaptic cellular targets in the glomerular layer (Vaaga et al., 2017). Moreover, *in vivo* studies showed that blocking either D1LRs or D2LRs (Escanilla et al., 2009) or lack of DA transporters or D2LRs impairs odor discrimination in animals (Tillerson et al., 2006; Taylor et al., 2009) whereas olfactory deprivation upregulates D2LR density in the OB (Guthrie et al., 1991). Interestingly, a mating-triggered DA surge in the main OB of female mice impairs their perception of social odors contained in male urine (Serguera et al., 2008). Additionally, dopaminergic SACs exhibit high level of activity-dependent plasticity. For example, naris closure leads to a drastic reduction in the number of TH-immunoreactive cells and processes (Cave and Baker, 2009; Parrish-Aungst et al., 2011; Lazarini et al., 2014; Bonzano et al., 2016). Furthermore, majority of DAergic SACs originate from postnatal neurogenesis and are continuously subject to replenishment during adult life (Lazarini et al., 2014; Bonzano et al., 2016). All these previous findings suggest that DA actively participates in modulating signal processing in the OB. However, the mechanistic actions of DA at the cellular and circuit levels in the OB are not well understood.

The DAergic/GABAergic SACs have somata and processes confined to the glomerular layer (Kosaka and Kosaka, 2008; Kiyokage et al., 2010), where excitatory and inhibitory circuits are formed among the axonal terminals of olfactory sensory neurons (OSNs), apical dendrites of ETCs and the OB output neurons mitral and tufted cells (MTCs), and two major populations of inhibitory interneurons types – SACs and periglomerular cells (PGCs) (Lledo et al., 2005; Wilson and Mainen, 2006; Nagayama et al., 2014; Burton, 2017; Pignatelli and Belluzzi, 2017). Thus, the DAergic/GABAergic SACs are well-situated to modulate olfactory signal processing at the initial site of synaptic integration in the whole olfactory system. Physiological evidence suggests that functional operation of the SAC-derived circuit depends on postsynaptic cellular targets. For instance, DA is coreleased with GABA from SACs to mediate a biphasic excitatory-inhibitory sequential response in ETCs (Liu et al., 2013) while the transmission from SACs to MTCs or PGCs is mediated by GABAergic and electrical synapses (Banerjee et al., 2015; Liu et al., 2016) or GABA alone but not by DA (Shao et al., 2019). Alternatively, DA potentially functions as a neuromodulator in the OB through volume transmission (Cragg et al., 2001). A recent study revealed that DA release from SACs in the OB was quantal and calcium-dependent but was asynchronous and lasted for tens of seconds (Borisovska et al., 2013), supporting volume transmission. Thus, in the present study we designed experiments to examine actions of exogenous DA on both excitatory and inhibitory transmission in the glomerular circuit and analyzed the underlying cellular mechanisms.

MATERIALS AND METHODS

Animals

Both male and female C57BL/6J mice were purchased from Charles River. The GAD2gfp mice provided of courtesy by Dr. Gabor Szabo were initially from the GAD65_3e/gfp5.5 #30 line on a genetic background of C57BL6 backcrossed to B6CBAF1/J wild-type mice to generate the transgene heterozygotes (Lopez-Bendito et al., 2004). TH-GFP mice were initially courtesy of Dr. Kobayashi (Matsushita et al., 2002) and generated using a 9.0 kb 5′-flanking region of the TH gene on a genetic background of C57BL/6J to crossbreed with DBA/2J mice. These TH-GFP transgenic mice were then backcrossed to C57BL/6J mice to generate heterozygotes for experimental usage. All animals were maintained with a standard 12-h light/dark cycle with *ad libitum* access to food and water. All experimental procedures were carried out in accordance with protocols submitted to and approved by the Howard University Institutional Animal Care and Use Committee.

Slice Preparation

Acute OB slices were prepared from 6- to 8-week-old male or female mice as described previously (Liu et al., 2013). Briefly, horizontal slices (350 μm) were cut with a VT1200s vibratome (Nussloch, Germany) in an ice-cold and oxygenated (95% O_2–5% CO_2) sucrose-based artificial CSF (sucrose-ACSF) containing (in mM) 210 sucrose, 3 KCl, 1.2 NaH_2PO_4, 2.6 $MgSO_4$, 0.5 $CaCl_2$, 26 $NaHCO_3$, 10 glucose. After 30 min incubation in normal ACSF at 30°C, slices were then transferred to ACSF at room temperature until they were used for recordings. Normal ACSF was continuously bubbled with 95% O_2–5% CO_2 and had the following composition (in mM): 124 NaCl, 3 KCl, 1.25 NaH_2PO_4, 2.0 $MgSO_4$, 2.0 $CaCl_2$, 26 $NaHCO_3$, 10 glucose.

During experiments, slices were perfused at 3 ml/min with ACSF equilibrated with 95% O_2–5% CO_2 and warmed to 30°C.

Electrophysiology

Whole cell patch clamp recordings were made from OB neurons visualized using Axio Examiner (Zeiss, Oberkochen, Germany) fixed-stage upright microscope with near-infrared differential interference contrast (DIC) optics. Short axon (SACs) and periglomerular cells (PGCs) were identified by their expression of TH- or GAD65-EGFP in corresponding transgenic mice, respectively.

External tufted cells (ETCs) were initially reported in previous studies with Golgi staining (Romon and Cajal, 1909; Pinching and Powell, 1971a,b; Macrides and Schneider, 1982). Recent work more rigorously characterized the morphological and electrophysiological properties of ETCs (Hayar et al., 2004b; Antal et al., 2006). Based on findings from these studies, we redefined and identified ETCs with the following criteria: (1) spontaneous and intrinsic burst spiking that is resistant to blockers of fast synaptic transmitter receptors; (2) soma residing in the deep half of the glomerular layer with "pear" appearance viewed in near-IR DIC optics; (3) an apical dendrite tuft extensively ramifying in a single glomerulus but lack of lateral dendrites in the external plexiform layer (EPL).

To localize apical dendrite tufts of the recorded mitral/tufted cells (MTCs) in the glomerular layer, Alexa-594 (10 μM) was added to the recording electrode solution. Whole cell current or voltage signals were recorded with a MultiClamp 700B amplifier (Molecular Devices, Palo Alto, CA, United States) and low-pass filtered at 4 kHz and sampled at 10 kHz with a DIGIDATA 1550B 16-bit analog-to-digital converter (Molecular Devices) using Clampex 11.0.3 (Molecular Devices). Patch recording electrodes were pulled from standard-wall glass capillary tubes without filament (Sutter Instrument, Novato, CA, United States). Patch pipettes (4–7 MΩ) for whole cell current clamp recording contained (in mM) 115 K-gluconate, 5.0 EGTA, 0.63 $CaCl_2$, 5.5 $MgCl_2$, 10 HEPES, 3 Na_2-ATP, 0.3 Na_3-GTP, and 14 Tris-phosphocreatine (pH 7.3, 285–295 mOsm). Voltage clamp recordings of spontaneous excitatory (sEPSCs) or inhibitory postsynaptic currents (sIPSCs) were made with internal solution containing (in mM) 133 $CsCH_3O_3S$, 3 EGTA, 0.4 $CaCl_2$, 5 QX-314, 4 $MgCl_2$, 10 HEPES, 3 Na_2-ATP, 0.3 Na_3-GTP (pH 7.3, 285–295 mOsm). Cells were voltage clamped at −70 mV, the reversal potential of Cl^-, to minimize the Cl-mediated sIPSCs thus to optimize the recording of sEPSCs. Cells were voltage clamped at 0 mV, the reversal potential of AMPA and NMDA receptor-mediated sEPSCs, to optimize recording of sIPSCs. Before bath application of the $GABA_A$ receptor blocker gabazine (GBZ), NBQX (10 μM) and APV (50 μM) were pre-applied to block fast glutamate receptors thus preventing epileptic activity.

Electrical Stimulation

Electrical stimulation was delivered by bipolar glass electrodes made from theta borosilicate tubes (Sutter Instrument). The isolated and constant current stimulation pulses (100 μs) were triggered by a Master-9 stimulator (AMPI, Jerusalem, Israel).

Data Analysis

Amplitudes and frequencies of sEPSCs or sIPSCs were measured with Wdetecta.[1] Drug effects on sEPSCs and sIPSCs were determined by measuring these parameters from 1 min duration traces taken immediately before or 1 min (micropuffing) or 2 min (bath application) after drug application in each condition for each cell. Other data were measured and analyzed with Clampfit 11.0.3 (Molecular Devices) and Origin Pro 2019 (Origin Lab, Northampton, MA, United States). Statistical significance of population responses was calculated by using paired Student's *t*-test or ANOVA One-way repeated measure with Bonferroni *post hoc* comparisons in Origin Pro 2019.

Drugs Delivery and Chemicals

Drugs were applied by either bath perfusion to treat the whole slices or micropuffing to target the relevant glomeruli by 2 ms and 30 psi pneumatic pressure generated by a picospritzer (Parker Instruments, Cleveland, OH, United States). Micropuffing pipettes were made from thick wall borosilicate glass capillaries without filament (Sutter Instrument) with a 6-μm tip diameter. These parameters were calibrated to deliver an injection volume of ∼20 nl and were previously shown to deliver drug coverage restricted to a single glomerulus (Shao et al., 2012).

D-2-Amino-5-phosphonopentanoic acid sodium salt (APV, 50 μM), 2,3-Dioxo-6-nitro-1,2,3,4-tetrahydrobenzo[f]quinoxaline-7-sulfonamide disodium salt (NBQX disodium salt, 10 μM), Gabazine (SR95531, 10 μM), 8-Bromo-2,3,4,5-tetrahydro-3-methyl-5-phenyl-1H-3-benzazepin-7-ol hydrobromide (SKF83566 bromide, 10 μM), (S)-(-)-5-Aminosulfonyl-*N*-[(1-ethyl-2-pyrrolidinyl)methyl]-2-methoxybenzamide [(S)-(-)-Sulpiride, 100 μM], (2S)-3-[[(1S)-1-(3,4-Dichlorophenyl)ethyl]amino-2-hydroxypropyl](phenylmethyl)phosphinic acid hydrochloride (CGP55845 hydrochloride, 10 μM) were purchased from Tocris Cookson (Ellisville, MO, United States). Dopamine chloride (DA, 20 μM or 100 μM) and all other chemicals were purchased from Sigma-Aldrich (St. Louis, MO, United States). All drugs were dissolved in distilled water as stock solution and diluted 1000 times with ACSF to final concentrations.

RESULTS

Dopamine Inhibits Spontaneous EPSCs in Glomerular Interneurons via D1LRs

Previous studies have shown that optogenetic activation of SACs leads to GABA and DA corelease (Liu et al., 2013). The coreleased GABA and DA orchestrate to modulate ETC physiological behaviors in such a way that DA enhances I_h to boost the rebound excitation following the $GABA_A$ receptor-mediated inhibition (Liu et al., 2013). Consistently, exogenous DA increases the I_h-dependent bursts of action potentials in ETCs. As a major excitatory element in the glomerular circuit,

[1] https://hlab.stanford.edu/wdetecta.php

ETCs monosynaptically drive vast majority of the inhibitory periglomerular cells (PGCs) and SACs (Shao et al., 2009; Kiyokage et al., 2010). All these findings lead us to predict that DA increases spontaneous excitatory synaptic activities in the ETC-driven PGCs and SACs. To test this, we recorded sEPSCs in PGCs and SACs in OB slices under voltage clamp and examined effects of exogenous DA. As PGCs and SACs exclusively express the key enzyme of GABA biosynthesis GAD65 and the rate-limiting enzyme of dopamine biosynthesis tyrosine hydroxylase (TH), respectively (Kiyokage et al., 2010), PGCs and SACs were accordingly identified in GAD65-GFP (**Figure 1A**) and TH-GFP (not shown) mice. To differentiate the ON-driven and ETC-driven PGCs and SACs, we started with recording their responses to ON stimulation. Consistent with previous findings (Shao et al., 2009; Kiyokage et al., 2010), vast majority of PGCs (8/13) or SACs (8/12) respond to ON-stimulation with long and inconsistent latencies (4.3 ± 0.31 ms, n = 8 PGCs; 4.6 ± 0.42, n = 8 SACs) EPSCs and exhibit bursts of sEPSCs (**Figures 1B,C**), indicating that they are ETC-driven glomerular interneurons. The rest PGCs (5/13) and SACs (4/12) responded to ON stimulation with short latencies (2.3 ± 0.15 ms, n = 5 PGCs; 2.1 ± 0.17, n = 4 SACs), suggesting that they are ON-driven glomerular interneurons. Surprisingly, bath application of DA reversibly suppressed sEPSCs in all tested PGCs (n = 13, **Figures 1C–F,H**) and SACs (n = 12). sEPSC frequency and amplitude in PGCs (n = 13) were 63.0 ± 6.7 Hz and 57.4 ± 5.0 pA in ACSF, 29.2 ± 3.0 Hz (P < 0.0001 vs. in ACSF) and 32.3 ± 3.4 pA (P < 0.0001 vs. in ACSF) in DA (20 μM), and 61.3 ± 6.3 Hz (P = 1 vs. in ACSF) and 55.7 ± 5.0 pA (P = 1 vs. in ACSF) after DA washout. Similarly, sEPSC frequency and amplitude in 12 SACs were 64.3 ± 8.4 Hz and 71.0 ± 9.0 pA in ACSF, 28.8 ± 3.6 (P < 0.0001 vs. ACSF) and 37.4 ± 4.3 pA Hz (P < 0.0001 vs. ACSF) in DA, 63.6 ± 8.5 Hz (P = 1 vs. ACSF) and 70.3 ± 8.8 pA (P = 1 vs. ACSF) after DA washout (**Figures 1I,K**). While the DA suppression of sEPSCs in the ON-driven PGCs and SACs is consistent with previous findings that DA inhibits glutamate release from the ON terminals (Hsia et al., 1999; Berkowicz and Trombley, 2000; Ennis et al., 2001; Maher and Westbrook, 2008; Vaaga et al., 2017), the similar DA action on the ETC-driven PGCs and SACs may indicate dopaminergic modulation of glutamate release from ETC apical dendritic terminals in the glomerular layer. Given that burst sEPSCs reflect spontaneous burst firing activities in presynaptic ETCs, we also measured the sEPSC burst frequencies and found that the frequency of sEPSC bursts was also reduced by DA (**Figures 1G,J**). sEPSC burst frequencies in PGCs (n = 8) and SACs (n = 8) were 6.1 ± 1.0 Hz and 7.8 ± 1.1 Hz in ACSF, 4.1 ± 0.7 Hz (P < 0.0001 vs. ACSF) and 5.3 ± 0.8 Hz (P < 0.0001 vs. ACSF) in DA, 6.1 ± 0.9 Hz (P = 1 vs. ACSF) and 7.7 ± 1.0 Hz (P = 1 vs. ACSF) after DA washout, respectively. Collectively, these results indicate that DA inhibits glutamate release from presynaptic ETC apical dendrites to PGCs and SACs thus reduces burst sEPSCs.

Dopamine actions are mediated by two major categories of G protein-coupled receptors – D1LRs and D2LRs (Beaulieu and Gainetdinov, 2011). Evidence shows that D2LRs in ON terminals mediate presynaptic inhibition of glutamate release to their postsynaptic targets in the glomerular layer (Nickell et al., 1991; Aroniadou-Anderjaska et al., 2000; McGann, 2013). This explains why DA suppresses sEPSCs in the ON-driven PGCs and SACs. All ETCs receive direct ON input (Hayar et al., 2004a; De Saint et al., 2009; Gire and Schoppa, 2009), does DA inhibit ON terminals via D2LRs to reduce ETC burst firing thus indirectly suppresses burst sEPSCs in the ETC-driven PGCs and SACs? To test this, we treated OB slices with bath application of (S)-(-)-Sulpiride (100 μM), a selective D2LR antagonist, for 10 min before addition of DA (**Figure 2A**). In these conditions, DA reduced sEPSC frequency by 46.8 ± 1.9% (n = 7) in PGCs and 49.7 ± 1.9% (n = 6) in SACs, amplitude by 47.9 ± 3.7% (n = 7) in PGCs and 48.3 ± 3.0% (n = 6) in SACs (**Figures 2A–C**) in the presence of (S)-(-)-Sulpiride. Specifically, sEPSC frequency and amplitude in PGCs (n = 7) were 76.8 ± 11.9 Hz and 75.1 ± 11.6 pA in (S)-(-)-Sulpiride, 40.3 ± 5.9 Hz [P < 0.0001 vs. (S)-(-)-Sulpiride] and 39.0 ± 6.8 pA [P < 0.0001 vs. (S)-(-)-Sulpiride] in (S)-(-)-Sulpiride+DA, and 77.4 ± 12.4 Hz [P = 1 vs. (S)-(-)-Sulpiride] and 74.0 ± 11.7 pA [P = 1 vs. (S)-(-)-Sulpiride] after washout DA, respectively (**Figures 2D,E**). Similar results were observed in SACs (n = 6) with average frequency and amplitude of 68.2 ± 11.4 Hz and 65.7 ± 12.1 pA in (S)-(-)-Sulpiride, 34.2 ± 6.0 Hz [P < 0.0001 vs. (S)-(-)-Sulpiride] and 34.3 ± 6.7 pA [P < 0.0001 vs. (S)-(-)-Sulpiride] in the addition of DA, and 67.1 ± 12.0 Hz [P = 1 vs. (S)-(-)-Sulpiride] and 64.3 ± 11.8 pA [P = 1 vs. (S)-(-)-Sulpiride] after DA washout (**Figures 2D,E**). These findings suggest that D2LRs do not mediate presynaptic inhibition of glutamate release from ON terminals to ETCs to PGCs and SACs.

Then we examined DA effects on sEPSCs in PGCs and SACs in the presence of the selective D1LR antagonist SKF83566 (10 μM). However, in these conditions, DA altered neither frequency nor amplitude of sEPSCs in either population of glomerular interneurons (**Figures 2F–J**), implying that the DA suppression of sEPSCs in both PGCs and SACs is mediated by D1LRs.

Altogether, our results support that DA reduces sEPSCs in the ETC-driven PGCs and SACs by activation of D1LRs but this action is not due to reduced ETC activities, which result from activation of D2LRs on ON terminals to reduce glutamate release.

DA Enhances Spontaneous IPSCs in Glomerular Neurons

Since activation of D1LRs on ETCs produces an excitatory effect (Liu et al., 2013) whereas ON terminals are devoid of D1LRs (Levey et al., 1993; Coronas et al., 1997; Beaulieu and Gainetdinov, 2011), we hypothesized that the DA via D1LRs directly excites PGCs and/or SACs to release GABA, which activates $GABA_B$ receptors on ETC apical dendrites (Karpuk and Hayar, 2008) to reduce glutamate release onto PGCs and SACs. In this scenario, DA should elevate the glomerular inhibition. To test this, we recorded spontaneous inhibitory postsynaptic currents (sIPSCs) in voltage clamp in all three populations of glomerular neurons including PGCs, SACs and ETCs, which all have apical dendrites or processes confined to the glomerular layers thus could manifest potential DA-enhanced glomerular inhibition. To maximize detection sIPSCs, which have reversal potential around −70 mV based on chloride concentrations of our internal and

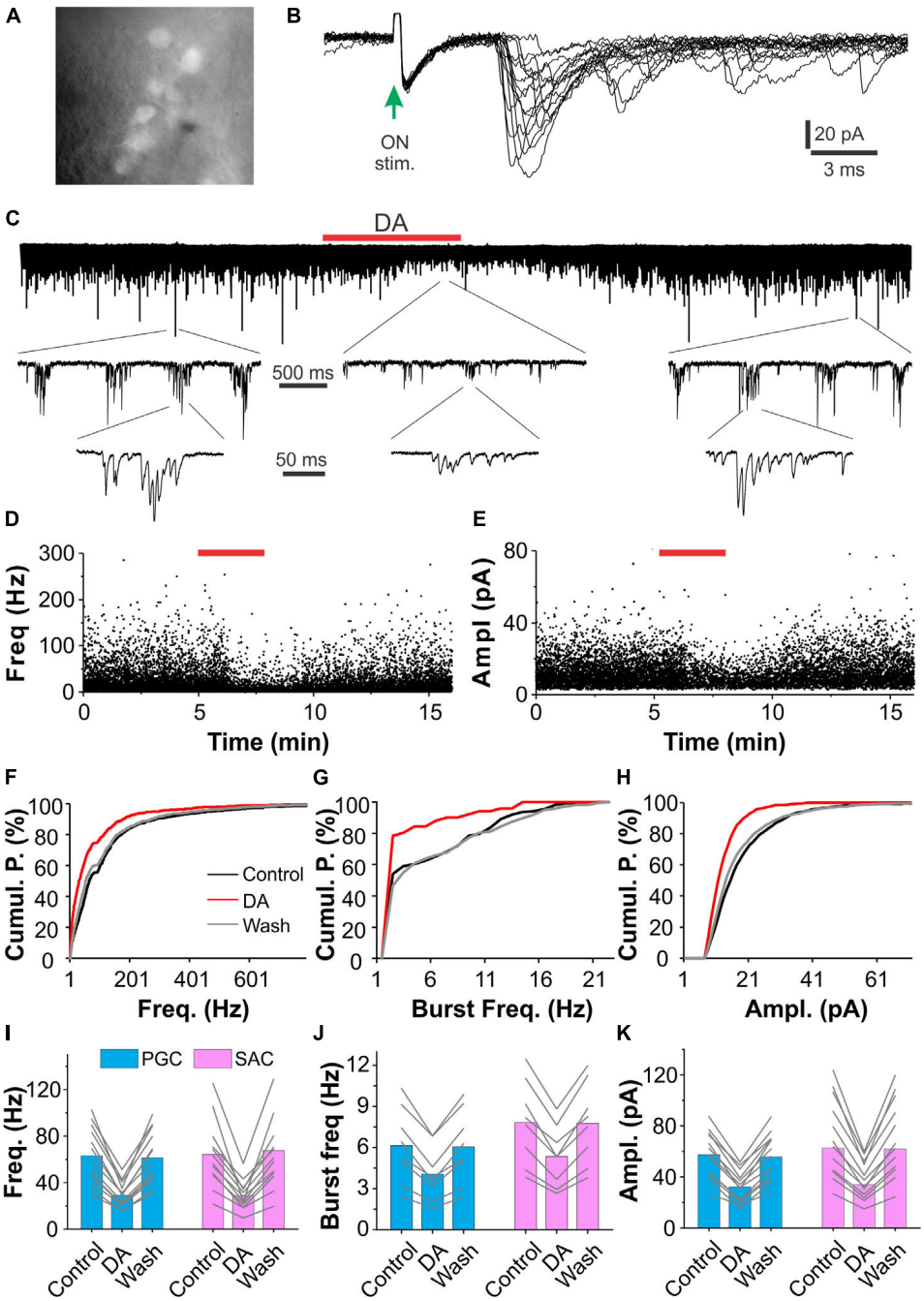

FIGURE 1 | DA suppresses sEPSCs in glomerular interneurons. **(A)** Photo graph showing GFP-expressing periglomerular cells (PGCs) in the glomerular layer of an OB slice prepared from a GAD65-GFP mouse. **(B)** Typical excitatory postsynaptic current (EPSCs) traces in a PGC evoked by stimulation of the olfactory nerves (ON-stim.). Note that EPSC onset latencies are longer than 3 ms and varies among traces. **(C)** A representative voltage clamp recording trace showing that bath-applied DA (20 μM, red horizontal bar) reduces both frequency and amplitude of spontaneous burst EPSCs in a PGC (top). Middle and bottom traces are blown-up. **(D,E)**: plotting graphs showing changes in instant frequency **(D)** and amplitude **(E)** of sEPSCs before, during and after DA application in the same trace in **(C)**. **(F–H)** Line graphs of cumulative probability (Cumul. P.) against frequency of individual **(F)** or burst **(G)** sEPSCs, or amplitude (Ampl., **H**) of individual sEPSCs before (control), during (DA), and after (wash) DA application. **(I–K)** Pooled data showing that DA reduces both frequency of individual **(I)** or burst **(J)** sEPSCs and amplitude **(K)** of sEPSCs in both PGCs (n = 13) and short-axon cells (SACs, n = 12).

external solutions, and minimize sEPSCs, which have a reversal potential at 0 mV, we voltage clamped cells at 0 mV in the presence of NBQX (10 μM) and D-APV (50 μM) to block AMPA and NMDA receptors thus minimize circuit influence. In these conditions, bath application of DA (20 μM) reversibly enhanced sIPSCs in PGCs (**Figure 3A**). When sIPSCs were completely

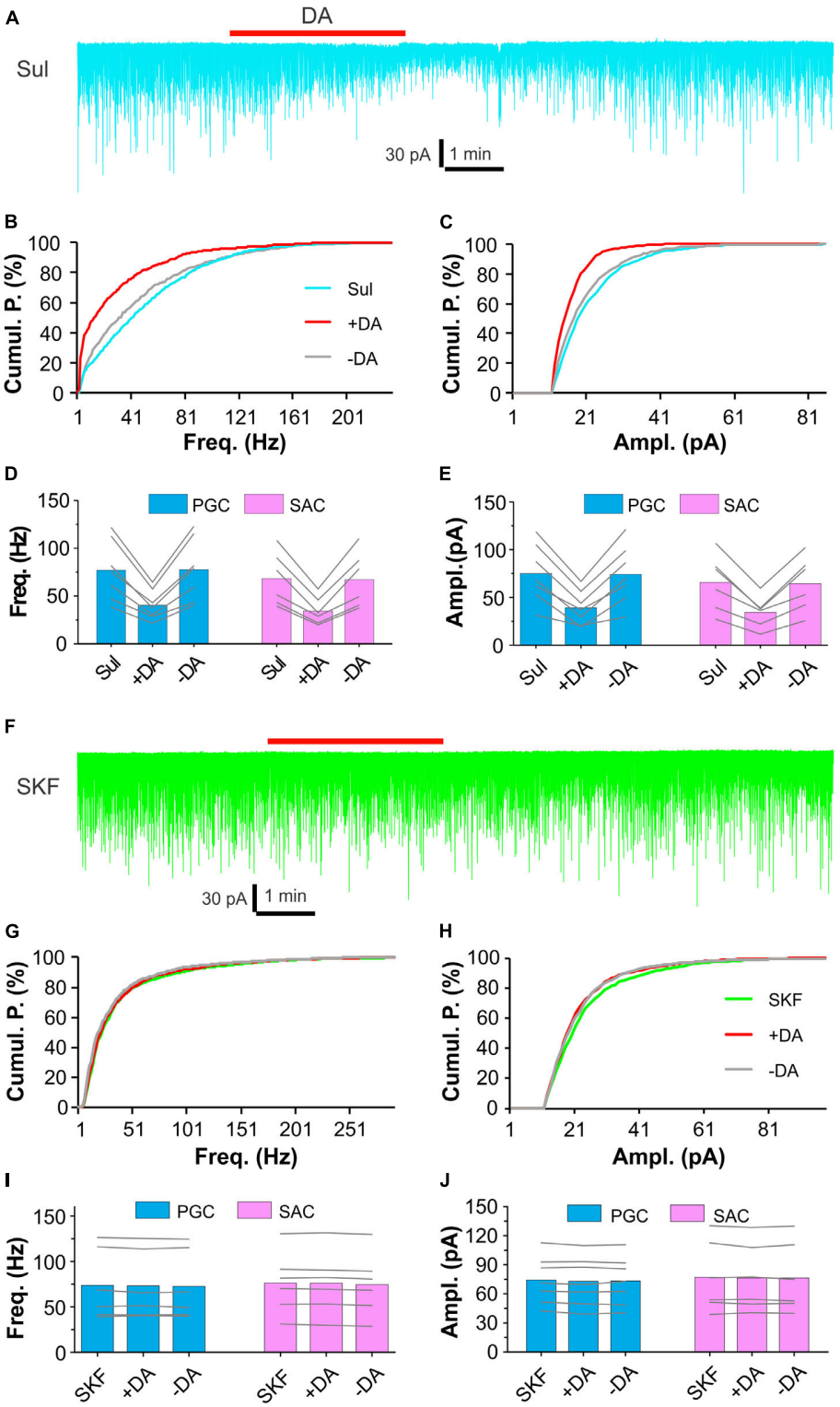

FIGURE 2 | D1LRs mediate DA actions on sEPSCs in glomerular interneurons. **(A)** A representative recording trace showing DA effects on sEPSCs in a PGC in the presence of 100 μM (S)-(-)-Sulpiride (Sul), a selective D2LR antagonist. **(B,C)** Graphs plotting cumulative probability against frequency **(B)** or amplitude **(C)** of sEPSCs shown in **(A)**. **(D,E)** Pooled data showing that DA reduces both frequency **(D)** and amplitude **(E)** of sEPSCs in both PGCs (n = 7) and SACs (n = 6) in the presence of (S)-(-)-Sulpiride. **(F)** A representative recording trace showing that DA has no effect on sEPSCs in a PGC in the presence of 10 μM SKF83566 (SKF), a selective D1LR antagonist. **(G,H)** Graphs plotting cumulative probability against frequency **(G)** or amplitude **(H)** of sEPSCs shown in **(F)**. **(I,J)** Pooled data showing that DA has effect on neither frequency **(I)** nor amplitude **(J)** of sEPSCs in either PGCs (n = 7) or SACs (n = 6) in the presence of SKF83566.

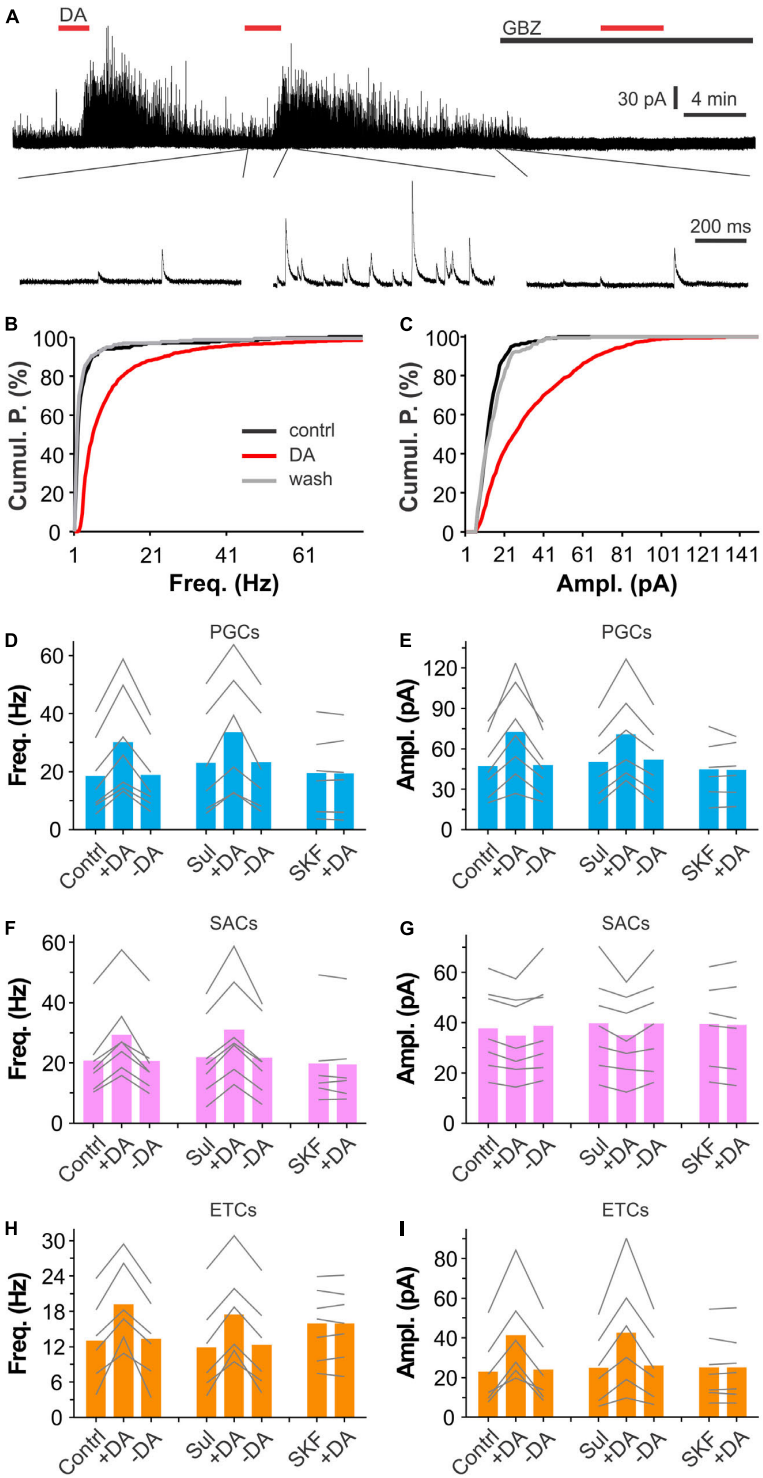

FIGURE 3 | DA enhances synaptic inhibition of glomerular neurons. **(A)** A typical trace (top) showing that bath-applied two doses of DA (20 μM) reversibly and reproducibly enhances spontaneous inhibitory postsynaptic currents (sIPSCs) in a PGC voltage clamped at 0 mV in the presence of NBQX and APV. Note that sIPSCs are completely eliminated by bath-application of the selective $GABA_A$ receptor blocker gabazine (10 μM). Bottom traces are blown up from the top traces. **(B,C)** Graphs showing cumulative probability of frequency **(B)** or amplitude **(C)** of sIPSCs presented in A before (control) or during (DA) DA application, or after DA washout (wash). **(D–I)** Pooled data showing that DA significantly enhances sIPSC frequency in PGCs **(D)**, SACs **(F)**, or ETCs **(H)**, and amplitude in both PGCs **(E)** and ETCs **(I)** but not in SACs **(G)** in either control (contrl, n = 7 PGCs, 7 SACs, 6 ETCs) or in the presence of 100 μM (S)-(-)-Sulpiride (Sul, n = 6 PGCs, 7 SACs, 6 ETCs) while DA has effect on neither frequency nor amplitude of sIPSCs in all three populations of glomerular neurons in the presence of 10 μM SKF83566 (SKF, n = 6 PGCs, 6 SACs, 7 ETCs).

abolished by the selective $GABA_A$ receptor blocker gabazine (GBZ, 10 μM, **Figure 3A**), DA showed no effect on the holding current, suggesting that DA does not affect PGCs *per se*. Further analysis revealed that both frequency and amplitude of sIPSCs in PGCs were elevated by DA (**Figures 3B,C**). To determine what receptors mediate these actions, either (S)-(-)-Sulpiride (100 μM) or SKF83566 (10 μM) was bath-applied before DA addition in another set of experiments. It turned out that SKF83566 rather than (S)-(-)-Sulpiride completely blocked DA effects on sIPSCs in all tested PGCs (**Figures 3D,E**), indicating mediation by D1LRs. Specifically, the average frequency and amplitude of sIPSCs in seven PGCs were 18.4 ± 5.0 Hz and 47.1 ± 8.7 pA in ACSF, 30.0 ± 6.8 Hz ($p < 0.0001$ vs. in ACSF) and 72.5 ± 13.4 pA in DA ($p < 0.0001$ vs. in ACSF), and 18.8 ± 4.8 Hz ($p = 1$ vs. in ACSF) and 47.9 ± 8.5 pA ($p = 1$ vs. in ACSF) after DA washout, respectively. In the presence of (S)-(-)-Sulpiride, average frequency and amplitude of sIPSCs in another set of six PGCs were 23.0 ± 7.5 Hz and 50.2 ± 11.0 pA, 33.6 ± 8.7 Hz ($P < 0.0001$ vs. Sul) and 70.7 ± 14.1 pA ($P < 0.0001$ vs. Sul) with addition of DA, 23.2 ± 7.3 Hz ($p = 1$ vs. Sul) and 51.8 ± 11.1 pA ($p = 1$ vs. Sul), respectively. However, with SKF83566 in the bath, average frequency and amplitude of sIPSCs in six PGCs were 19.5 ± 5.7 Hz and 44.6 ± 9.0 pA, 19.4 ± 5.6 Hz ($p = 1$ vs. SKF) and 44.4 ± 8.3 pA ($p = 1$ vs. SKF) with addition of DA, respectively. Similar pharmacological results of DA actions on sIPSCs were observed in both SACs and ETCs (**Figures 3F–I**) except DA did not show significant effect on sIPSC amplitude in SACs (**Figure 3G**), supporting our prediction that DA increases overall glomerular inhibition.

In sum, our results demonstrate that DA enhances both frequency and amplitude of sIPSCs similarly in both PGCs and ETCs while in SACs DA increased only frequency but not amplitude of sIPSCs. Pharmacological analyses suggest that all these elevating effects in all three populations of glomerular neurons are mediated by D1LRs.

Glomerular Application of DA Augments sIPSCs in Mitral Cells (MCs)

MCs, the principal OB output neurons, have apical dendrites ramifying in single glomeruli where they receive glomerular inhibition. Thus, it was plausible to predict that DA potentiated glomerular inhibition of MCs. To examine this possibility, we voltage clamped MCs at −0 mV in OB slices to maximize sIPSC detection in the presence of NBQX and APV. MC responses to DA (100 μM) micropuffed (30 psi for 2 ms) to the glomeruli receiving apical dendrites of the recorded cells were recorded as described previously (Shao et al., 2012). Alexa 594 (10 μM) was included in internal solution to visualize the recorded cells and their apical dendrites thus facilitate DA micropuffing

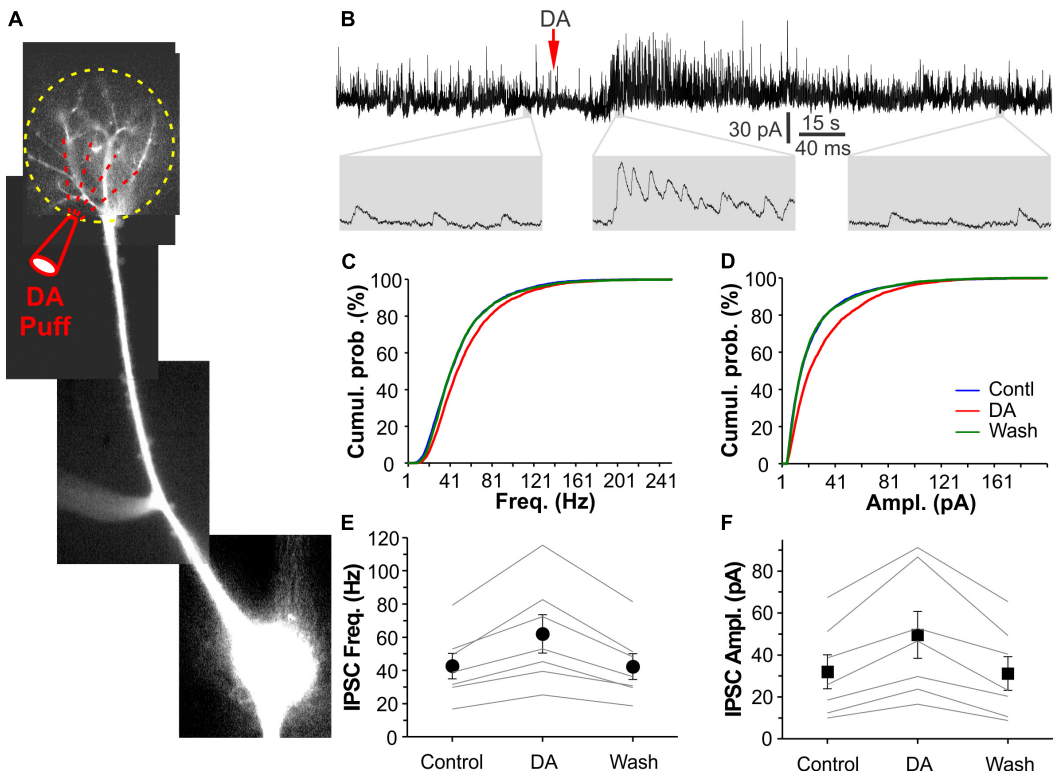

FIGURE 4 | DA elevates glomerular inhibition in MCs. **(A)** Photo graph of a mitral cell filled with Alexa594 via patch clamp pipette in an OB slice. **(B)** The top trace shows that DA (red arrow head) micropuffed to the glomerulus receiving the apical dendrite of the recorded MC as shown in **(A)** potentiates sIPSCs in the MC voltage clamped at 0 mV. Bottom traces are blown up. **(C,D)** Plotting graph showing cumulative probability of sIPSC frequency **(C)** or amplitude **(D)** in control, in the presence of DA, and after DA washout. **(E,F)** Pooled data showing effects of the micropuffed DA on sIPSC frequency **(E)** or amplitude **(F)** in seven MCs.

(**Figure 4A**). In these conditions, micropuffing DA reversibly increased both frequency and amplitude of sIPSCs in all tested seven MCs (**Figures 4B–F**). The average frequency and amplitude of sIPSCs in seven cells were 42.6 ± 7.7 Hz and 32.0 ± 8.7 pA in ACSF (control), 62.0 ± 11.6 Hz ($p < 0.001$ vs. control) and 49.6 ± 11.2 pA ($p < 0.001$ vs. control) in DA, and 42.3 ± 7.8 Hz ($p = 1$ vs. control) and 31.1 ± 8.0 pA ($p = 1$ vs. control) after DA washout, respectively. Collectively, our results demonstrate that DA enhances glomerular inhibition of MCs.

Dopamine Selectively Excites Short Axon Cells

Periglomerular cells and SACs are two major populations of inhibitory glomerular interneurons. To test whether DA activates them to release GABA and increase glomerular inhibition, we did both voltage and current clamp recordings from both SACs and PGCs in the presence of synaptic transmission blockers NBQX (10 μM), APV (50 μM) and GBZ (10 μM) to eliminate circuit influence. SACs responded to bath application of DA with an inward current (**Figure 5A**) in voltage clamp ($V_{hold} = -65$ mV) or depolarization with spikes in current clamp (**Figure 5C**) while PGCs did not respond to the same dose of DA (**Figures 5B,D**). The average amplitude of the DA-induced inward current in five SACs was 13.0 ± 2.6 pA in ACSF and 0.2 ± 0.1 pA in the presence of SKF83566 ($p < 0.01$ vs. in ACSF) while in five PGCs the average amplitude was 0.4 ± 0.1 pA (**Figure 5E**). In current clamp, the average amplitude of DA-induced depolarization in five SACs was 5.1 ± 0.6 mV in ACSF and 0.3 ± 0.1 mV ($p < 0.01$ vs. in ACSF) in the presence of SKF83566 while there was no depolarization in five PGCs (0.2 ± 0.1 mV) (**Figure 5F**). Taken together, our results demonstrate that DA selectively excites SACs via D1LRs.

$GABA_B$ Receptors Mediate the DA Suppressive Effects on sEPSCs in Glomerular Interneurons

Dopamine and GABA are coreleased from SACs (Maher and Westbrook, 2008; Borisovska et al., 2013; Liu et al., 2013; McGann, 2013) whereas activation of D2LRs or $GABA_B$ receptors produces presynaptic inhibition in many brain areas including the OB (Nickell et al., 1994; Aroniadou-Anderjaska et al., 2000; Ennis et al., 2001; Isaacson and Vitten, 2003; Wachowiak et al., 2005; Beaulieu and Gainetdinov, 2011; McGann, 2013). To test whether activation of $GABA_B$ receptors is required for the DA actions we observed, sEPSCs were recorded in both PGCs and SACs and their responses to DA were compared between with and without the selective $GABA_B$ receptor antagonist CGP55845 (10 μM) in the bath. As shown in **Figures 6A–C**, neither CGP55845 nor CGP55845 plus DA showed effect on sEPSCs in a PGC compared to control. Further analysis revealed DA effect on neither frequency nor amplitude of sEPSCs in six PGCs or

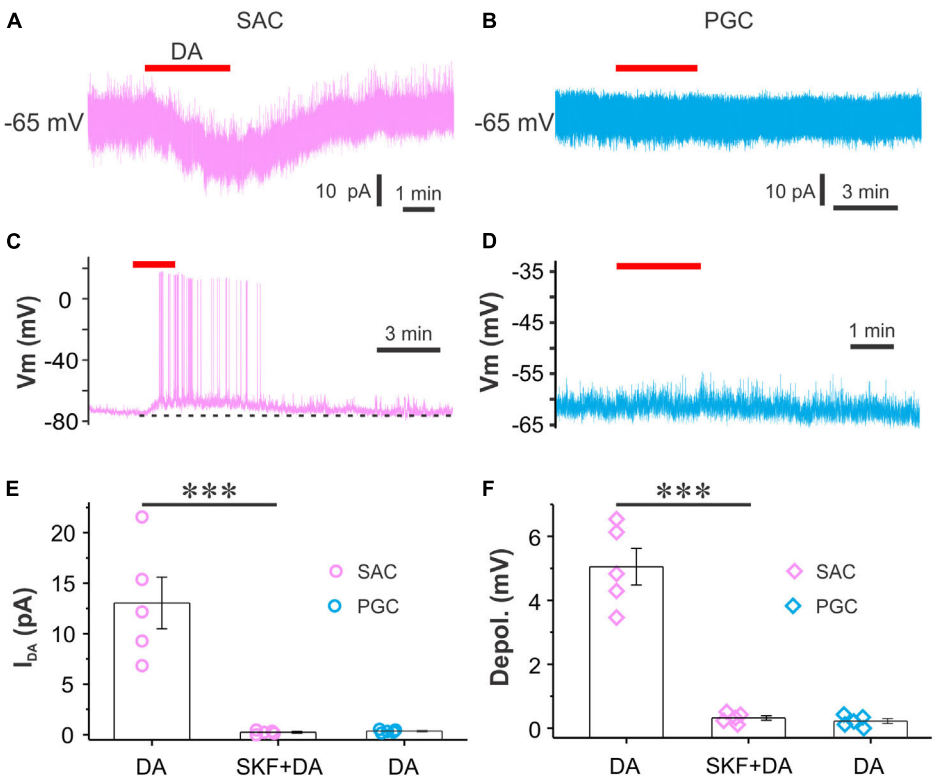

FIGURE 5 | DA directly excites SACs but not PGCs. **(A,B)** Recording traces showing that bath-applied DA produces an inward current in a SAC **(A)** but not in a PGC **(B)** when cells are voltage clamped at –60 mV in the presence of NBQX, APV and GBZ. **(C,D)** Current clamp traces showing that DA depolarizes a SAC **(C)** but not a PGC **(D)**. **(E,F)** Pooled data showing amplitude **(E)** of the DA-induced inward current or depolarization **(F)** in SACs ($n = 5$) but not in PGCs ($n = 5$). ***$P < 0.01$.

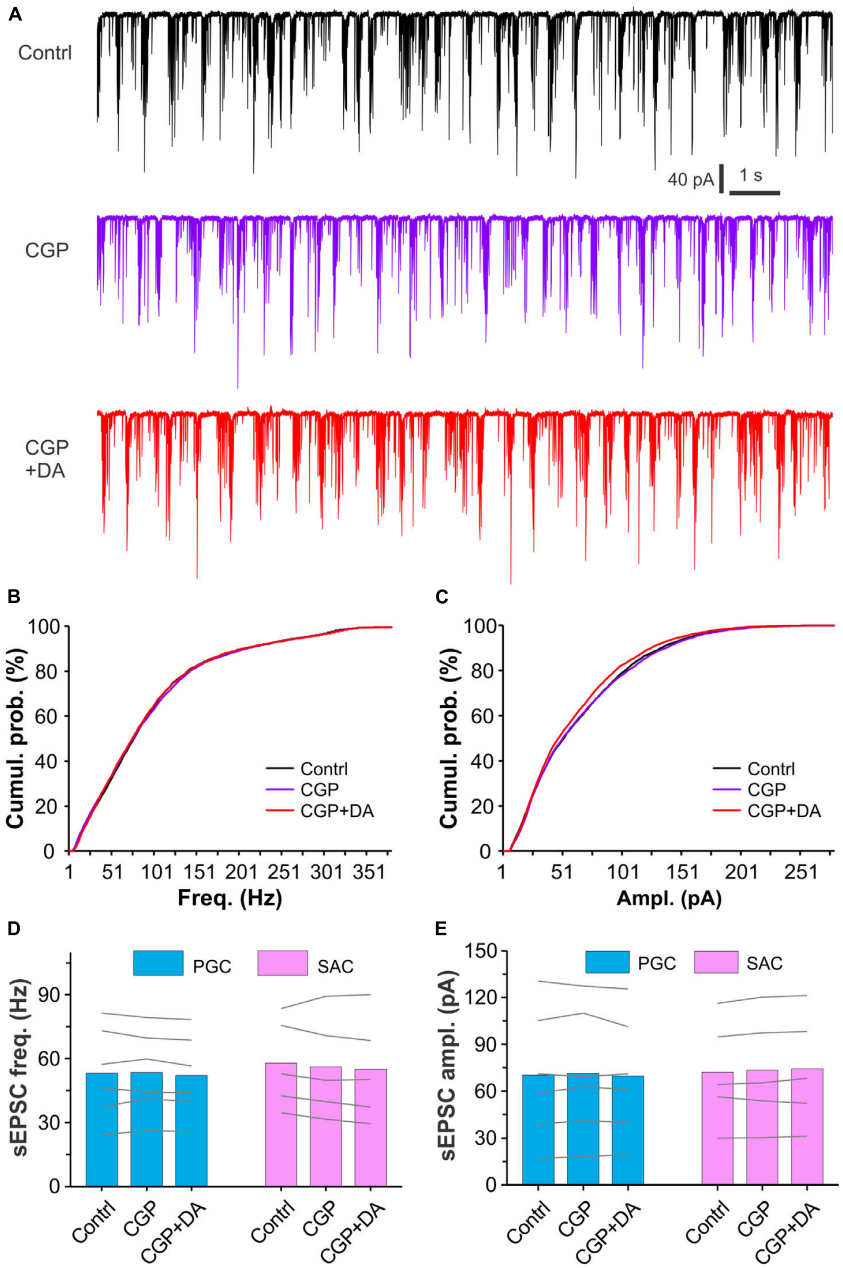

FIGURE 6 | Antagonizing $GABA_B$ receptors eliminates DA effects on sEPSCs in glomerular interneurons. **(A)** Typical recording traces showing burst sEPSCs in a PGC before (top), during (middle) bath application of CGP55845 (CGP, 10 μM), a selective $GABA_B$ receptor antagonist, or addition of DA (bottom) in the presence of CGP. **(B,C)** Graphs showing cumulative probability of frequency **(B)** or amplitude **(C)** of sEPSCs presented in **(A)**. **(D,E)** Pooled data showing that DA has effect on neither frequency **(D)** nor amplitude **(E)** of sEPSCs in either PGCs (n = 6) or SACs (n = 5) in the presence of CGP55845.

five SACs (**Figures 6D,E**), suggesting that activation of $GABA_B$ receptors is required for the DA suppressive effects on sEPSCs in PGCs and SACs.

DA Produces an Excitatory Net Effect on MCs

External tufted cells provide direct excitatory input to MCs and contribute to long-lasting depolarization (LLD) (De Saint et al., 2009; Gire and Schoppa, 2009). Our previous study showed that DA increases ETC spontaneous spike burst frequency (Liu et al., 2013), indicating that DA increase LLD frequency. However, our present results showed that DA enhanced glomerular inhibition at least partially due to its selective activation of SACs, indicating that DA inhibits MC output. What will be the DA net effects on MC output with integration of these two directionally opposite actions? To answer this question, we first recorded MCs in voltage clamp with a holding potential at −60 mV and observed their responses

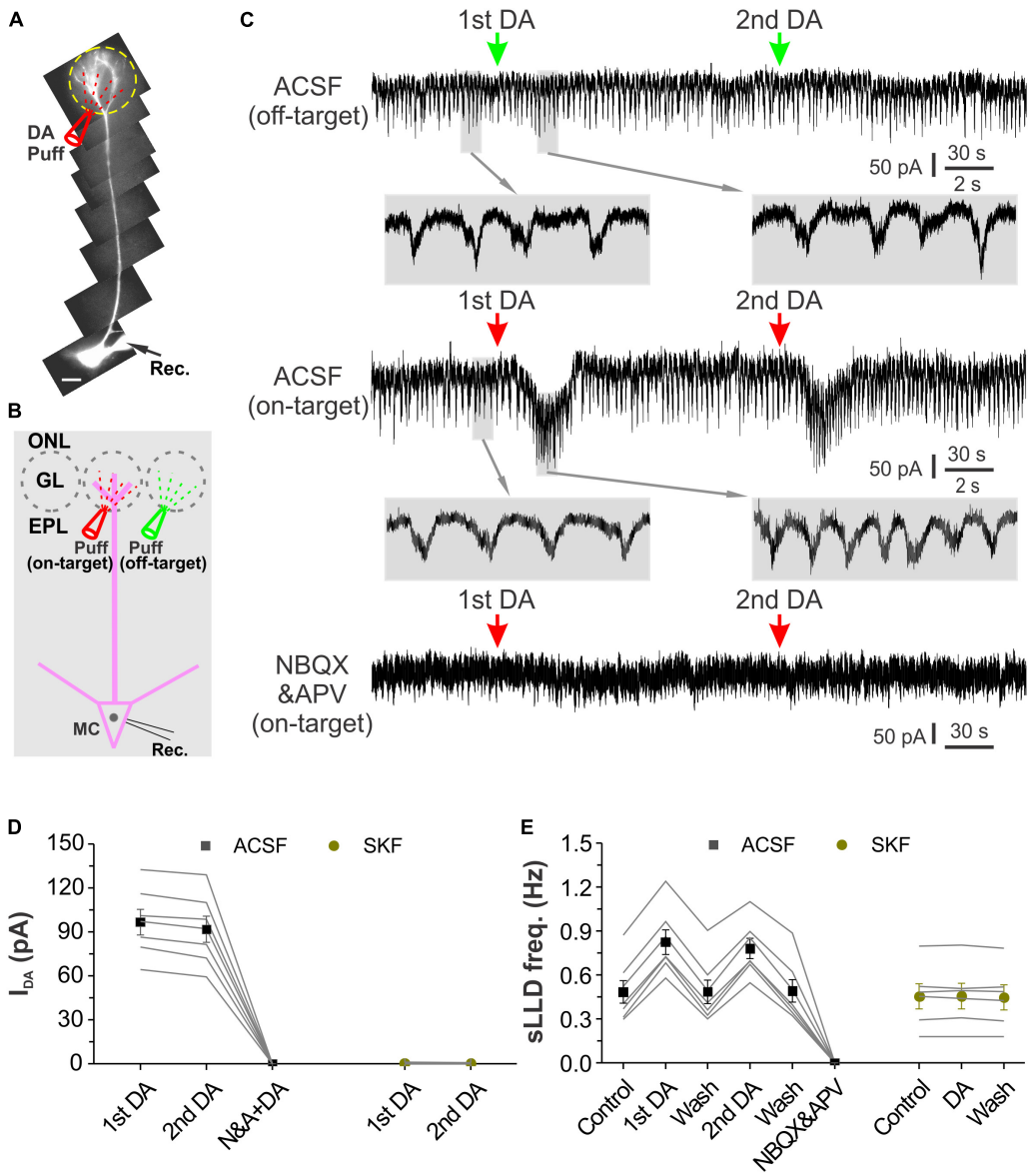

FIGURE 7 | Glomerular application of DA produces an inward current and increases sLLD frequency in MCs. **(A)** Photo graph of a MC filled with Alexa594 via patch clamp pipette in an OB slice. **(B)** Diagram illustration of DA application to the glomerulus (on-target) receiving the apical dendrites of the recorded MC or its adjacent glomerulus (off-target). **(C)** Recording traces showing the rhythmic long-lasting depolarizing (LLD)/inward currents recorded in a MC voltage clamped at –60 mV and their responses to off-target (top), on-target application of DA as shown in **(B)** in control condition (middle) or in the presence of NBQX and APV to block fast glutamate receptors (bottom). Traces at expanded time scale beneath the top and middle traces show changes in LLD current frequency after DA application. **(D)** Graphs of pooled data from two groups of MCs. Data of the first group of MCs (n = 7) show the amplitude of the inward currents induced by the first (1st) and second (2nd) dose of DA in ACSF, in the presence of NBQX and APV (N&A). The second group of MCs (n = 6) show effects of two doses of DA on-target application on the holding current in the presence of SKF83566, a selective D1LR antagonist. **(E)** Pooled data from two groups of MCs. Data of the first group of MCs (n = 7) show the frequency of the spontaneous LLD (sLLD) currents in ACSF (control), addition of the first dose of dopamine (1st DA), washout of the first dose of DA, application of the second dose of DA (2nd DA), washout of the second dose of DA, or in the presence of NBQX and APV. Data of the second group of MCs (n = 6) show sLLD frequency in the presence of SKF83566 before (control) or during (DA) DA application, and after DA washout (wash).

to glomerular application of DA as shown by **Figures 7A,B**. Alexa 594 (10 μM) was included in the patch pipette to visualize the recorded MC somata and their apical dendrites. In these conditions, micropuffing DA (100 μM, 2 ms) to glomeruli (off-target) next to the ones receiving the apical dendrites of the recorded cells did not evoke alteration in the spontaneous LLD (sLLD, **Figure 7C** top traces). However, when the puffing electrode was moved to target the glomerulus innervated by the apical dendrite of the recorded cell (on-target), DA reversibly induced an inward current in MCs (**Figure 7C** middle traces). The frequency of the spontaneous LLD superimposed on the inward current was increased compared to that before DA

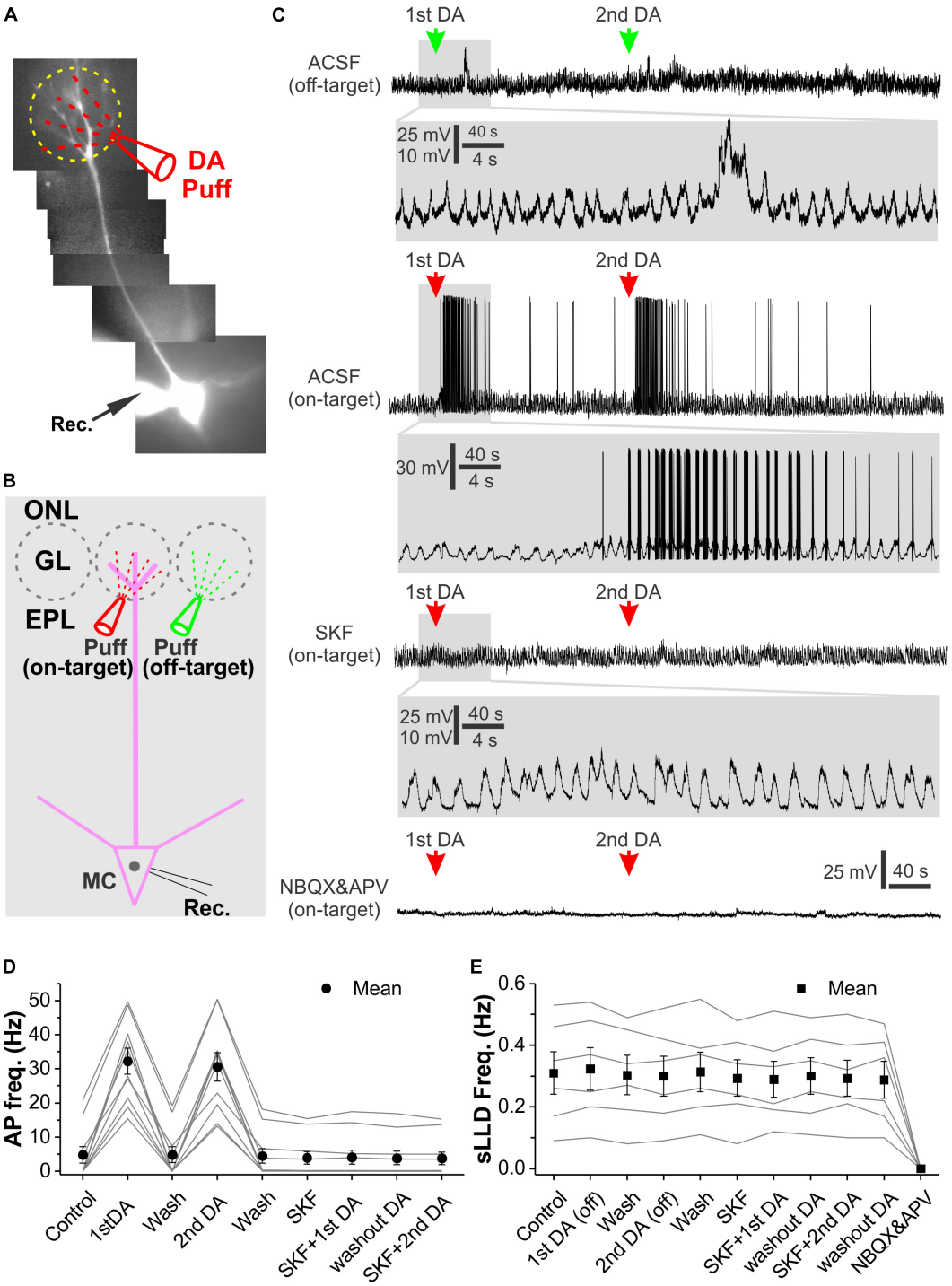

FIGURE 8 | Glomerular application of DA elevates OB output from MCs. **(A)** Photo graph of a MC filled with Alexa594 via patch clamp pipette in an OB slice. **(B)** Diagram illustration of DA application to the glomerulus (on-target) receiving the apical dendrites of the recorded MC or its adjacent glomerulus (off-target). **(C)** Recording traces showing the spontaneous rhythmic long-lasting depolarization (LLD) recorded in a MC in current clamp and their responses to off-target (top) or on-target application of DA as shown in **(B)** in ACSF, in the presence of SKF83566 to block D1LRs (middle) or NBQX and APV to block fast glutamate receptors (bottom). sLLDs are completely eliminated by NBQX and APV. Blown-up traces show DA effects on sLLD frequency or spike firing in each condition. **(D)** Graphs of pooled data from 10 MCs showing effects of two doses of on-target DA on action potential (AP) frequency in ACSF or in the presence of SKF83566. **(E)** Graphs of pooled data from six MCs showing effects of two doses of off-target DA or two doses of on-target DA on sLLD frequency in the presence of SKF83566 as well as effect of NBQX and APV.

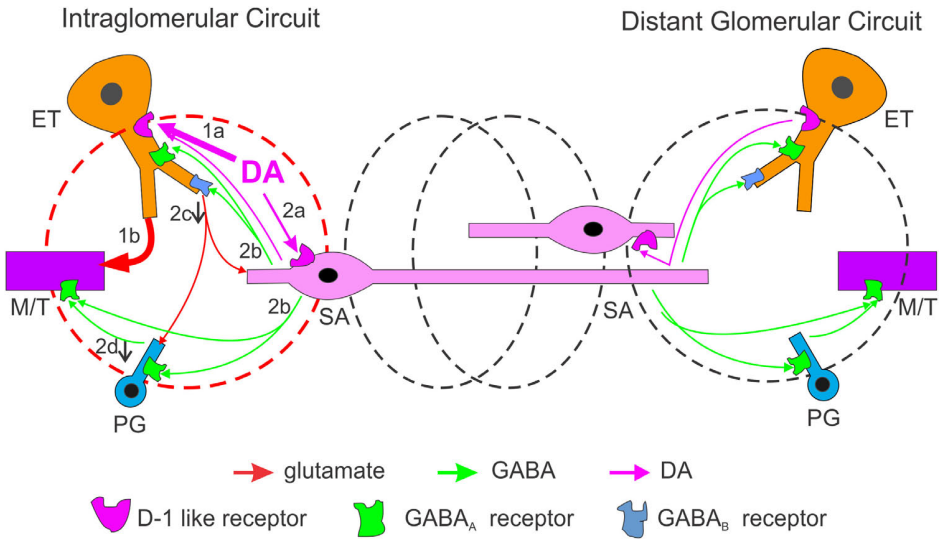

FIGURE 9 | Schematic summarizing DA regulation of OB output through intra- and inter-glomerular circuits. In the activated glomerulus (left, red), the DA net effect on output neurons is excitatory. DA directly excites two glomerular neuron types via D1LRs: the external tufted cells (ETCs, 1a) and short axon cells (SACs, 2a). Excitation of ETCs increases MC output (1b) while excited SACs corelease GABA and DA (2b) which lead to multiple consequences: (1) GABA activates $GABA_B$ receptors on ETC apical dendrites to reduce glutamate release and suppress sEPSCs in postsynaptic periglomerular cells (PGCs) and SACs (2c); (2) GABA activates $GABA_A$ receptors on PGCs to reduce glomerular inhibition of MCs (disinhibition) leading to further increase in MC output (2d); (3) GABA also inhibits MCs directly, but this inhibition is surpassed by the ETC-MC pathway-derived excitation. In the neighboring or distal glomeruli (black), output neurons are inhibited mainly by GABA-mediated interglomerular action. Thus, DA enhances the system's sensitivity through a mechanism similar to center-surround inhibition.

application (**Figure 7C** middle blown-up traces). After bath application of the glutamatergic receptor blockers NBQX and APV, sLLDs disappeared and glomerular application of DA showed no effect on the holding current (**Figure 7C** bottom trace), indicating that DA does not affect MC intrinsic properties and the DA-induced inward current is mediated by glutamate from ETCs. Consistently, further experiments showed that DA effects on MCs were completely blocked by SKF83566 (**Figures 7D,E**), indicating that they are due to activation of D1LRs in ETCs (Liu et al., 2013). In seven MCs, the average amplitude of the first and second dose of DA-induced inward current was 96.8 ± 8.7 pA and 91.9 ± 8.9 pA, respectively (**Figure 7D**). The sLLD frequency in seven MCs was increased from 0.48 ± 0.08 Hz in control to 0.83 ± 0.08 Hz by the first dose of DA but resumed to 0.49 ± 0.08 Hz after DA washout. The second dose of DA elevated this frequency to 0.78 ± 0.07 Hz ($p < 0.05$ compared to washout of first dose of DA) followed by a recovery (0.49 ± 0.08 Hz). In sum, these voltage clamp data showed that glomerular application of DA produced an excitatory net effect on MCs via D1LRs.

This conclusion led us to predict that DA enhance MC output to downstream centers. To test this, we repeated the prior experiments in current clamp (**Figures 8A,B**). Again, off-target glomerular application of DA did not evoke significant effect on MC membrane potential or sLLD frequency (**Figure 8C** top traces and **Figure 8E**) while on-target DA reversibly and reliably evoked spike responses in MCs (**Figure 8C** middle traces and **Figure 8C**). Consistent with voltage clamp results, after treatment of OB slices with SKF83566 for 10 min, on-target DA neither elicited spike response nor affected sLLDs (**Figures 8C,E**) whereas DA no longer showed any effect in the presence of NBQX and APV to completely block sLLDs (**Figure 8C** bottom trace). The first dose of DA increased the average instant frequency of spikes in 10 MCs from 4.8 ± 2.4 Hz to 32.2 ± 3.8 Hz ($p < 0.0001$) followed by a complete recovery (4.9 ± 2.4 Hz, $p = 1$ compared to pre-DA) while the second dose of DA reversibly elevated it up to 30.6 ± 4.2 Hz ($p < 0.0001$ compared to first DA washout). These actions were completely blocked by SKF83566 (**Figure 8D**).

Taken together, our results demonstrate that DA produces an excitatory net effect on MCs and consequently increases OB output to downstream olfactory centers.

DISCUSSION

We characterized DA actions on both excitatory and inhibitory transmission in the glomerular circuit followed by analysis of the underlying cellular mechanisms and DA impact on OB output with five major findings (**Figure 9**). First, DA via D1LRs suppresses sEPSCs in the ETC-driven inhibitory glomerular interneurons, contradicting with DA excitatory actions on ETCs. Second, activation of D1LRs potentiates sIPSCs in all glomerular neurons, indicating enhancement of glomerular inhibition. Consistently, glomerular application of DA elevates sIPSCs in MCs. Third, the depression of sEPSCs in inhibitory glomerular interneurons is blocked by inhibition of $GABA_B$ receptors, implying that DA increases GABA release from inhibitory glomerular interneurons to inhibit glutamate release from ETC apical dendrites. Fourth, DA selectively excites the GABAergic SACs but not PGCs via D1LRs. Finally, DA produces a net

excitatory effect on MC output via D1LRs. This effect is mediated by glutamate, suggesting the DA excitation of ETCs surpasses the enhanced glomerular inhibition thus potentiates the OB output to downstream targets.

DA Regulates the Excitation–Inhibition Balance in the Glomerular Circuit

Our previous study demonstrates that endogenous DA released from SACs or exogenous DA enhances ETC output by elevating the hyperpolarization-activated cation current (I_h) (Liu et al., 2013). ETCs do not have lateral dendrites and their sole apical dendrites ramify in individual glomeruli (Pinching and Powell, 1971a; Macrides and Schneider, 1982; Hayar et al., 2004b; Antal et al., 2006). Thus, they are generally considered as local excitatory interneurons participating in the operation of glomerular circuit. ETC apical dendrites form glutamatergic dendrodendritic synapses with vast majority of PGCs and SACs (Shao et al., 2009; Kiyokage et al., 2010), and apical dendrites of MTCs (De Saint et al., 2009; Gire and Schoppa, 2009) so that the overall excitation level at the glomerular level has been thought to be controlled or coordinated by ETC activities (De Saint et al., 2009). Subsequent studies with optogenetic approaches did not reveal endogenous DA actions on other postsynaptic targets of SACs including MTCs and PGCs (Banerjee et al., 2015; Liu et al., 2016; Shao et al., 2019), suggesting that DA functions as a neurotransmitter to mediate wiring transmission only from SACs to ETCs. In this context, by activating ETCs DA should increase synaptic excitation across all neuron populations in the glomerular layer. However, DA may alternatively function as a neuromodulator to mediate volume transmission given its long-lasting small quantal release from SACs (Cragg et al., 2001; Borisovska et al., 2013). In this scenario, actions of endogenous DA released from SACs may alter synaptic activities at dendritic terminals without detectable changes in membrane current or potential at cell somata where recordings are normally made from with conventional electrophysiological approaches. In other words, DA could act on neurons other than ETCs to subtly alter the synaptic excitation–inhibition balance among distinct neuron populations. Consistently, findings of the present study support this prediction, i.e., exogenous DA excites only MTCs but not the ETC-driven inhibitory glomerular interneurons PGCs and SACs, in which DA via D1LRs decreases spontaneous excitatory synaptic activities instead. Our further analysis supports that the excitatory actions of DA on MTCs are not due to direct activation of MTCs but instead are through ETC intermediation because they are eliminated by blocking the glutamatergic receptors AMPA and NMDA receptors, which mediate the transmission from ETCs to MTCs (De Saint et al., 2009; Gire and Schoppa, 2009). Thus, DA differentiates the ETC-driven MTCs from ETC-driven PGCs and SACs by resetting the ETC-derived excitatory synaptic input to postsynaptic targets. These findings are consistent with previous studies showing that:(1) DA activates ETCs (Liu et al., 2013) which provide excitatory feedforward to MTCs (De Saint et al., 2009; Gire and Schoppa, 2009); (2) D1LRs are broadly expressed in the OB including the glomerular layer (Coronas et al., 1997; Beaulieu and Gainetdinov, 2011). Therefore, the overall impact of DA actions is to enhance the OB output by enhancing the ETC-intermediated excitatory feedforward to MTCs and weakening ETC-driven excitatory synaptic input to the local GABAergic interneurons PGCs and SACs, which provide inhibitory feedforward to MTCs.

Cellular Mechanisms Underlying DA Actions

Our mechanistic analysis revealed that the DA-induced suppression of excitatory synaptic activities in ETC-driven PGCs and SACs requires activation of $GABA_B$ receptors. Activation of $GABA_B$ receptors on OSN axon terminals inhibits glutamate releases (Nickell et al., 1994; Aroniadou-Anderjaska et al., 2000; Wachowiak et al., 2005; McGann, 2013) whereas $GABA_B$ receptors are also present in OB glomerular neurons (Fritschy et al., 1999; Panzanelli et al., 2004). Consistent with previous work showing that $GABA_B$ receptors inhibit dendrodendritic transmission from MTCs to granule cells in the OB (Isaacson and Vitten, 2003), our finding suggests that GABA released from local interneurons in response to DA activates $GABA_B$ receptors on ETC apical dendrites to reduce glutamate release causing suppression of excitatory synaptic activities in postsynaptic PGCs and SACs. This interpretation is supported by our findings that DA via D1LRs augments spontaneous inhibitory synaptic activities in all glomerular neurons and MTCs, suggesting DA increases GABA release from inhibitory interneurons in the glomerular layer. Interestingly, DA selectively excites or depolarizes SACs and increases their spontaneous firing frequency without detectable effect on PGCs. Taken together, these findings lead us to conclude that DA excites SACs, which release GABA to activate $GABA_B$ receptors on ETC apical dendrites and reduce glutamate release causing suppression of spontaneous excitatory synaptic activities in PGCs and SACs (**Figure 9**). Recent studies showed that another type of inhibitory neurons termed deep short axon cells (dSACs) have processes extending into the glomerular layer (Eyre et al., 2008; Burton et al., 2017). Future work needs to examine DA effect on dSACs to see if this population of interneuron are also subject to DAergic modulation.

Functional Implications

Similar to other brain regions like the striatum, activation of D1LR or D2LRs produces opposite effects on olfactory processing (Yue et al., 2004). In contrast to activation of D2LRs that generally produces inhibitory effects on odor discrimination and transmission of the first synapse from OSNs to postsynaptic targets in the OB (Nickell et al., 1991; Aroniadou-Anderjaska et al., 2000; Ennis et al., 2001; Yue et al., 2004; Tillerson et al., 2006; Escanilla et al., 2009; McGann, 2013), activation of D1LRs improves odor detection and discrimination (Doty et al., 1998; Yue et al., 2004). Consistently, our findings in the present study show that overall net effect of DA on OB output is the D1LR-mediated excitation, which depolarizes the output neurons MTCs to bring their resting membrane potential closer to the threshold of action potential generation, meanwhile, activation

of D1LRs selectively excites SACs. Since SACs have long processes connecting multiple glomeruli (Kosaka and Kosaka, 2008; Kiyokage et al., 2010), DA activation of SACs is speculated to extend inhibition to ETCs (Liu et al., 2013; Whitesell et al., 2013) and output neurons (Banerjee et al., 2015; Liu et al., 2016) in neighboring or distal glomeruli. Thus, we propose that activation of D1LRs is to produce a center-surrounding effect thus enhances OB output from the activated glomeruli to facilitate odor detection and discrimination. Further work by knocking out D1LRs or chemogenetic inhibition of D1LRs in the OB would provide insight into this speculation.

DATA AVAILABILITY STATEMENT

All datasets generated for this study are included in the manuscript.

ETHICS STATEMENT

The animal study was reviewed and approved by Howard University Animal Care and Use Committees.

AUTHOR CONTRIBUTIONS

SL planned and performed the experiments, analyzed the data, performed the statistical analysis, interpreted the results, wrote the manuscript, and approved the content.

FUNDING

This project was supported by the National Institutes of Health, NIDCDR01DC014447 to SL.

REFERENCES

Antal, M., Eyre, M., Finklea, B., and Nusser, Z. (2006). External tufted cells in the main olfactory bulb form two distinct subpopulations. *Eur. J. Neurosci.* 24, 1124–1136. doi: 10.1111/j.1460-9568.2006.04988.x

Aroniadou-Anderjaska, V., Zhou, F. M., Priest, C. A., Ennis, M., and Shipley, M. T. (2000). Tonic and synaptically evoked presynaptic inhibition of sensory input to the rat olfactory bulb via GABA(B) heteroreceptors. *J. Neurophysiol.* 84, 1194–1203. doi: 10.1152/jn.2000.84.3.1194

Banerjee, A., Marbach, F., Anselmi, F., Koh, M. S., Davis, M. B., Garcia da Silva, P., et al. (2015). An Interglomerular circuit gates glomerular output and implements gain control in the mouse olfactory bulb. *Neuron* 87, 193–207. doi: 10.1016/j.neuron.2015.06.019

Beaulieu, J. M., and Gainetdinov, R. R. (2011). The physiology, signaling, and pharmacology of dopamine receptors. *Pharmacol. Rev.* 63, 182–217. doi: 10.1124/pr.110.002642

Berkowicz, D. A., and Trombley, P. Q. (2000). Dopaminergic modulation at the olfactory nerve synapse. *Brain Res.* 855, 90–99. doi: 10.1016/s0006-8993(99)02342-2

Bjorklund, A., and Dunnett, S. B. (2007a). Dopamine neuron systems in the brain: an update. *Trends Neurosci.* 30, 194–202. doi: 10.1016/j.tins.2007.03.006

Bjorklund, A., and Dunnett, S. B. (2007b). Fifty years of dopamine research. *Trends Neurosci.* 30, 185–187. doi: 10.1016/j.tins.2007.03.004

Bonzano, S., Bovetti, S., Gendusa, C., Peretto, P., and De Marchis, S. (2016). Adult born olfactory bulb dopaminergic interneurons: molecular determinants and experience-dependent plasticity. *Front. Neurosci.* 10:189.

Borisovska, M., Bensen, A. L., Chong, G., and Westbrook, G. L. (2013). Distinct modes of dopamine and GABA release in a dual transmitter neuron. *J. Neurosci.* 33, 1790–1796. doi: 10.1523/jneurosci.4342-12.2013

Burton, S. D. (2017). Inhibitory circuits of the mammalian main olfactory bulb. *J. Neurophysiol.* 118, 2034–2051. doi: 10.1152/jn.00109.2017

Burton, S. D., LaRocca, G., Liu, A., Cheetham, C. E., and Urban, N. N. (2017). Olfactory bulb deep short-axon cells mediate widespread inhibition of tufted cell apical dendrites. *J. Neurosci.* 37, 1117–1138. doi: 10.1523/jneurosci.2880-16.2016

Cave, J. W., and Baker, H. (2009). Dopamine systems in the forebrain. *Adv. Exp. Med. Biol.* 651, 15–35. doi: 10.1007/978-1-4419-0322-8_2

Coronas, V., Srivastava, L. K., Liang, J. J., Jourdan, F., and Moyse, E. (1997). Identification and localization of dopamine receptor subtypes in rat olfactory mucosa and bulb: a combined in situ hybridization and ligand binding radioautographic approach. *J. Chem. Neuroanat.* 12, 243–257. doi: 10.1016/s0891-0618(97)00215-9

Cragg, S. J., Nicholson, C., Kume-Kick, J., Tao, L., and Rice, M. E. (2001). Dopamine-mediated volume transmission in midbrain is regulated by distinct extracellular geometry and uptake. *J. Neurophysiol.* 85, 1761–1771. doi: 10.1152/jn.2001.85.4.1761

Dahlstroem, A., and Fuxe, K. (1964). Evidence for the existence of monoamine-containing neurons in the central nervous system. I. Demonstration of monoamines in the cell bodies of brain stem neurons. *Acta Physiol. Scand. Suppl,* 232, 231–255.

De Saint, J. D., Hirnet, D., Westbrook, G. L., and Charpak, S. (2009). External tufted cells drive the output of olfactory bulb glomeruli. *J. Neurosci.* 29, 2043–2052. doi: 10.1523/jneurosci.5317-08.2009

Doty, R. L., Li, C., Bagla, R., Huang, W., Pfeiffer, C., Brosvic, G. M., et al. (1998). SKF 38393 enhances odor detection performance. *Psychopharmacology* 136, 75–82. doi: 10.1007/s002130050541

Ennis, M., Zhou, F. M., Ciombor, K. J., Aroniadou-Anderjaska, V., Hayar, A., Borrelli, E., et al. (2001). Dopamine D2 receptor-mediated presynaptic inhibition of olfactory nerve terminals. *J. Neurophysiol.* 86, 2986–2997. doi: 10.1152/jn.2001.86.6.2986

Escanilla, O., Yuhas, C., Marzan, D., and Linster, C. (2009). Dopaminergic modulation of olfactory bulb processing affects odor discrimination learning in rats. *Behav. Neurosci.* 123, 828–833. doi: 10.1037/a0015855

Eyre, M. D., Antal, M., and Nusser, Z. (2008). Distinct deep short-axon cell subtypes of the main olfactory bulb provide novel intrabulbar and extrabulbar GABAergic connections. *J. Neurosci.* 28, 8217–8229. doi: 10.1523/jneurosci.2490-08.2008

Fritschy, J. M., Meskenaite, V., Weinmann, O., Honer, M., Benke, D., and Mohler, H. (1999). GABAB-receptor splice variants GB1a and GB1b in rat brain: developmental regulation, cellular distribution and extrasynaptic localization. *Eur. J. Neurosci.* 11, 761–768. doi: 10.1046/j.1460-9568.1999.00481.x

Gire, D. H., and Schoppa, N. E. (2009). Control of on/off glomerular signaling by a local GABAergic microcircuit in the olfactory bulb. *J. Neurosci.* 29, 13454–13464. doi: 10.1523/jneurosci.2368-09.2009

Guthrie, K. M., Pullara, J. M., Marshall, J. F., and Leon, M. (1991). Olfactory deprivation increases dopamine D2 receptor density in the rat olfactory bulb. *Synapse* 8, 61–70. doi: 10.1002/syn.890080109

Gutierrez-Mecinas, M., Crespo, C., Blasco-Ibanez, J. M., Gracia-Llanes, F. J., Marques-Mari, A. I., Nacher, J., et al. (2005). Distribution of D2 dopamine receptor in the olfactory glomeruli of the rat olfactory bulb. *Eur. J. Neurosci.* 22, 1357–1367. doi: 10.1111/j.1460-9568.2005.04328.x

Hayar, A., Karnup, S., Ennis, M., and Shipley, M. T. (2004a). External tufted cells: a major excitatory element that coordinates glomerular activity. *J. Neurosci.* 24, 6676–6685. doi: 10.1523/jneurosci.1367-04.2004

Hayar, A., Karnup, S., Shipley, M. T., and Ennis, M. (2004b). Olfactory bulb glomeruli: external tufted cells intrinsically burst at theta frequency and are entrained by patterned olfactory input. *J. Neurosci.* 24, 1190–1199. doi: 10.1523/jneurosci.4714-03.2004

Hsia, A. Y., Vincent, J. D., and Lledo, P. M. (1999). Dopamine depresses synaptic inputs into the olfactory bulb. *J. Neurophysiol.* 82, 1082–1085. doi: 10.1152/jn.1999.82.2.1082

Isaacson, J. S., and Vitten, H. (2003). GABA(B) receptors inhibit dendrodendritic transmission in the rat olfactory bulb. *J. Neurosci.* 23, 2032–2039. doi: 10.1523/jneurosci.23-06-02032.2003

Karpuk, N., and Hayar, A. (2008). Activation of postsynaptic GABAB receptors modulates the bursting pattern and synaptic activity of olfactory bulb juxtaglomerular neurons. *J. Neurophysiol.* 99, 308–319. doi: 10.1152/jn.01086.2007

Kiyokage, E., Pan, Y. Z., Shao, Z., Kobayashi, K., Szabo, G., Yanagawa, Y., et al. (2010). Molecular identity of periglomerular and short axon cells. *J. Neurosci.* 30, 1185–1196. doi: 10.1523/jneurosci.3497-09.2010

Klein, M. O., Battagello, D. S., Cardoso, A. R., Hauser, D. N., Bittencourt, J. C., and Correa, R. G. (2019). Dopamine: functions, signaling, and association with neurological diseases. *Cell Mol. Neurobiol.* 39, 31–59. doi: 10.1007/s10571-018-0632-3

Kosaka, T., and Kosaka, K. (2008). Tyrosine hydroxylase-positive GABAergic juxtaglomerular neurons are the main source of the interglomerular connections in the mouse main olfactory bulb. *Neurosci. Res.* 60, 349–354. doi: 10.1016/j.neures.2007.11.012

Lazarini, F., Gabellec, M. M., Moigneu, C., de Chaumont, F., Olivo-Marin, J. C., and Lledo, P. M. (2014). Adult neurogenesis restores dopaminergic neuronal loss in the olfactory bulb. *J. Neurosci.* 34, 14430–14442. doi: 10.1523/jneurosci.5366-13.2014

Levey, A. I., Hersch, S. M., Rye, D. B., Sunahara, R. K., Niznik, H. B., Kitt, C. A., et al. (1993). Localization of D1 and D2 dopamine receptors in brain with subtype-specific antibodies. *Proc. Natl. Acad. Sci. U.S.A.* 90, 8861–8865. doi: 10.1073/pnas.90.19.8861

Liu, S., Plachez, C., Shao, Z., Puche, A., and Shipley, M. T. (2013). Olfactory bulb short axon cell release of GABA and dopamine produces a temporally biphasic inhibition-excitation response in external tufted cells. *J. Neurosci.* 33, 2916–2926. doi: 10.1523/jneurosci.3607-12.2013

Liu, S., Puche, A. C., and Shipley, M. T. (2016). The interglomerular circuit potently inhibits olfactory bulb output neurons by both direct and indirect pathways. *J. Neurosci.* 36, 9604–9617. doi: 10.1523/jneurosci.1763-16.2016

Lledo, P. M., Gheusi, G., and Vincent, J. D. (2005). Information processing in the mammalian olfactory system. *Physiol. Rev.* 85, 281–317. doi: 10.1152/physrev.00008.2004

Lopez-Bendito, G., Sturgess, K., Erdelyi, F., Szabo, G., Molnar, Z., and Paulsen, O. (2004). Preferential origin and layer destination of GAD65-GFP cortical interneurons. *Cereb. Cortex* 14, 1122–1133. doi: 10.1093/cercor/bhh072

Macrides, F., and Schneider, S. P. (1982). Laminar organization of mitral and tufted cells in the main olfactory bulb of the adult hamster. *J. Comp. Neurol.* 208, 419–430. doi: 10.1002/cne.902080410

Maher, B. J., and Westbrook, G. L. (2008). Co-transmission of dopamine and GABA in periglomerular cells. *J. Neurophysiol.* 99, 1559–1564. doi: 10.1152/jn.00636.2007

Matsushita, N., Okada, H., Yasoshima, Y., Takahashi, K., Kiuchi, K., and Kobayashi, K. (2002). Dynamics of tyrosine hydroxylase promoter activity during midbrain dopaminergic neuron development. *J. Neurochem.* 82, 295–304. doi: 10.1046/j.1471-4159.2002.00972.x

McGann, J. P. (2013). Presynaptic inhibition of olfactory sensory neurons: new mechanisms and potential functions. *Chem. Sens.* 38, 459–474.

Nagayama, S., Homma, R., and Imamura, F. (2014). Neuronal organization of olfactory bulb circuits. *Front. Neural. Circ.* 8:98.

Nickell, W. T., Behbehani, M. M., and Shipley, M. T. (1994). Evidence for GABAB-mediated inhibition of transmission from the olfactory nerve to mitral cells in the rat olfactory bulb. *Brain Res. Bull.* 35, 119–123. doi: 10.1016/0361-9230(94)90091-4

Nickell, W. T., Norman, A. B., Wyatt, L. M., and Shipley, M. T. (1991). Olfactory bulb DA receptors may be located on terminals of the olfactory nerve. *Neuroreport* 2, 9–12. doi: 10.1097/00001756-199101000-00002

Panzanelli, P., Lopez-Bendito, G., Lujan, R., and Sassoe-Pognetto, M. (2004). Localization and developmental expression of GABA(B) receptors in the rat olfactory bulb. *J. Neurocytol.* 33, 87–99. doi: 10.1023/b:neur.0000029650.28943.b2

Parrish-Aungst, S., Kiyokage, E., Szabo, G., Yanagawa, Y., Shipley, M. T., and Puche, A. C. (2011). Sensory experience selectively regulates transmitter synthesis enzymes in interglomerular circuits. *Brain Res.* 1382, 70–76. doi: 10.1016/j.brainres.2011.01.068

Pignatelli, A., and Belluzzi, O. (2017). Dopaminergic neurones in the main olfactory bulb: an overview from an electrophysiological perspective. *Front. Neuroanat.* 11:7.

Pinching, A. J., and Powell, T. P. (1971a). The neuron types of the glomerular layer of the olfactory bulb. *J. Cell Sci.* 9, 305–345.

Pinching, A. J., and Powell, T. P. (1971b). The neuropil of the periglomerular region of the olfactory bulb. *J. Cell Sci.* 9, 379–409.

Romon, Y., and Cajal, S. (1909). *Histologie du SysteÌme Nerveux de l'homme & des Verteibreès*. Paris: Maloine.

Serguera, C., Triaca, V., Kelly-Barrett, J., Banchaabouchi, M. A., and Minichiello, L. (2008). Increased dopamine after mating impairs olfaction and prevents odor interference with pregnancy. *Nat. Neurosci.* 11, 949–956. doi: 10.1038/nn.2154

Shao, Z., Puche, A. C., Kiyokage, E., Szabo, G., and Shipley, M. T. (2009). Two GABAergic intraglomerular circuits differentially regulate tonic and phasic presynaptic inhibition of olfactory nerve terminals. *J. Neurophysiol.* 101, 1988–2001. doi: 10.1152/jn.91116.2008

Shao, Z., Puche, A. C., Liu, S., and Shipley, M. T. (2012). Intraglomerular inhibition shapes the strength and temporal structure of glomerular output. *J. Neurophysiol.* 108, 782–793. doi: 10.1152/jn.00119.2012

Shao, Z., Liu, S., Zhou, F., Puche, A. C., and Shipley, M. T. (2019). Reciprocal inhibitory glomerular circuits contribute to excitation-inhibition balance in the mouse olfactory bulb. *eNeuro* 6:ENEURO.0048-19. doi: 10.1523/ENEURO.0048-19.2019

Taylor, T. N., Caudle, W. M., Shepherd, K. R., Noorian, A., Jackson, C. R., Iuvone, P. M., et al. (2009). Nonmotor symptoms of Parkinson's disease revealed in an animal model with reduced monoamine storage capacity. *J. Neurosci.* 29, 8103–8113. doi: 10.1523/jneurosci.1495-09.2009

Tillerson, J. L., Caudle, W. M., Parent, J. M., Gong, C., Schallert, T., and Miller, G. W. (2006). Olfactory discrimination deficits in mice lacking the dopamine transporter or the D2 dopamine receptor. *Behav. Brain Res.* 172, 97–105. doi: 10.1016/j.bbr.2006.04.025

Vaaga, C. E., Yorgason, J. T., Williams, J. T., and Westbrook, G. L. (2017). Presynaptic gain control by endogenous cotransmission of dopamine and GABA in the olfactory bulb. *J. Neurophysiol.* 117, 1163–1170. doi: 10.1152/jn.00694.2016

Wachowiak, M., McGann, J. P., Heyward, P. M., Shao, Z., Puche, A. C., and Shipley, M. T. (2005). Inhibition [corrected] of olfactory receptor neuron input to olfactory bulb glomeruli mediated by suppression of presynaptic calcium influx. *J. Neurophysiol.* 94, 2700–2712. doi: 10.1152/jn.00286.2005

Whitesell, J. D., Sorensen, K. A., Jarvie, B. C., Hentges, S. T., and Schoppa, N. E. (2013). Interglomerular lateral inhibition targeted on external tufted cells in the olfactory bulb. *J. Neurosci.* 33, 1552–1563. doi: 10.1523/jneurosci.3410-12.2013

Wilson, R. I., and Mainen, Z. F. (2006). Early events in olfactory processing. *Annu. Rev. Neurosci.* 29, 163–201. doi: 10.1146/annurev.neuro.29.051605.112950

Yu, Q., Liu, Y. Z., Zhu, Y. B., Wang, Y. Y., Li, Q., and Yin, D. M. (2019). Genetic labeling reveals temporal and spatial expression pattern of D2 dopamine receptor in rat forebrain. *Brain Struct. Funct.* 224, 1035–1049. doi: 10.1007/s00429-018-01824-2

Yue, E. L., Cleland, T. A., Pavlis, M., and Linster, C. (2004). Opposing effects of D1 and D2 receptor activation on odor discrimination learning. *Behav. Neurosci.* 118, 184–190. doi: 10.1037/0735-7044.118.1.184

Conflict of Interest: The author declares that the research was conducted in the absence of any commercial or financial relationships that could be construed as a potential conflict of interest.

frontiers in Cellular Neuroscience

ORIGINAL RESEARCH
published: 18 December 2020
doi: 10.3389/fncel.2020.593309

Pregnancy Changes the Response of the Vomeronasal and Olfactory Systems to Pups in Mice

Cinta Navarro-Moreno[1†], Maria Jose Sanchez-Catalan[1†], Manuela Barneo-Muñoz[1], Rafael Goterris-Cerisuelo[1], Maria Belles[1], Enrique Lanuza[2], Carmen Agustin-Pavon[2] and Fernando Martinez-Garcia[1]*

[1] Lab of Functional Neuroanatomy (NeuroFun-UJI-UV), Unitat Predepartamental de Medicina, Faculty of Health Sciences, Universitat Jaume I, Castellón de la Plana, Spain, [2] Lab of Functional Neuroanatomy (NeuroFun-UJI-UV), Departament de Biologia Cellular, Funcional i Antropologia, Faculty of Biological Sciences, Universitat de València, Valencia, Spain

OPEN ACCESS

Edited by:
Pablo Chamero,
INRA Centre Val de Loire, France

Reviewed by:
Martina Pyrski,
Saarland University, Germany
Yu-Feng Wang,
Harbin Medical University, China

***Correspondence:**
Fernando Martinez-Garcia
femartin@uji.es

[†]These authors have contributed equally to this work

Specialty section:
This article was submitted to Cellular Neurophysiology, a section of the journal Frontiers in Cellular Neuroscience

Received: 10 August 2020
Accepted: 16 November 2020
Published: 18 December 2020

Citation:
Navarro-Moreno C, Sanchez-Catalan MJ, Barneo-Muñoz M, Goterris-Cerisuelo R, Belles M, Lanuza E, Agustin-Pavon C and Martinez-Garcia F (2020) Pregnancy Changes the Response of the Vomeronasal and Olfactory Systems to Pups in Mice. Front. Cell. Neurosci. 14:593309. doi: 10.3389/fncel.2020.593309

Motherhood entails changes in behavior with increased motivation for pups, induced in part by pregnancy hormones acting upon the brain. This work explores whether this alters sensory processing of pup-derived chemosignals. To do so, we analyse the expression of immediate early genes (IEGs) in the vomeronasal organ (VNO; Egr1) and centers of the olfactory and vomeronasal brain pathways (cFos) in virgin and late-pregnant females exposed to pups, as compared to buttons (socially neutral control). In pup-exposed females, we quantified diverse behaviors including pup retrieval, sniffing, pup-directed attack, nest building and time in nest or on nest, as well as time off nest. Pups induce Egr1 expression in the VNO of females, irrespective of their physiological condition, thus suggesting the existence of VNO-detected pup chemosignals. A similar situation is found in the accessory olfactory bulb (AOB) and posteromedial part of the medial bed nucleus of the stria terminalis (BSTMPM). By contrast, in the medial amygdala and posteromedial cortical amygdala (PMCo), responses to pups-vs-buttons are different in virgin and late-pregnant females, thus suggesting altered sensory processing during late pregnancy. The olfactory system also shows changes in sensory processing with pregnancy. In the main olfactory bulbs, as well as the anterior and posterior piriform cortex, buttons activate cFos expression in virgins more than in pregnant females. By contrast, in the anterior and especially posterior piriform cortex, pregnant females show more activation by pups than buttons. Correlation between IEGs expression and behavior suggests the existence of two vomeronasal subsystems: one associated to pup care (with PMCo as its main center) and another related to pup-directed aggression observed in some pregnant females (with the BSTMPM as the main nucleus). Our data also suggest a coactivation of the olfactory and vomeronasal systems during interaction with pups in pregnant females.

Keywords: pregnancy, pup chemosignals, vomeronasal system, olfactory system, mice, IEGs

INTRODUCTION

Maternal behavior can be defined as any interaction of an adult female with infant conspecifics that helps the latter to survive until their maturity (Numan and Insel, 2003). Maternal behavior has therefore a strong impact on reproductive success, but it is also very beneficial for infant neurodevelopment (Curley and Champagne, 2016). Indeed, well-adapted mammalian dams are frequently engaged in devoted maternal care (pup-directed behaviors) consisting of retrieving the pups to the nest, crouching over the pups to keep them warm and nurturing them by means of lactation while frequently licking-grooming their bodies. In addition, dams also show an intense activity not directed to pups, such as building and maintaining the nest already before parturition and defending it against adult conspecific intruders that might constitute a threat for their pups (maternal aggression) (Numan and Insel, 2003).

The enormous investment of time and energy that these behaviors require may explain why females only exhibit fully motivated maternal behavior during peripartum (for a review see Kohl et al., 2017; Salais-López et al., 2020). Although maternal behaviors are normally expressed after delivery, when pups are present, they are already facilitated during pregnancy. Thus, pregnant females already show nest building (Lisk, 1971) and maternal aggression (prepartum aggression, Mann et al., 1984). In addition, it was shown that primigravid female rats that were hysterectomized before parturition, also displayed facilitated pup-directed behaviors (Rosenblatt and Siegel, 1975; Bridges et al., 1978). By contrast, it has been reported that pregnancy also facilitates pup attacks in both rats (Peters and Kristal, 1983; Mayer and Rosenblatt, 1984) and mice (McCarthy and Vom Saal, 1985). Although this may seem a contradiction in terms, infanticide may constitute an adaptive behavior during motherhood in some circumstances (Blaffer Hrdy, 1979; Latham and Mason, 2004; Kuroda and Tsuneoka, 2013) and this may include late pregnancy.

The most likely mechanism underlying this timely, temporary enhancement of maternal responses to pups is their facilitation by hormones associated to pregnancy, as indeed it has been demonstrated for several mammalian species (Bridges, 2020). For instance, sexual steroids together with prolactin and/or placental lactogens (Bridges and Ronsheim, 1990; Bridges and Freemark, 1995), acting onto centers of the sociosexual brain network (singularly the medial preoptic area; Brown et al., 2017), accelerate the onset of maternal behaviors in virgin rats.

Therefore, the current view of the neurobiology of motherhood assumes that hormonal events of late pregnancy prime specific brain circuits mediating maternal behaviors (the socio-sexual brain network), so that parturient females react properly to infant-derived stimuli, but once maternal behavior is initiated, it continues without the need of further hormonal regulation (Numan and Insel, 2003).

In this context, it is important to understand what sensory channels are involved in the detection of the relevant pup stimuli. Although the identity of specific pup chemosignals has not been elucidated yet, since rodents are macrosmatic animals it is likely that pup-derived chemosignals have a critical role in eliciting maternal behavior. In fact, altered chemosensing has dramatic consequences on maternal responses in rodents. Thus, bulbectomy (Gandelman et al., 1971; Vandenbergh, 1973) and nasal epithelium lesions (Seegal and Denenberg, 1974), result in nearly systematic pup-killing by lactating females. Moreover, null mutations of genes encoding critical molecules for olfactory transduction not only result in anosmia, but also lead to maternal neglect of pups and deficient nest maintenance (Belluscio et al., 1998; Wang and Storm, 2011). By contrast, null-trpc2 mice, whose vomeronasal organ (VNO) is not functional (Leypold et al., 2002; Stowers et al., 2002), show just reduced maternal care (Kimchi et al., 2007), as well as deficient nest maintenance but complete lack of maternal aggression (Leypold et al., 2002; Hasen and Gammie, 2011). In addition, Lepri et al. (1985) reported reduced pup retrieval after VNO ablation. Together, these findings suggest a key role of chemosensory olfactory stimuli in maternal care. By contrast, vomeronasal stimuli seem to play a clear role in aggression, including maternal nest defense, but there is conflicting evidence on its function in pup-directed maternal behaviors.

Conversely, the VNO is critical for the response of males to pups. First, VNO ablation reduces infanticide in sexually naïve males (Tachikawa et al., 2013). Also, targeted mutations abolishing VNO function (trpc2 knockout, Nakahara et al., 2016) provoke paternal behavior, inducing pup care similar to that of lactating dams. Surprisingly, the VNO of mice possess a population of cells that express non-canonically a receptor of the olfactory family (olf692) that has been related to pup-derived odor detection. In sex-naïve males, which are infanticidal, a high

Abbreviations: 3V, 3rd ventricle; ac, anterior commissure; ADP, anterodorsal preoptic nucleus; AHiPM, amygdalohippocampal area, posteromedial part; AI, agranular insular cortex; AOB, anterior olfactory bulb; AON, anterior olfactory nucleus; APir, anterior lobe of pituitary; Astr, amygdalostriatal transition area; BLA, basolateral amygdaloid nucleus, anterior part; BLP, basolateral amygdaloid nucleus, posterior part; BM, basomedial amygdaloid nucleus; BMA, basomedial amygdaloid nucleus, anterior part; bl, basal layer; BSTIA, bed nucleus of the stria terminalis, intraamygdaloid division; BSTMPI, bed nucleus of the stria terminalis, posterointermediate part; BSTMPL, bed nucleus of the stria terminalis, posterolateral part; BSTMPM, bed nucleus of the stria terminalis, posteromedial part; CA3, field CA3 of the hippocampus; CeC, central amygdaloid nucleus, capsular part; CeL, central amygdaloid nucleus, lateral division; Cl, caudal interstitial nucleus of the medial longitudinal fasciculus; CPu, caudate putamen (striatum); DAB, diaminobenzidine tetrahydrochloride; DEn, dorsal endopiriform nucleus; *dlo*, dorsal lateral olfactory tract; D3V, dorsal 3rd ventricle; EPI, external plexiform layer of the olfactory bulb; *ec*, external capsule; *f*, fornix; gl, glomerular layer of the olfactory bulb; Gr, granular layer of the olfactory bulbs; Gl, glomerular layer of the olfactory bulb; *ic*, internal capsule; IEGs, immediate early genes; IPl, inner plexiform layer of the olfactory bulbs; ir, immunoreactive; *lo*, lateral olfactory tract; LP, late-pregnant; LSS, lateral stripe of the striatum; MB, mushroom body of the VNO; mcl, mitral cell layer of the accessory olfactory bulb; mdl, midline; MePD, posterodorsal medial amygdala; MePV, medial amygdaloid nucleus, posteroventral part; Mi, mitral cell layer of the main olfactory bulb; MOB, main olfactory bulb; mv, microvillar layer; NSE, non-sensory epithelium of the VNO; OB, olfactory bulb; OE, olfactory epithelium; *opt*, optic tract; PB, phosphate buffer; PBS, phosphate saline buffer; pe, external plexiform layer of the accessory olfactory bulb; PFA, paraformaldehyde; PirAnt, anterior piriform cortex; PirPost, posterior piriform cortex; PLCo, posterolateral cortical amygdaloid nucleus; PMCo, posteromedial cortical amygdaloid nucleus; PRh, perirhinal cortex; SE, sensory epithelium of the VNO; *sm*, stria medullaris of the thalamus; *st*, stria terminalis; TB, tris buffer; TBS, tris saline buffer; Vd, vomeronasal duct; VEn, ventral endopiriform nucleus; Vn, vomeronasal nerve; VNO, vomeronasal organ; Vv, vomeronasal vein.

proportion of olf692-expressing VNO cells are activated by pup odors. In contrast, in paternal males and in females (irrespective of their status, virgins or dams) a much smaller proportion of these cells are activated following pup exposure (Nakahara et al., 2016).

All these data indicate that pup chemosignals are important in the response of adult rodents to infants, and in females this is especially critical during motherhood, when altered chemosensing has a strong impact on maternal behaviors. However, the specific role of each sensory channel, e.g., olfactory and vomeronasal, in this communication is still unclear. In addition, there is a surprising lack of information on possible functional changes in these systems induced by pregnancy hormones, which might explain, at least in part, the enhanced reinforcing properties of pups for females during motherhood (Hauser and Gandelman, 1985; Salais-López et al., 2017, 2020).

Thus, to study the possible changes in both main and accessory olfactory systems during pregnancy, we recorded and scored the behavior of late-pregnant (LP) (E18) and virgin female mice in response to pups' exposure. Afterwards, in these females, we assessed activation of the VNO by means of immunohistochemical detection of Egr1 expression, and the primary and secondary olfactory and vomeronasal brain centers by means of cFos detection. As a control stimulus, we used a non-social object (buttons) of approximately the same size as pups. Since both variables (behavior and brain activation) were measured in the same animals, we were able to analyse possible correlations between brain activity and specific aspects of maternal behavior. The results confirm the presence of pup-derived chemosignals activating the VNO of females and suggest changes in stimulus processing in both chemosensory systems during late pregnancy. In addition, these findings suggest the existence of two distinct pathways in the vomeronasal system of females related to pup care and pup-directed attacks, respectively.

MATERIALS AND METHODS

Animals

For the present study, we used 10-weeks-old virgin female mice ($n = 16$) and late-pregnant female mice ($n = 14$) of the CD1 strain. Late-pregnant mice (LP) were bred in the animal facility and parturition (usually occurring at gestational day 19) was expected 1–2 days after behavioral testing. Females were housed in homologous pairs, in order to avoid isolation stress. Pairs of same condition females were housed together at least 20 days before the experiment (pairs of LP females were mated by the same male) in polypropylene cages with a controlled temperature of ∼24°C and a 12-hr light/dark cycle (lights on at 08:00 h) with *ad libitum* water and food supply. The pregnant day was considered as the one in which a pair of LP females were mated with a male (housed together overnight). Experimental procedures were approved by the Committee of Ethics and Animal Experimentation of the Universitat Jaume I and treated throughout according to the European Union Council Directive of June 3rd, 2010 (6106/1/10 REV1).

Experimental Design and Behavior Analysis

Experimental females were exposed to pups or buttons, plastic and round objects from similar size than pups, which constitute socially neutral stimuli. Pups in postnatal day 4 were obtained from different female donors. Thus, we used four female groups: (1) LP exposed to pups, (2) virgins exposed to pups, (3) LP exposed to buttons, and (4) virgins exposed to buttons.

Two days prior the behavioral testing, females underwent a habituation phase. Eight glass marbles were deposited in the females' home cage once per day for 2 days at the time in which experiments were scheduled to be performed, in order to habituate the animals to the procedure. In the test day, pairs of virgins and of pregnant female mice were exposed to eight buttons or eight pups, placed in distal areas of the home cage relative to the nest (consisting on pieces of shredded paper). Buttons (**Figure 2A**) were round, white, with four holes and made of plastic. Two different sizes (13 and 20 mm in diameter) but similar weight (0.69 and 0.63 g, respectively) were used. Four buttons of each class were introduced in each cage. The behavior of the females exposed to pups was video recorded for 90 min, although observation of maternal behavior was restricted to the first 8 min since it is mainly expressed immediately following pup introduction (Martín-Sánchez et al., 2015) and may better reflect the expression of IEGs observed, which reaches its maximum 60–90 min after stimulation occurred (Hoffman et al., 1993). Within these 8 min, 32 5-s periods were analyzed (four 5-s periods per min, separated by 10-s intervals). For each 5-s period, we registered the most maternal behavior exhibited by the female, according to the following hierarchy: *pup retrieval*, females carried the pups to the nest; *in nest*, females stayed inside the nest in close contact with pups; *nest building*, females gathered pieces of nest material; *on nest*, females were located on the nest, near the pups but not in contact with them; *approach to pups*, olfactory exploration of pups out of the nest, not followed by retrieval; and *off nest*, females were out of the nest and show no interaction with pups. Then, 32 behavioral events were registered in each animal, distributed among the items described above. Nests were big and well-organized so that during in-nest periods the female and the pups could not be observed. Therefore, specific pup-care items occurring within the nest (licking grooming, arch-back posture of the female) were not assessed.

Moreover, those behavioral items were used to calculate maternal and chemosensory scores for each animal. The maternal score is a weighted sum of those episodes in which female's behavior reflects a maternal state (pup retrieval, nest building, in nest, and on nest):

$$\begin{aligned} \textit{Maternal Score} = {} & 5\ x\ \textit{Retrieval} + 5\ x\ \textit{In Nest} \\ & + 4\ x\ \textit{Nest Building} + 2\ x\ \textit{On Nest} \end{aligned}$$

In the same way, the chemosensory score is composed of a weighted sum of episodes in which the females are likely interacting and sniffing at pups:

$$\begin{aligned} \textit{Chemosensory Score} = {} & 5\ x\ \textit{In Nest} + 3\ x\ \textit{Retrieval} \\ & + 3\ x\ \textit{Approach To Pups} + 1\ x\ \textit{On Nest} \end{aligned}$$

At the end of experiment, we observed 1–3 pups killed, sometimes partially mutilated, in the cages of LP females. Then, we revised the video/audio-recordings and identified those moments in which pup-directed attacks occurred, which were easy to recognize as they always occurred while the female was out of the nest, licking-grooming a pup, which suddenly started emitting strong distress vocalizations which stopped after a few seconds. We measured the latency to each attack to a pup and assigned it to the female that displayed pup-directed aggression. For each female we calculated a pup aggression score:

$$Pup\ Aggression\ Score = \sum_{i=1}^{i=8} (25 - latency\ to\ attack\ pup\ i)$$

A latency of 25 min was assigned for those females not attacking pups (all pup attacks occurred during the first 24 min). This way, pup aggression score was zero for the females not expressing any pup-directed aggression, and it was higher for those females attacking more pups and/or attacking pups with a lower latency.

Finally, the interaction between females in the same cage was also measured for each of these 32 5-s periods as present (1) or not present (0), considering an interaction when a female sniffed the other.

Since we were initially interested only in pup-directed behaviors, we did not record behavioral responses of the females exposed to buttons.

Tissue Processing and Immunohistochemistry

Following 90 min of stimulus introduction, females were overdosed with an intraperitoneal injection of sodium pentobarbital (Vetoquinol, Madrid, Spain; 0.02 mg/g of body weight, Shipley and Adamek, 1984) and transcardially perfused with 4% paraformaldehyde (PFA) in 0.1 M phosphate buffer (PB), pH 7.4. Brains were dissected from the skull, snouts were separated from the skull and muscles removed in order to obtain a block with the VNO. Both, brains and snouts were post-fixed overnight in 4% PFA at 4°C. After fixation, snouts were washed 3 × 10′ in 0.01 M phosphate buffer (PB) with 0.9% NaCl (PBS), decalcified using 250 mM EDTA in 0.1 M PB during 5 days at 4°C and washed 3 × 10′ in 0.05 M Tris Buffer (TB) with 0.9% NaCl (TBS), pH 7.6. Then they were placed into a cast of warm 15% gelatine in 0.05 M TB, kept at 4°C overnight, trimmed and placed in 4% formaldehyde in 0.1 M PB for 2 h at 4°C.

Brains and snout blocks were cryoprotected in 30% sucrose in 0.01 M PB at 4°C until they sank, and then coronal sections (snouts 30 μm-thick; brains 40 μm-thick) were obtained using a freezing microtome (Microm HM-450, Walldorf, Germany), collected in five parallel series in 30% sucrose in PB and stored at −20°C.

One series of snout sections of each animal was processed for free-floating immunohistochemistry of Egr-1 protein, in order to assess the activity of VNO sensory neurons (Isogai et al., 2011). To do so, sections were (a) rinsed 4 × 5 min in TBS; (b) immersed in 1% H_2O_2 and 0,3% Triton X-100 in TBS solution for 30 min for endogenous peroxidase inhibition; (c) rinsed 3 × 5 min in TBS; (d) immersed for an hour in a blocking solution containing 4% normal goat serum and 0.3% Triton X-100 in TBS 0.01 M, pH 8; (e) incubated overnight at room temperature with the primary antibody (rabbit anti-Egr1, no. 4153S; Cell Signaling Technology) diluted 1:500 in the blocking solution; (f) rinsed 5 × 5 min in TBS; (g) incubated in 1:400 dilution of biotinylated goat anti-rabbit secondary antibody (Vector BA1000) in the blocking solution for 2 h; (h) rinsed 5 × 5 min in TBS; (i) transferred to 1:50 avidin-biotin-peroxidase complex (Vectastain-Elite, Vector Laboratories) in TBS for 90 min; (j) rinsed 3 × 5 min in TBS and 3 × 5 min in 0.05 M TB, pH 7.6; and finally, (k) the peroxidase activity was revealed with diaminobenzidine tetrahydrochloride (DAB) reaction (0.025% DAB and 0.01% H_2O_2 in TB). The reaction was stopped by successive rinsing of sections in TB. Sections were mounted on slides and coverslipped in DPX (Scharlau Laboratory).

In parallel, a series of brain free-floating sections were processed for cFos immunohistochemistry. Sections were (a) rinsed 3 × 10 min in TBS; (b) immersed in 1% H_2O_2 in TBS solution for 30 min for endogenous peroxidase inhibition; (c) rinsed 3 × 10 min in TBS; (d) immersed for an hour in a blocking solution containing 3% normal goat serum, 3% bovine serum and 0.3% Triton X-100 in 0.01 M TBS, pH 8; (e) incubated overnight at room temperature with the primary antibody (rabbit anti-cFos n°. 226003; Synaptic Systems) diluted 1:5,000 in the blocking solution; (f) rinsed 3 × 10 min in TBS; (g) incubated in 1:200 dilution of biotinylated goat anti-rabbit secondary antibody (Vector BA1000) in the blocking solution for 2 h; (h) rinsed 3 × 10 min in TBS; (i) transferred to 1:50 avidin-biotin-peroxidase complex (Vectastain-Elite, Vector Laboratories) in TBS for 90 min; (j) rinsed 2 × 10 min in TBS and 2 × 10 min in TB (Tris Buffer 0.05 M pH 7.6); and finally, (k) the peroxidase activity was revealed with diaminobenzidine tetrahydrochloride (DAB) reaction (0.025% DAB and 0.01% H_2O_2 in TB). The reaction was stopped by successive rinsing of sections in TB. Sections were mounted on slides and coverslipped in DPX (Scharlau Laboratory).

For each immunohistochemistry (Egr1 and cFos), sections of animals of the different groups (LP and virgin females exposed to buttons and pups) were processed simultaneously using the same batches of reagents and antibodies, in order to minimize inter-individual variability and to avoid inter-group bias.

Image Analysis

For the assessment of Egr1 expression, images of all VNO sections of a series (1 in 5) were acquired at 10× using a digital camera (DFC495) attached to a microscope Leitz DMRG (Leica, AG, Germany) and evaluated with ImageJ (NIH). Acquisition conditions included gamma = 1 and a level of exposure just high enough as to avoid white saturation in void areas of the image. For each picture VNO Egr1 immunoreactive cells (Egr1-ir cells) were manually counted (cell counter tool, ImageJ) by a person who was blind to the experimental conditions of the samples. VNO area was calculated on Image J software (NIH). Then, for each animal, Egr1 density (Egr1-ir cells/mm^2) was calculated by dividing the total number of Egr1-ir cells counted in all the VNO sections by the total area of these sections.

Expression of cFos was assessed in a selection of brain nuclei involved in chemosensory processing, including nuclei from both vomeronasal and olfactory systems. For the vomeronasal system we sampled the accessory olfactory bulb (AOB, mitral cell layer) and its main synaptic targets, the posteromedial cortical amygdaloid nucleus (PMCo), the medial amygdala (posterodorsal division, MePD) and the medial part of the posteromedial division of the bed nucleus of the stria terminalis (BSTMPM). Concerning the olfactory system, we analyzed the main olfactory bulb (MOB, granular cell layer) and the anterior and posterior divisions of the piriform cortex (PirAnt and PirPost, respectively). The expression of IEGs in the granular layer of the MOB is a good estimator of the activity of the center and reflects the activity of the projection neurons (mitral cells; see Bepari et al., 2012).

For each nucleus, we sampled specific frames at particular anteroposterior levels, as indicated in **Figures 2**, **3** (Paxinos and Franklin, 2004). We acquired images of both hemispheres as described above and, in the case of the MePD, selected a triangle-shaped region of interest to exclude the optic tract (**Figure 2C**). Image processing and analysis were conducted on ImageJ software (NIH). Briefly, the RGB color image was converted to grayscale by selecting the green channel. Images were then binarized setting the threshold at 75% of the mode of the gray histogram, so that every pixel below this threshold was considered labeled. The resulting binary images were further filtered using commands "fill holes," "open" (3 iterations), and "watershed." Then, particles were automatically counted, discarding those smaller than half the average size of the cells from that specific nucleus (calculated in turn by measuring the average area of six randomly selected intensely labeled cells in the nucleus).

For most nuclei the density of cFos-ir cells (cells/mm^2) was calculated by dividing the total number of particles in both hemispheres, by the sum of the areas of the regions of interest. In the AOB and the MOB the high density of cells and intensity of immunostaining made it difficult to separate single cells using the image analysis procedure described above. Therefore, we simply measured the area fraction occupied by labeling after thresholding (immunoreactive area/total area).

Statistical Analysis

We first compared the behavior of the females (virgins and LP females) exposed to pups. To do so, after testing for normality with the Kolmogorov-Smirnov test, data derived from most of the behavioral events did not follow a normal distribution or showed normality but not homogeneous variance. Then, behavioral differences (behavioral events or scores) between virgin and LP females exposed to pups were evaluated using a two-sample *t*-test for non-homogenous variances (for samples showing normality) or a Wilcoxon test for those displaying no normal distribution.

Regarding the analysis of Egr-1 and c-Fos expression, when data accomplished normality (Kolmogorov-Smirnov test) and homoscedasticity (Levene test), a two-way ANOVA was performed, with "FEMALE" (virgin or LP) and "STIMULUS" (buttons or pups) as factors. Significant FEMALE × STIMULUS interactions were explored by *post-hoc* pairwise comparison with Bonferroni corrections. If data did not fulfill normality and homoscedasticity, we applied the two-way ANOVA after logarithmic transformation (Log10 [n + 1]). If the transformation failed to render normality and/or homoscedasticity, a two-sample *t*-test for non-homogenous variances (for samples showing normality) or a Wilcoxon test for those displaying no normal distribution, was performed with non-transformed data to assess the differences between FEMALE (virgin vs. LP) and between STIMULUS (buttons vs. pups).

When inspecting the VNO sections, we realized that cross-sections through the center of the VNO showed few Egr-1 positive cells whereas, very often, small sections through the tips of the VNO were rich in labeled cells (see **Figures 2B–D**). Therefore, we tested if specific populations located at the ends of the VNO were sensitive to pup-derived stimuli (see **Supplementary Figure 1**).

After that, we explored Spearman correlations between behavioral data and immediate early gene expression levels (IEGs) (Egr1-ir for the VNO; cFos-ir for the brain) separately in LP and virgin females exposed to pups. This allows investigating the relationship between activity in specific olfactory and vomeronasal nuclei with the expression of specific maternal behaviors and exploring this relationship during pregnancy.

In addition, we also performed Spearman correlation analysis between IEGs expression in the VNO and the different chemosensory brain centers in both groups of pup-exposed females. This allows investigating patterns of neural activity in the centers of the olfactory and vomeronasal systems during interaction with pups and exploring whether hormones acting during late pregnancy may change these patterns of brain activity.

Statistical analysis was performed using SPSS software package (IBM). The significance level was set at $p < 0.05$.

RESULTS

Behavior of Late-Pregnant and Virgin Female Mice Following Exposure to Pups

During exposure to pups, we scored several of the behavioral events displayed by females: pup retrieval, in nest, nest building, on nest, approach to pups, off nest and pup-directed aggression and interfemale interaction. Statistical analysis revealed non-significant differences for most behaviors between LP and virgin females (pup retrieval, $Z = -1.289$, $p = 0.197$; in nest, $t = -0.760$, $p = 0.461$; nest building, $Z = -0.368$, $p = 0.713$; on nest, $t = 1.722$, $p = 0.109$; approach to pups, $Z = -0.544$, $p = 0.587$; off nest, $t = 1.105$, $p = 0.289$) (**Figure 1**). In a similar way, there were no differences between females concerning the maternal score ($t = -1.141$, $p = 0.274$) and the chemosensory score ($t = -1.252$, $p = 0.233$). Four out of 7 LP females displayed pup aggression: one attacked three pups, one attacked two pups, and two attacked one pup each. By contrast, virgin

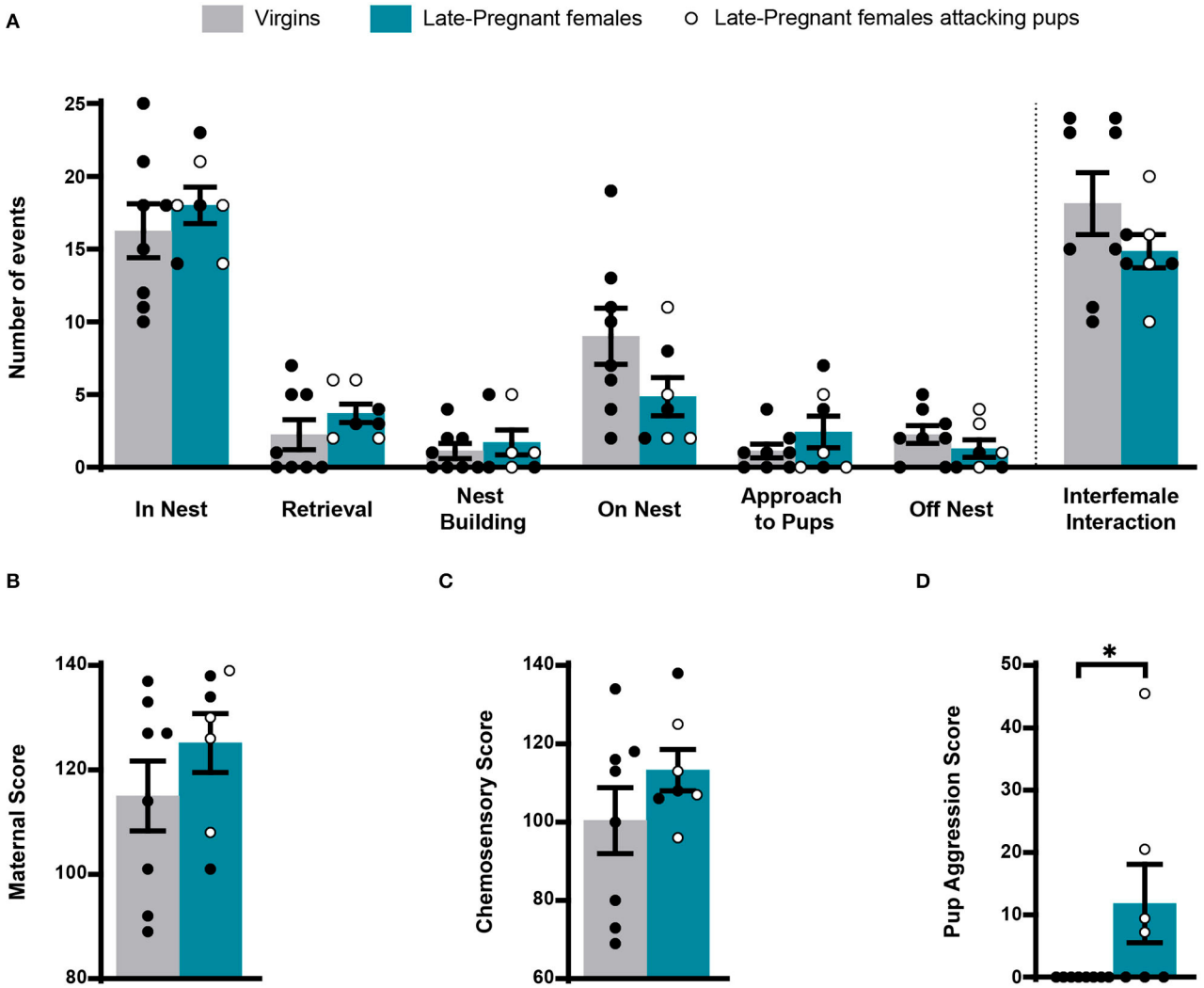

FIGURE 1 | Behavior of virgin and late pregnant (LP) female mice following exposure to pups. Histogram showing the occurrence of maternal behaviors and interfemale interactions (mean ± SEM), scored as number of events during the first 8 min after pup introduction (in nest, retrieval, nest building, on nest, approach to pup and off nest; see text), did not show significant differences between female groups **(A)**. Similarly, the maternal score **(B)** and chemosensory score **(C)** were similar in virgins and late-pregnant females. Finally, the pup aggression score **(D)** was significantly different between female groups, since only some of the LP females performed pup-directed aggression (*$p < 0.05$). Individual data are also show, with empty circles corresponding to the LP females displaying pup-directed aggression, and black filled ones corresponding to those females not displaying aggression.

females did not attack pups. Accordingly, comparison of pup aggression score rendered significant differences between females ($Z = -2.376$, $p = 0.017$). Finally, interfemale contact did not differ between the LP and virgin females ($Z = -1.108$, $p = 0.268$) (**Figure 1**).

Overall, these results show that maternal behavior does not differ substantially between LP and virgin females. Also, possible differences in the activity of chemosensory brain centers between females (or the VNO) cannot be attributed to differences in interaction with pups, since with exception of pup-directed aggression, LP and virgin females displayed similar behavior. Moreover, differences in IEGs-ir between females cannot be attributed to interfemale interactions.

Response of the Vomeronasal System to Pup-Derived Stimuli

One of the aims of this work is to explore the response of the vomeronasal system to possible pup-derived chemosignals detected by the VNO, and the possibility that adult females change their sensitivity to these stimuli and/or their sensory processing mechanisms during late pregnancy. To do so, we analyzed the neuronal response of the VNO and the primary and secondary vomeronasal brain centers by using quantification of IEGs expression in LP and virgin female mice.

First, we analyzed the response of the VNO to pups or buttons exposure in LP and virgin females. A two-way ANOVA of log-transformed Egr1-ir cell density detected a significant main effect

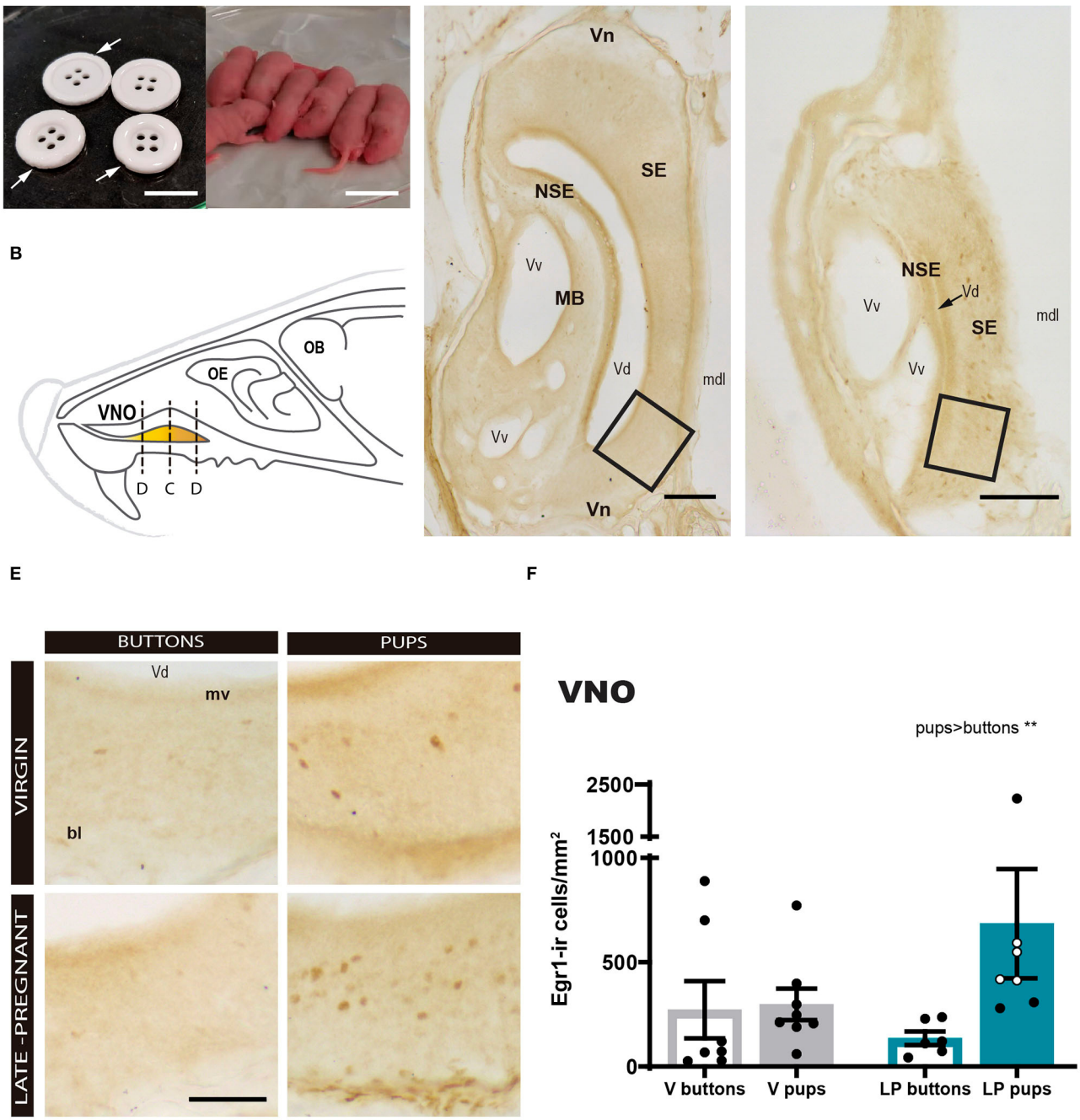

FIGURE 2 | Expression of Egr1 in the vomeronasal organ (VNO) of females (virgin or late-pregnant) exposed to pups or buttons. Buttons are of a size comparable to pups **(A)** and are not avoided but actually gnawed (arrowheads point to notches). Diagram of the VNO **(B)** illustrating the levels of the sections shown in **(C,D)**, which are two low-power photographs of the VNO showing the main anatomical landmarks at two different antero-posterior levels (C, center of the VNO; D, tip of the VNO). Examples similar to the framed areas in **(C,D)** are shown at higher magnification in **(E)** for each experimental group. A bar histogram of raw data (mean ± SEM) of Egr1-positive cells in the VNO of the different groups is shown in **(F)**, where individual data are also plotted. The empty circles correspond to those females displaying pup-directed aggression. Statistical analysis of the density was performed on the log transformed values to achieved normality and homocedasticity (see text). Egr1 expression is increased in response to pups (**$p < 0.01$) as compared to a socially neutral stimulus (buttons), but there is no difference between virgin and late-pregnant females. Scale bars: **(A)** 2 cm; **(C,D)** 100 μm; **(E)** 50 μm.

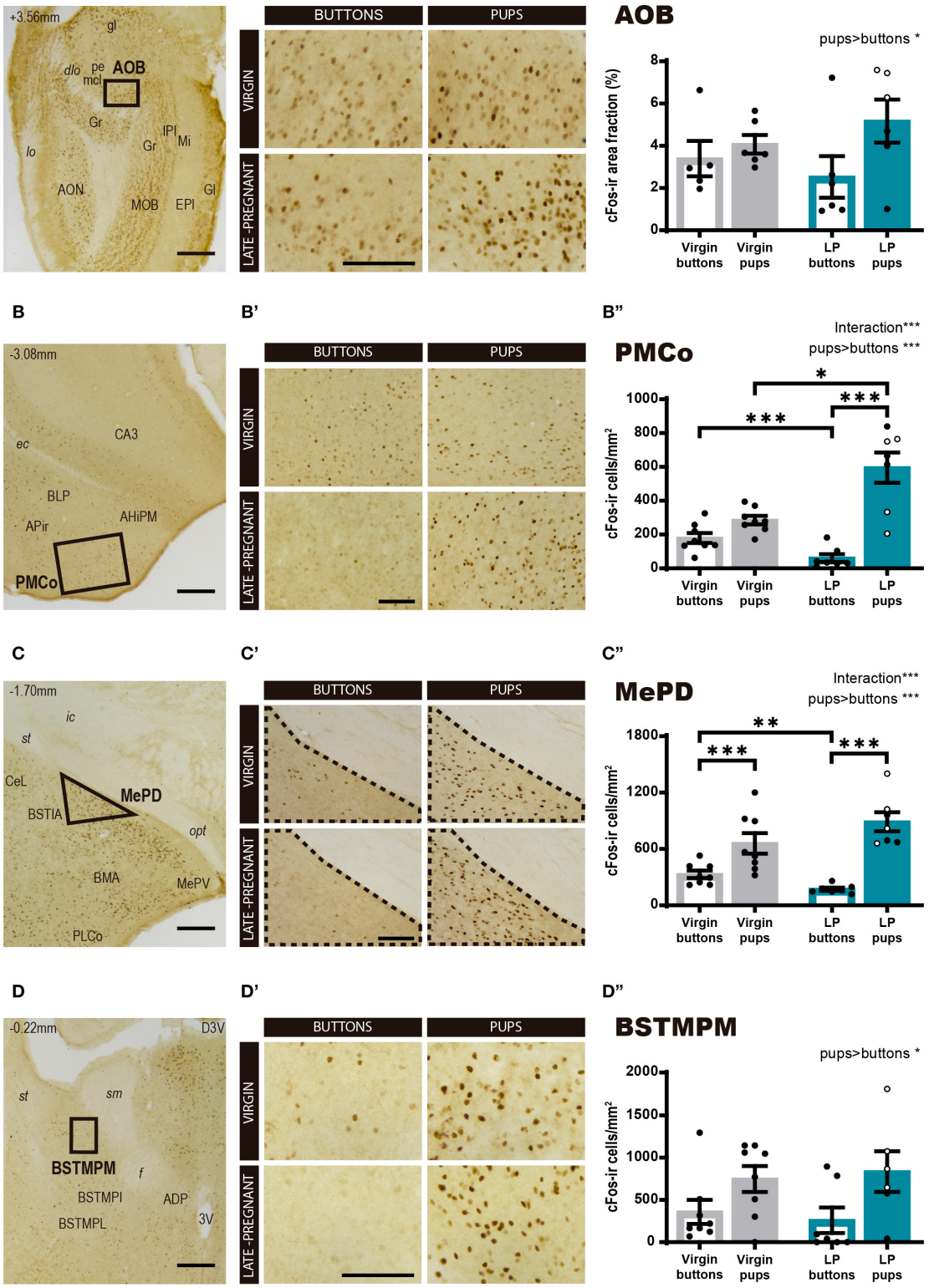

FIGURE 3 | Expression of cFos in brain areas of the vomeronasal system following exposure to pups or non-social control stimulus. **(A–D)** Low power photomicrographs showing cFos expression in the AOB **(A)**, the PMCo **(B)**, the MePD **(C)**, and the BSTMPM **(D)**. The numbers in the left upper part of the images

(Continued)

FIGURE 3 | indicate the approximate anteroposterior coordinate of the sections relative to bregma (Paxinos and Franklin, 2004). The framed areas, shown at higher magnification in **(A′-D′)**, indicate the regions where cFos expression was analyzed. **(A′-D′)** Example of photomicrographs of the brain regions analyzed for each experimental group: virgin/buttons, virgin/pups, late-pregnant/buttons, and late-pregnant/pups. Images correspond to the AOB **(A′)**, the PMCo **(B′)**, the MePD **(C′)**, and the BSTMPM **(D′)**. Scale bars, 250 μm **(A–D)** and 100 μm **(A′-D′)**. **(A″-D″)** Bar histogram showing the cFos positive cell density (mean ± SEM) in the vomeronasal system. Individual data are also indicated, with empty circles corresponding to the females displaying pup-directed aggression. Raw data are represented although they were log transformed for statistical analysis when necessary (AOB, PMCo, MePD, see text). Significant main effects revealed by the statistical analysis are indicated for each histogram. When FEMALE × STIMULUS interaction is observed, the results of *post-hoc* pairwise comparisons are indicated using asterisks: ***$p < 0.001$, **$p < 0.01$, and *$p < 0.05$.

for STIMULUS ($F_{1, 24} = 10.259$, $p = 0.004$), but no significant differences for FEMALE ($F_{1, 24} = 1.249$, $p = 0.275$) and no FEMALE × STIMULUS interaction ($F_{1, 24} = 1.223$, $p = 0.280$). As expected, pups induced a higher Egr1-ir cell density in the VNO compared to buttons in both LP and virgin females (**Figure 2**). This suggests that pups secrete chemosignals that are detected by the VNO of adult females.

We realized that small cross sections, e.g., sections though the tip of the VNO, apparently displayed more Egr1-ir cells than large cross sections, e.g., sections through the center of the organ (compare **Figures 2C** and **D**). Therefore, we explored a possible non-homogenous expression of Egr1 in the VNO by performing a correlation analysis between Egr1-ir cell density and section area. The results confirmed that the larger sections display the lower the Egr1-ir cell density (see **Supplementary Figure 1**). Next, we tested whether this might be due to heterogeneous distribution of specific cell population responding to pups. To do so, we selected the two largest (central) and the two smallest sections (tip) of each animal and analyzed whether they showed different density of Egr1-ir cells in Virgin and LP females exposed to pups and buttons, using a three-way ANOVA (see **Figure 1**). The results confirmed a strong effect of the stimulus (pups rendered higher density of Egr1-ir cells than buttons; $p = 0.013$) and the level (tip sections having significantly higher density of Egr1-ir cells than central sections; $p < 0.001$). Interactions between factors, LEVEL × FEMALE, LEVEL × STIMULUS, STIMULUS × FEMALE, or LEVEL × STIMULUS × FEMALE were not significant ($p > 0.6$ in all cases). Therefore, although expression of Egr1 was dependent on the stimulus and the level or the VNO (heterogeneous distribution), this was not dependent on the female (does not change with pregnancy) or stimulus.

Then, we explored cFos expression in primary and secondary vomeronasal brain centers. For the AOB (**Figure 3A**), a two-way ANOVA of Log cFos-ir area fraction revealed a significant main effect for STIMULUS ($F_{1, 19} = 4.527$, $p = 0.047$), but no significant differences for FEMALE ($F_{1, 19} = 0.272$, $p = 0.608$) neither FEMALE × STIMULUS interaction ($F_{1, 19} = 1.288$, $p = 0.270$). Thus, pups evoked a higher expression of c-Fos in the AOB as compared to buttons in both groups of females (**Figures 3A–A″**).

However, for the secondary vomeronasal brain centers, e.g., the PMCo (vomeronasal cortex), the MePD and the BSTMPM, statistical analysis revealed further significant differences. Thus, the two-way ANOVA of Log cFos-ir cell density in the PMCo (**Figure 3B**) showed a significant main effect for STIMULUS ($F_{1, 26} = 51.313$, $p < 0.001$) and significant FEMALE × STIMULUS interaction ($F_{1, 26} = 21.597$, $p < 0.001$), but no differences were found for FEMALE factor ($F_{1, 26} = 2.346$, $p = 0.138$). *Post-hoc* pairwise comparisons revealed that pups elicited higher response in LP than in virgin females ($p = 0.037$), whereas buttons raised higher response in the virgin group than in the pregnant females ($p < 0.001$). In the LP group, pups elicited higher cFos response than buttons ($p < 0.001$), whereas this difference did not reach significance in virgin females ($p = 0.077$) (**Figures 3B–B″**). Likewise, the two-way ANOVA of Log cFos-ir cell density in the MePD showed a significant main effect of STIMULUS ($F_{1, 26} = 81.312$, $p < 0.001$) and FEMALE × STIMULUS interaction ($F_{1, 2} = 15.27$, $p = 0.001$), but no main effect of FEMALE ($F_{1, 26} = 1.143$, $p = 0.295$). *Post-hoc* analysis of these effects revealed that pups elicited higher cFos response than buttons in both LP ($p < 0.001$) and virgins ($p = 0.001$) (**Figures 3C–C″**). On the other hand, exposure to buttons elicited a higher level of cFos in virgins than LP ($p = 0.002$), but interfemale differences in pup-induced cFos-ir cell density did not reach significance ($p = 0.055$). Overall, our results revealed that pup exposure induced a higher neuronal response in the PMCo (not significant for the MePD) of LP vs. virgin females, whereas buttons, used as neutral vomeronasal stimulus, induced a lower neuronal response in LP than in virgin females in both brain areas.

Concerning the BSTMPM, Wilcoxon test comparing stimuli rendered significant differences ($Z = -2.426$, $p = 0.015$), with pups eliciting higher cFos levels than buttons, whereas comparison of females did not reveal significant differences ($Z = -0.725$, $p = 0.469$) (**Figures 3D–D″**). The pattern of activity in the BSTMPM (cFos expression) in the different females exposed to pups and buttons, was similar to the one observed for VNO and AOB, and different to the one seen in PMCo and MePD.

In sum, the pattern of cFos expression observed in response to pups and buttons differs between LP and virgin females in some secondary vomeronasal centers (PMCo and MePD), whereas both groups of females show similar response in the VNO, AOB, and BSTMPM. In general, pups elicit more activation than buttons, thus suggesting that buttons are a good control stimulus for vomeronasal stimulation.

Response of the Main Olfactory System to Pup-Derived Stimuli

Regarding the main olfactory system, we studied the cFos response in the MOB and the olfactory cortex, PirAnt and PirPost, following pups or neutral stimulus exposure in LP and virgin mice. The statistical analysis for Log cFos-ir area

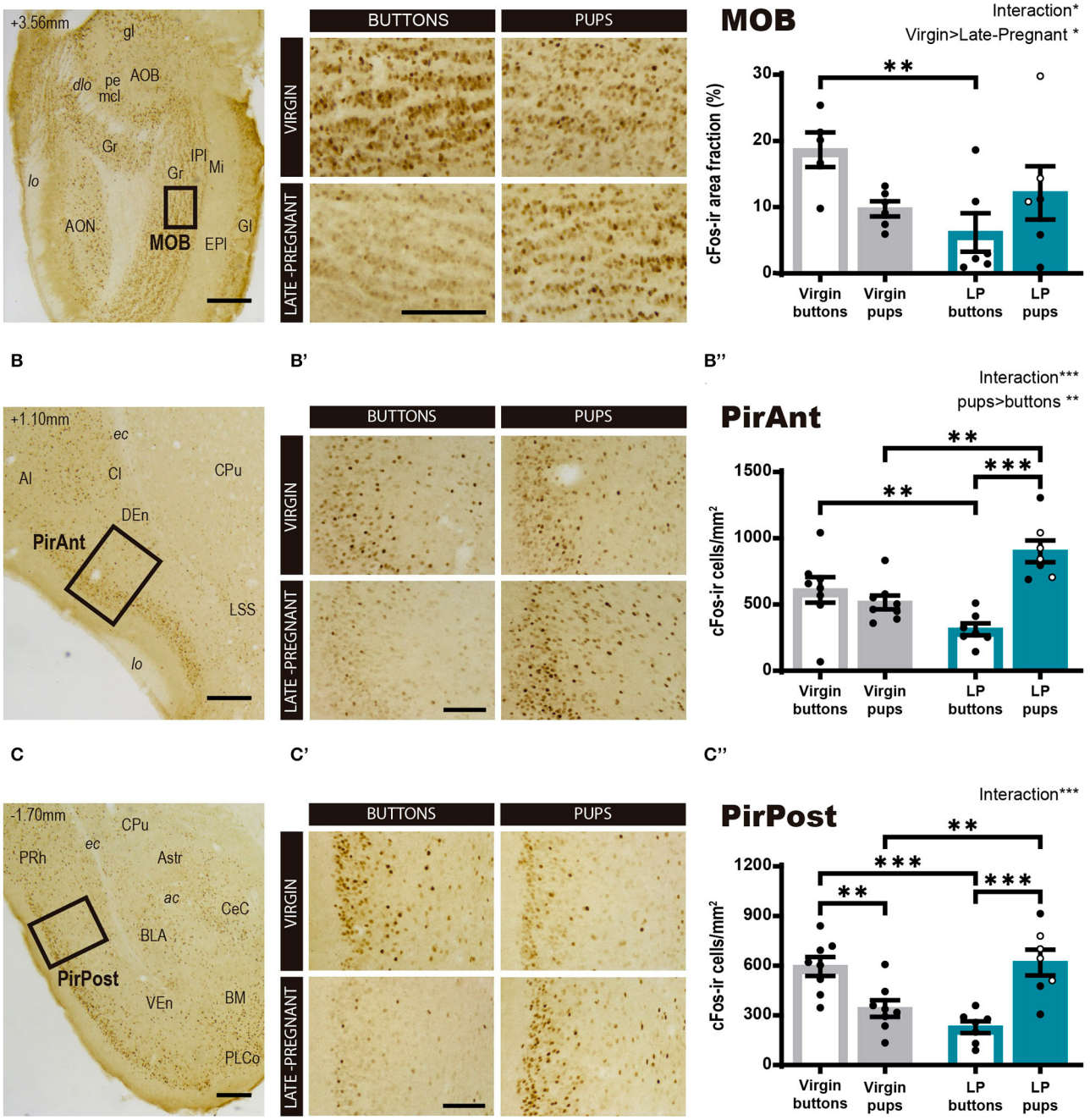

FIGURE 4 | cFos response in brain areas of the main olfactory system following exposure to pups or non-social control stimulus. **(A–D)** Low power photomicrographs showing the cFos immunohistochemistry in the MOB **(A)**, the PirAnt **(B)**, and the PirPost **(C)**. The numbers in the left upper corner of the images indicate anteroposterior levels of the sections relative to bregma (Paxinos and Franklin, 2004). Framed areas, shown at higher magnification in **(A′-C′)**, indicate the specific zones where cFos expression was analyzed. **(A′-C′)** High-power photomicrographs of the brain centers analyzed for each experimental group: virgin/buttons, virgin/pups, late-pregnant/buttons, and late-pregnant/pups. Images correspond to the MOB **(A′)**, the PirAnt **(B′)**, and the PirPost **(C′)**. Scale bars, 250 μm **(A–C)** and 100 μm **(A′-C′)**. **(A″-C″)** Bar histogram showing the density (mean ± SEM) of cFos-expressing cells in the main olfactory system (raw data are displayed although data were log transformed for statistical analysis in the MOB, see text). Individual data are also indicated, with empty circles corresponding to the females displaying pup-directed aggression. Significant main effects revealed by the statistical analysis are indicated for each histogram. When FEMALE × STIMULUS interaction is observed, the results of *post-hoc* pairwise comparisons are indicated using asterisks: ***$p < 0.001$, **$p < 0.01$, and *$p < 0.05$.

fraction in the MOB showed significant differences for FEMALE ($F_{1, 19} = 5.611$, $p = 0.029$) in favor of virgins, and a FEMALE × STIMULUS interaction effect ($F_{1, 19} = 4.678$, $p = 0.044$), whereas no differences were found for STIMULUS condition ($F_{1, 19} = 0.027$, $p = 0.872$). *Post-hoc* analysis of the interaction revealed that interfemale differences are mainly due to a significantly higher response of virgins to buttons as compared to LP females ($p = 0.006$) (**Figures 4A–A″**), as females do not differ in their response to pups. Those results evidence that pups do not evoke a different response between female groups, but buttons raised a MOB response higher in virgins than in LP mice.

On the other hand, the ANOVA for the cFos-ir cell density in the PirAnt showed significant differences for STIMULUS ($F_{1, 26} = 11.425$, $p = 0.002$; pups elicit more cFos-ir than buttons) and a FEMALE × STIMULUS interaction effect ($F_{1, 26} = 21.748$, $p < 0.001$), but no significant main effect of FEMALE factor ($F_{1, 26} = 0.358$, $p = 0.555$). *Post-hoc* comparisons showed that pups elicited higher cFos-ir density than buttons in LP females ($p < 0.001$) but not in virgins (**Figures 4B–B″**). In fact, when comparing animals exposed to pups, LP females displayed significantly higher cFos-ir than virgin animals ($p = 0.001$), and conversely, buttons elicited higher cFos expression in virgin than in LP females ($p = 0.008$).

For the PirPost a two-way ANOVA showed a significant FEMALE × STIMULUS interaction ($F_{1, 26} = 32.209$, $p <$ 001), but no significant main effects for either FEMALE ($F_{1, 26} = 0.620$, $p = 0.438$) or STIMULUS ($F_{1, 26} = 1.436$, $p = 0.242$) (**Figures 4C–C″**). *Post-hoc* analysis showed that pups elicited higher response in LP than in virgin females ($p = 0.002$), while buttons induced higher response in virgins compared to LP females ($p < 0.001$). Moreover, differential effects of the stimuli were found within each female condition. Thus, LP females showed higher response to pups than to buttons ($p < 0.001$), whereas virgin females had a higher response to buttons than to pups ($p = 0.003$). Altogether, our results of neuronal activation in centers of the main olfactory system prompts to a differential stimulus discrimination, with higher activation by buttons in virgin females and by pup-derived stimuli in LP females.

Correlation Analysis of Female Behavior and IEGs Expression

Finally, we performed correlation analysis between behavioral measures and the levels of IEGs expression in the vomeronasal and olfactory systems of virgin and LP female mice exposed to pups. Spearman analysis revealed a different pattern of correlation in LP and virgin females (see **Table 1**, **Supplementary Figure 2**). Thus, LP, but not virgins, displayed a significant positive correlation between "off nest" behavior and the cFos response in the AOB ($p = 0.020$) and the MOB ($p = 0.001$). On the contrary, the behavior "approach to pups," consisting in sniffing a pup far from the nest without retrieving it afterwards, showed a significant positive correlation to cFos response in the AOB ($p = 0.011$) and the MePD ($p = 0.017$) in virgins, but not in LP females. Moreover, "nest building" was significantly and positively correlated with cFos response in the PirAnt ($p = 0.011$) in LP females, but not in virgins.

The behavior "pup retrieval" was the only one displaying a significant positive correlation to neuronal response in the PMCo of both virgin females ($p = 0.036$) and in LP females ($p = 0.012$). In addition, in LP but not virgins, maternal score showed a significant positive correlation with the response in the PMCo ($p = 0.023$) and chemosensory score to the response in the MePD ($p = 0.023$). Finally, pup-directed aggression score correlated to the neural response in the AOB ($p = 0.005$) and in the BSTMPM ($p < 0.05$) only in LP females. The behaviors "on nest," "in nest," and "interfemale interaction" did not correlate with IEGs expression in any vomeronasal/olfactory brain region analyzed. In fact, Egr1 expression in the VNO did not correlate with any behavioral item or score. Overall, those positive correlations showed that in LP females, pup-directed and non-directed behaviors are mainly correlated to signal processing in some of the vomeronasal-related nuclei.

Finally, we also performed a correlation analysis of the levels of IEGs expression between vomeronasal and olfactory structures of females exposed to pups (**Table 2**, **Supplementary Figure 3**). Interestingly, this analysis revealed that VNO activation correlated with cFos expression in the MOB ($p = 0.042$), the PirAnt ($p = 0.023$), and the PirPost ($p = 0.003$) of LP females, while no similar correlations were found in virgins. Moreover, in LP females (but not virgins) AOB response displayed a positive correlation with MOB ($p = 0.042$) and with the BSTMPM ($p < 0.001$), whereas MOB and BSTMPM display no mutual correlation. By contrast, in virgin females, the BSTMPM displayed a significant negative correlation to PMCo ($p = 0.040$) and to MOB ($p = 0.036$), whereas the PirAnt positively correlated to MePD ($p = 0.002$) and the PirPost ($p = 0.047$).

Overall, those results suggest that when exposed to pups LP females display an associated activity of the olfactory and vomeronasal systems. By contrast, in virgins, correlations mirror somehow the connectivity within the vomeronasal and olfactory pathways.

DISCUSSION

In the present study, we explored pregnancy-induced adaptations of the response of the chemosensory systems to pups in female mice. To do so, we analyzed the expression of IEGs in the VNO, as well as in the main centers of the vomeronasal and olfactory systems of virgin and LP female mice, in response to pups or to a non-social stimulus (buttons). This allows assessing changes in sensory processing of pup-derived chemosignals occurring by the end of pregnancy, most likely associated to the action of pregnancy hormones known to be relevant for inducing full maternal behavior. Last, we ascertained possible correlations between patterns of brain activity and behavior. Overall, our results confirm that pup-derived chemosignals activate the VNO and reveal changes in stimulus processing in chemosensory systems by the end of pregnancy. In addition, our data suggest that activation of different vomeronasal pathways are likely underlying pup care or pup attack in LP females.

TABLE 1 | Correlation analysis of IEGs expression in the VNO and centers of the chemosensory systems with behavior in late-pregnant (blue) and virgin females (light gray) exposed to pups.

			NUCLEUS							
Behavior	**Female group**	**Statistics**	**VNO**	**AOB**	**PMCo**	**MePD**	**BSTMPM**	**MOB**	**PirAnt**	**PirPost**
Off nest	Virgin	*rs*	0.454	0.617	0.172	0.061	−0.278	0.370	−0.098	0.049
		p-value	0.258	0.192	0.684	0.885	0.505	0.470	0.817	0.908
		N	8	6	8	8	8	6	8	8
	Late pregnant	*Rs*	0.561	**0.883***	0.112	0.393	0.559	**0.971****	0.449	0.374
		p-value	0.190	**0.020**	0.811	0.383	0.249	**0.001**	0.312	0.408
		N	7	**6**	7	7	6	**6**	7	7
Approach to pups	Virgin	*rs*	−0.350	**0.912***	0.350	**0.801***	0.164	−0.441	0.626	0.175
		p-value	0.395	**0.011**	0.395	**0.017**	0.699	0.381	0.097	0.678
		N	8	**6**	8	**8**	8	6	8	8
	Late pregnant	*rs*	−0.482	−0.116	−0.556	0.148	0.030	−0.290	−0.148	−0.704
		p-value	0.274	0.827	0.195	0.751	0.954	0.577	0.751	0.077
		N	7	6	7	7	6	6	7	7
On nest	Virgin	*rs*	−0.024	−0.657	−0.476	−0.143	0.263	−0.086	−0.143	−0.238
		p-value	0.955	0.156	0.233	0.736	0.528	0.872	0.736	0.570
		N	8	6	8	8	8	6	8	8
	Late pregnant	*rs*	0.000	−0.152	−0.185	−0.630	−0.290	−0.395	0.185	0.037
		p-value	1.000	0.774	0.691	0.129	0.577	0.439	0.691	0.937
		N	7	6	7	7	6	6	7	7
Nest building	Virgin	*rs*	0.447	0.555	−0.243	0.089	0.373	−0.123	0.153	−0.128
		p-value	0.267	0.252	0.563	0.833	0.363	0.816	0.717	0.763
		N	8	6	8	8	8	6	8	8
	Late pregnant	*rs*	0.624	0.525	0.208	−0.567	0.359	0.309	**0.869***	0.624
		p-value	0.135	0.285	0.655	0.184	0.485	0.552	**0.011**	0.135
		N	7	6	7	7	6	6	**7**	7
Pup retrieval	Virgin	*rs*	0.013	0.541	**0.741***	0.294	−0.707	0.439	0.192	0.396
		p-value	0.976	0.268	**0.036**	0.480	0.050	0.383	0.650	0.332
		N	8	6	**8**	8	8	6	8	8
	Late pregnant	*rs*	−0.165	0.088	**0.863***	−0.441	−0.206	0.000	−0.092	−0.165
		p-value	0.723	0.868	**0.012**	0.323	0.695	1.000	0.845	0.723
		N	7	6	**7**	7	6	6	7	7
In nest	Virgin	*rs*	−0.287	0.029	0.108	−0.252	0.108	−0.348	−0.168	−0.120
		p-value	0.490	0.957	0.799	0.548	0.798	0.499	0.691	0.778
		N	8	6	8	8	8	6	8	8
	Late pregnant	*Rs*	−0.056	−0.324	0.150	0.636	0.093	0.000	−0.487	0.150
		p-value	0.905	0.531	0.749	0.125	0.862	1.000	0.268	0.749
		N	7	6	7	7	6	6	7	7
Maternal score	Virgin	*rs*	−0.096	−0.029	0.192	−0.240	−0.145	0.203	−0.144	0.048
		p-value	0.821	0.957	0.649	0.568	0.733	0.700	0.734	0.910
		N	8	6	8	8	8	6	8	8
	Late pregnant	*rs*	0.143	−0.086	**0.821***	0.000	−0.029	0.200	−0.143	0.321
		p-value	0.760	0.872	**0.023**	1.000	0.957	0.704	0.760	0.482
		N	7	6	**7**	7	6	6	7	7
Chemosensory score	Virgin	*rs*	−0.405	0.086	0.238	−0.024	0.012	−0.143	0.000	−0.048
		p-value	0.320	0.872	0.570	0.955	0.978	0.787	1.000	0.911
		N	8	6	8	8	8	6	8	8
	Late pregnant	*rs*	−0.393	−0.371	−0.214	**0.821***	−0.029	−0.086	−0.714	−0.357
		p-value	0.383	0.468	0.645	**0.023**	0.957	0.872	0.071	0.432
		N	7	6	7	**7**	6	6	7	7

(Continued)

TABLE 1 | Continued

Behavior	Female group	Statistics	NUCLEUS							
			VNO	AOB	PMCo	MePD	BSTMPM	MOB	PirAnt	PirPost
Pup aggression score	Virgin	*rs*	–	–	–	–	–	–	–	–
		p-value	–	–	–	–	–	–	–	–
		N	8	6	8	8	8	6	8	8
	Late pregnant	*rs*	0.371	**0.941****	−0.556	0.259	**0.812***	0.698	0.259	0.408
		p-value	0.413	**0.005**	0.195	0.574	**0.050**	0.123	0.574	0.364
		N	7	**6**	7	7	**6**	6	7	7
Interfemale interaction	Virgin	*rs*	−0.291	0.120	0.048	0.436	0.122	0.000	0.509	0.097
		p-value	0.484	0.822	0.909	0.280	0.774	1.000	0.197	0.819
		N	8	6	8	8	8	6	8	8
	Late pregnant	*rs*	−0.374	−0.463	0.019	−0.412	−0.030	−0.772	−0.337	−0.056
		p-value	0.408	0.355	0.968	0.359	0.954	0.072	0.460	0.905
		N	7	6	7	7	6	6	7	7

*$p < 0.05$; **$p < 0.01$. Bold values indicate statistically significant correlation.

Methodological Issues and Behavioral Response to Pups

Our experimental design has several advantages. First, it prevents a differential novelty effect of pups in late-pregnant and virgin females, since both female groups were completely pup-naïve. This is relevant since novelty has a strong impact on exploratory behaviors (Rinaldi et al., 2010). Second, the use of a non-social control stimulus, buttons, is another advantage, since using non-exposed animals as controls does not allow to interpret IEGs expression as due to a specific stimulus (pups). Third, the females were housed in pairs at least 20 days before the experiment, and tested also in pairs, which avoided isolation stress along the procedure. Moreover, in order to avoid possible competition for stimuli between both females, we introduced a large number of pups/buttons into the test cage (eight), so that both females could interact with them simultaneously and independently. Fourth, when designing a IEGs experiment, using LP instead of postpartum females to check the activity induced by pups, has the additional advantage that does not require mother-infant separation. This suppresses another potentially confounding factor for interpreting the expression of IEGs in brain centers, e.g., pup-separation-induced stress (Aguggia et al., 2013).

Moreover, we are aware of some caveats in our procedure. The presence of two females in the same cage during the experiment may have interfered in the procedure, as an adult female is a source of chemosignals. Nonetheless, we minimized this possibility as we paired same-condition females for a long period and objects used as stimuli were introduced in large number to avoid competition, as above described. In any case, there were no significant differences in interfemale interactions between groups exposed to pups, and therefore, differences in IEGs expression are unlikely due to this factor, as supported also by the behavior-IEG expression correlation analysis.

When analyzing the behavior of virgin and LP females during exposure to pups, we observed no differences in any pup-directed or non-pup-directed behavior item, except for pup-directed aggression performed by some LP females (4 females out of 7) (see below). Our results on that issue agree with previous reports showing that virgin female mice having no previous experience with pups do not display pup aversion. Instead, pups constitute a highly attractive stimulus for pup-naïve females (Stolzenberg and Rissman, 2011; Alsina-Llanes et al., 2015; Martín-Sánchez et al., 2015). In those previous reports, authors demonstrated that maternal females (lactating dams or pup-sensitized virgins) display faster pup retrieval compared to pup-naïve virgins; however, in those experiments maternal females had previous pup-experience, while control virgins did not. Therefore, the lack of differences in most of the measured behavioral items between LP and virgin females in our experiment is likely due to pups being an equally novel stimulus for both kinds of females.

Although expression of IEG by neurons in vomeronasal and olfactory centers is mainly driven by detection of chemical stimuli, pups also emit distress vocalizations that are relevant in the context of maternal behaviors (Smotherman et al., 1974), together with olfactory cues with multisensory integration occurring at the level of the primary auditory cortex (Cohen et al., 2011). Whether, and to what extent, these stimuli might contribute to IEG expression in secondary olfactory and vomeronasal centers is not known. However, an analysis of the response of neurons in the primary auditory cortex to pup vocalizations (Marlin et al., 2015) revealed very faint response in pup-naïve virgins, as compared to pup-experienced virgins and dams. Since our females, both LP and virgins, had no previous experience with pups before the trial, we can safely assume that most, if not all the activity (IEG expression) observed in the centers of the vomeronasal and olfactory systems, is due to pup-derived chemosignals.

TABLE 2 | Correlation analysis of the IEGs expression between the different centers of the chemosensory systems (including the VNO) in late-pregnant (blue) and virgin females (light gray) exposed to pups.

		VNO	AOB	PMCo	MePD	BSTMPM	MOB	PirAnt	PirPost
VNO	*rs*		−0.257	−0.548	−0.524	0.072	0.714	−0.452	−0.119
	p-value		0.623	0.160	0.183	0.866	0.111	0.260	0.779
	N		6	8	8	8	6	8	8
AOB	*rs*	0.600		0.486	0.714	0.145	−0.314	0.771	0.143
	p-value	0.208		0.329	0.111	0.784	0.544	0.072	0.787
	N	6		6	6	6	6	6	6
PMCo	*rs*	0.071	−0.143		0.667	**−0.731***	0.143	0.643	0.690
	p-value	0.879	0.787		0.071	**0.040**	0.787	0.086	0.058
	N	7	6		8	**8**	6	8	8
MePD	*rs*	0.071	0.200	−0.464		−0.240	−0.143	**0.905****	0.571
	p-value	0.879	0.704	0.294		0.568	0.787	**0.002**	0.139
	N	7	6	7		8	6	**8**	8
BSTMPM	*rs*	0.257	**1.000****	−0.543	0.314		**−0.841***	−0.228	−0.707
	p-value	0.623		0.266	0.544		**0.036**	0.588	0.050
	N	6	**5**	6	6		**6**	8	8
MOB	*rs*	**0.829***	**0.829***	0.029	0.486	0.700		0.029	0.657
	p-value	**0.042**	**0.042**	0.957	0.329	0.188		0.957	0.156
	N	**6**	**6**	6	6	5		6	6
PirAnt	*rs*	**0.821***	0.543	0.036	−0.321	0.314	0.543		**0.714***
	p-value	**0.023**	0.266	0.939	0.482	0.544	0.266		**0.047**
	N	**7**	6	7	7	6	6		**8**
PirPost	*rs*	**0.929****	0.543	0.143	0.036	0.143	0.771	0.679	
	p-value	**0.003**	0.266	0.760	0.939	0.787	0.072	0.094	
	N	**7**	6	7	7	6	6	7	

*$p < 0.05$; **$p < 0.01$. Bold values indicate statistically significant correlation.

Vomeronasal System Function and Behavioral Response to Pups

There is solid evidence indicating that VNO-detected chemosignals are likely crucial for some pup-directed responses, both parental and infanticide (Kimchi et al., 2007; Tachikawa et al., 2013; Nakahara et al., 2016; Isogai et al., 2018). In that respect, our results on Egr1 expression in the VNO demonstrate that pups are a source of vomeronasal stimuli for adult females (**Figures 2E,F**; **Supplementary Figures 1**, **2**). Unlike other previous reports, we use a control, non-social novel stimulus, and compare the Egr1 expression in the VNO induced by buttons to that induced by pups. A role of VNO-detected stimuli in maternal behavior was proposed by Lepri et al. (1985), who reported delayed pup retrieval in lactating dams that had undergone removal of the VNO, as compared to sham-operated dams. Moreover, mice with impaired VNO function (null-trpc2 mice) display reduced maternal care (Kimchi et al., 2007), deficient nest maintenance and reduced nursing (Hasen and Gammie, 2011). Taken together, these data strongly suggest that pups emit chemosignals that are detected by the VNO of females and mediate adult female-pup interactions in the context of motivated maternal behavior.

However, our results indicate that pup exposure did not elicit differential Egr1 expression in the VNO of LP and virgin females (**Figure 2** and **Supplementary Figure 1**), thus suggesting that hormone-induced changes in neurogenesis during pregnancy (Oboti et al., 2015) or hormone-induced changes in sensory transduction at the level of the VNO (Dey et al., 2015) might not be very relevant in the context of detection of pup chemosignals. By contrast, those changes may be relevant for the response of females to adult male chemosignals (e.g., major urinary proteins, Dey et al., 2015) perhaps in the context of nest defense (Martín-Sánchez et al., 2015), which is displayed by LP females (Mann and Svare, 1982). This lack of differences in VNO response to pups between females makes very unlikely that changes in pup-directed behaviors associated to pregnancy are due to altered sensitivity of the VNO. Instead, they should be attributed to altered sensory processing in the CNS during pregnancy. In this respect, our results also indicate that although pups induced an increase in cFos expression in the AOB (as compared to buttons) of females, this response was indistinguishable between virgin and LP females exposed to pups and a similar situation is found in the BSTMPM (compare **Figures 3A″** and **D″**). This suggests that, like sensory transduction of pup chemosignals in the VNO, response to pups in the AOB-BSTMPM pathway is not under strong influence of pregnancy hormones.

Otherwise, in the vomeronasal cortex (PMCo) and the medial amygdaloid nucleus (MePD) the response to pups was different between LP and virgin females. Surprisingly, this is due in part to a higher activation of both nuclei by buttons in virgins, as

compared to LP females. Since buttons are non-social objects, we assume that they do not directly activate vomeronasal neurons, so that the differential activation of these nuclei between button-exposed LP and virgins may be due to other afferents rather than direct vomeronasal inputs, as will be discussed later.

Importantly, in both secondary vomeronasal nuclei, LP females show increased activation by pups as compared to buttons, whereas virgins only show this pup-specific increase in cFos expression in the MePD, but not in the PMCo (where both stimuli elicit a similar activation). Consequently, in the PMCo, pup-induced cFos expression is significantly higher in LP than virgins. This indicates that sensory processing in the AOB-PMCo and AOB-MePD is modified during pregnancy. In the PMCo, this differential discrimination results in significant pup-button differences occurring only in LP females, suggesting that pregnancy modifies the functioning of specific vomeronasal pathways resulting in pup-specific activation of the vomeronasal cortex. This may be associated to reported changes in gene expression of key genes for endocrine signaling (e.g., receptor for prolactin) in afferents to the PMCo, such as the AOB and medial amygdala, during peripartum period in mice (Canavan et al., 2011). In addition, PMCo neurons display estrogen and progesterone receptors in rodents (Hagihara et al., 1992; Shughrue et al., 1997; Mitra et al., 2003). Thus, the important changes in steroid hormone levels occurring during late pregnancy (progesterone withdrawal, estrogen rise) may affect neural processing in the PMCo, altering the response to pup chemosignals.

An interesting finding of this work is the highly significant correlation observed between pup retrieval and cFos activity in the PMCo in both, LP and virgins. This points to a previous unknown role of this neural structure in the control of maternal behavior (the vomeronasal cortex, Gutiérrez-Castellanos et al., 2014), which fits the impact of VNO lesion in pup retrieval (Lepri et al., 1985). In addition, in LP females (but not virgins), the expression of cFos in the PMCo shows a remarkable positive correlation with the maternal score, a weighted sum of episodes in which female's behavior reflects a maternal state (pup retrieval, nest building, in nest and on nest). Although this suggests a relationship between both phenomena, PMCo activity and maternal behavior, the causal relationship it is not clear, e.g., whether the PMCo becomes activated by pups' stimuli during LP female interaction with them, or the PMCo activation is part of the neural mechanism responsible of the induction of maternal behavior. The PMCo projects to the BMA and to some extent to the BLA (Gutiérrez-Castellanos et al., 2014) and these nuclei of the basolateral amygdala are involved in goal-directed (e.g., pup-directed) behaviors via its projections to the accumbens-ventral pallidum (Numan and Woodside, 2010). Therefore, it is tempting to suggest that the PMCo may influence motivational aspects of maternal behavior using intra-amygdaloid pathways.

Concerning the MePD, its pattern of activation during exposure to pups/buttons looks rather similar to the one found in the PMCo, with some slight significant differences, as previously described. The MePD shows a very strong expression of steroid hormone receptors (Hagihara et al., 1992; Shughrue et al., 1997; Mitra et al., 2003), and, compared to virgins, pregnant females display a significant increase in pSTAT5-immunoreactive cell density, probably induced by placental lactogens (Salais-López et al., 2017). Thus, the influence of pregnancy hormones in LP females may underlie the correlation of cFos expression in the MePD with the chemosensory score, a weighted average of the episodes in which female-infant interactions are likely to include chemoinvestigation of pups. In contrast, in virgins, cFos expression in the MePD significantly correlates with the number of episodes in which the female exhibits "pup approach," a kind of risk-assessment behavior directed to pups, in which the female approaches a pup but retreats afterwards without trying to retrieve it. Although indirect, these data suggest that activity in the MePD is mainly related to chemosensory stimulation in both kinds of females, but in LP this mainly occurs in the context of maternal approaches to pups, whereas in virgins it seems more related to pup-directed exploratory behavior.

Vomeronasal Function and Pup-Directed Aggression

The role of vomeronasal stimuli in pup-directed aggression has been well-established in males. Thus, Tachikawa et al. (2013) demonstrated that infanticide in sexually naïve male mice is VNO-dependent, and accordingly, virgin infanticide males displayed much higher pup-induced activation (evaluated as cFos expression) in the VNO and AOB than sexually experienced, paternal males (Tachikawa et al., 2013). In line with this, Nakahara et al. (2016) showed that pups induced activation of an atypical subpopulation of neurons in the VNO that expresses a specific gene in the OR family, Olfr692. More recently, Isogai et al. (2018) demonstrated the implication of V2R-expressing VNO cells in the detection of specific molecules covering pup's bodies during postpartum (salivary secretions from the dam; hemoglobin) that induce pup killing in virgin males. In contrast, Trouillet et al. (2019) suggested the involvement of V1R/Galphai2-detected volatiles in virgin male infanticide.

Although the number of LP females exhibiting and not exhibiting pup-directed aggression is not large enough to establish two groups and compare their brain activity using robust statistics tools, the correlations between occurrence of pup aggression and brain activity renders interesting results. Our data show a positive correlation of AOB and BSTMPM activation (cFos expression) with pup-aggression score in LP females (**Table 1**; **Supplementary Figure 2**). This suggests that some vomeronasal-detected pup chemosignals might induce attacks in LP females, as it occurs in males, although the kind of VNO receptors involved is still unknown. In males transition from infanticide (sexually naïve males) to paternal care (sexually experienced males) seems associated to altered sensitivity of Olfr692-expressing VNO cells to pups (Nakahara et al., 2016) probably due to changes in sensory transduction in Galphai2/V1R-expressing cells (Trouillet et al., 2019). By contrast, our results suggest that in females other mechanisms seem to be at play. Thus, according to our results, LP and virgin females show similar Egr1-ir cell density in the VNO in response to pups, differences being observed only in some central

vomeronasal centers, such as the PMCo. This again suggests that pregnancy-induced altered functioning of central circuits, rather than changes in vomeronasal sensory transduction, might mediate infant-directed aggression observed in some LP females.

A highly significant positive correlation was also observed in the group of LP females, between pup-induced cFos expression in the two nuclei whose activity is correlated with pup-aggression: BSTMPM and AOB (**Table 2**, **Supplementary Figure 3**). Therefore, our data suggest that the AOB-BSTMPM pathway may be involved in pup-directed aggression. The effects of pregnancy hormones in the BSTMPM or its afferents (Salais-López et al., 2017) might promote a pattern of activity that would facilitate pup-attack in LP females.

The medial posterior BST, as part of the medial extended amygdala, is a heterogeneous brain region (Dong and Swanson, 2006a,b) involved in social behavior (part of the sociosexual brain network) including parenting, mating and aggressive behavior (Tsuneoka et al., 2015; Fukui et al., 2019). Studies carried out in males suggest that caring of pups or attacking them results from the activity of a specific circuit within the BST-preoptic area (Tsuneoka et al., 2015), and also that the estrogen receptor signaling in the BST is likely contributing to infanticidal behavior (Fukui et al., 2019). In addition, this nucleus is involved in the regulation of inter-male aggression by VNO-detected male chemosignals (see also Trouillet et al., 2019). Our data suggests that in females, the BSTMPM may be part of an activated brain circuit associated to pup attack by the end of pregnancy, but future studies are needed to explore this possibility.

By contrast, virgin females did not show pup attacks, and this might be related to the significant negative correlation observed in virgins (but not in LP females) between the activity in the PMCo/MOB and the one in the BSTMPM (see **Table 2**, **Supplementary Figure 3**). This suggests that tonic inhibition of the BSTMPM by these two nuclei inhibits pup attack in virgin females, whereas this inhibition may be reduced to a certain degree in some LP females, thus facilitating pup-directed aggression.

Olfaction and Behavioral Response to Pups: Vomeronasal-Olfactory Integration

Pup chemosignals are also detected by the main olfactory epithelium and processed by the associated brain pathway to trigger maternal behaviors (Seegal and Denenberg, 1974; Belluscio et al., 1998; Wang and Storm, 2011; Fraser and Shah, 2014). At the level of the MOB, however, our results reveal no preferential activation by either stimulus, but a differential response of the two kinds of females, with virgins showing globally a higher cFos density than LP females. This is mainly due to buttons inducing significantly higher cFos activation in virgins than LP females and indicates that buttons are not olfactory neutral. Our results on the MOB also suggest that pups are a source of olfactory stimuli, with no changes in olfactory sensitivity to pups associated to pregnancy. By contrast, either pregnancy hormones reduce sensitivity to button-derived odorants (Kanageswaran et al., 2016), or more likely, LP females explore buttons to a lesser extent than virgins. Very likely, top-down centrifugal projections within the olfactory systems (de Olmos et al., 1978; Shipley and Ennis, 1996; Wachowiak, 2010; Mohedano-Moriano et al., 2012; Aqrabawi et al., 2016), change their activity during pregnancy resulting in a reduced chemoinvestigation of buttons, which constitute novel, salient stimuli for virgin females.

Concerning exploration of pups, even if pups induced similar levels of cFos expression in the olfactory bulbs of LP and virgin females, it is interesting to note that MOB and AOB cFos levels show a positive and very significantly correlation in LP but not in virgin females (**Table 2**, **Supplementary Figure 3**). In addition, cFos-expressing cell density in both olfactory bulbs correlate with the number of periods that LP females were off nest (**Table 1**, **Supplementary Figure 2**). These data suggest a coupled activation of both chemosensory systems during exploration of the cage, far from the nest, further reinforcing the view that the main and accessory olfactory pathways are not parallel systems, but they work in tandem and play complementary roles in chemical analysis of the environment (see Martinez-Garcia et al., 2009). Indeed, there is anatomical evidence indicating that the olfactory and vomeronasal pathways converge on several secondary centers (Cádiz-Moretti et al., 2013). Moreover, our data suggest that, at least during pregnancy, both chemosensory systems are functionally interrelated already in their first central rely, the main and accessory olfactory bulbs, as pointed out by Pardo-Bellver et al. (2017) using an electrophysiological approach. This olfactory-vomeronasal functional relationship also results in correlation of pup-induced Egr1 expression in the VNO with the MOB and the piriform cortex of LP females (see **Table 2** and **Supplementary Figure 3**).

Although the anatomical substrate of the reciprocal influence between vomeronasal and olfactory systems (probably consistent of multiple indirect connections) is currently unknown, our findings indicate that functional coupling of MOB and AOB is probably associated to specific behaviors, such as chemoinvestigation of the environment (off nest, rather than pup-directed conducts), as reported by Pardo-Bellver et al. (2017). Our data also suggest that behavior-specific coupling is facilitated under some physiological circumstances, such as late pregnancy. A possible explanation for this could be an increased sniffing-induced vomeronasal pumping during investigation of the environment by LP females (Meredith and O'Connell, 1979), although more experiments are needed to test this hypothesis.

The pattern of cFos expression indicates that, in females, the activity of the olfactory cortex in response to the presence of pups or buttons is different to what we found in the main olfactory bulbs. Thus, whereas in LP the olfactory cortex is preferentially activated by pup odors, such higher activation does not occur in virgin females, which show a preferential activation by button odors instead, at least in the PirPost. Since the chemosensory score, likely related to detection of pup odors, does not differ between both kinds of females, these data suggest that processing of odorant stimuli through the olfactory pathway is altered during pregnancy favoring response to pup odors. This may reflect a role of the piriform cortex as an associative rather than a primary sensory cortex (see review by Haberly, 2001), where some neurons

respond preferentially to rewarded odors (Schoenbaum and Eichenbaum, 1995; Meissner-Bernard et al., 2019). Functional changes induced in the brain of females by the action of pregnancy hormones might increase the rewarding properties of pup-derived stimuli (Londei et al., 1989) and, consequently, it would increase the response of Pir cells to this stimulus. Indeed, enhanced response to pups in the olfactory cortex of LP females might be caused by changes in gene expression observed during the peripartum in the Pir and other centers of the olfactory systems in mice, such as reduced expression of oxytocin receptor to less than a half or a 2- to 3-fold increase in the expression of prolactin receptor (Canavan et al., 2011).

Although the functional consequences of this pup-biased response of the piriform cortex in LP females are difficult to ascertain yet, it is tempting to suggest that pup-induced activity in the Pir may be related with the expression of both, pup-directed and to non-pup-directed maternal behaviors. In fact, in LP females (but not virgins) there is a positive, significant correlation between nest building episodes and cFos expression in the PirAnt (see **Table 1**, **Supplementary Figure 2**). This suggests that cFos-related activity in the olfactory cortex, at least in PirAnt, is not a mere consequence of pup chemoinvestigation, but probably has a causal role in the induction of maternal behaviors.

CONCLUSIONS

In summary, our results reveal that pups are a source of chemical signals detected by the VNO, as demonstrated using quantitative assessment of Egr1 in the VNO. In LP females, processing of these chemosignals involves co-activation of the olfactory and vomeronasal systems, already at the level of the olfactory bulbs. Our data also depict two different subsystems within the vomeronasal system. On the one hand, in the pathway from the AOB to the PMCo and MePD sensory processing seems to be altered during late pregnancy so that discrimination between pups and buttons is enhanced. In addition, in LP females the activity in this pathway seems associated to pro-maternal behaviors, including pup retrieval and nest building. On the other hand, the pathway from the AOB to the BSTMPM shows no evidence of differential sensory processing in LP and virgin females. Although globally, activity in these centers is higher in pup- as compared to button-exposed females, within the group of LP females activity in both centers is correlated to pup-directed aggression, thus suggesting a role of vomeronasal stimulation of the BSTMPM in inducing pup attacks in females (during pregnancy), similar to what has been reported in virgin males for other portions of the BST.

DATA AVAILABILITY STATEMENT

The raw data supporting the conclusions of this article will be made available by the authors, without undue reservation.

ETHICS STATEMENT

The animal study was reviewed and approved by Committee of Ethics and Animal Experimentation of the Universitat Jaume I.

AUTHOR CONTRIBUTIONS

CN-M, MB-M, and FM-G designed the experiments. CN-M, MS-C, MB-M, RG-C, and MB performed the experiments. CN-M, MS-C, and FM-G analyzed the data. CN-M, MS-C, EL, CA-P, and FM-G drafted the manuscript. All authors contributed to the article and approved the submitted version.

FUNDING

This work was supported by the Spanish Ministry of Economy and Competitiveness-FEDER (BFU2016-77691-C2-2-P and C2-1-P), the Spanish Ministry of Science and Innovation (PID2019-107322GB-C21), the Generalitat Valenciana (PROMETEO/2016/076), the Universitat Jaume I de Castelló (UJI-B2016-45 and UJIA2019-14). CN-M and MB-M have been a pre-doctoral and post-doctoral fellow of the programme of the Universitat Jaume I, respectively. Funding sources had no further role in study design; in the collection, analysis and interpretation of data; in the writing of the manuscript; and in the decision to submit the paper for publication.

ACKNOWLEDGMENTS

The authors were indebted to the staff of the animal facility (SEA) of the Universitat Jaume I, for their help during the experimental procedure, and to Alejandra Amiguet Comins for her help in analyzing Egr1 expression in the VNO.

SUPPLEMENTARY MATERIAL

The Supplementary Material for this article can be found online at: https://www.frontiersin.org/articles/10.3389/fncel.2020.593309/full#supplementary-material

REFERENCES

Aguggia, J. P., Suárez, M. M., and Rivarola, M. A. (2013). Early maternal separation: neurobehavioral consequences in mother rats. *Behav. Brain Res.* 248, 25–31. doi: 10.1016/j.bbr.2013.03.040

Alsina-Llanes, M., De Brun, V., and Olazábal, D. E. (2015). Development and expression of maternal behavior in naïve female C57BL/6 mice. *Dev. Psychobiol.* 57, 189–200. doi: 10.1002/dev.21276

Aqrabawi, A. J., Browne, C. J., Dargaei, Z., Garand, D., Khademullah, C. S., Woodin, M. A., et al. (2016). Top-down modulation of olfactory-guided behaviours by the anterior olfactory nucleus pars medialis and ventral hippocampus. *Nat. Commun.* 7, 1–9. doi: 10.1038/ncomms13721

Belluscio, L., Gold, G. H., Nemes, A., and Axel, R. (1998). Mice deficient in G(olf) are anosmic. *Neuron* 20, 69–81. doi: 10.1016/S0896-6273(00)80435-3

Bepari, A. K., Watanabe, K., Yamaguchi, M., Tamamaki, N., and Hirohide, T. (2012). Visualization of odor-induced neuronal activity by immediate

early gene expression. *BMC Neurosci.* 13, 140. doi: 10.1186/1471-2202-13-140

Blaffer Hrdy, S. (1979). Infanticide among animals: a review, classification, and examination of the implications for the reproductive strategies of females. *Ethol. Sociobiol.* 1, 13–40. doi: 10.1016/0162-3095(79)90004-9

Bridges, R. S. (2020). The behavioral neuroendocrinology of maternal behavior: Past accomplishments and future directions. *Horm. Behav.* 120:104662. doi: 10.1016/j.yhbeh.2019.104662

Bridges, R. S., and Freemark, M. S. (1995). Human placental lactogen infusions into the medial preoptic area stimulate maternal behavior in steroid-primed, nulliparous female rats. *Horm. Behav.* 29, 216–26. doi: 10.1006/hbeh.1995.1016

Bridges, R. S., and Ronsheim, P. M. (1990). Prolactin (PRL) regulation of maternal behavior in rats: bromocriptine treatment delays and PRL promotes the rapid onset of behavior. *Endocrinology* 126, 837–848. doi: 10.1210/endo-126-2-837

Bridges, R. S., Rosenblatt, J. S., and Feder, H. H. (1978). Stimulation of maternal responsiveness after pregnancy termination in rats: effect of time of onset of behavioral testing. *Horm. Behav.* 10, 235–245. doi: 10.1016/0018-506X(78)90067-3

Brown, R. S. E., Aoki, M., Ladyman, S. R., Phillipps, H. R., Wyatt, A., Boehm, U., et al. (2017). Prolactin action in the medial preoptic area is necessary for postpartum maternal nursing behavior. *Proc. Natl. Acad. Sci. U.S.A.* 114, 10779–10784. doi: 10.1073/pnas.1708025114

Cádiz-Moretti, B., Martínez-García, F., and Lanuza, E. (2013). "Neural substrate to associate odorants and pheromones: convergence of projections from the main and accessory olfactory bulbs in mice," in *Chemical Signals in Vertebrates 12*, eds M. L. East and M. Dehnhard (New York, NY: Springer Science), 269–275. doi: 10.1007/978-1-4614-5927-9_1

Canavan, S. V., Mayes, L. C., and Treloar, H. B. (2011). Changes in maternal gene expression in olfactory circuits in the immediate postpartum period. *Front. Psychiatry* 2, 1–9. doi: 10.3389/fpsyt.2011.00040

Cohen, L., Rothschild, G., and Mizrahi, A. (2011). Multisensory integration of natural odors and sounds in the auditory cortex. *Neuron* 72, 357–369. doi: 10.1016/j.neuron.2011.08.019

Curley, J. P., and Champagne, F. A. (2016). Influence of maternal care on the developing brain: mechanisms, temporal dynamics and sensitive periods. *Front. Neuroendocrinol.* 40, 52–66. doi: 10.1016/j.yfrne.2015.11.001

de Olmos, J., Hardy, H., and Heimer, L. (1978). The afferent connections of the main and the accessory olfactory bulb formations in the rat: an experimental HRP-study. *J. Comp. Neurol.* 181, 213–244. doi: 10.1002/cne.901810202

Dey, S., Chamero, P., Pru, J. K., Chien, M. S., Ibarra-Soria, X., Spencer, K. R., et al. (2015). Cyclic regulation of sensory perception by a female hormone alters behavior. *Cell* 161, 1334–1344. doi: 10.1016/j.cell.2015.04.052

Dong, H. W., and Swanson, L. W. (2006a). Projections from bed nuclei of the stria terminalis, anteromedial area: cerebral hemisphere integration of neuroendocrine, autonomic, and behavioral aspects of energy balance. *J. Comp. Neurol.* 494, 142–178. doi: 10.1002/cne.20788

Dong, H. W., and Swanson, L. W. (2006b). Projections from bed nuclei of the stria terminalis, dorsomedial nucleus: Implications for cerebral hemisphere integration of neuroendocrine, autonomic, and drinking responses. *J. Comp. Neurol.* 494, 75–107. doi: 10.1002/cne.20790

Fraser, E. J., and Shah, N. M. (2014). Complex chemosensory control of female reproductive behaviors. *PLoS ONE* 9:e90368. doi: 10.1371/journal.pone.0090368

Fukui, K., Uki, H., Minami, M., and Amano, T. (2019). Effect of gonadal steroid hormone levels during pubertal development on social behavior of adult mice toward pups and synaptic transmission in the rhomboid nucleus of the bed nucleus of the stria terminalis. *Neurosci. Lett.* 708:134357. doi: 10.1016/j.neulet.2019.134357

Gandelman, R., Zarrow, M. X., Denenberg, V. H., and Myers, M. (1971). Olfactory bulb removal eliminates maternal behavior in the mouse. *Science* 171, 210–211. doi: 10.1126/science.171.3967.210

Gutiérrez-Castellanos, N., Pardo-Bellver, C., Martínez-García, F., and Lanuza, E. (2014). The vomeronasal cortex–afferent and efferent projections of the posteromedial cortical nucleus of the amygdala in mice. *Eur. J. Neurosci.* 39, 141–158. doi: 10.1111/ejn.12393

Haberly, L. B. (2001). Parallel-distributed processing in olfactory cortex: new insights from morphological and physiological analysis of neuronal circuitry. *Chem. Senses* 26, 551–576. doi: 10.1093/chemse/26.5.551

Hagihara, K., Hirata, S., Osada, T., Hirai, M., and Kato, J. (1992). Distribution of cells containing progesterone receptor mRNA in the female rat di- and telencephalon: an *in situ* hybridization study. *Mol. Brain Res.* 14, 239–249. doi: 10.1016/0169-328X(92)90179-F

Hasen, N. S., and Gammie, S. C. (2011). Trpc2-deficient lactating mice exhibit altered brain and behavioral responses to bedding stimuli. *Behav. Brain Res.* 217, 347–353. doi: 10.1016/j.bbr.2010.11.002

Hauser, H., and Gandelman, R. (1985). Lever pressing for pups: evidence for hormonal influence upon maternal behavior of mice. *Horm. Behav.* 19, 454–468. doi: 10.1016/0018-506X(85)90041-8

Hoffman, G. E., Smith, M. S., and Verbalis, J. G. (1993). c-Fos and related immediate early gene products as markers of activity in neuroendocrine systems. *Front. Neuroendocrinol.* 14, 173–213. doi: 10.1006/frne.1993.1006

Isogai, Y., Si, S., Pont-Lezica, L., Tan, T., Kapoor, V., Murthy, V. N., et al. (2011). Molecular organization of vomeronasal chemoreception. *Nature* 478, 241–245. doi: 10.1038/nature10437

Isogai, Y., Wu, Z., Love, M. I., Ahn, M. H. Y., Bambah-Mukku, D., Hua, V., et al. (2018). Multisensory logic of infant-directed aggression by males. *Cell* 175, 1827–1841.e17. doi: 10.1016/j.cell.2018.11.032

Kanageswaran, N., Nagel, M., Scholz, P., Mohrhardt, J., Gisselmann, G., and Hatt, H. (2016). Modulatory effects of sex steroids progesterone and estradiol on odorant evoked responses in olfactory receptor neurons. *PLoS ONE* 11:e159640. doi: 10.1371/journal.pone.0159640

Kimchi, T., Xu, J., and Dulac, C. (2007). A functional circuit underlying male sexual behaviour in the female mouse brain. *Nature* 448, 1009–1014. doi: 10.1038/nature06089

Kohl, J., Autry, A. E., and Dulac, C. (2017). The neurobiology of parenting: a neural circuit perspective. *BioEssays* 39, 1–11. doi: 10.1002/bies.201600159

Kuroda, K. O., and Tsuneoka, Y. (2013). "Assessing postpartum maternal care, alloparental behavior, and infanticide in mice: with notes on chemosensory influences," in *Pheromone Signaling: Methods and Protocols* (Tokyo: Humana Press; Springer), 331–347. doi: 10.1007/978-1-62703-619-1_25

Latham, N., and Mason, G. (2004). From house mouse to mouse house: the behavioural biology of free-living Mus musculus and its implications in the laboratory. *Appl. Anim. Behav. Sci.* 86, 261–289. doi: 10.1016/j.applanim.2004.02.006

Lepri, J. J., Wysocki, C. J., and Vandenbergh, J. G. (1985). Mouse vomeronasal organ: effects on chemosignal production an maternal behavior. *Physiol. Behav.* 35, 809–814. doi: 10.1016/0031-9384(85)90416-0

Leypold, B. G., Yu, C. R., Leinders-Zufall, T., Kim, M. M., Zufall, F., and Axel, R. (2002). Altered sexual and social behaviors in trp2 mutant mice. *Proc. Natl. Acad. Sci. U.S.A.* 99, 6376–81. doi: 10.1073/pnas.082127599

Lisk, R. D. (1971). Oestrogen and progesterone synergism and elicitation of maternal nest-building in the mouse (*Mus musculus*). *Anim. Behav.* 19, 606–610. doi: 10.1016/S0003-3472(71)80118-5

Londei, T., Segala, P., and Leone, V. G. (1989). Mouse pup urine as an infant signal. *Physiol. Behav.* 45, 579–583. doi: 10.1016/0031-9384(89)90076-0

Mann, M. A., Konen, C., and Svare, B. (1984). The role of progesterone in pregnancy-induced aggression in mice. *Horm. Behav.* 18, 140–160. doi: 10.1016/0018-506X(84)90039-4

Mann, M. A., and Svare, B. (1982). Factors influencing pregnancy-induced aggression in mice. *Behav. Neural Biol.* 36, 242–258. doi: 10.1016/S0163-1047(82)90867-6

Marlin, B. J., Mitre, M., D'Amour, J. A., Chao, M. V., and Froemke, R. C. (2015). Oxytocin enables maternal behaviour by balancing cortical inhibition. *Nature* 520, 499–504. doi: 10.1038/nature14402

Martinez-Garcia, F., Martinez-Ricos, J., Agustin-Pavon, C., Martinez-Hernandez, J., Novejarque, A., and Lanuza, E. (2009). Refining the dual olfactory hypothesis: pheromone reward and odour experience. *Behav. Brain Res.* 200, 277–286. doi: 10.1016/j.bbr.2008.10.002

Martín-Sánchez, A., Valera-Marín, G., Hernández-Martínez, A., Lanuza, E., Martínez-García, F., and Agustín-Pavón, C. (2015). Wired for motherhood: induction of maternal care but not maternal aggression in virgin female CD1 mice. *Front. Behav. Neurosci.* 9:197. doi: 10.3389/fnbeh.2015.00197

Mayer, A. D., and Rosenblatt, J. S. (1984). Prepartum changes in maternal responsiveness and nest defense in *Rattus norvegicus*. *J. Comp. Psychol.* 98, 177–188. doi: 10.1037/0735-7036.98.2.177

McCarthy, M. M., and Vom Saal, F. S. (1985). The influence of reproductive state on infanticide by wild female house mice (*Mus musculus*). *Physiol. Behav.* 35, 843–849. doi: 10.1016/0031-9384(85)90248-3

Meissner-Bernard, C., Dembitskaya, Y., Venance, L., and Fleischmann, A. (2019). Encoding of odor fear memories in the mouse olfactory cortex. *Curr. Biol.* 29, 367–380.e4. doi: 10.1016/j.cub.2018.12.003

Meredith, M., and O'Connell, R. J. (1979). Efferent control of stimulus access to the hamster vomeronasal organ. *J. Physiol.* 286, 301–316. doi: 10.1113/jphysiol.1979.sp012620

Mitra, S. W., Hoskin, E., Yudkovitz, J., Pear, L., Wilkinson, H. A., Hayashi, S., et al. (2003). Immunolocalization of estrogen receptor beta in the mouse brain: comparison with estrogen receptor alpha. *Endocrinology* 144, 2055–2067. doi: 10.1210/en.2002-221069

Mohedano-Moriano, A., de la Rosa-Prieto, C., Saiz-Sanchez, D., Ubeda-Bañon, I., Pro-Sistiaga, P., de Moya-Pinilla, M., et al. (2012). Centrifugal telencephalic afferent connections to the main and accessory olfactory bulbs. *Front. Neuroanat.* 6:19. doi: 10.3389/fnana.2012.00019

Nakahara, T. S., Cardozo, L. M., Ibarra-Soria, X., Bard, A. D., Carvalho, V. M. A., Trintinalia, G. Z., et al. (2016). Detection of pup odors by non-canonical adult vomeronasal neurons expressing an odorant receptor gene is influenced by sex and parenting status. *BMC Biol.* 14:12. doi: 10.1186/s12915-016-0234-9

Numan, M., and Insel, T. R. (2003). *The Neurobiology of Parental Behavior*. New York, NY: Springer-Verlag.

Numan, M., and Woodside, B. (2010). Maternity: neural mechanisms, motivational processes, and physiological adaptations. *Behav. Neurosci.* 124, 715–741. doi: 10.1037/a0021548

Oboti, L., Ibarra-Soria, X., Pérez-Gómez, A., Schmid, A., Pyrski, M., Paschek, N., et al. (2015). Pregnancy and estrogen enhance neural progenitor-cell proliferation in the vomeronasal sensory epithelium. *BMC Biol.* 13:104. doi: 10.1186/s12915-015-0211-8

Pardo-Bellver, C., Martínez-Bellver, S., Martínez-García, F., Lanuza, E., and Teruel-Martí, V. (2017). Synchronized activity in the main and accessory olfactory bulbs and vomeronasal amygdala elicited by chemical signals in freely behaving mice. *Sci. Rep.* 7:9924. doi: 10.1038/s41598-017-10089-4

Paxinos, G., and Franklin, K. B. J. (2004). *The Mouse Brain in Stereotaxic Coordinates*. San Diego, CA: Elsevier Academic Press.

Peters, L. C., and Kristal, M. B. (1983). Suppression of infanticide in mother rats. *J. Comp. Psychol.* 97, 167–177. doi: 10.1037/0735-7036.97.2.167

Rinaldi, A., Romeo, S., Agustín-Pavón, C., Oliverio, A., and Mele, A. (2010). Distinct patterns of Fos immunoreactivity in striatum and hippocampus induced by different kinds of novelty in mice. *Neurobiol. Learn. Mem.* 94, 373–381. doi: 10.1016/j.nlm.2010.08.004

Rosenblatt, J., and Siegel, H. (1975). Hysterectomy-induced maternal behavior during pregnancy in the rat. *J. Comp. Physiol. Psychol.* 89, 685–700. doi: 10.1037/h0077052

Salais-López, H., Abellan-Alvaro, M., Bellés, M., Lanuza, E., Agustin-Pavon, C., and Martínez-García, F. (2020). Maternal motivation: exploring the roles of prolactin and pup stimuli. *Neuroendocrinology*. doi: 10.1159/000510038. [Epub ahead of print].

Salais-López, H., Lanuza, E., Agustín-Pavón, C., and Martínez-García, F. (2017). Tuning the brain for motherhood: prolactin-like central signalling in virgin, pregnant, and lactating female mice. *Brain Struct. Funct.* 222, 895–921. doi: 10.1007/s00429-016-1254-5

Schoenbaum, G., and Eichenbaum, H. (1995). Information coding in the rodent prefrontal cortex. I. Single-neuron activity in orbitofrontal cortex compared with that in pyriform cortex. *J. Neurophysiol.* 74, 733–750. doi: 10.1152/jn.1995.74.2.733

Seegal, R. F., and Denenberg, V. H. (1974). Maternal experience prevents pup-killing in mice induced by peripheral anosmia. *Physiol. Behav.* 13, 339–341. doi: 10.1016/0031-9384(74)90056-0

Shipley, M. T., and Adamek, G. D. (1984). The connections of the mouse olfactory bulb: a study using orthograde and retrograde transport of wheat germ agglutinin conjugated to horseradish peroxidase. *Brain Res. Bull.* 12, 669–688. doi: 10.1016/0361-9230(84)90148-5

Shipley, M. T., and Ennis, M. (1996). Functional organization of olfactory system. *J. Neurobiol.* 30, 123–176. doi: 10.1002/(SICI)1097-4695(199605)30:1<123::AID-NEU11>3.0.CO;2-N

Shughrue, P. J., Lane, M. V., and Merchenthaler, I. (1997). Comparative distribution of estrogen receptor-alpha and -beta mRNA in the rat central nervous system. *J. Comp. Neurol.* 388, 507–525. doi: 10.1002/(SICI)1096-9861(19971201)388:4<507::AID-CNE1>3.0.CO;2-6

Smotherman, W. P., Bell, R. W., Starzec, J., Elias, J., and Zachman, T. A. (1974). Maternal responses to infant vocalizations and olfactory cues in rats and mice. *Behav. Biol.* 12, 55–66. doi: 10.1016/S0091-6773(74)91026-8

Stolzenberg, D. S., and Rissman, E. F. (2011). Oestrogen-independent, experience-induced maternal behaviour in female mice. *J. Neuroendocrinol.* 23, 345–354. doi: 10.1111/j.1365-2826.2011.02112.x

Stowers, L., Holy, T. E., Meister, M., Dulac, C., and Koentges, G. (2002). Loss of sex discrimination and male-male aggression in mice deficient for TRP2. *Science* 295, 1493–1500. doi: 10.1126/science.1069259

Tachikawa, K. S., Yoshihara, Y., and Kuroda, K. O. (2013). Behavioral transition from attack to parenting in male mice: a crucial role of the vomeronasal system. *J. Neurosci.* 33, 5120–5126. doi: 10.1523/JNEUROSCI.2364-12.2013

Trouillet, A. C., Keller, M., Weiss, J., Leinders-Zufall, T., Birnbaumer, L., Zufall, F., et al. (2019). Central role of G protein Gαi2 and Gαi2 + vomeronasal neurons in balancing territorial and infant-directed aggression of male mice. *Proc. Natl. Acad. Sci. U.S.A.* 116, 5135–5143. doi: 10.1073/pnas.1821492116

Tsuneoka, Y., Tokita, K., Yoshihara, C., Amano, T., Esposito, G., Huang, A. J., et al. (2015). Distinct preoptic-BST nuclei dissociate paternal and infanticidal behavior in mice. *EMBO J.* 34, 2652–2670. doi: 10.15252/embj.201591942

Vandenbergh, J. G. (1973). Effects of central and peripheral anosmia on reproduction of female mice. *Physiol. Behav.* 10, 257–261. doi: 10.1016/0031-9384(73)90307-7

Wachowiak, M. (2010). "Active sensing in olfaction," in *The Neurobiology of Olfaction*, ed A. Menini (Boca Raton, FL: CRC Press). doi: 10.1201/9781420071993

Wang, Z., and Storm, D. R. (2011). Maternal behavior is impaired in female mice lacking type 3 adenylyl cyclase. *Neuropsychopharmacology* 36, 772–781. doi: 10.1038/npp.2010.211

Conflict of Interest: The authors declare that the research was conducted in the absence of any commercial or financial relationships that could be construed as a potential conflict of interest.

frontiers in Cellular Neuroscience

ORIGINAL RESEARCH
published: 02 February 2021
doi: 10.3389/fncel.2021.635837

Dynamic Cholinergic Tone in the Basal Forebrain Reflects Reward-Seeking and Reinforcement During Olfactory Behavior

Elizabeth Hanson[1], *Katie L. Brandel-Ankrapp*[2] *and Benjamin R. Arenkiel*[1]*

[1] Department of Molecular and Human Genetics, Baylor College of Medicine, Houston, TX, United States,
[2] Postbaccalaureate Research Education Program, Baylor College of Medicine, Houston, TX, United States

Sensory perception underlies how we internalize and interact with the external world. In order to adapt to changing circumstances and interpret signals in a variety of contexts, sensation needs to be reliable, but perception of sensory input needs to be flexible. An important mediator of this flexibility is top-down regulation from the cholinergic basal forebrain. Basal forebrain projection neurons serve as pacemakers and gatekeepers for downstream neural networks, modulating circuit activity across diverse neuronal populations. This top-down control is necessary for sensory cue detection, learning, and memory, and is disproportionately disrupted in neurodegenerative diseases associated with cognitive decline. Intriguingly, cholinergic signaling acts locally within the basal forebrain to sculpt the activity of basal forebrain output neurons. To determine how local cholinergic signaling impacts basal forebrain output pathways that participate in top-down regulation, we sought to define the dynamics of cholinergic signaling within the basal forebrain during motivated behavior and learning. Toward this, we utilized fiber photometry and the genetically encoded acetylcholine indicator GAChR2.0 to define temporal patterns of cholinergic signaling in the basal forebrain during olfactory-guided, motivated behaviors and learning. We show that cholinergic signaling reliably increased during reward seeking behaviors, but was strongly suppressed by reward delivery in a go/no-go olfactory-cued discrimination task. The observed transient reduction in cholinergic tone was mirrored by a suppression in basal forebrain GABAergic neuronal activity. Together, these findings suggest that cholinergic tone in the basal forebrain changes rapidly to reflect reward-seeking behavior and positive reinforcement and may impact downstream circuitry that modulates olfaction.

Keywords: acetylcholine, olfaction, basal forebrain, go/no-go, reward, discrimination, GABA, top-down

OPEN ACCESS

Edited by:
Shaina M. Short,
The University of Utah, United States

Reviewed by:
Christiane Linster,
Cornell University, United States
Jocelyn M. Richard,
University of Minnesota Twin Cities, United States

***Correspondence:**
Benjamin R. Arenkiel
arenkiel@bcm.edu

Specialty section:
This article was submitted to Cellular Neurophysiology, a section of the journal Frontiers in Cellular Neuroscience

Received: *30 November 2020*
Accepted: *11 January 2021*
Published: *02 February 2021*

Citation:
Hanson E, Brandel-Ankrapp KL and Arenkiel BR (2021) Dynamic Cholinergic Tone in the Basal Forebrain Reflects Reward-Seeking and Reinforcement During Olfactory Behavior. Front. Cell. Neurosci. 15:635837. doi: 10.3389/fncel.2021.635837

INTRODUCTION

Rapid and precise sensory processing is critical for properly interpreting the external world. As a chemical sense, olfaction requires the ability to sample a vast, non-continuous sensory space with a wide range of stimulus intensities (Ache and Young, 2005). For this, the olfactory system must quickly separate and identify trace amounts of volatilized signals from a complex, noisy background (Rokni et al., 2014). However, as an animal moves through the world, the contexts in which it

encounters odors, as well as its own internal drives, are constantly changing. Therefore, olfactory processing must be flexible as well as sensitive in order to facilitate these changing needs. Flexible olfactory processing depends, in part, on top-down regulation (Restrepo et al., 2009; Pashkovski et al., 2020). Top-down regulation is a feature of sensory systems through which information about an animal's context, internal state, or previous experience modulates circuit function to sculpt the way stimuli are perceived (Gilbert and Sigman, 2007). In olfaction, for example, top-down regulatory mechanisms are recruited during active sensing in ways that improve odor detection and discrimination (Jordan et al., 2018), allow odor detection within a single sniff (Laing, 1986; Rinberg et al., 2006), and facilitate adaptive filtering during high frequency bouts of sniffing (Verhagen et al., 2007). Top-down regulation also allows for rapid changes in odor responses depending on context (Kay and Laurent, 1999; Beshel et al., 2007; Kudryavitskaya et al., 2020), and directly influences plasticity within the olfactory system (Fletcher and Wilson, 2003; Fletcher and Chen, 2010; Lepousez et al., 2014; Hanson et al., 2020).

An important source of top-down regulation in olfaction comes from the horizontal limb of the diagonal band of Broca (HDB) in the basal forebrain (Zaborszky et al., 1986; Mandairon et al., 2006; Gracia-Llanes et al., 2010; Ma and Luo, 2012; Rothermel et al., 2014). Basal forebrain neurons mediate state-dependent top-down regulation through signaling mechanisms that span diverse time scales ranging from milliseconds to hours (Buzsaki et al., 1988; Détári et al., 1999; Muñoz and Rudy, 2014). Fast, phasic signals from the basal forebrain mediate effects of attention on sensory processing, decision making, and sensory cued task performance (Parikh et al., 2007; Lin and Nicolelis, 2008; Pinto et al., 2013; Muñoz and Rudy, 2014; Hangya et al., 2015; Gritton et al., 2016). It has long been hypothesized that basal forebrain cholinergic signaling in particular mediates attentional effects on sensory processing circuits (Mandairon et al., 2006; Herrero et al., 2008; Chaudhury et al., 2009; Ghatpande and Gelperin, 2009; Goard and Dan, 2009; Ma and Luo, 2012; Chapuis and Wilson, 2013; Zhan et al., 2013; Rothermel et al., 2014). However, it has also been found that that non-cholinergic neuronal activity better predicts behavioral variables associated with attention in an auditory-cued go/no-go task (Hangya et al., 2015). Additionally, a recent study has described anticipatory activity among both cholinergic and non-cholinergic neurons in the basal forebrain during an olfactory-cued go/no-go task (Nunez-Parra et al., 2020). Importantly, in agreement with these earlier studies (Dannenberg et al., 2015; Xu et al., 2015), cholinergic neurons were also noted to collateralize within the basal forebrain to influence the activity of neighboring non-cholinergic neurons during task performance (Nunez-Parra et al., 2020). Together, this evidence suggests that non-cholinergic basal forebrain neurons mediate effects of attention on sensory processing, and it raises the question of how communication between cell types within the basal forebrain controls state-dependent basal forebrain output.

Parallel cholinergic and GABAergic projections from the basal forebrain to the olfactory bulb mediate distinct features of top-down regulation (Böhm et al., 2020). Separately, the cholinergic and GABAergic projections control gain, signal-to-noise ratio, habituation, oscillatory activity, and odor discrimination (Ma and Luo, 2012; Nunez-Parra et al., 2013; Rothermel et al., 2014; Ogg et al., 2018; Villar et al., 2020). Though both types of basal forebrain projections are important modulators of olfactory bulb odor and sniff responses, the upstream mechanisms that control basal forebrain output remain largely unknown. Ultimately, understanding how the basal forebrain mediates state-dependent changes in olfactory processing requires a more detailed knowledge of signaling within the HDB, and how it controls HDB output during olfaction and complex olfactory-guided behavior.

Here we describe temporal patterns of cholinergic signaling within the HDB during an olfactory-cued go/no-go discrimination task where mice learn to associate one of two odors with a reward. Historically, monitoring acetylcholine directly, *in vivo*, with high temporal resolution, has been challenging. However, with the advent of the genetically encoded GPCR Activation-Based (GRAB) fluorescent sensor for acetylcholine (GACh2.0) we directly recorded rapid fluctuations in acetylcholine levels from freely moving, behaving animals (Jing et al., 2018). Combining targeted sensor expression with implanted fiber optics and fiber photometry, we directly recorded acetylcholine signaling from the basal forebrain chronically, during freely moving behavior. We found that acetylcholine levels within the basal forebrain are dynamic and bidirectionally regulated during performance of a go/no-go discrimination task. Reward seeking behavior reliably evoked rapid increases in HDB acetylcholine, while positive feedback transiently suppressed cholinergic tone. These dynamics suggest that local cholinergic signaling is rapidly modulated in the HDB circuitry and may impact basal forebrain output pathways important for regulating olfaction.

RESULTS

Fiber Photometry of a Genetically Encoded Acetylcholine Sensor Reveals Real-Time Cholinergic Signaling in the Basal Forebrain

Defining the temporal profile of basal forebrain cholinergic signaling during complex behavior is a necessary step in determining how local cholinergic signaling impacts HDB circuit function and state-dependent output. To directly monitor cholinergic signals within the basal forebrain we injected wildtype mice with an adeno-associated virus (AAV) engineered to drive pan-neuronal expression of the acetylcholine sensor GACh2.0 (AAV hsyn-GACh). At the same time, we implanted a fiberoptic over the HDB (**Figure 1A**). GACh is a genetically-encoded fusion of a conformationally sensitive GFP and muscarinic acetylcholine receptor that fluoresces in response to binding acetylcholine. Imaging GACh fluorescence with fiber photometry allowed us to directly record changes in cholinergic tone within the HDB. Viral expression and implant targeting were verified *post-hoc* in all mice via immunofluorescence and histology (**Figure 1B**). After implantation and injection, mice

were allowed to recover and given 3 weeks to express the sensor prior to photometric recordings (**Figure 1C**). We first examined cholinergic signaling in freely moving mice during exploration of an open field arena. For this, we video-recorded mice exploring an open field while simultaneously using fiber photometry to record activity-dependent changes in GACh fluorescence in the HDB (**Figures 1C,D**). During open field exploration, we observed both excitation and suppression events (**Figure 1E**). Notably, detected events were not correlated with motion or position in the open field (**Figure 1F**), and the amplitude of fluorescence signals (dF/F) were not correlated with speed (cm/s) over time (Pearson's correlation $= -0.043 \pm 0.025$, $N = 4$ animals, 1 session per animal). These results revealed frequent spontaneous cholinergic signaling events in the HDB during behavior, which was not triggered by, or directly correlated with, voluntary locomotion.

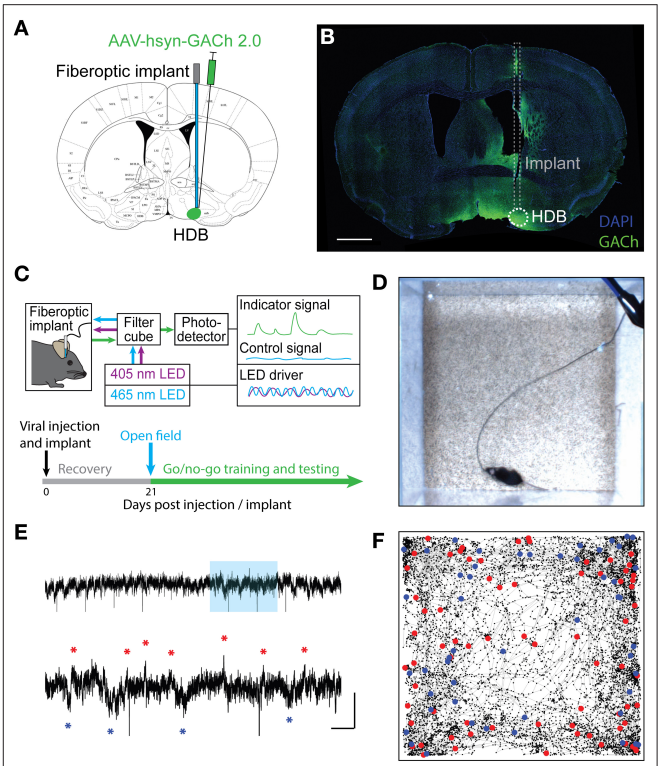

FIGURE 1 | Fiber photometry of a genetically encoded acetylcholine sensor in the HDB reveals real-time cholinergic signaling during freely moving behavior. **(A)** Coronal section schematic showing AAV injection and implant targeting the HDB. **(B)** IHC of a coronal section showing GACh2.0 expression and implant targeting in the HDB. Scale bar = 1 mm. **(C)** Schematic of photometry system showing light paths, LED control systems, filtering, and photodetection. Timeline of surgery, recovery, and photometry recording during open field exploration, followed by behavioral training and testing. **(D)** Still frame from video of open field exploration with photometric recording. **(E)** (Top panel) Isosbestic-subtracted GACh dF/F trace during open-field arena exploration. Y scale bar = 1 dF/F and X scale bar = 60 s. (Bottom panel) zoom of blue shaded portion of trace in top panel with excitation events marked with red asterisks and suppression events marked with blue asterisks. Y Scale bar = 1 dF/F, X scale bar = 10 s. **(F)** Track of mouse location over 20 min of open field exploration with locations corresponding to increases in HDB cholinergic signaling (excitation events) marked with red dots and decreases (suppression events) marked with blue dots.

Basal Forebrain Cholinergic Signaling Rapidly Fluctuates With Reward-Seeking and Positive Reinforcement

If HDB cholinergic signaling influences state-dependent basal forebrain output, we reasoned that the cholinergic reporter responses may dynamically change with behavioral states during the performance of complex, olfactory-guided, operant behaviors. To test this, we recorded photometry signals from freely moving mice performing an olfactory-cued go/no-go discrimination task ($N = 33$ sessions, 6 animals) (**Figures 2A,B**). Mice first underwent a shaping period of 10–14 days where they learned the mechanics of the task without photometry recording. During shaping, mice were trained to self-initiate trials by poking their nose into a port where they were presented with one of two odors. They then learned to distinguish between the delivery of an S+ odor, which indicated the availability of a water droplet at a separate reward port, and an S– odor, which indicated that no reward was available. A correct response to the S+ odor where a reward was obtained was considered a "Hit." A correct response to the S– odor where a new trial was initiated without reward-seeking was considered a "Correct Reject." An incorrect attempt to seek a reward after the S– odor was considered a "False Alarm" and an incorrect trial re-initiation after presentation of the S+ odor was considered a "Miss" (**Figure 2A**). Notably, this freely moving go/no-go task did not include punishment in response to False Alarms. Thus, feedback during odor-association learning was limited to positive reinforcement of a water reward in Hit trials, and negative reinforcement of a 4 s timeout after false alarms. This form of negative reinforcement is only mildly aversive, as demonstrated by a bias toward reward seeking trials (i.e., False Alarm Rate > Miss Rate) in all sessions where odors were effectively learned. Another feature of the freely moving task was that animals were required to self-initiate trials and reward seeking. Thus, the timing of trial initiation and reward seeking was determined entirely by the mouse, and it required both active engagement with the task and locomotion (**Figure 2B**).

Following the shaping period, we next recorded photometric signals from the basal forebrain while mice learned to discriminate novel odor pairs. As mice learned new odor pairs, accuracy within a block of 20 trials (calculated as (*Hits* + *Correct Rejects*)/(*Total Trials*)) increased. An odor pair was considered "learned" after two consecutive trial blocks with accuracy > 85% (**Figure 2C**). Once proficient at the task, mice typically learned new odor-reward associations within a single training session of 200–300 trials (Trials to learn $= 104.6 \pm 8.3$, $N = 56$ sessions, 12 animals). Using the timing of IR beam breaks at the odor port and reward port, individual trials of the go/no-go task were segmented into periods before and after trial initiation and, in the case of Hit and False Alarm trials, before and after reward seeking. Aligning trials by initiation times, and separating them by trial type, revealed distinct temporal patterns of cholinergic signaling in each trial (**Figure 2D**). Averaging across trials showed that bidirectional

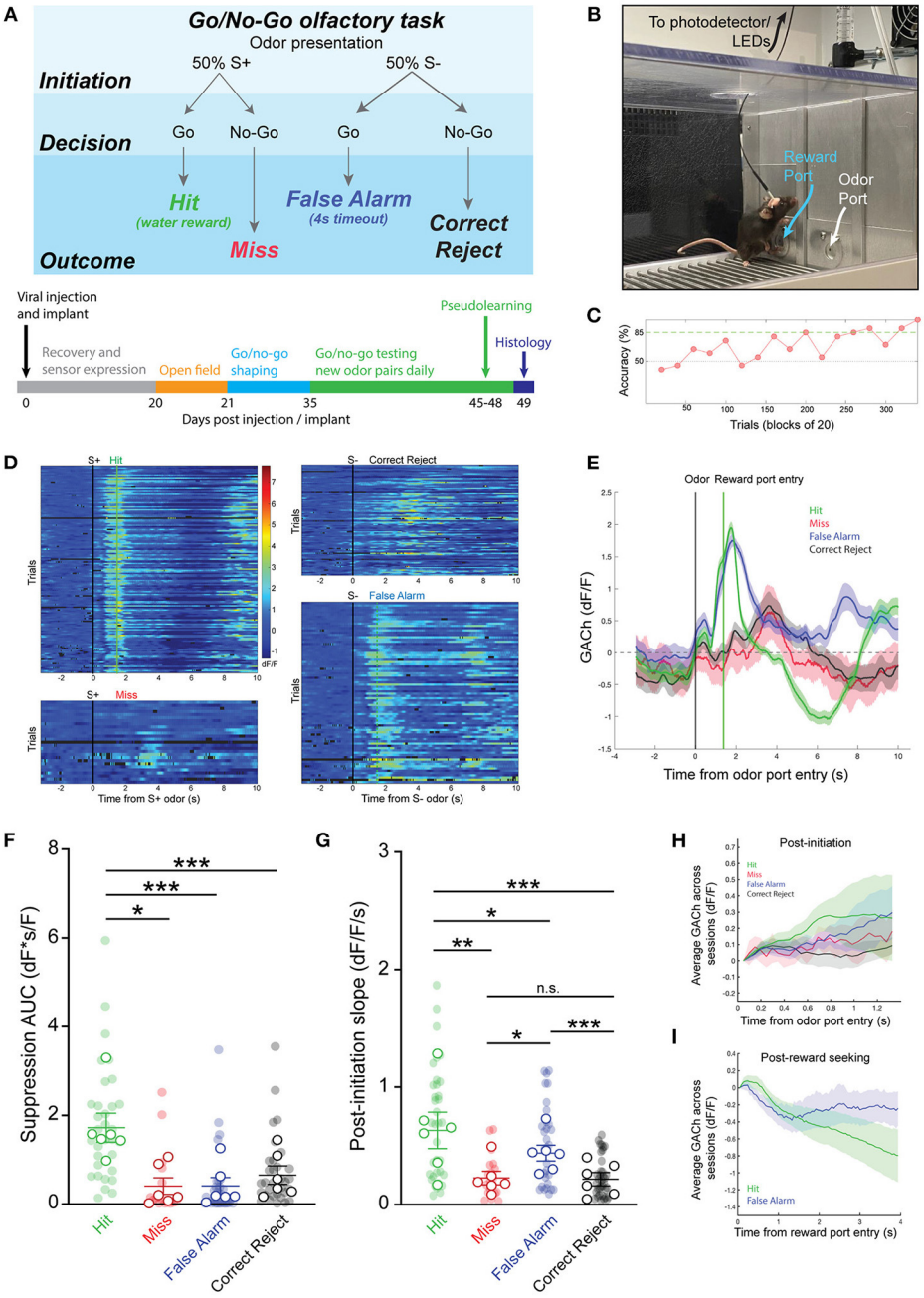

FIGURE 2 | Basal forebrain cholinergic signaling reflects reward-seeking and positive reinforcement in an olfactory-cued go/no-go discrimination task. **(A)** (Top panel) Schematic of olfactory-cued go/no-go discrimination task showing odor presentation, decisions, and possible trial outcomes (Hit, Miss, False Alarm, and Correct Reject). (Bottom panel) Timeline of surgery, recovery, and behavioral shaping and testing with photometry recording. **(B)** Picture of mouse performing go/no-go task during photometric recording. **(C)** Accuracy in blocks of 20 trials for a go/no-go testing session with novel odors highlighting chance (50%) and criteria (85%) levels. Accuracy is from the same session as the trials shown in **(D,E)**. **(D)** Heatmap showing isosbestic-subtracted GACh dF/F from individual trials in a single go/no-go testing session. Trials are aligned by trial initiation time and divided by trial outcome. **(E)** Average GACh dF/F traces for each trial type in the session shown in **(D)**. Shaded areas represent 95% confidence intervals. Black line marks trial initiation time. Green line marks the average reward port entry time in Hit and False Alarm trials. **(F)** Area under the curve of suppression below baseline across trial types and testing sessions. Transparent circles represent individual testing sessions. Hollow circles represent mean values from all sessions completed by individual mice. Lines and error bars show mean ± SEM of means from each animal. $^{*}p < 0.05$, $^{***}p < 0.001$ two-way nested repeated measures ANOVA with Tukey correction for multiple comparisons. **(G)** Slopes of GACh dF/F after trial initiation across trial types and testing sessions. Transparent circles represent individual testing sessions. Hollow circles represent mean values from all sessions completed by individual mice. Lines and error bars show mean ± SEM of means from each animal. $^{*}p < 0.05$, $^{**}p < 0.01$, $^{***}p < 0.001$ two-way nested repeated measures ANOVA with Tukey correction for multiple comparisons. **(H)** Average of mean GACh dF/F traces for across all sessions, separated by trial type, and baseline subtracted at the time of trial initiation. Shaded areas represent 95% confidence intervals. **(I)** Mean GACh dF/F traces for Hit and False alarm trials, averaged across all sessions, aligned to reward port entry time. Shaded areas represent 95% confidence intervals.

changes in HDB cholinergic signaling were consistent within trial types, but distinct across trials (**Figure 2E**).

A notable feature of the signal specific to Hit trials was the suppression of HDB cholinergic tone following reward delivery. The magnitude of the suppression, calculated as the area under the curve (AUC), was significantly larger in Hit trials (1.73 ± 0.33 dF*s/F) compared to Miss trials (0.42 ± 0.18 dF*s/F, $p < 0.05$), False Alarm trials (0.42 ± 0.12 dF*s/F, $p < 0.001$), or Correct Reject trials (0.66 ± 0.21 dF*s/F, $p < 0.001$) across animals and odor-pairs (**Figure 2F**). At the same time, in both Hit and False Alarm trials, HDB acetylcholine rapidly increased leading up to beam breaks at the reward port. Quantifying the slopes of the traces after odor delivery revealed that Hit trials exhibited steeper slopes (0.63 ± 0.12 dF/F/s) than Miss trials (0.23 ± 0.06 dF/F/s, $p < 0.01$), False Alarm trials (0.44 ± 0.07 dF/F/s, $p < 0.05$), and Correct Reject trials (0.22 ± 0.06 dF/F/s, $p < 0.001$). However, slopes in False Alarm trials were also significantly steeper compared to Miss ($p < 0.05$) and Correct Reject trials ($p < 0.001$) (**Figure 2G**). When post-initiation traces for each trial type were averaged across all sessions from every animal, however, the large variability between animals and sessions led to wide confidence intervals (**Figure 2H**). This supported a nested analysis within animals to compare trial types within sessions in a pairwise manner. However, even taking into account the variability in amplitude and timing across animals and sessions, the average traces from Hit and False Alarm trials showed a trend toward steeper slopes compared to the Correct Reject and Miss trials. Finally, to account for variability in the time to seek a reward in Hit and False Alarm trials, we aligned those traces to the reward-port entry times (as opposed to the trial initiation time), and averaged across all animals and sessions (**Figure 2I**). Correct Reject and Miss trials were excluded from this analysis since they did not include a reward port entry. Averaged post-reward seeking traces, with baseline subtracted at the time of reward-port entry, showed initial decreases in both trial types after reward-port entry. However, False Alarm trials quickly returned to baseline while Hit trials were further suppressed. Together, these data revealed increases in basal forebrain cholinergic tone which corresponded to reward seeking behavior in both Hit and False Alarm trials. However, only subsequent reward delivery in Hit trials led to a large, slow suppression of HDB cholinergic tone.

Reward-Seeking and Reinforcement Linked Patterns of HDB Cholinergic Signaling Are Independent of Learning

We next questioned whether patterns of cholinergic signaling in the HDB changed over the course of new odor-reward association learning. To determine this, we selected experiments with slower rates of learning, in which at least 3 blocks were performed with < 70% success, but criteria for learning were eventually met within 300 trials ($N = 16$ sessions, 5 animals). This paradigm allowed us to compare, within a testing session, cholinergic signaling from pre-learning blocks (blocks with < 70% accuracy), to responses after an odor association had been effectively learned (first two consecutive blocks and subsequent blocks > 85% accuracy) (**Figure 3A**). Comparing pre-learning vs. learned blocks revealed similar patterns of cholinergic signaling in the HDB during both reward seeking and after reward delivery in both Hit and False Alarm trials (**Figure 3B**). In agreement with the data from whole sessions (**Figure 2**), we found that the magnitude of the reward-related suppression in learned blocks was larger in Hit (1.60 ± 0.54 dF*s/F) than in False Alarm trials (0.57 ± 0.36 dF*s/F, $p < 0.05$). However, there was no difference in the magnitude of the reward-related suppression between pre-learning (Hit $= 1.48 \pm 0.42$ dF*s/F, False Alarm $= 0.47 \pm 0.20$ dF*s/F) compared to learned blocks in either Hit ($p = 0.96$) or False Alarm trials ($p = 0.99$) (**Figure 3C**). Additionally, across animals and odor pairs, the slope of the cholinergic signal after odor presentation was the same between pre-learning (Hit $= 1.31 \pm 0.32$ dF/F/s, False Alarm $= 0.90 \pm 0.17$ dF/F/s) and learned blocks (Hit $= 1.41 \pm 0.40$ dF/F/s, False Alarm $= 0.81 \pm 0.19$ dF/F/s) for both Hit ($p = 0.84$) and False Alarm trials ($p = 0.89$) (**Figure 3D**). These data suggest that HDB cholinergic signaling increases during reward seeking behavior and decreases with reward delivery, regardless of whether the odor-reward association has been effectively learned. These data, however, do not address whether patterns of HDB cholinergic signaling drive the formation of an odor-reward association, or depend on the context of an odor reward association.

Reward Related Suppression of HDB Cholinergic Signaling Is Task Dependent and Relies on Association Between Odor Cue and Reward

We next sought to determine whether patterns of basal forebrain cholinergic signaling were influenced by the context of the olfactory task, including the requirement for odor discrimination and the reliable association between odor and reward. An alternative possibility was that the observed pattern in HDB cholinergic signaling may simply reflect reward seeking and consumption behaviors, independent of odor discrimination or odor-reward association. While task dependence would suggest that HDB cholinergic signaling is involved in top-down regulation, the latter possibility would suggest that HDB cholinergic signaling responds to bottom-up cues. To distinguish between these possibilities, we recorded basal forebrain cholinergic signals during a version of the go/no-go task, in which there was no association between the odor presented and the availability of the reward (pseudo-learning, $N = 10$ sessions, 4 animals). In the pseudo-learning paradigm, S+ and S– odors were each presented 50% of the time, and a water reward was available on 50% of the trials at random (**Figure 4A**). This version of the task retains odor presentations, odor detection, reward seeking, and reward delivery, removing only the odor-reward association and the need for odor discrimination. Importantly, this also uncouples expectation from odor-evoked responses. During pseudo-learning, mice typically obtained ∼50% success rate with a mix of trial types biased toward positive, reward-seeking responses (Pseudo FA

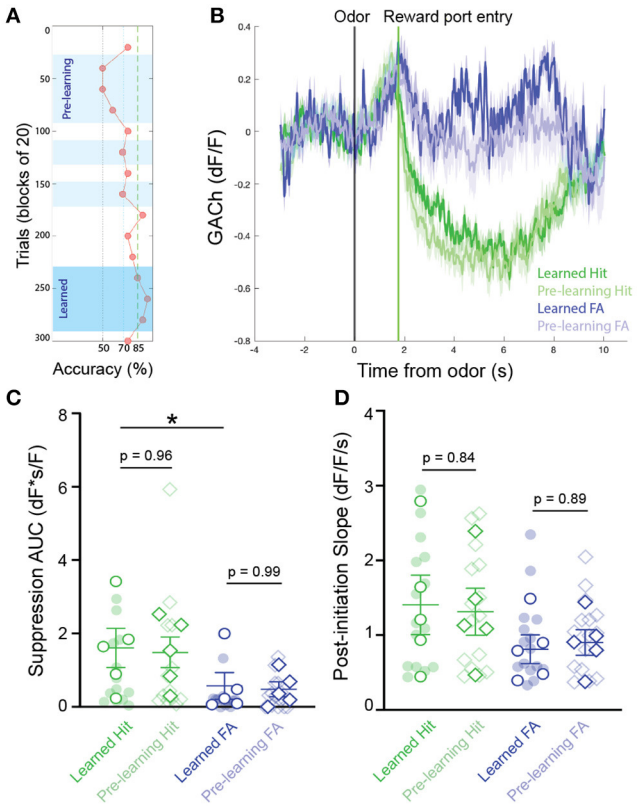

FIGURE 3 | Temporal profile of cholinergic signaling in the HDB does not change with within-session discrimination learning. **(A)** Accuracy in blocks of 20 trials for a go/no-go testing session highlighting blocks analyzed as "pre-learning" (light blue shading) and "learned" (dark blue shading). **(B)** Average GACh dF/F traces for Hit and False Alarm trials separated into pre-learning and learned trials. Shaded areas represent 95% confidence intervals. Black line marks trial initiation time. Green line marks the average reward port entry time. **(C)** Area under the curve of suppression below baseline across trial types in pre-learning and learned blocks. Transparent circles and diamonds represent individual testing sessions. Hollow opaque circles and diamonds represent mean values from all sessions completed by individual mice. Lines and error bars show mean ± SEM of means from each animal. *$p < 0.05$, two-way nested repeated measures ANOVA with Tukey correction for multiple comparisons. **(D)** Slopes of GACh dF/F after trial initiation across trial types in pre-learning and learned blocks. Transparent circles and diamonds represent individual testing sessions. Hollow opaque circles and diamonds represent mean values from all sessions completed by individual mice. Lines and error bars show mean ± SEM of means from each animal. Two-way nested repeated measures ANOVA with Tukey correction for multiple comparisons.

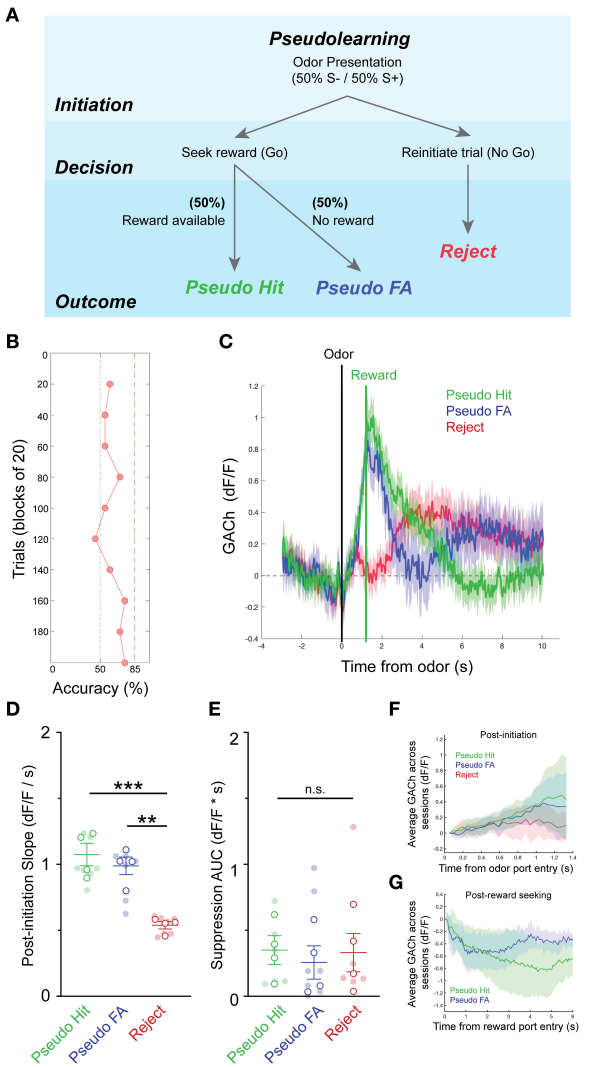

FIGURE 4 | Pseudo-learning reveals task-dependence of dynamic basal forebrain cholinergic tone. **(A)** Schematic of olfactory-cued go/no-go pseudo-learning task showing odor presentation, decisions, and possible trial outcomes (Pseudo-Hit, Pseudo-False Alarm, Reject). **(B)** Accuracy in blocks of 20 trials for a pseudo-learning testing session showing performance near chance. **(C)** Average GACh dF/F traces for Pseudo-Hit, Pseudo-False Alarm and Reject trials. Shaded areas represent 95% confidence intervals. Black line marks trial initiation time. Green line marks the average reward port entry time in reward-seeking trials. **(D)** Slopes of GACh dF/F after trial initiation across trial types and testing sessions. Transparent circles represent individual testing sessions. Hollow circles represent mean values from all sessions completed by individual mice. Lines and error bars show mean ± SEM of means from each animal. **$p < 0.01$, *** $p < 0.001$, two-way nested repeated measures ANOVA with Tukey correction for multiple comparisons. **(E)** Area under the curve of suppression below baseline across trial types and testing sessions. Transparent circles represent individual testing sessions. Hollow circles represent mean values from all sessions completed by individual mice. Lines and error bars show mean ± SEM of means from each animal. Two-way nested repeated measures ANOVA with Tukey correction for multiple comparisons. **(F)** Average of mean GACh dF/F traces for across all sessions, separated by trial type, and baseline subtracted at the time of trial initiation. Shaded areas represent 95% confidence intervals. **(G)** Mean GACh dF/F traces for Hit and False alarm trials, averaged across all sessions, aligned to reward port entry time. Shaded areas represent 95% confidence intervals.

and Pseudo Hit trials), and against negative (Reject) responses (**Figure 4B**).

Averaging across trials of the pseudo-learning task showed similar patterns of basal forebrain cholinergic signaling between Pseudo-Hit and Pseudo-FA trials, both of which differed from Reject trials (**Figure 4C**). In both Pseudo-Hits and Pseudo-FA trials, cholinergic signaling increased after odor presentation as mice seek rewards. This was reflected in significantly shallower slopes after trial initiation for Reject trials (0.54 ± 0.03 dF/F/s), compared to Pseudo-Hit trials (1.07 ± 0.09 dF/F/s, $p < 0.001$),

and Pseudo-FA trials (0.99 ± 0.07 dF/F/s, $p < 0.01$) (**Figure 4D**), suggesting that increased HDB acetylcholine reflects reward seeking behavior independent of an odor-reward association. Strikingly, however, we did not observe a slow suppression in cholinergic tone following reward delivery in Pseudo-Hit trials. The total magnitude of suppression was not larger in Pseudo-Hit trials (0.35 ± 0.12 dF*s/F) compared to Pseudo-FA (0.26 ± 0.13 dF*s/F, $p = 0.96$) or Reject trials (0.33 ± 0.15 dF*s/F, $p = 0.98$) (**Figure 4E**). Averaging across all sessions and animals revealed a trend toward a steadily increasing slope in Hit and False Alarm trials, while Reject trials flattened (**Figure 4F**). Aligning the False Alarm and Hit trials to the reward port entries revealed an initial decrease in traces from both trial types, though neither trial type showed strong prolonged suppression (**Figure 4G**). Together, these data indicate that the reward-related suppression of basal forebrain cholinergic tone does not merely reflect reward delivery or reward consumption. Rather, the suppression depends on the task context and requires an association between odor and reward. This suggests that anticipation of an available reward linked to an odor presentation is an important driver of the post-reward suppression.

HDB GABAergic Neuronal Activity Mirrors Cholinergic Tone in Response to Positive Reinforcement

Having revealed dynamic cholinergic signaling in the HDB during olfactory-guided behavior, we next examined a potential target of local cholinergic signaling. Basal forebrain GABAergic neurons express both metabotropic and nicotinic acetylcholine receptors, and have been shown to respond to local cholinergic signaling (Yang et al., 2014; Xu et al., 2015). We hypothesized that HDB GABAergic neuronal activity would be controlled, in part, by local cholinergic signaling and that GABAergic neuronal activity would follow a similar pattern of activation and suppression across phases of go/no-go task performance. To test this, we selectively expressed GCaMP in HDB GABAergic neurons by injecting an AAV encoding cre-dependent GCaMP6M (AAV flex-GCaMP6M) into Vgat-Cre mice (**Figure 5A**). We then recorded GABAergic neuronal activity via fiber photometry during performance of the go/no-go task. After behavioral shaping, new odor learning was accomplished within sessions of 200–300 trials (**Figure 5B**). Aligning individual trials by trial initiation time revealed bidirectional modulation of GABAergic neuronal activity with excitation following odor deliver and suppression following reward delivery in Hit trials (**Figures 5C,D**). Similar to the changes we observed in cholinergic tone, HDB GABAergic neuronal activity was reliably suppressed following reward delivery. Areas under the curve of the suppression below baseline were significantly larger in Hit trials (8.36 ± 1.25 dF*s/F) than in False Alarm (1.69 ± 0.48 dF*s/F, $p < 0.001$), Correct Reject (0.85 ± 0.30 dF*s/F, $p < 0.001$), or Miss trials (1.72 ± 0.94 dF*s/F, $p < 0.001$) (**Figure 5E**). In contrast to changes in cholinergic tone, however, HDB GABAergic neurons responded to both the S+ and S– odors. This was reflected in positive slopes of the GCaMP signal following trial initiation in Hit (1.67 ± 0.33 dF/F/s, $p < 0.05$), Miss (1.61 ± 0.26 dF/F/s, $p < 0.01$), False Alarm (1.64 ± 0.32 dF/F/s, $p < 0.05$), and Correct Reject trials (1.33 ± 0.24 dF/F/s, $p = < 0.05$) (**Figure 5F**). Additionally, slopes from different trial types were not significantly different from each other ($p = 0.34$). Even with large variability, comparing post-initiation traces for the four trial types, averaged across sessions and animals, further showed a ubiquitous and rapid GABAergic response to both S+ and S– odors (**Figure 5G**). This consistent response to both the S+ and S– odors implied that basal forebrain GABAergic neurons receive bottom-up olfactory information, and that their activity may reflect odor detection or active sensing. Finally, in contrast to the cholinergic signal, aligning False Alarm and Hit trials to reward port entries revealed no initial decrease in False Alarm trials, but a large and sustained suppression in Hit trials (**Figure 5H**). Together these data raise the intriguing possibility that HDB acetylcholine levels decrease in anticipation of a reward, while HDB GABAergic neuronal activity is suppressed by the reinforcement itself.

DISCUSSION

Sensory perception relies on a combination of bottom-up sensory input, and top-down behavioral state-dependent regulation. The basal forebrain serves as a key mediator of top-down regulation related to the behavioral states of attention, arousal, and wakefulness (Muir et al., 1993; Voytko et al., 1994; Szymusiak, 1995; Sarter and Bruno, 1999; Hasselmo and McGaughy, 2004; Herrero et al., 2008; Goard and Dan, 2009; Anaclet et al., 2015; Kim et al., 2015; Zant et al., 2016). Many of these effects are thought to be mediated by cholinergic signaling at downstream sensory circuits. Supporting this, in olfactory, visual, and auditory circuits, cholinergic neuromodulation has been shown to increase gain, improve signal to noise ratios, increase pattern separation, and increase the weight of bottom-up sensory input (Mandairon et al., 2006; Herrero et al., 2008; Chaudhury et al., 2009; Ghatpande and Gelperin, 2009; Goard and Dan, 2009; Ma and Luo, 2012; Chapuis and Wilson, 2013; Zhan et al., 2013; Rothermel et al., 2014). However, mounting evidence suggests that parallel GABAergic outputs from the basal forebrain also play a significant role sculpting downstream circuit activity (Nunez-Parra et al., 2013, 2020; Kim et al., 2015; Xu et al., 2015; Böhm et al., 2020; Villar et al., 2020).

In olfaction, input from the basal forebrain significantly impacts the earliest stages of signal transduction in the olfactory bulb. Separately, the cholinergic, and GABAergic projection pathways from the HDB drive distinct changes in olfactory bulb neuronal activity. For example, GABAergic projections from the HDB synapse onto inhibitory granule cells and periglomerular interneurons in the olfactory bulb where they mediate disinhibition and desynchronization of Mitral Cell firing bulb (Gracia-Llanes et al., 2010; Sanz Diez et al., 2019; Villar et al., 2020). Moreover, experiments implementing chemogenetic inhibition showed that basal forebrain GABAergic projections are required for effective odor discrimination (Nunez-Parra et al., 2020). On the other hand, other experiments have revealed that basal forebrain cholinergic projections to the olfactory

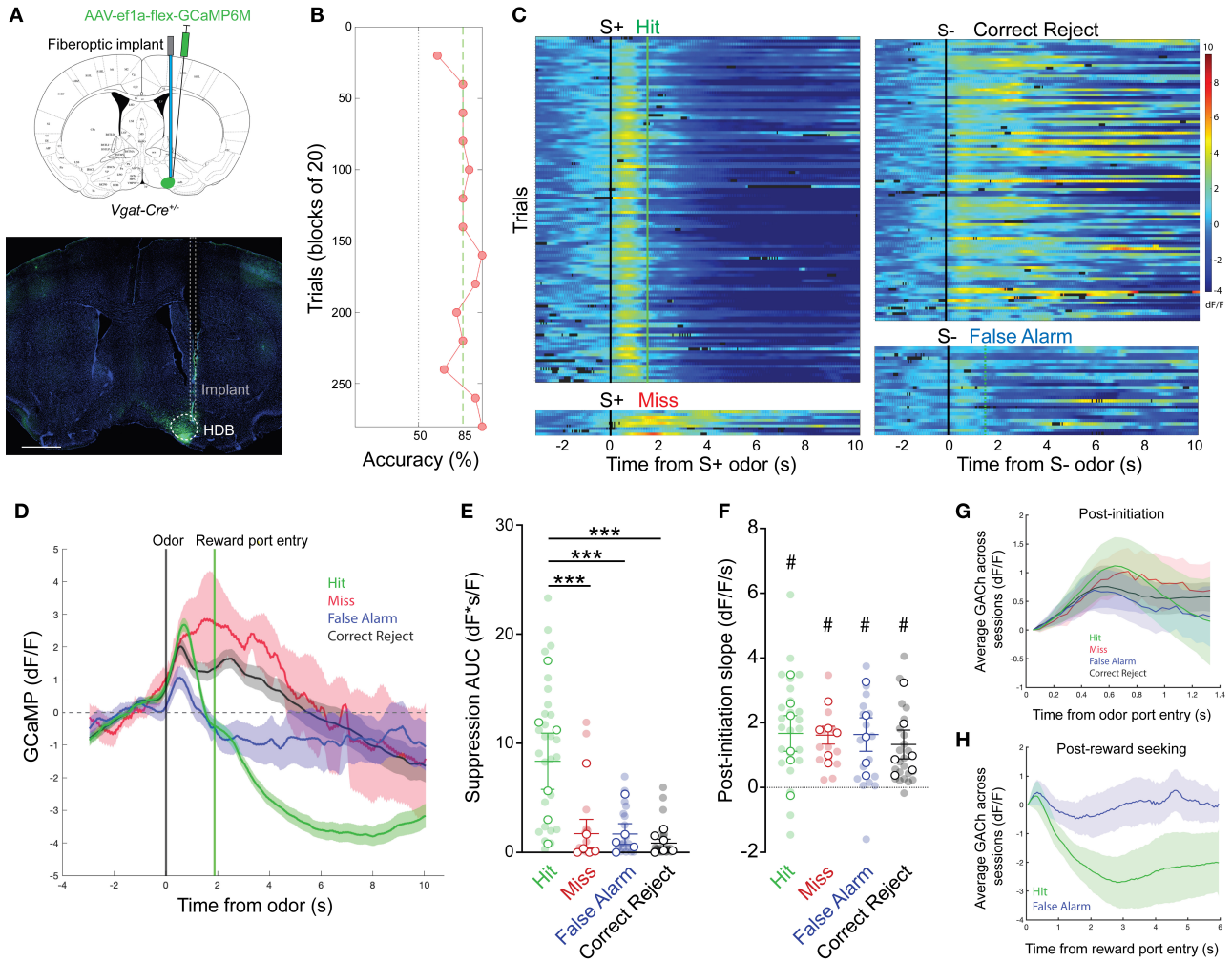

FIGURE 5 | HDB GABAergic neuronal activity mirrors cholinergic tone in response to positive reinforcement. **(A)** (Top panel) Coronal section schematic showing AAV injection and implant targeting the HDB. (Bottom panel) IHC of a coronal section showing GCaMP6M expression and implant targeting in the HDB. Scale bar = 1 mm. **(B)** Accuracy in blocks of 20 trials for a go/no-go testing session with novel odors highlighting chance (50%) and criteria (85%) levels. Accuracy is from the same session as the trials shown in **(D,E)**. **(D,C)** Heatmap showing isosbestic-subtracted GCaMP dF/F from individual trials in a single go/no-go testing session. Trials are aligned by trial initiation time and divided by trial outcome. **(D)** Average GCaMP dF/F traces for each trial type in the session shown in **(C)**. Shaded areas represent 95% confidence intervals. Black line marks trial initiation time. Green line marks the average reward port entry time in Hit and False Alarm trials. **(E)** Area under the curve of suppression below baseline across trial types and testing sessions. Transparent circles represent individual testing sessions. Hollow circles represent mean values from all sessions completed by individual mice. Lines and error bars show mean ± SEM of means from each animal. $^{***}p < 0.001$ two-way nested repeated measures ANOVA with Tukey correction for multiple comparisons. **(F)** Slopes of GCaMP dF/F after trial initiation across trial types and testing sessions. Transparent circles represent individual testing sessions. Hollow circles represent mean values from all sessions completed by individual mice. $\#p < 0.05$, nested one sample *t*-test comparing trial type values to 0. Two-way nested repeated measures ANOVA with Tukey correction for multiple comparisons shows $p = 0.36$ for differences between trial types. **(G)** Average of mean GCaMP dF/F traces for across all sessions, separated by trial type, and baseline subtracted at the time of trial initiation. Shaded areas represent 95% confidence intervals. **(H)** Mean GCaMP dF/F traces for Hit and False alarm trials, averaged across all sessions, aligned to reward port entry time. Shaded areas represent 95% confidence intervals.

bulb increase excitability, modulate signal to noise ratios in mitral cell firing, and can rapidly dishabituate olfactory bulb odor responses (Ma and Luo, 2012; Rothermel et al., 2014; Ogg et al., 2018). Finally, more recent studies have directly compared optogenetic stimulation of basal forebrain cholinergic and GABAergic terminals within the olfactory bulb (Böhm et al., 2020), describing that local stimulation of cholinergic terminals increased mitral cell firing during sniffing regardless of odor presentation, whereas stimulation of GABAergic terminals decreased spontaneous mitral cell firing and increased firing during sniffing only when odors were presented. Together, these findings imply that basal forebrain cholinergic and GABAergic neurons mediate distinct features of top-down regulation, and that both types of basal forebrain projections modulate olfactory bulb odor and sniff responses.

Importantly, cholinergic and GABAergic neurons in the basal forebrain work together to modulate downstream circuit function (Dannenberg et al., 2015; Böhm et al., 2020). An

outstanding question is how parallel cholinergic and GABAergic output pathways are coordinated during behavior at the level of the basal forebrain. In the current study, we show that cholinergic signaling within the basal forebrain is dynamically regulated during olfactory-guided behavior. We also show that distinct changes in basal forebrain cholinergic tone correspond to changes in neighboring GABAergic neuronal activity. These results raise the possibility that cholinergic signaling within the basal forebrain dynamically impacts basal forebrain output pathways, potentially relaying behavioral state information from the basal forebrain to the olfactory system.

Bidirectional Changes in Basal Forebrain Cholinergic Tone During Olfactory Task Performance

Though basal forebrain neuronal activity has been characterized across a variety of behavioral states and in a number of sensory discrimination and association learning tasks (Mandairon and Linster, 2009; Devore et al., 2015; Hangya et al., 2015; Xu et al., 2015; Harrison et al., 2016; Nunez-Parra et al., 2020), how this activity is regulated by local signaling within the basal forebrain remains largely unknown. To investigate local cholinergic signaling within the basal forebrain we used a GPCR Activation-Based sensor for acetylcholine (Jing et al., 2018) combined with fiber photometry. This approach allowed us to record changes in acetylcholine from the basal forebrain with sub-second temporal resolution, in freely behaving animals.

With this approach we were able to record rapid changes in cholinergic tone from the HDB during free exploration of an open field arena, and during olfactory-cued operant behavior. Basal forebrain neuronal activity has been previously correlated with locomotion and slow changes in arousal (Sarter and Bruno, 1999; Goard and Dan, 2009; Xu et al., 2015). However, while we observed frequent spontaneous activation and suppression signaling events during exploration, significant changes in GACh fluorescence were not correlated with locomotion. This highlights an interesting discrepancy between cholinergic neuron activity and the local cholinergic signaling itself. Our data indicate that basal forebrain acetylcholine changes on a rapid timescale, which was not solely reflective of slow changes in behavioral state. Instead, changes in basal forebrain cholinergic tone were temporally precise based on behavioral action. This raises the possibility that changes in HDB cholinergic tone reflect rapid changes in behavioral states that align with complex olfactory-guided behavior.

To examine cholinergic signaling dynamics during complex olfactory guided behavior, we tested mice on a freely moving, olfactory-cued go/no-go discrimination task. The task included self-initiation of trials, followed by periods of active sensing, odor detection, discrimination, reward-seeking, and positive/negative reinforcement. We hypothesized that cholinergic signaling would be dynamically regulated within trials of the go/no-go task, reflecting changing needs for basal forebrain mediated top-down regulation during different behaviors, and in response to reinforcement. Supporting this hypothesis, we observed rapid, bidirectional changes in acetylcholine that were time-locked to phases of the go/no-go task. Specifically, we found that acetylcholine increased rapidly in the basal forebrain during reward-seeking behavior. Once the availability of a reward was ascertained, acetylcholine responses decreased rapidly. Finally, if a reward was successfully obtained, acetylcholine decreased slowly, but transiently, below baseline levels. Recent studies reported decreased activity in a subset of basal forebrain neurons following both stimulus presentation and reward delivery (Nunez-Parra et al., 2020). However, in a small population of identified cholinergic neurons, no reliable changes in firing rate were detected with reward delivery. This discrepancy may further suggest a disconnect between neuronal activity and local cholinergic tone. Alternatively, these data may reflect differences in the task requirements between a freely moving task and previously described head-fixed experiments (Nunez-Parra et al., 2020). Ultimately, the complex cholinergic signaling dynamics that we observed suggest that local cholinergic signaling corresponds to distinct features of the go/no-go task, perhaps reflecting reward-seeking behavior and subsequent reward delivery. The reward-related suppression of cholinergic signaling in Hit trials was particularly interesting given the implication that a baseline cholinergic tone in the basal forebrain is selectively suppressed in response to positive feedback.

Task-Dependent and Learning-Independent Patterns of Cholinergic Signaling in the Basal Forebrain

These observations led us to question whether cholinergic signaling dynamics in the basal forebrain were (1) a driver of odor-reward association learning, (2) a consequence of association learning, or (3) independent of odor-reward association, and instead linked to the performance of task-related behaviors. To directly investigate these possibilities, we examined cholinergic signaling dynamics over the course of odor-reward association learning, and in the absence of odor-reward associations. If task-linked cholinergic signaling dynamics are a consequence of odor-reward association learning, we might have expected temporal profiles of cholinergic signaling to change over the course of single sessions, where new odor-reward associations are being learned. For example, reward expectation scales with increasing success over a go/no-go session as new odor-reward associations are effectively learned (Tremblay et al., 1998). Thus, if increased cholinergic signaling in the basal forebrain reflects reward expectation, we would expect reporter responses to change over the course of learning within sessions. Indeed, a recent study recording neuronal activity in the basal forebrain found that a higher percentage of cholinergic and non-cholinergic neurons changed their firing rates in response to an odor cue after an odor-reward association was learned in a go/no-go task (Nunez-Parra et al., 2020). However, examining cholinergic tone directly, we find that changes in acetylcholine during go/no-go trials are stable over the course of odor-reward association learning. Neither increased acetylcholine during reward-seeking, nor suppressed acetylcholine following reward delivery, change over the course of a learning session.

Intriguingly, rapid changes in basal forebrain cholinergic tone during reward seeking did not reflect the strength of reward expectation. Such stability of basal forebrain cholinergic signaling over the course go/no-go testing sessions suggests that acetylcholine release within the basal forebrain is either an upstream driver of learning—relating specific perceptual decisions to positive and negative outcomes—or it may be all together independent of odor-reward associations—reflecting only reward-seeking and reward-consumption behaviors.

To distinguish between these possibilities, we examined cholinergic signaling during pseudo-learning, a version of the go/no-go task in which rewards were randomly available 50% of the time, regardless of the odor presented. Pseudo-learning preserves odor detection (the animals can only seek a reward after receiving an odor presentation), reward seeking, and reward delivery, but removes the association between odor and reward. If basal forebrain cholinergic signaling is simply a reflection of behavioral responses (i.e., reward seeking and consumption) rather than changing behavioral states (i.e., expectation, attention, surprise, etc.), we would have expected to observe the same stable patterns of cholinergic signaling with reward-seeking and reward delivery that we observed in the go/no-go discrimination task. Alternatively, if basal forebrain cholinergic signaling serves a role in relating the odor-discrimination context of the task to reward seeking behavioral choices or positive reinforcement outcomes, we would expect to observe differences in the patten of HDB cholinergic signaling when the rules of the task are changed. Indeed, in the pseudo-learning task, removing the cue-reward association led to a decrease in the reward-related suppression of basal forebrain cholinergic tone. However, increased cholinergic tone during reward seeking behavior occurred regardless of odor-reward association. Surprisingly, patterns of basal forebrain cholinergic signaling were stable over the course of pseudo-learning sessions. It's possible that this was because mice quickly realized that the context of the task had changed and rapidly altered their strategy to fit the new rules of the pseudo-learning task. If so, the reward-related suppression of cholinergic signaling may not only reflect reward delivery but also take into account knowledge of the task itself.

Odor Evoked Activity and Reward Related Suppression of Basal Forebrain GABAergic Neurons During Olfactory Task Performance

GABAergic neurons in the HDB express cholinergic receptors and respond to local acetylcholine release (Yang et al., 2014; Xu et al., 2015). At the same time, GABAergic output from the HDB mediates distinct forms of top-down regulation important for state-dependent active sensing and odor discrimination (Nunez-Parra et al., 2013; Böhm et al., 2020). Having found that local cholinergic tone is dynamically regulated during performance of an olfactory-cued go/no-go task, we next examined whether changes in local cholinergic tone corresponded to changes in basal forebrain GABAergic neuronal activity. We reasoned that if HDB GABAergic neuronal activity is dynamically controlled by local cholinergic signaling, we might expect to observe correlations between temporal profiles of GABAergic neuronal activity and cholinergic tone during olfactory discrimination tasks. However, in contrast to the observed cholinergic signaling patterns, we observed GABAergic responses to both the S+ and S– odors across all trial types, regardless of reward seeking behavior. Intriguingly, recent studies report that stimulating GABAergic projections to the olfactory bulb enhanced sniff-locked odor responses from a subset of mitral cells, while suppressing spontaneous activity (Böhm et al., 2020). Inhibiting these projections, on the other hand, reduced odor discrimination (Nunez-Parra et al., 2013). In this context, our data show that HDB GABAergic neurons respond broadly during odor discrimination, and they suggest that they may mediate enhanced odor discrimination during active sniffing.

At the same time, we observed similar changes in cholinergic tone and GABAergic neuronal activity in response to positive reinforcement. Both GABAergic neuronal activity and cholinergic tone were suppressed following reward delivery in Hit trials. Suppression below baseline implies that a population of GABAergic neurons in the basal forebrain are tonically active. Notably, tonic and rhythmic neuronal firing has been observed in basal forebrain, and is strongly dependent on behavioral state (Nunez, 1996; Détári et al., 1999; Szymusiak et al., 2000). The similarity between the suppression of basal forebrain GABAergic neuronal activity and local cholinergic signaling following reward delivery suggests that activity of basal forebrain GABAergic neurons is influenced by local cholinergic tone. Importantly however, our data do not distinguish whether basal forebrain GABAergic neurons are a target of tonic excitement from local acetylcholine. Indeed, other studies have reported that cholinergic collateralization within the basal forebrain directly activates local non-cholinergic and/or GABAergic neurons (Yang et al., 2014; Dannenberg et al., 2015; Xu et al., 2015; Nunez-Parra et al., 2020). In this context, our data raise the possibility that higher ambient cholinergic tone and increased tonic activity of basal forebrain GABAergic neurons in awake states create an environment where such signals can be bidirectionally modulated to solidify learned cue-reward associations.

Here we have revealed rapid, bidirectional changes in cholinergic tone within the basal forebrain during complex, olfactory-guided behavior. Characterization of the cholinergic signal itself through visualization of the GACh reporter signal is a first step toward understanding how cholinergic drive influences basal forebrain circuitry, and thus, top-down regulation of sensory processing. Future work will be needed to determine the mechanistic impact of dynamic cholinergic tone on specific HDB projection neuron populations. The current data, however, support the idea that cholinergic tone changes rapidly in the basal forebrain during olfactory-guided behavior, making local cholinergic signaling an intriguing candidate for coordinating fast state-dependent effects on HDB circuits and projection outputs.

MATERIALS AND METHODS

Animals

Mice were maintained on a 12 h light-dark cycle and were treated in compliance with the US Department of Health

and Human Services and Baylor College of Medicine IACUC guidelines. C56Bl6/J and Vgat-cre mice underwent surgery at 2–4 months old. Equal numbers of male and female mice were included in each experiment. Vgat-Cre (*Slc32a1*tm2(cre) Lowl, Stock: 028862) mice were originally purchased from Jackson Laboratories.

Surgical Procedures

Mice were anesthetized with 4% isoflurane in O2 and maintained under anesthesia with 1–2% isoflurane in O_2. Craniotomies were made over the sites of stereotaxic injections and fiberoptic implants that were guided by Angle Two software (Leica) normalized to Bregma. To target viral expression to the HDB, a unilateral injection of virus was made into the left HDB (from Bregma: ML −1.0 mm, AP 0.1 mm, DV −5.45 mm). Viruses were packaged in-house and included AAV-hsyn-GACh2.0, Serotype DJ8 injected into C57Bl6/J (WT) mice and AAV-ef1α-flex-GCaMP6M, Serotype DJ8, injected into Vgat-cre mice. The plasmid containing GACh2.0 was a generous gift from the Yulong Li Lab (Jing et al., 2018). Two hundred and fifty Nanoliters of virus was injected into the HDB over 10 min. Following viral injection, the injection needle was removed and a custom fiber optic implant (0.48 na, 200 um core diameter, RWD systems) was lowered to a target 0.1 mm dorsal to the injection target. The implant was then fixed in place with Metabond dental cement (Parkell). Mice were allowed to recover for 3 weeks before behavioral experiments. HDB targeting was verified in all cases with immunofluorescence imaging of the implant track and viral expression within the HDB.

TABLE 1 | Monomolecular odors used in go/no-go shaping and testing.

Odorant	*Molar Mass (g/mol)*	*Vapor Pressure (mmHg)*	*Functional Group*
(–) Carvone	150.22	0.16	Cyclic ketone, 10C, 1 double bond
(+) Carvone	150.22	0.16	Cyclic ketone, 10C, 1 double bond
1-Butanol	74.12	7	Straight chain alcohol, 4C
1-heptanol	116.2	0.2163	Straight chain alcohol, 7C
1-Hexanol	102.18	1	Straight chain alcohol, 6C
1-Pentanol	88.15	44.6	Straight chain alcohol, 5C
Acetophenone	120.15	0.397	Aromatic ketone
alpha-Pinene	136.24	3	Cyclic, 7C, 1 double bond
Citral	152.24	0.22	Aldehyde, 10C
Ethyl Acetate	88.11	93.2	Ester, 4C
Eucalyptol	154.249	1.9	Cyclic ether, monoterpinoid
Eugenol	164.2	0.0221	Aromatic alcohol, ether
Isoamyl acetate	130.19	4	Ester, 7C
(–) Limonene	150.22	0.16	Cyclic monoterpene, 10C, 2 double bonds
(+) Limonene	150.22	0.16	Cyclic monoterpene, 10C, 2 double bonds
Menthone	154	0.895	Cyclic ketone, 10C, no double bonds
Methyl Acetate	74.08	173	Ester, 3C
Methyl Salicylate	152.15	0.0343	Aromatic alcohol, ester

Go/No-Go Behavior

Prior to photometric recording, mice underwent behavioral shaping, allowing them to learn the mechanics of the go/no-go task. Mice progressed through 5 behavioral shaping stages over the course of 10–14 days as described previously (Quast et al., 2016; Liu et al., 2017). Briefly, mice were water-restricted to no < 85% of their baseline weight for 2 d before shaping. Water was restricted to 40 mL per kg, per day during the restriction period. Mice trained using a go/no-go paradigm in a behavioral chamber with infrared nose pokes (Med Associates Inc.). All mice were first trained to poke their nose into the odor port for at least 300 ms, before moving to the side water port to retrieve water reward within 5 s (**Figure 2**). Water rewards were dispensed at an average volume of 5.0 with a standard deviation of 0.56 μL per Hit trial. After preliminary training sessions (∼30–60 min/d for ∼5–6 d) mice were trained to respond to the S+ odor cue (1% Eugenol in mineral oil) by moving to the water port for a reward and were trained to respond to the S– odor (1% Methylsalicylate in mineral oil) by refraining from poking into the reward port and, instead, initiating a new trial. We required mice to sample odors for at least 100 ms before responding and to respond within 5 s after trial initiation. False alarms (incorrect response to S– odor) caused a 4 s timeout punishment. S+ and S– stimuli (**Table 1**) were presented to the mice in random sequences during training. Mice were trained for 20 trials per block and ∼10–15 blocks per day. Throughout shaping and testing accuracy was calculated by block of 20 trials. Odors pairs were considered "learned" after two consecutive blocks > 85% accuracy (calculated as (*Hits* + *Correct Rejects*)/(*Total Trials*)). After 3–6 d of odor training, the mice performed at over 85% correct responses. Mice were then tested on new odors (**Table 1**) diluted to 1% in mineral oil during photometric recording. For pseudo learning (**Figure 4**), S+ and S– odors were presented randomly, each 50% of the time, as in the go/no-go discrimination task. Reward availability was also randomly determined with rewards available upon reward-port entry 50% of the time.

Photometry

To allow stimulation and recording of fluorescent transients through the same fiberoptic implant, we utilized a fiber photometry system from Doric lenses. Two light emitting diodes (465 and 405 nm wavelength) were coupled to a filter cube by 0.48 na, 400 um core diameter fiber optic cables. The filter cube separated excitation and emission wavelengths, directing the excitation wavelengths along a 0.48 na, 200 um core diameter fiber optic toward the mouse through a rotary connector attached to the behavior box. Emission wavelengths were carried from the mouse to the filter cube along the same fiber, then directed to a femtowatt photodetector (Newport) through a 0.48 na, 600 um core diameter fiber optic cable. Excitation and emission were controlled and recorded, respectively, in Doric Studio software. Both GACh2.0 and GCaMP6M were excited at 465 to record either acetylcholine (for GACh2.0) or calcium binding

(for GCaMP). Additionally, excitation at the isosbestic point for GCaMP (405 nm) generates emission which is insensitive to calcium binding. Thus, a photometric recording of GCaMP with excitation at 405 nm is a useful control for motion artifacts and other calcium-independent noise. For GACh2.0, the isosbestic point is near 405 allowing it to serve as a control signal in a similar manner. To record from the control channel (excited at 405 nm) and the experimental channel (excited at 465 nm) simultaneously, we employed a "locked-in" strategy where each LED was modulated at a different high frequency. Emission resulting from both modes of excitation was recorded by the same photodetector and the signal was demodulated online in Doric Studio to separate the control channel form the experimental channel. Both signals were then converted to df/f and the control channel was subtracted from the experimental channel to reduce noise.

Histology

For immunohistochemistry, mice were deeply anesthetized then transcardially perfused with PBS followed by 4% PFA. Brains were removed and immersion fixed in 4% PFA overnight at 4°C. Brains were transferred to 30% sucrose and allowed to equilibrate, then they were frozen and sectioned at 40 μm on a cryostat (Leica). The sections were washed in 0.3% PBS-T, then incubated in a blocking solution composed of 10% normal goat serum, 0.3% PBS-T, and 3M glycine for 1 h at room temperature or overnight at 4°C. Following blocking, slices were incubated in chicken ∞ GFP primary antibody (1:1,000, Abcam, ab13970) diluted in blocking buffer overnight at 4°C. The next day slices were washed 3× in 0.3% PBS-T then incubated in Goat ∞ Chicken:488 secondary antibody (1:1,000, Invitrogen, A32931) for 2 h at room temperature. Slices were then washed 3× in 0.3% PBS-T with Hoescht included in the middle wash. After the final wash slices were transferred to 0.5× PBS and mounted on glass slides with glycerol-based mounting media (Southern Biotech). Slices were imaged on a Leica SP8 Confocal with 10× air objectives.

Statistics and Data Analysis

For correlations of speed with dF/F, isosbestic-subtracted dF/F traces were compared to motion in the open field experiment. One session was analyzed per mouse. Mice were tracked in open field videos using deep lab cut (Mathis et al., 2018). Using the x and y positions of the mouse output by deep lab cut, speed was calculated as $speed\,(t) = \left(\sqrt{(x_t - x_{t-1})^2 + \left(y_t - y_{t-1}\right)^2}\right) t/\Delta t$ and then aligned to the corresponding isosbestic-subtracted photometry trace. The correlations between speed and photometry traces were calculated for each mouse with a Pearson's correlation. For go/no-go photometry analysis, isosbestic-subtracted dF/F traces were extracted and segmented according to the timing of IR beam breaks during go/no-go behavior using custom MATLAB scripts. Photometry traces for individual trials were separated by trial outcome and averaged within sessions. Importantly, we do not apply trial-to-trial or trial-averaged baseline subtraction or amplitude normalization. Thus, values reported reflect isosbestic-subtracted dF/F. Ninety five percentage of confidence intervals were calculated within sessions using traces from individual trials. For learning-related analyses (**Figure 3**) sessions with 3 or more blocks < 70% accuracy and with 2 or more consecutive blocks > 85% accuracy were sub-selected from the larger dataset. Hit and False Alarm trials from blocks < 70% accuracy were grouped and analyzed separately as "pre-learning" trials. Hit and False Alarm trials from the first two consecutive blocks > 85% accuracy and from subsequent blocks > 85% accuracy were grouped and analyzed separately as "learned" trials. In all cases, post-initiation slopes were calculated by linearly fitting the data after trial initiation before. Areas under the curve were calculated by summing negative values of average traces after trial initiation and dividing by sampling rate. In all cases, comparisons of post-initiation slopes and areas under the curve between trial types utilized a nested, two-way, repeated measures ANOVA. This analysis maintains the relationship between trial types within a single session (repeated measures). Additionally, nesting multiple sessions recorded from the same animal provides a conservative statistical measure which consider all sessions from a single animal together. In the case of post-initiation slopes of GCaMP traces from GABAergic neurons, values were also compared to 0 using a nested one-sample *t*-test. All reported values reflect means from the nested analyses ± SEM and in all cases $p < 0.05$ was considered significant.

DATA AVAILABILITY STATEMENT

The raw data supporting the conclusions of this article will be made available by the authors, without undue reservation.

ETHICS STATEMENT

The animal study was reviewed and approved by Baylor College of Medicine IACUC.

AUTHOR CONTRIBUTIONS

EH designed and conducted experiments, analyzed data, and wrote the manuscript. KB-A conducted experiments, analyzed data, and helped write and edit the manuscript. BA acquired funding, provided guidance on experimental design, data analysis, interpretation, and helped edit the manuscript. All authors contributed to the article and approved the submitted version.

FUNDING

This project was supported by NIH NINDS R01NS078294 (BA) and U01NS111692 (BA), NIH NICHD U54HD083092 (BA), NIH NIDDK R01DK109934 (BA), DOD-PRMP PR180451 (BA), NIH NINDS T32 NS043124-15 (EH), and NIH NIGMS R25 GM 069234 (KB-A).

ACKNOWLEDGMENTS

We would like to thank the Postbaccalaureate Research Education Program (PREP) at Baylor college of

medicine for their support of KB-A, the neurobehavioral core at Baylor College of Medicine for sharing behavioral equipment, and the Arenkiel lab for many helpful discussions.

REFERENCES

Ache, B. W., and Young, J. M. (2005). Olfaction: diverse species, conserved principles. *Neuron* 48, 417–430. doi: 10.1016/j.neuron.2005.10.022

Anaclet, C., Pedersen, N. P., Ferrari, L. L., Venner, A., Bass, C. E., Arrigoni, E., et al. (2015). Basal forebrain control of wakefulness and cortical rhythms. *Nat. Commun.* 6:8744. doi: 10.1038/ncomms9744

Beshel, J., Kopell, N., and Kay, L. M. (2007). Olfactory bulb gamma oscillations are enhanced with task demands. *J. Neurosci.* 27, 8358–8365. doi: 10.1523/JNEUROSCI.1199-07.2007

Böhm, E., Brunert, D., and Rothermel, M. (2020). Input dependent modulation of olfactory bulb activity by HDB GABAergic projections. *Sci. Rep.* 10:10696. doi: 10.1038/s41598-020-67276-z

Buzsaki, G. Y., Bickford, R. G., Ponomareff, G., Thal, L. J., Mandel, R., and Gage, F. H. (1988). Nucleus basalis and thalamic control of neocortical activity in the freely moving rat. *J. Neurosci.* 8, 4007–4026. doi: 10.1523/JNEUROSCI.08-11-04007.1988

Chapuis, J., and Wilson, D. A. (2013). Cholinergic modulation of olfactory pattern separation. *Neurosci. Lett.* 545, 50–53. doi: 10.1016/j.neulet.2013.04.015

Chaudhury, D., Escanilla, O., and Linster, C. (2009). Bulbar acetylcholine enhances neural and perceptual odor discrimination. *J. Neurosci.* 29, 52–60. doi: 10.1523/JNEUROSCI.4036-08.2009

Dannenberg, H., Pabst, M., Braganza, O., Schoch, S., Niediek, J., Bayraktar, M., et al. (2015). Synergy of direct and indirect cholinergic septo-hippocampal pathways coordinates firing in hippocampal networks. *J. Neurosci.* 35, 8394–8410. doi: 10.1523/JNEUROSCI.4460-14.2015

Détári, L., Rasmusson, D. D., and Semba, K. (1999). The role of basal forebrain neurons in tonic and phasic activation of the cerebral cortex. *Prog. Neurobiol.* 58, 249–277. doi: 10.1016/S0301-0082(98)00084-7

Devore, S., Pender-Morris, N., Dean, O., Smith, D., and Linster, C. (2015). Basal forebrain dynamics during nonassociative and associative olfactory learning. *J. Neurophysiol.* 115, 423–433. doi: 10.1152/jn.00572.2015

Fletcher, M. L., and Chen, W. R. (2010). Neural correlates of olfactory learning: critical role of centrifugal neuromodulation. *Learn. Mem.* 17, 561–570. doi: 10.1101/lm.941510

Fletcher, M. L., and Wilson, D. A. (2003). Olfactory bulb mitral-tufted cell plasticity: odorant-specific tuning reflects previous odorant exposure. *J. Neurosci.* 23, 6946–6955. doi: 10.1523/JNEUROSCI.23-17-06946.2003

Ghatpande, A. S., and Gelperin, A. (2009). Presynaptic muscarinic receptors enhance glutamate release at the mitral/tufted to granule cell dendrodendritic synapse in the rat main olfactory bulb. *J. Neurophysiol.* 101, 2052–2061. doi: 10.1152/jn.90734.2008

Gilbert, C. D., and Sigman, M. (2007). Brain states: top-down influences in sensory processing. *Neuron* 54, 677–696. doi: 10.1016/j.neuron.2007.05.019

Goard, M., and Dan, Y. (2009). Basal forebrain activation enhances cortical coding of natural scenes. *Nat. Neurosci.* 12, 1444–1449. doi: 10.1038/nn.2402

Gracia-Llanes, F. J., Crespo, C., Blasco-Ibáñez, J. M., Nacher, J., Varea, E., Rovira-Esteban, L., et al. (2010). GABAergic basal forebrain afferents innervate selectively GABAergic targets in the main olfactory bulb. *Neuroscience* 170, 913–922. doi: 10.1016/j.neuroscience.2010.07.046

Gritton, H. J., Howe, W. M., Mallory, C. S., Hetrick, V. L., Berke, J. D., and Sarter, M. (2016). Cortical cholinergic signaling controls the detection of cues. *Proc. Natl. Acad. Sci. U.S.A.* 113, E1089–E1097. doi: 10.1073/pnas.1516134113

Hangya, B., Ranade, S. P., Lorenc, M., and Kepecs, A. (2015). Central cholinergic neurons are rapidly recruited by reinforcement feedback. *Cell* 162, 1155–1168. doi: 10.1016/j.cell.2015.07.057

Hanson, E., Swanson, J., and Arenkiel, B. R. (2020). GABAergic input from the basal forebrain promotes the survival of adult-born neurons in the mouse olfactory bulb. *Front. Neural. Circuits* 14:17. doi: 10.3389/fncir.2020.00017

Harrison, T. C., Pinto, L., Brock, J. R., and Dan, Y. (2016). Calcium imaging of basal forebrain activity during innate and learned behaviors. *Front. Neural. Circuits* 10:36. doi: 10.3389/fncir.2016.00036

Hasselmo, M. E., and McGaughy, J. (2004). High acetylcholine levels set circuit dynamics for attention and encoding and low acetylcholine levels set dynamics for consolidation. *Prog. Brain Res.* 145, 207–231. doi: 10.1016/S0079-6123(03)45015-2

Herrero, J. L., Roberts, M. J., Delicato, L. S., Gieselmann, M. A., Dayan, P., and Thiele, A. (2008). Acetylcholine contributes through muscarinic receptors to attentional modulation in V1. *Nature* 454, 1110–1114. doi: 10.1038/nature07141

Jing, M., Zhang, P., Wang, G., Feng, J., Mesik, L., Zeng, J., et al. (2018). A genetically encoded fluorescent acetylcholine indicator for *in vitro* and *in vivo* studies. *Nat. Biotechnol.* 36, 726–737. doi: 10.1038/nbt.4184

Jordan, R., Fukunaga, I., Kollo, M., and Schaefer, A. T. (2018). Active sampling state dynamically enhances olfactory bulb odor representation. *Neuron* 98, 1214–1228. doi: 10.1016/j.neuron.2018.05.016

Kay, L. M., and Laurent, G. (1999). Odor-and context-dependent modulation of mitral cell activity in behaving rats. *Nat. Neurosci.* 2, 1003–1009. doi: 10.1038/14801

Kim, T., Thankachan, S., McKenna, J. T., McNally, J. M., Yang, C., Choi, J. H., et al. (2015). Cortically projecting basal forebrain parvalbumin neurons regulate cortical gamma band oscillations. *Proc. Natl. Acad. Sci. U.S.A.* 112, 3535–3540. doi: 10.1073/pnas.1413625112

Kudryavitskaya, E., Marom, E., Pash, D., and Mizrahi, A. (2020). Flexible representations of odour categories in the mouse olfactory bulb. *bioRxiv*. doi: 10.1101/2020.03.21.002006

Laing, D. G. (1986). Identification of single dissimilar odors is achieved by humans with a single sniff. *Physiol. Behav.* 37, 163–170. doi: 10.1016/0031-9384(86)90400-2

Lepousez, G., Nissant, A., Bryant, A. K., Gheusi, G., Greer, C. A., and Lledo, P. M. (2014). Olfactory learning promotes input-specific synaptic plasticity in adult-born neurons. *Proc. Natl. Acad. Sci. U.S.A.* 111, 13984–13989. doi: 10.1073/pnas.1404991111

Lin, S.-C., and Nicolelis, M. A. L. (2008). Neuronal ensemble bursting in the basal forebrain encodes salience irrespective of valence. *Neuron* 59, 138–149. doi: 10.1016/j.neuron.2008.04.031

Liu, G., McClard, C. K., Tepe, B., Swanson, J., Pekarek, B., Panneerselvam, S., et al. (2017). Olfactory cued learning paradigm. *Bio Protoc.* 7:e2251. doi: 10.21769/BioProtoc.2251

Ma, M., and Luo, M. (2012). Optogenetic activation of basal forebrain cholinergic neurons modulates neuronal excitability and sensory responses in the main olfactory bulb. *J. Neurosci.* 32, 10105–10116. doi: 10.1523/JNEUROSCI.0058-12.2012

Mandairon, N., Ferretti, C. J., Stack, C. M., Rubin, D. B., Cleland, T. A., and Linster, C. (2006). Cholinergic modulation in the olfactory bulb influences spontaneous olfactory discrimination in adult rats. *Eur. J. Neurosci.* 24, 3234–3244. doi: 10.1111/j.1460-9568.2006.05212.x

Mandairon, N., and Linster, C. (2009). Odor perception and olfactory bulb plasticity in adult mammals. *J. Neurophysiol.* 101, 2204–2209. doi: 10.1152/jn.00076.2009

Mathis, A., Mamidanna, P., Cury, K. M., Abe, T., Murthy, V. N., Mathis, M. W., et al. (2018). DeepLabCut: markerless pose estimation of user-defined body parts with deep learning. *Nat. Neurosci.* 21, 1281–1289. doi: 10.1038/s41593-018-0209-y

Muir, J. L., Page, K. J., Sirinathsinghji, D. J. S., Robbins, T. W., and Everitt, B. J. (1993). Excitotoxic lesions of basal forebrain cholinergic neurons: effects on learning, memory and attention. *Behav. Brain Res.* 57, 123–131. doi: 10.1016/0166-4328(93)90128-D

Muñoz, W., and Rudy, B. (2014). Spatiotemporal specificity in cholinergic control of neocortical function. *Curr. Opin. Neurobiol.* 26, 149–160. doi: 10.1016/j.conb.2014.02.015

Nunez, A. (1996). Unit activity of rat basal forebrain neurons: relationship to cortical activity. *Neuroscience* 72, 757–766. doi: 10.1016/0306-4522(95)00582-X

Nunez-Parra, A., Maurer, R. K., Krahe, K., Smith, R. S., and Araneda, R. C. (2013). Disruption of centrifugal inhibition to olfactory bulb granule cells impairs olfactory discrimination. *Proc. Natl. Acad. Sci.U.S.A.* 110, 14777–14782. doi: 10.1073/pnas.1310686110

Nunez-Parra, A., Rio, C. D., Christian, A., Huntsman, M. M., and Restrepo, D. (2020). The basal forebrain modulates neuronal response in an active olfactory discrimination task. *Front. Cell. Neurosci.* 14:141. doi: 10.3389/fncel.2020.00141

Ogg, M. C., Ross, J. M., Bendahmane, M., and Fletcher, M. L. (2018). Olfactory bulb acetylcholine release dishabituates odor responses and reinstates odor investigation. *Nat. Commun.* 9:1868. doi: 10.1038/s41467-018-04371-w

Parikh, V., Kozak, R., Martinez, V., and Sarter, M. (2007). Prefrontal acetylcholine release controls cue detection on multiple timescales. *Neuron* 56, 141–154. doi: 10.1016/j.neuron.2007.08.025

Pashkovski, S. L., Iurilli, G., Brann, D., Chicharro, D., Drummey, K., Franks, K., et al. (2020). Structure and flexibility in cortical representations of odour space. *Nature* 583, 253–258. doi: 10.1038/s41586-020-2451-1

Pinto, L., Goard, M. J., Estandian, D., Xu, M., Kwan, A. C., Lee, S. H., et al. (2013). Fast modulation of visual perception by basal forebrain cholinergic neurons. *Nat. Neurosci.* 16, 1857–1863. doi: 10.1038/nn.3552

Quast, K. B., Ung, K., Froudarakis, E., Huang, L., Herman, I., Addison, A. P., et al. (2016). Developmental broadening of inhibitory sensory maps. *Nat. Neurosci.* 20, 189–199. doi: 10.1038/nn.4467

Restrepo, D., Doucette, W., Whitesell, J. D., McTavish, T. S., and Salcedo, E. (2009). From the top down: flexible reading of a fragmented odor map. *Trends Neurosci.* 32, 525–531. doi: 10.1016/j.tins.2009.06.001

Rinberg, D., Koulakov, A., and Gelperin, A. (2006). Speed-accuracy tradeoff in olfaction. *Neuron* 51, 351–358. doi: 10.1016/j.neuron.2006.07.013

Rokni, D., Hemmelder, V., Kapoor, V., and Murthy, V. N. (2014). An olfactory cocktail party: figure-ground segregation of odorants in rodents. *Nat. Neurosci.* 17, 1225–1232. doi: 10.1038/nn.3775

Rothermel, M., Carey, R. M., Puche, A., Shipley, M. T., and Wachowiak, M. (2014). Cholinergic inputs from Basal forebrain add an excitatory bias to odor coding in the olfactory bulb. *J. Neurosci.* 34, 4654–4664. doi: 10.1523/JNEUROSCI.5026-13.2014

Sanz Diez, A., Najac, M., and De Saint Jan, D. (2019). Basal forebrain GABAergic innervation of olfactory bulb periglomerular interneurons. *J. Physiol.* 597, 2547–2563. doi: 10.1113/JP277811

Sarter, M., and Bruno, J. P. (1999). Cortical cholinergic inputs mediating arousal, attentional processing and dreaming: differential afferent regulation of the basal forebrain by telencephalic and brainstem afferents. *Neuroscience* 95, 933–952. doi: 10.1016/S0306-4522(99)00487-X

Szymusiak, R. (1995). Magnocellular nuclei of the basal forebrain: substrates of sleep and arousal regulation. *Sleep* 18, 478–500. doi: 10.1093/sleep/18.6.478

Szymusiak, R., Alam, N., and McGinty, D. (2000). Discharge patterns of neurons in cholinergic regions of the basal forebrain during waking and sleep. *Behav. Brain Res.* 115, 171–182. doi: 10.1016/S0166-4328(00)00257-6

Tremblay, L., Hollerman, J. R., and Schultz, W. (1998). Modifications of reward expectation-related neuronal activity during learning in primate striatum. *J. Neurophysiol.* 80, 964–977. doi: 10.1152/jn.1998.80.2.964

Verhagen, J. V., Wesson, D. W., Netoff, T. I., White, J. A., and Wachowiak, M. (2007). Sniffing controls an adaptive filter of sensory input to the olfactory bulb. *Nat. Neurosci.* 10, 631–639. doi: 10.1038/nn1892

Villar, P. S., Hu, R., and Araneda, R. C. (2020). Long-range GABAergic inhibition modulates spatiotemporal dynamics of the output neurons in the olfactory bulb. *bioRxiv*. doi: 10.1101/2020.07.08.194324

Voytko, M., Lou, O. D. S., Richardson, R. T., Gorman, L. K., Tobin, J. R., and Price, D. L. (1994). Basal forebrain lesions in monkeys disrupt attention but not learning and memory [published erratum appears in J Neurosci 1995 Mar; 15 (3): following table of contents]. *J. Neurosci.* 14, 167–186. doi: 10.1523/JNEUROSCI.14-01-00167.1994

Xu, M., Chung, S., Zhang, S., Zhong, P., Ma, C., Chang, W. C., et al. (2015). Basal forebrain circuit for sleep-wake control. *Nat. Neurosci.* 18, 1641–1647. doi: 10.1038/nn.4143

Yang, C., McKenna, J. T., Zant, J. C., Winston, S., Basheer, R., and Brown, R. E. (2014). Cholinergic neurons excite cortically projecting basal forebrain GABAergic neurons. *J. Neurosci.* 34, 2832–2844. doi: 10.1523/JNEUROSCI.3235-13.2014

Zaborszky, L., Carlsen, J., Brashear, H. R., and Heimer, L. (1986). Cholinergic and GABAergic afferents to the olfactory bulb in the rat with special emphasis on the projection neurons in the nucleus of the horizontal limb of the diagonal band. *J. Comp. Neurol.* 243, 488–509. doi: 10.1002/cne.902430405

Zant, J. C., Kim, T., Prokai, L., Szarka, S., McNally, J., McKenna, J. T., et al. (2016). Cholinergic neurons in the basal forebrain promote wakefulness by actions on neighboring non-cholinergic neurons: an opto-dialysis study. *J. Neurosci.* 36, 2057–2067. doi: 10.1523/JNEUROSCI.3318-15.2016

Zhan, X., Yin, P., and Heinbockel, T. (2013). The basal forebrain modulates spontaneous activity of principal cells in the main olfactory bulb of anesthetized mice. *Front. Neural. Circuits* 7:148. doi: 10.3389/fncir.2013.00148

Conflict of Interest: The authors declare that the research was conducted in the absence of any commercial or financial relationships that could be construed as a potential conflict of interest.

frontiers in Cellular Neuroscience

ORIGINAL RESEARCH
published: 17 February 2021
doi: 10.3389/fncel.2021.638800

Sensory Detection by the Vomeronasal Organ Modulates Experience-Dependent Social Behaviors in Female Mice

*Anne-Charlotte Trouillet[1], Chantal Moussu[1], Kevin Poissenot[1], Matthieu Keller[1], Lutz Birnbaumer[2,3], Trese Leinders-Zufall[4], Frank Zufall[4] and Pablo Chamero[1]**

[1] Laboratoire de Physiologie de la Reproduction et des Comportements, UMR 0085 INRAE-CNRS-IFCE-University of Tours, Nouzilly, France, [2] Neurobiology Laboratory, National Institute of Environmental Health Sciences, National Institutes of Health, Durham, NC, United States, [3] School of Medical Sciences, Institute of Biomedical Research (BIOMED), Catholic University of Argentina, Buenos Aires, Argentina, [4] Center for Integrative Physiology and Molecular Medicine, Saarland University, Homburg, Germany

In mice, social behaviors are largely controlled by the olfactory system. Pheromone detection induces naïve virgin females to retrieve isolated pups to the nest and to be sexually receptive to males, but social experience increases the performance of both types of innate behaviors. Whether animals are intrinsically sensitive to the smell of conspecifics, or the detection of olfactory cues modulates experience for the display of social responses is currently unclear. Here, we employed mice with an olfactory-specific deletion of the G protein Gαi2, which partially eliminates sensory function in the vomeronasal organ (VNO), to show that social behavior in female mice results from interactions between intrinsic mechanisms in the vomeronasal system and experience-dependent plasticity. In pup- and sexually-naïve females, Gαi2 deletion elicited a reduction in pup retrieval behavior, but not in sexual receptivity. By contrast, experienced animals showed normal maternal behavior, but the experience-dependent increase in sexual receptivity was incomplete. Further, lower receptivity was accompanied by reduced neuronal activity in the anterior accessory olfactory bulb and the rostral periventricular area of the third ventricle. Therefore, neural mechanisms utilize intrinsic sensitivity in the mouse vomeronasal system and enable plasticity to display consistent social behavior.

Keywords: olfactory, Gαi2, maternal, lordosis, sex preference, kisspeptin

OPEN ACCESS

Edited by:
Emmanuel Valjent, Centre National de la Recherche Scientifique (CNRS), France

Reviewed by:
Michael Baum, Boston University, United States
Kazushige Touhara, The University of Tokyo, Japan

****Correspondence:***
Pablo Chamero
pablo.chamero-benito@inrae.fr

Specialty section:
This article was submitted to Cellular Neurophysiology, a section of the journal Frontiers in Cellular Neuroscience

Received: *07 December 2020*
Accepted: *28 January 2021*
Published: *17 February 2021*

Citation:
Trouillet A-C, Moussu C, Poissenot K, Keller M, Birnbaumer L, Leinders-Zufall T, Zufall F and Chamero P (2021) Sensory Detection by the Vomeronasal Organ Modulates Experience-Dependent Social Behaviors in Female Mice. Front. Cell. Neurosci. 15:638800. doi: 10.3389/fncel.2021.638800

INTRODUCTION

The onset of female-specific behaviors in mice results from interactions between sensory detection mechanisms and plastic neuronal pathways. Rapid responses in females' behaviour—such as pup care (Lévy et al., 2004), or sexual receptivity to males (Keller et al., 2009)—start with the detection of chemical signals by the olfactory system. Although these olfactory-driven responses are typically hard-wired, aspects of female behavior may evolve after social experience. For example, virgin females recognize pup odors and retrieve isolated pups to the nest to some extent, but maternity greatly increases this type of parental behavior (Stolzenberg and Rissman, 2011; Kohl et al., 2017).

Similarly, the display of sexual receptivity in females, indexed by the incidence of lordosis stance, largely depends on the detection of olfactory signals by the vomeronasal organ (VNO) (Keller et al., 2006; Oboti et al., 2014; Hellier et al., 2018) and is considerably enhanced by experience (Thompson and Edwards, 1971; Bonthuis et al., 2011). Plastic changes in central brain areas have been shown to modulate instinctive olfactory-mediated female behaviors (Stowers and Liberles, 2016), but whether sensory detection by the olfactory system also influences social experience remains unexplored.

Pheromones play a key role in the regulation of innate reproductive responses in female mice and are largely detected by sensory neurons in the VNO (Chamero et al., 2012; Stowers and Kuo, 2015; Ishii and Touhara, 2019). Genetic ablation of Trpc2, the primary signal transduction pathway of VNO neurons, results in several behavioral deficits in mice, such as display of sexual behavior toward both males and females indiscriminately, lack of maternal aggression in females as well as enhanced pup care in males (Leypold et al., 2002; Stowers et al., 2002; Kimchi et al., 2007; Hasen and Gammie, 2009; Wu et al., 2014). We have previously shown that the G protein Gαo is necessary for sensory function of basal vomeronasal sensory neurons (VSNs), maternal aggression, and lordosis behavior in female mice (Chamero et al., 2011; Oboti et al., 2014). By contrast, apical VSNs, which express Gαi2 and V1R receptors, are critical for pup-directed aggression and parental care in males (Trouillet et al., 2019) and have also been associated with maternal aggression (Del Punta et al., 2002; Norlin et al., 2003). This suggests that both apical and basal vomeronasal pathways control female-typical behaviors activating certain behaviors and repressing others. However, the neural VNO mechanisms involved and the role of social experience in controlling the display of female-typical behaviors remain largely unknown.

To uncover the neuronal VNO substrate leading to specific female behaviors, we used female mice with a conditional knockout of Gαi2, in which the apical half of the VNO lacks sensory function (Trouillet et al., 2019). We used two different behavioral paradigms, pup retrieval, and sexual receptivity, in which female mice were naïve to the stimuli, either a mouse infant or an adult male. Mutant females showed reduced pup retrieval behavior, whereas sexual receptivity was not different from control mice in the initial tests. Then, we evaluated the effect of social experience in the display of these behaviors. Remarkably, Gαi2 mutant females displayed normal pup retrieval behavior and maternal aggression after parturition, while sexual experience was not sufficient for Gαi2 mutants to reach control levels of sexual receptivity. These results demonstrate the role of V1R and Gαi2+ neurons in the display of lordosis and detection of pup cues. Unexpectedly, social experience in Gαi2 deficient mice leads to divergent effects on behavior: improvement of pup retrieval without any beneficial effects on the acquisition of high lordosis performance. Altogether, our data suggest that the detection of pheromones by the VNO influences olfactory-mediated behavior in females after social experience, although with distinctive traits for different behaviors.

MATERIALS AND METHODS

Mice

Animal care and experimental procedures were performed following French and European guidelines on the protection of animals used for scientific purposes and approved by an ethical committee for animal experimentation (CEEA Val de Loire project 12785). Mice were kept under standard 12 h light/dark cycles with food and water *ad libitum*. cGαi2$^{-/-}$ and cGαi2$^{+/-}$ mice were generated as described (Trouillet et al., 2019). Briefly, floxed *Gnai2* (*Gnai2*$^{fx/fx}$) mice with mixed 129sv × C57BL/6 background were crossed with mice carrying a transgene directing the expression of Cre recombinase under the control of the OMP promoter (*Omp*-Cre mice; B6; 129P2-*Omp*$^{tm4(cre)Mom}$/ MomJ; The Jackson Laboratory, JR# 006668; backcrossed into C57BL6/J for 8 generations; neomycin cassette is absent). *Gnai2*$^{fx/fx}$ mice carry loxP sites inserted into the introns that flank exons 2 and 4. Breeding established offspring that were homozygous for the floxed *Gnai2* alleles and heterozygous for Cre and *Omp* (*Gnai2*$^{fx/fx}$ *Omp*$^{cre/+}$ or cGαi2$^{-/-}$). In these mice, Cre-mediated *Gnai2* deletion was restricted to *Omp*-positive cells. Animals heterozygous for both alleles (*Gnai2*$^{fx/+}$ *Omp*$^{cre/+}$ or cGαi2$^{+/-}$) served as controls. Adult females (more than 8 weeks) were used except specified otherwise. Adult (8 weeks or older) C57BL/6 males and females (Janvier Labs) and Balb/c males (Janvier Labs) were used as stimulus animals.

Surgery

Stimulus females used for the mounting behavior assay and experimental females used in lordosis, habituation-dishabituation, and olfactory preference tests were ovariectomized under general anesthesia (xylazine 10 mg/kg, ketamine 100 mg/kg), implanted with a SILASTIC capsule filled with estradiol-benzoate (1:1 mix with cholesterol; Sigma-Aldrich). Females were allowed to recover from surgery at least 2 weeks before testing. Females were subcutaneously treated with progesterone (1 mg/100 μl in sesame oil, Sigma-Aldrich) to induce a pharmacological estrus state 4 h before each test. Juvenile (P18-22) C57BL/6 stimulus males were castrated under isoflurane general anesthesia and used in adulthood.

Behavior

Mice were moved to the experimental room 2 h before testing. Assays were conducted 2 h before the start of the dark period. Experiments were videotaped and subsequently analyzed by a blind experimenter.

Parental Behaviors in Virgin Females

Sexually naïve females (N = 12 of each genotype) were tested for behavior in the presence of an alien 1–2 day old C57BL/6 (wild type) neonate introduced into the home-cage of the test mouse for 10 min. Females were individually housed for 1 week before testing. To minimize handling and stress to the pups, one single pup was taken from the nest immediately prior to the test avoiding prolonged exposure to cold. Mice were categorized as parental if they retrieved a pup into their nest, and otherwise

as neutral. We did not observe aggressive behavior. Latency to retrieve a pup, pup grooming, and nesting times were scored.

Maternal Aggression

Sexually naïve females (20 cGαi2$^{+/-}$ and 16 cGαi2$^{-/-}$) were paired with a C57BL/6 male for 1 week. Bedding and nesting materials were changed before parturition and left until the end of the experiments. On postnatal days 2–4, females were tested daily for maternal aggression using the resident—intruder paradigm (Chamero et al., 2011). Before testing, pups were placed in a box next to their mother's cage to avoid potential injuries by the intruder. Testing lasted 10 min and began when a sexually inexperienced intruder (Balb/c adult male, group-housed) was placed in the home cage of the test female mouse (resident). Residents were not exposed twice to the same intruder. Aggressive behavior was defined as lunging, biting, chasing, tail rattling, wrestling, and kicking. Attack bouts were defined as a succession of aggressive events separated by <3 s. Proportion of females attacking the intruder, latency to attack, and cumulative attack duration and episodes of 3 consecutive tests were scored.

Pup Retrieval

After maternal aggression, the same females were tested for retrieval of their own pups. On postnatal day 5, five pups were randomly dispersed at the opposite side of the nest. The latencies to retrieve each pup to the nest were scored.

Olfactory Habituation Dishabituation Assay

Sexually naïve females (10 cGαi2$^{+/-}$ and 9 cGαi2$^{-/-}$) were evaluated for their ability to distinguish urine sources. Females were ovariectomized, supplemented in estradiol, and subcutaneously treated with progesterone 4 h before the experiment. The test was conducted in the female's home-cage and an odor stimulus was placed on a cotton-tipped applicator through the hole of the cage lid. Direct contact with the applicator was allowed. Food and water were removed from the grid and mice were allowed to familiarize themselves with a clean applicator for 30 min before the test. The test started with a first exposition for 1 min to distilled water (10 μl). This procedure was repeated three times with 1 min intervals, followed by a single presentation of intact male urine (10 μl, collected and pooled from 4 C57BL/6 group-housed adult mice). The time spent sniffing in close contact with the applicator was measured for each presentation.

Olfactory Preference Test

Sexually naïve females (10 cGαi2$^{+/-}$ and 9 cGαi2$^{-/-}$) were tested for their male-directed odor preference in a Y-maze apparatus as described previously (Jouhanneau et al., 2014). Females were ovariectomized, supplemented in estradiol, and subcutaneously treated with progesterone 4 h before the experiment. Two days before the test assay, mice were accustomed to the maze for 9 min in absence of an odor stimulus. On test day, urine from two distinct sources were placed in the arms' ends of the Y-maze on a filter paper in a plastic weigh boat behind a perforated wall. The apparatus was cleaned with 20% ethanol between subjects. Each animal was tested twice: first, with either intact male or estrous female urine; and second, with either intact or castrated male urine. Equal urine volumes from 4 C57BL/6 animals per condition were pooled and the estrus status of female donors was assessed by vaginal cytology. The time of chemosensory investigation was recorded. Preference scores were calculated as the difference between times spent on each urine source over total time of chemosensory investigation.

Mounting Behavior

Sexually naïve females (20 cGαi2$^{+/-}$ and 17 cGαi2$^{-/-}$) were individually housed for 1 week before testing. Testing lasted 10 min and began when a sexually inexperienced intruder (either male, female in pharmacological estrus, or castrated male, group-housed) was placed in the home cage of the test mouse (female resident), whose bedding had not been changed for at least 4 days. Each female was tested with every intruder in a randomized order. The proportion of females mounting the intruder was recorded.

Female Sexual Receptivity (Lordosis)

Sexually naïve females (10 cGαi2$^{+/-}$ and 9 cGαi2$^{-/-}$) were tested for their sexual receptivity toward male mounting. Females were ovariectomized, supplemented in estradiol, and subcutaneously treated with progesterone 4 h before the experiment. The test began when the female was introduced in the home cage of a sexually experienced C57BL/6 stud male and lasted for 20 min or until the female received 20 mounts. Stud males were previously trained, and only males showing a mounting latency of less than 5 min were used. Females were not exposed twice to the same stud male. Females were tested three times with a 4 days interval between tests. Lordosis was scored when the female arched her back, lift her tail and adopted a rigid posture standing on all four paws, independently of whether the male was able to achieve intromission. The lordosis quotient (number of lordosis responses/number of mounts) was scored.

Immunostaining

Tissue Preparation

90 min after sexual behavior or interaction with a neonate, mice were anesthetized by an overdose of pentobarbital (Ceva) and perfused transcardially with 0.9% saline solution followed by 0.1 M phosphate buffer (PB) containing 4% paraformaldehyde (PFA). Brains were removed, postfixed overnight in 4% PFA, and cryoprotected in 0.1 M PB containing 30% sucrose. Brain and olfactory bulbs (OB) were embedded separately in Tissue-Tek® O.C.T™ compound, snap-frozen in cold isopentane, and processed on a Leica CM 3050S cryostat. Samples were cut in 30 μm serial free-floating sections (coronal for brains, sagittal for OB) using tris-buffered saline solution (TBS) containing 0.1% sodium azide.

c-Fos Immunolabeling

Sections were washed (3 × 5 min) in TBS, endogenous peroxidases were blocked for 30 min in TBS containing 3% H_2O_2. Sections were incubated in blocking solution (TBS containing 0.1% Triton X-100, TBS-T, and 5% donkey serum) 2 h at room

temperature (RT), and overnight at 4°C in blocking solution supplemented with the c-Fos primary antibody (1:500; rabbit polyclonal #sc-52, Santa Cruz Biotechnology). Sections were then washed in TBS and incubated in TBS-T supplemented with secondary antibody (1:1,000; biotinylated donkey anti-rabbit IgG, Jackson ImmunoResearch) for 2 h at RT. Signals were amplified with VECTASTAIN ABC kit (Vector) and visualized with diaminobenzidine (DAB 0,02%, 0,01% H_2O_2 in 0,05 M Tris, pH 7,4). Slides were mounted with DPX (Sigma-Aldrich).

Kisspeptin/c-Fos Immunolabeling

Sections were washed in TBS, incubated in blocking solution (TBS containing 0.1% Triton X-100, TBS-T, and 5% donkey serum) 2 h at RT, incubated 72 h at 4°C in blocking solution supplemented with c-Fos (1:500; rabbit polyclonal #sc-52, Santa Cruz Biotechnology) and kisspeptin [1:10,000; sheep polyclonal #AC053, generous gift of I. Franceschini (Franceschini et al., 2013)] primary antibodies. Sections were then washed in TBS and incubated in TBS-T supplemented with secondary antibodies (1:500; Cy3 donkey anti-rabbit-IgG and Alexa-488 donkey anti-sheep-IgG, Jackson ImmunoResearch) for 2 h at RT. Nuclei were counterstained with 4′,6-diamidino-2-phenylindole (DAPI; 0.5 μg/ml, Sigma-Aldrich) for 2 min. Slides were mounted with Fluoromount^{TM} (Sigma-Aldrich).

Analysis

For c-Fos experiments, slides were scanned using an automatic slide scanner (Axio Scan.Z1, Zeiss). Regions of interest were drawn based on the Paxinos mouse brain atlas using Zen (blue edition 3.0, Zeiss). The number of c-Fos+ nuclei was automatically counted bilaterally in these regions using the particle analyzer plug-in of Fiji. 2–3 images of the accessory olfactory bulb (AOB), 3 images of the rostral periventricular area of the third ventricle (RP3V), 2 images of the ventrolateral part of the ventromedial hypothalamic nucleus (VMHvl) and 4 images of the medial preoptic area (MPA) per animal were analyzed. Kisspeptin/c-Fos co-expression was quantified in 3–5 RP3V images/animal acquired on a Zeiss LSM-700 confocal laser-scanning microscope at 10× magnification. Images were manually analyzed in the entire *z*-axis with 3 μm step intervals.

Reproductive Physiology

Young prepubertal females (17 cGαi2$^{+/-}$ and 15 cGαi2$^{-/-}$) were monitored daily for evidence of vaginal opening from postnatal day 15, and then for their first estrus by vaginal smears sampling. Briefly, vaginal smears were flushed with 15 μl of NaCl 0.9% solution and the estrus phase was identified by light microscopy after methylene-blue coloration of the smears. Adult females (47 cGαi2$^{+/-}$ and 45 cGαi2$^{-/-}$) were also examined daily for estrus status for 2 weeks using the same protocol. Adult females (61 cGαi2$^{+/-}$ and 49 cGαi2$^{-/-}$) were sacrificed during their diestrus or estrus phase to collect trunk blood and measure the weight of ovaries and uteri. Blood sera were obtained by centrifugation (2,500 × *g* for 25 min) and levels of progesterone were measured by immunoenzymatic assay. Assay sensitivity is 0.25 ng/ml. Sexually naïve females (76 cGαi2$^{+/-}$ and 67 cGαi2$^{-/-}$) were paired for 7 days with a C57BL/6 male. The proportion of pregnant females, the latency to deliver, and the number of pups born were collected.

Statistics

Statistical analyses were performed using GraphPad Prism 9.0 (GraphPad Software, Inc.), and OriginPro 2016G (OriginLab Corporation). Assumptions of normality and homogeneity of variance were tested before conducting the following statistical approaches. Student's *t*-test was used to measure the significance of the differences between two distributions. In case the results failed the test of normality, Mann-Whitney or Kolmogorov-Smirnov test was performed. Multiple groups were compared using a two- or three-way repeated-measures analysis of variance (ANOVA) with Bonferonni's tests as *post hoc* comparison. Kruskal-Wallis test with Dunn's multiple comparisons, or Friedman multiple comparisons in case of paired values, were used for non-normal distributions. Categorical data were analyzed with Fisher's exact test, and correlations were assessed by the Pearson coefficient. The probability of error level (alpha) was chosen to be 0.05. Unless otherwise stated, results are presented as means ± SEM and documentation of individual data points.

RESULTS

Inactivation of the Apical Vomeronasal Cell Layer Reduces Pup Retrieval in Virgin Females

VNO activity is necessary for the display of important pup-directed behaviors in male mice, such as pup-directed aggression (Tachikawa et al., 2013; Wu et al., 2014; Isogai et al., 2018; Trouillet et al., 2019), inhibition of sexual behaviors toward pups (Ferrero et al., 2013), and increased pup-retrieval and parenting behaviors (Wu et al., 2014; Trouillet et al., 2019). In virgin females, the role of the VNO in pup-directed behaviors is less clear. While some studies suggest that genetic ablation of VNO function in Trpc2$^{-/-}$ females increase parenting behavior toward alien juveniles (Nakahara et al., 2016), this view is not supported by others (Wu et al., 2014).

To determine whether the vomeronasal pathway may partially regulate pup parenting in virgin females, we used mice carrying Olfactory Marker Protein (OMP)-dependent deletion of Gαi2 (cGαi2$^{-/-}$), which impairs sensory signaling in apical VNO neurons (Trouillet et al., 2019). We exposed pup-naïve virgin females to 1–2 days old pups (**Figure 1A**) and the majority of females retrieved the pups to the nest, although the proportion of retrieving females was lower in cGαi2$^{-/-}$ when compared to heterozygous controls (58 vs. 92%; **Figure 1A**). Measurement of the latency to retrieve pups showed that cGαi2$^{-/-}$ virgin females retrieved pups with longer latency ($P < 0.05$; **Figure 1B**), even if they displayed more time sniffing the pups before retrieving ($P < 0.05$; **Figure 1B**). Next, we used c-Fos immunolabeling to confirm the role of vomeronasal signaling in pup detection by virgin females

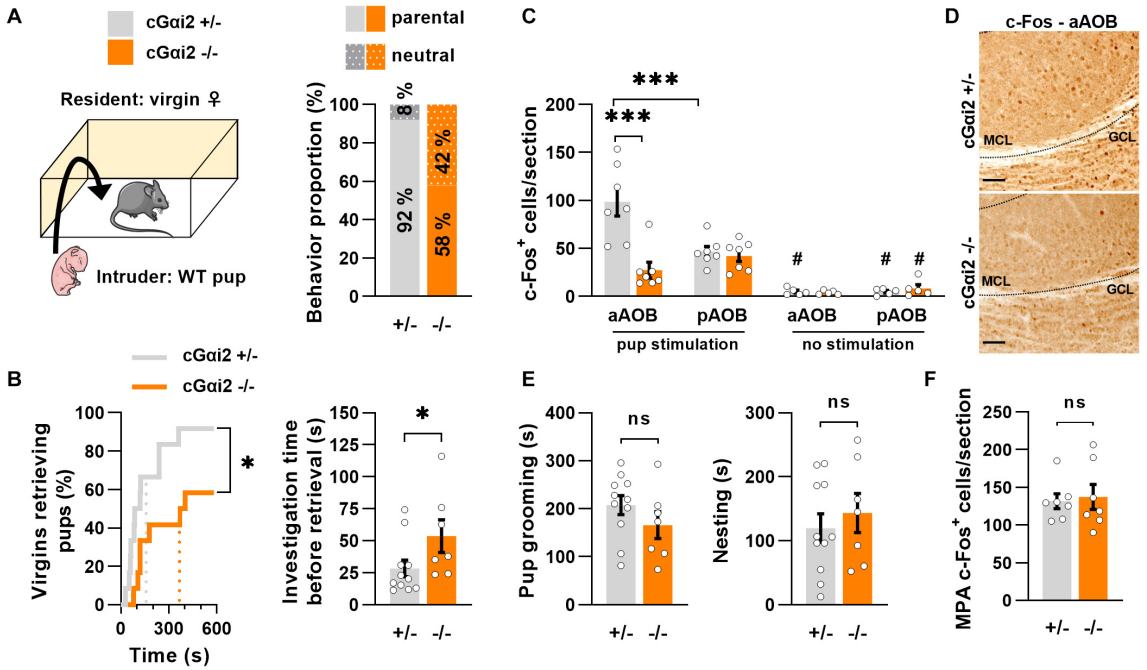

FIGURE 1 | Pup retrieval is altered in virgin cGαi2$^{-/-}$ females. **(A)** Comparison of pup-directed behavior of cGαi2$^{+/-}$ vs. cGαi2$^{-/-}$ virgin female residents (N = 12 per genotype). Wild type 1–2 day-old pups served as intruders. Females ignore (neutral) or retrieve neonates to their nest (parental). Females of both genotypes are predominantly parental (11 out of 12; 92% for cGαi2$^{+/-}$ and 7 out of 12; 58% for cGαi2$^{-/-}$). **(B)** *Left*, proportion of females retrieving pups over time (Kolmogorov-Smirnov test: $P < 0.05$). Dotted lines represent the mean latency. *Right*, time spent sniffing the pup before retrieval in cGαi2$^{-/-}$ (N = 7) and cGαi2$^{+/-}$ (N = 11) parental females (Mann-Whitney: $P < 0.05$). **(C)** Quantification of c-Fos+ cells per section of cGαi2$^{+/-}$ and cGαi2$^{-/-}$ virgin females (N = 7 per group) in control condition (no stimulation) and after exposure to an alien pup (pup stimulation) reveals a decreased c-Fos activation in the aAOB of cGαi2$^{-/-}$ compared to cGαi2$^{+/-}$ females, and a higher number of c-Fos+ cells in the anterior compared to the posterior part of the AOB of cGαi2$^{+/-}$ females only [Three-way repeated measures ANOVA: (genotype) $F_{(1,12)} = 6.719$, $P < 0.01$; (region) $F_{(1,12)} = 4.024$, $P = 0.068$; (stimulation) $F_{(1,12)} = 63.21$, $P < 0.001$; (genotype × region × stimulation) $F_{(1,4)} = 14.67$, $P < 0.05$; Bonferroni *post hoc* tests: cGαi2$^{+/-}$ aAOB vs. cGαi2$^{+/-}$ pAOB and cGαi2$^{+/-}$ aAOB vs. cGαi2$^{-/-}$ aAOB $P < 0.001$; $^{\#}P < 0.05$ vs. the stimulated equivalent condition; other comparison P = 0.3–0.9]. All three AOB layers were quantified. **(D)** Examples of c-Fos immunodetection in the aAOB of cGαi2$^{+/-}$ and cGαi2$^{-/-}$ virgin females exposed to an alien pup for 10 min. Scale bars, 25 μm. **(E)** The time spent grooming (*left*) and nesting (*right*) the neonates (*t*-test: P = 0.2–0.5). **(F)** Quantification of c-Fos^{+} cells per section in the MPA of cGαi2$^{+/-}$ and cGαi2$^{-/-}$ virgin females after exposure to an alien pup is not different (*t*-test: P = 0.8). AOB, accessory olfactory bulb (aAOB, anterior AOB; pAOB, posterior AOB); MCL, mitral cell layer; GCL, granular cell layer; MPA, medial preoptic area. $^{*}P < 0.05$; $^{***}P < 0.001$.

and examine whether pup odors were preferentially detected by either the apical or basal vomeronasal subsystems. We compared the density of c-Fos+ nuclei in all three layers of the accessory olfactory bulb (AOB), the first relay station of the pheromonal information transfer in the brain, after pup exposure in cGαi2$^{-/-}$ and cGαi2$^{+/-}$ virgin females (**Figures 1C,D**). After pup exposure, the density of c-Fos+ nuclei was nearly fourfold lower in the anterior part of the AOB of cGαi2$^{-/-}$females ($P < 0.001$; **Figure 1C**), consistent with reduced sensory input from the apical VNO. Furthermore, we observed twofold more c-Fos+ nuclei in the anterior vs. posterior part of the AOB in control females ($P < 0.001$; **Figure 1C**), suggesting a preferential activation of apical Gαi2-expressing VSNs by pup odors. Once pups were retrieved to the nest, measures of parental care—pup grooming and nesting time—were not significantly different in cGαi2$^{-/-}$ females (**Figure 1E**; P = 0.2–0.5). Consistent with this, the number of c-Fos+ cells in the medial preoptic area (MPA), a region involved in parenting (Numan, 1974), was also not significantly different in cGαi2$^{-/-}$ females (**Figure 1F**). Together, these results indicate that Gαi2-dependent VNO inputs participate in pup odor detection in virgin females and that deletion of Gαi2 reduces pup retrieval, although pup-parenting behaviors are still displayed after retrieval.

Deletion of Gαi2 Does Not Affect Maternal Behavior in Mothers

Both the main olfactory epithelium and VNO seem to be implicated in maternal behavior. Previous experiments using genetically altered mice showed that an intact main olfactory system is required for pup retrieval in lactating mice mothers (Weiss et al., 2011; Fraser and Shah, 2014), and that the VNO is necessary for the display of maternal aggression (Leypold et al., 2002; Hasen and Gammie, 2009; Chamero et al., 2011). Consequently, impairment of vomeronasal signaling in Trpc2$^{-/-}$ lactating females has no impact on pup retrieval behavior, even though these females are deficient in maternal aggression (Leypold et al., 2002; Hasen and Gammie, 2009).

Yet, the VNO neuronal subpopulation implicated in maternal aggression is not characterized with certainty. While maternal aggression is nearly absent in basal VNO signaling-deficient cGαo$^{-/-}$ females (Chamero et al., 2011), other studies have suggested some mediation from apical Gαi2/V1R-expressing VSNs (Del Punta et al., 2002; Norlin et al., 2003).

Thus, we aimed to investigate the requirement of Gαi2^{+} vomeronasal neurons for parental behaviors in mated females. We first quantified territorial aggression of cGαi2$^{-/-}$ vs. cGαi2$^{+/-}$ lactating females in the resident-intruder paradigm (**Figure 2**). We observed a high number of animals attacking an adult intact male intruder in both cGαi2$^{-/-}$ (14/16 mice; 87%) and cGαi2$^{+/-}$ mothers (14/20 mice; 70%) in three consecutive 10 min tests (P = 0.3; **Figure 2A**). Attack latency, total attack duration, and cumulative attack numbers were high in both cGαi2$^{-/-}$ and cGαi2$^{+/-}$ females (P = 0.4–0.9; **Figure 2B**), indicating that Gαi2 is dispensable for the display of maternal aggression. Consistent with previous findings indicating a minor role of the VNO in the display of pup retrieval behavior in mothers (Wysocki and Lepri, 1991), cGαi2$^{-/-}$ females exhibited normal pup retrieval when compared to heterozygous controls (**Figures 2C,D**). All females retrieved to the nest all of their pups randomly distributed in the home cage (**Figure 2C**), and the mean time to retrieve the 5 pups was less than 80 s in both groups (**Figure 2D**). Taken together, these results show that maternal aggression and pup retrieval by lactating females do not depend on Gαi2+ VSNs.

Incomplete Sexual Receptivity Acquisition in Gαi2-Mutant Females

An intact VNO is required for the display of major female sexual behaviors, such as gender discrimination and sexual receptivity (Leypold et al., 2002; Stowers et al., 2002; Keller et al., 2006; Kimchi et al., 2007; Martel and Baum, 2009; Oboti et al., 2014; Hellier et al., 2018).

To examine whether altered sexual behaviors of VNO-impaired mice might be related to a deficit in Gαi2 signaling, we measured olfactory preference to male odors in cGαi2$^{-/-}$ females. We used adult, sexually naïve females subjected to ovariectomy and primed with estradiol and progesterone to minimize estrus cycle-related variability and increase their motivation for male pheromones. First, we evaluated their ability to recognize urine from an adult male using the habituation-dishabituation paradigm. cGαi2$^{-/-}$ and cGαi2$^{+/-}$ females were exposed to a sequence of three successive odor presentations of water and a final presentation of male urine. All females were able to recognize the urine, as the time spent sniffing the first urine presentation was higher than the previous water presentations (**Figure 3A**). Next, we analyzed the preference for either intact male urine or estrus female urine in a two-choice preference test. cGαi2$^{-/-}$ and cGαi2$^{+/-}$ females displayed the same level of preference for intact male urine (P = 0.8; **Figure 3B**). We then compared the preference for urine from either intact or castrated males (**Figure 3B**). cGαi2$^{-/-}$ and cGαi2$^{+/-}$ females showed a strong preference for intact male urine (P = 0.4;

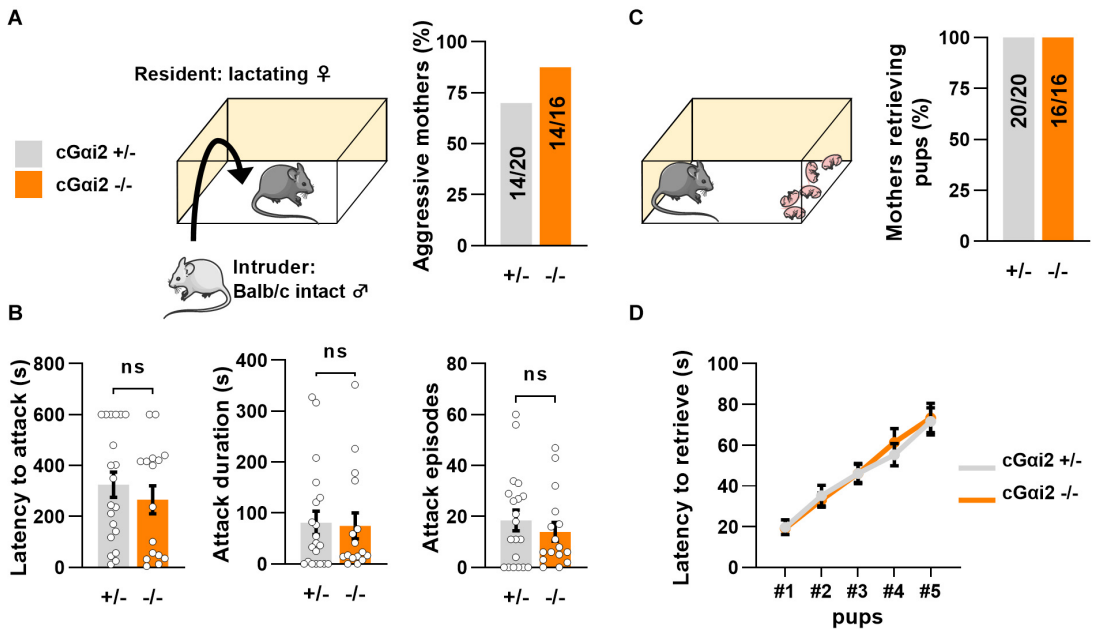

FIGURE 2 | Loss of Gαi2 does not affect maternal behavior in lactating females. **(A)** Maternal aggression in lactating cGαi2$^{+/-}$ (N = 20) vs. cGαi2$^{-/-}$ (N = 16) females during three consecutive exposures to an intact male intruder in the resident-intruder test. 70% of cGαi2$^{+/-}$ and 87% of cGαi2$^{-/-}$ females present at least one aggressive episode (Fisher's exact test: P = 0.3). **(B)** Measure of the aggression parameters latency to attack (*left*), cumulative attack duration (*middle*) and attack episodes (*right*) across genotypes (Mann-Whitney: P = 0.4–0.9). **(C)** 100% of cGαi2$^{+/-}$ (N = 20) and cGαi2$^{-/-}$ (N = 16) mothers retrieve five of their pups previously dispersed in the cage. **(D)** The latency to retrieve pups does not differ between groups (Dunn's multiple comparison tests cGαi2$^{+/-}$ vs. cGαi2$^{-/-}$ for each pup's latency $P > 0.9$).

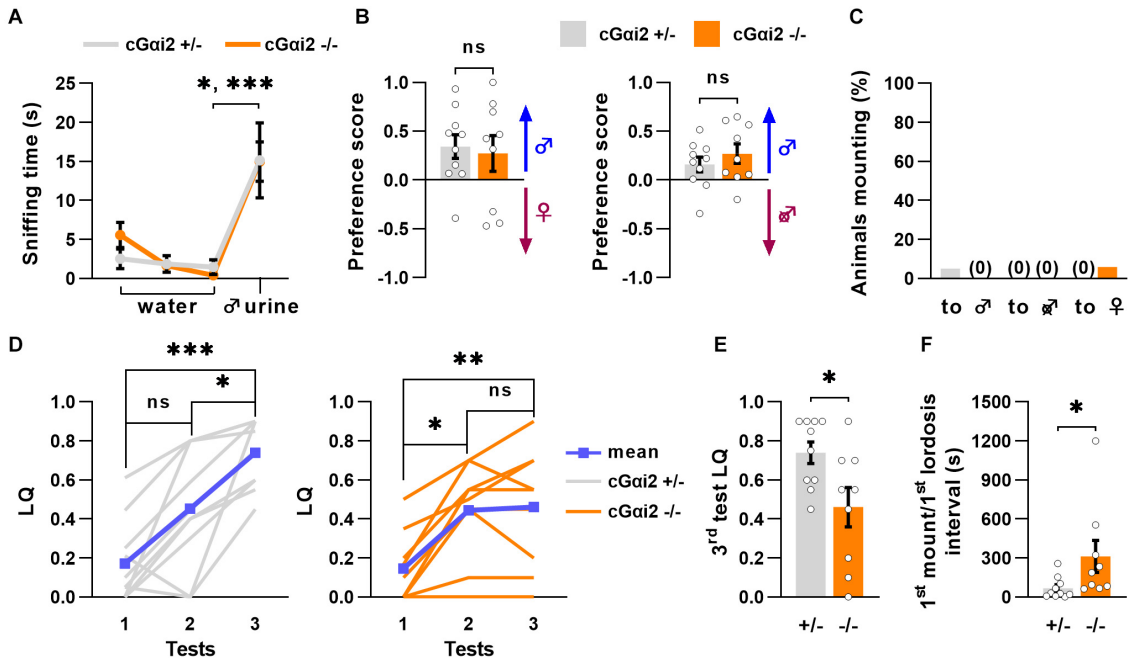

FIGURE 3 | Incomplete sexual receptivity in Gαi2 mutant females. **(A)** cGαi2$^{+/-}$ (N = 10) and cGαi2$^{-/-}$ (N = 9) are able to detect intact male urine in the habituation—dishabituation paradigm (Kruskal-Wallis: $P < 0.001$, Dunn's multiple comparison tests: water 3 vs. urine 1 cGαi2$^{+/-}$ $P < 0.05$, cGαi2$^{-/-}$ $P < 0.001$). **(B)** Olfactory preference of social cues in cGαi2$^{+/-}$ (N = 10) and cGαi2$^{-/-}$ (N = 9) female mice in a two-choice test. Females had the choice between male urine vs. estrus female (*left*) or castrated male (*right*) urine. cGαi2$^{+/-}$ and cGαi2$^{-/-}$ animals show a preference for male urine in both tests and no differences between genotypes are found (*t*-test: P = 0.4–0.7). **(C)** Ablation of Gαi2 in VSNs does not induce, in females, mounting behavior toward male, castrated male or female. The proportion of animals mounting is similar in cGαi2$^{+/-}$ (N = 20) and cGαi2$^{-/-}$ (N = 17) females (Fisher's exact test: P = 0.5–0.9). **(D–F)** Sexual receptivity of cGαi2$^{+/-}$ (N = 10) and cGαi2$^{-/-}$ (N = 9) females during exposition to a sexually experienced stud male over three tests. **(D)** The lordosis quotient (LQ) of cGαi2$^{+/-}$ (*left*) follows a normal increase over the tests (Kruskal-Wallis: $P < 0.001$, Friedman multiple comparisons: test 1 vs. 2 P = 0.5, test 1 vs. 3 $P < 0.001$, and test 2 vs. 3 $P < 0.05$), but in cGαi2$^{-/-}$ (*right*) the lordosis quotient does not increase in the third test (Kruskal-Wallis: $P < 0.001$, Friedman multiple comparisons: test 1 vs. 2 $P < 0.05$, test 1 vs. 3 $P < 0.01$, and test 2 vs. 3 P = 0.9). **(E)** Comparison of the lordosis quotient of cGαi2$^{+/-}$ and cGαi2$^{-/-}$ females during the third test reveals a reduction of sexual receptivity in mutant females (Mann-Whitney: $P < 0.05$). **(F)** Latency to exhibit a lordosis, measured from the first mount received, is significantly longer in cGαi2$^{-/-}$ females (Mann-Whitney: $P < 0.05$). *$P < 0.05$; **$P < 0.01$; ***$P < 0.001$.

Figure 3B), indicating that preference for male odors is intact in cGαi2$^{-/-}$ females.

Next, we assessed cGαi2$^{-/-}$ females for the display of male-typical behaviors by scoring mounting behavior of intact female residents to either male, female, or castrated male intruders, independently introduced into the female resident's home cage during a 10 min test period for 3 consecutive days. Very few animals displayed mounting behavior toward any intruder (female, male, or castrated male) for both cGαi2$^{-/-}$ and cGαi2$^{+/-}$ females. None of the cGαi2$^{-/-}$ females exhibited mounting to male or castrated intruders, although some low levels of mounting were observed in 6% of females, to female intruders (**Figure 3C**). Thus, deletion of Gαi2 in VSNs does not enhance the display of male-specific behaviors in female mice.

We next asked whether normal olfactory preference and lack of mounting to males and females led to normal display of sexual receptivity in cGαi2$^{-/-}$ females. To test this, we measured lordosis behavior, a female sexual stance held in response to male mounting that denotes sexual receptivity. Lordosis requires an intact VNO (Keller et al., 2006; Oboti et al., 2014; Hellier et al., 2018), and is significantly enhanced by experience (Thompson and Edwards, 1971; Bonthuis et al., 2011). Thus, we quantified lordosis response in the presence of a sexually experienced male in three tests separated by 4 days to mimic natural estrus occurrence. We observed low lordosis quotient (LQ; number of lordosis postures divided by the number of mounts received) values during the first test for all animals (LQ = 0.14–0.17; **Figure 3D**). The second test yielded an increase in LQ values of around 0.45, for both cGαi2$^{-/-}$ and cGαi2$^{+/-}$ females (**Figure 3D**). In the third test, however, cGαi2$^{-/-}$ females remained at LQ levels similar to those of the second test (LQ = 0.46; **Figure 3D**), whereas cGαi2$^{+/-}$ control females displayed a further LQ increase (from 0.45 to 0.74; **Figure 3D**). During the third test, each female received 20 mounts from the stud male, but cGαi2$^{-/-}$ females responded displaying less lordosis than cGαi2$^{+/-}$ controls ($P < 0.05$; **Figure 3E**). Furthermore, cGαi2$^{-/-}$ females exhibited a significantly longer latency to show the first lordosis episode (67.4 ± 26.2 s for cGαi2$^{+/-}$ females; 311.8 ± 123.1 s for cGαi2$^{-/-}$; $P < 0.05$; **Figure 3F**). Taken together, these results indicate that Gαi2 vomeronasal neurons play a critical role in the acquisition of complete sexual receptivity in females, but not in olfactory preference and sexual partner choice.

Reduced c-Fos Expression in the AOB and RP3V of Gαi2-Mutant Females

We further investigated neuronal activity after sexual behavior in downstream vomeronasal neural pathways in the brain. First, we quantified c-Fos expression in the AOB (**Figures 4A,B**). In control cGαi2$^{+/-}$ females, the number of c-Fos+ cells in the AOB was elevated (∼100 cells/section) in both the anterior and posterior AOB (**Figure 4A**). By contrast, cGαi2$^{-/-}$ females displayed significantly lower number of c-Fos+ in the anterior AOB (15 cells/section; $P < 0.001$; **Figure 4A**), while c-Fos+ cells in the posterior AOB was not significantly different from cGαi2$^{+/-}$ controls (58 cells/section; $P = 0.06$; **Figure 4A**). This

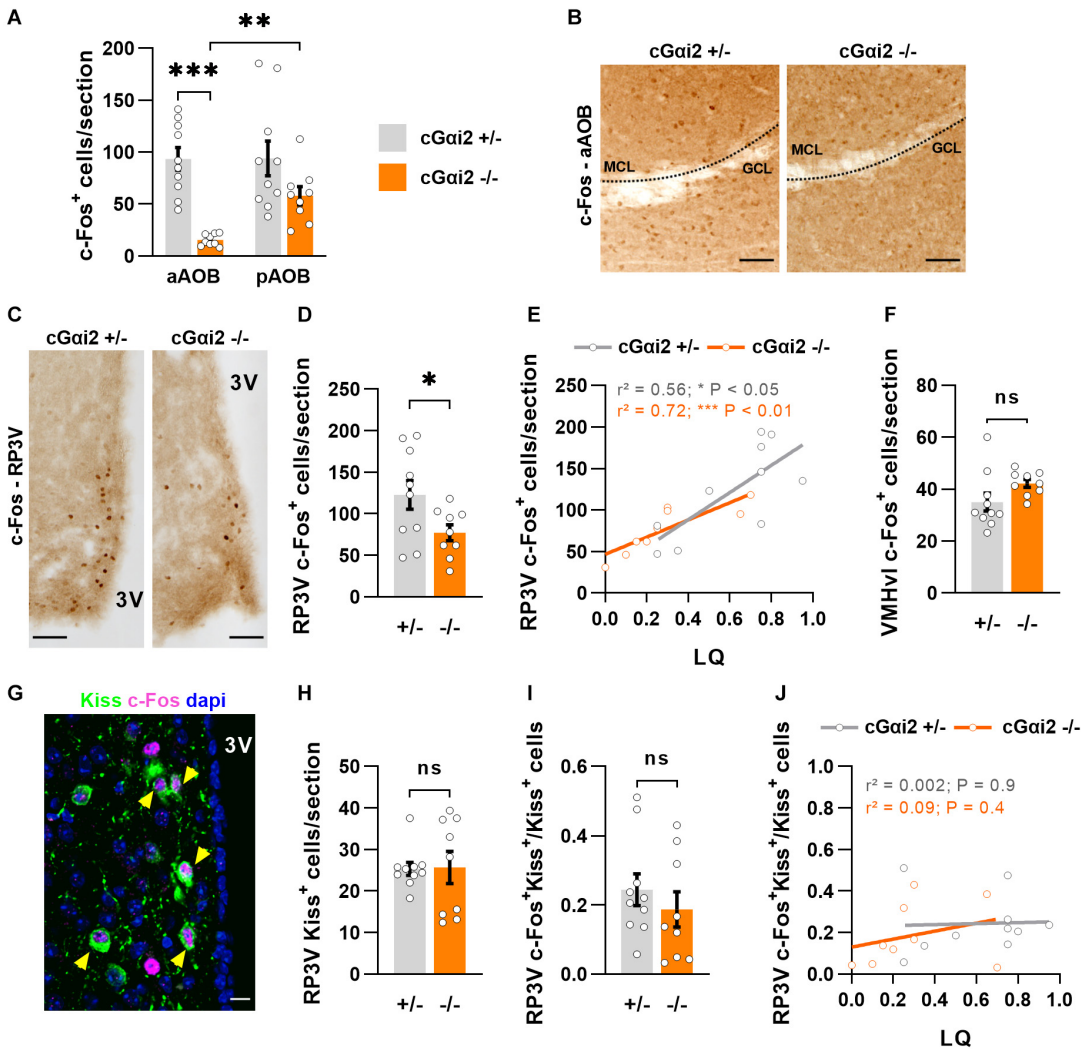

FIGURE 4 | Reduced neural activity in the AOB and RP3V of Gαi2-mutant females. **(A,B)** Analysis of c-Fos immunodetection in the AOB of cGαi2$^{+/-}$ ($N = 10$) and cGαi2$^{-/-}$ ($N = 9$) females after sexual behavior. **(A)** Quantification of c-Fos+ cells per section reveals a decreased c-Fos activation in the aAOB of cGαi2$^{-/-}$ [Two-way repeated measures ANOVA: (genotype) $F_{(1,17)} = 18.28$, $P < 0.001$; (region) $F_{(1,17)} = 5.82$, $P < 0.05$; (genotype × region) $F_{(1,17)} = 5.53$, $P < 0.05$; Bonferroni *post hoc* tests: cGαi2$^{-/-}$ aAOB vs. cGαi2$^{-/-}$ pAOB, $P < 0.01$; cGαi2$^{+/-}$ aAOB vs. cGαi2$^{-/-}$ aAOB $P < 0.001$; other comparisons $P = 0.06$–0.9). All three AOB layers were quantified. **(B)** Examples of c-Fos immunolabeling in the aAOB of cGαi2$^{+/-}$ and cGαi2$^{-/-}$females after sexual behavior. Scale bars, 50 μm. **(C–E)** c-Fos immunodetection in the RP3V of cGαi2$^{+/-}$ ($N = 10$) and cGαi2$^{-/-}$ ($N = 9$) females. **(C)** Examples of c-Fos immunodetection in the RP3V of cGαi2$^{+/-}$ and cGαi2$^{-/-}$females after sexual behavior. Scale bars, 50 μm. **(D)** Quantification of c-Fos+ cells per section in the RP3V of cGαi2$^{-/-}$ (*t*-test: $P < 0.05$). **(E)** Positive correlation between the number of RP3V-c-Fos+ cells and lordosis quotient (LQ) in cGαi2$^{+/-}$ and cGαi2$^{-/-}$ females (Pearson's correlation; cGαi2$^{+/-}$: $r^2 = 0.56$, $P < 0.05$; cGαi2$^{-/-}$: $r^2 = 0.72$, $P < 0.01$). **(F)** c-Fos immunodetection in the VMHvl of cGαi2$^{+/-}$ ($N = 10$) and cGαi2$^{-/-}$ ($N = 9$) females after sexual behavior. Quantification is not different between genotypes (*t*-test: $P = 0.08$). **(G–J)** Analysis of kisspeptin and c-Fos double immunostaining in the RP3V. **(G)** Example of Kiss and c-Fos immunostaining in the RP3V of a cGαi2$^{+/-}$ female. The yellow arrows indicate double labeled c-Fos-Kiss neurons. Scale bar, 10 μm. Quantifications of Kiss+ neurons **(H)** and double-labeled c-Fos+Kiss+ neurons **(I)** are not different between genotypes (Mann-Whitney: $P = 0.9$; *t*-test: $P = 0.4$, respectively). **(J)** Correlative analysis between the number of c-Fos+Kiss+ cells in the RP3V and the LQ (Pearson's correlation; cGαi2$^{+/-}$: $r^2 = 0.002$, $P = 0.9$; cGαi2$^{-/-}$: $r^2 = 0.09$, $P = 0.4$). AOB, accessory olfactory bulb (aAOB, anterior AOB; pAOB, posterior AOB); 3V, third ventricle; RP3V, rostral periventricular area of the third ventricle; VMHvl, ventrolateral part of the ventromedial hypothalamic nucleus; Kiss, kisspeptin. *$P < 0.05$; **$P < 0.01$; ***$P < 0.001$.

result suggests that Gαi2-independent VNO activity is sufficient for the display of basal levels of sexual receptivity.

We further asked whether this reduction of sensory information may have an impact on the neural activity of the rostral periventricular area of the third ventricle (RP3V), a hypothalamic region involved in the control of female sexual behavior and activated by male pheromones (Simerly, 2002; Bakker et al., 2010; Hellier et al., 2018; Inoue et al., 2019; **Figures 4C–E**). We thus counted c-Fos+ nuclei in the RP3V of the same females after sexual behavior. Consistent with a reduced sensory input, the density of c-Fos+ nuclei was lower in cGαi2$^{-/-}$ females vs. cGαi2$^{+/-}$ controls ($P < 0.05$; **Figures 4C,D**). To determine whether the extent of c-Fos+ cells in the RP3V was linked to sexual receptivity, we performed a correlation analysis between c-Fos cell density and LQ (**Figure 4E**). The number of c-Fos+ cells was positively correlated with the LQ in both genotypes (**Figure 4E**), suggesting that the level of sexual receptivity displayed may depend on RP3V neural activity. c-Fos activation in the ventrolateral part of the ventromedial hypothalamic nucleus (VMHvl), a region innervated by RP3V neurons and also involved in the control of female sexual behavior (Pfaff and Sakuma, 1979), revealed no significant differences (**Figure 4F**), suggesting that the observed alterations in cGαi2$^{-/-}$ female receptivity are likely coded upstream of VMHvl neurons.

To further characterize in more detail the activated RP3V neurons in cGαi2$^{-/-}$ females, we asked whether these cells belong to a neuronal subpopulation positive for the neuropeptide kisspeptin (Kiss), which is essential to trigger the lordosis response (Hellier et al., 2018; **Figures 4G–J**). Using double label immunostaining we found neurons that were positive for both c-Fos^{+} and Kiss in all animals (**Figure 4G**). We observed no difference in the density of Kiss^{+} neurons and the number of double-labeled c-Fos^{+}/Kiss^{+} neurons in both cGαi2$^{-/-}$ and cGαi2$^{+/-}$ females (P = 0.4–0.9; **Figures 4H,I**). To establish whether the level of sexual receptivity is linked to the number of activated kisspeptin neurons in the RP3V, we performed a correlation analysis between c-Fos+/Kiss+ cell density and the LQ (**Figure 4J**). We did not observe any obvious correlation between the number of activated kisspeptin neurons and the LQ for any of the two genotypes (r^2 = 0.002 and 0.09; **Figure 4J**), suggesting that an increase in sexual receptivity does not require the recruitment of additional kisspeptin neurons. Collectively, these results indicate that Gαi2 vomeronasal signaling is dispensable for the display of basal levels of lordosis, but participates in the acquisition of complete sexual receptivity, possibly through RP3V kisspeptin-negative neurons.

Gαi2 Deletion Has No Impact on Reproductive Physiology

Reduced receptivity to males could be a consequence of not only defective VNO chemodetection but also of altered reproductive physiology. Indeed, females with a total or partial ablation of VNO function (Trpc2$^{-/-}$ and cGαo$^{-/-}$ females) exhibit profound alterations in puberty onset and estrus cyclicity, even in the absence of external stimuli (Flanagan et al., 2011; Oboti et al., 2014).

Therefore, as a further control and to verify that the described loss of functions by the conditional Gαi2 ablation are indeed caused by a loss of VNO signaling and not by defective reproductive physiology, we investigated the impact of Gαi2 deletion on the timing of estrus and ovulation. First, we characterized puberty onset of juvenile female mice. Control cGαi2$^{+/-}$ and cGαi2$^{-/-}$ females were examined for the onset of vaginal opening and first estrus. Animals from

TABLE 1 | cGαi2$^{-/-}$ females show normal reproductive physiology.

		cGα i2$^{+/-}$	cGα i2$^{-/-}$	Statistic	*P*-value	
Puberty						
	Age at vaginal opening (days)	34.6 ± 0.8 (17)	35.1 ± 0.8 (15)	Unpaired *t*-test	0.6	*ns*
	Age at first estrus (days)	36.2 ± 0.7 (17)	36.8 ± 0.6 (15)	Unpaired *t*-test	0.5	*ns*
Estrus cycle						
	Cycle length (days)	4.9 ± 0.1 (47)	5.5 ± 0.2 (47)	Mann-Whitney	0.1	*ns*
	Proestrus + estrus days	6.6 ± 0.2 (47)	6.4 ± 0.2 (45)	Mann-Whitney	0.5	*ns*
Serum steroids levels						
Progesterone (ng.mL^{-1})	Follicular phase	3.2 ± 0.7 (10)	5.6 ± 1.3 (7)	Mann-Whitney	0.2	*ns*
	Luteal phase	7.9 ± 1.2 (36)	7.9 ± 1.5 (26)	Mann-Whitney	0.9	*ns*
Reproductive organs weight						
Ovaries (%bw)		0.033 ± 0.001 (27)	0.034 ± 0.002 (31)	Mann-Whitney	0.4	*ns*
Uterus (%bw)	Follicular phase	0.29 ± 0.02 (25)	0.32 ± 0.03 (21)	Kruskal-Wallis	0.9	*ns*
	Luteal phase	0.23 ± 0.02 (19) †	0.2 ± 0.01 (28) ‡		0.2	*ns*
Fertility						
	Pregnant females (%)	67/76 (88%)	54/67 (81%)	Fisher's exact test	0.2	*ns*
	Delivery latency (days)	22.4 ± 0.3 (76)	23.3 ± 0.4 (67)	Mann-Whitney	0.2	*ns*
	Litter size	7.8 ± 0.4 (76)	7.1 ± 0.5 (67)	Mann-Whitney	0.3	*ns*

† *and* ‡, *respectively, P < 0.05 and P < 0.001 vs. the uterus weight during the follicular phase. bw, body weight. Assessment of puberty onset, estrus cyclicity, sex steroids levels, reproductive organs weight, and fertility parameters of control and cGαi2*$^{-/-}$ *females. Values are means ± SEM of the indicated number (n) of females.*

both genotypes displayed vaginal opening around postnatal day 35 (P = 0.6; **Table 1**) and first estrus a day later (P = 0.5; **Table 1**), indicating normal puberty onset in Gαi2 mutants. Next, we analyzed estrus cycles of adult, group-housed female mice during a 2 week interval. Both control cGαi2$^{+/-}$ and cGαi2$^{-/-}$ females displayed consistent estrus cycles with no difference in the mean cycle duration (P = 0.1; **Table 1**) and similar number of proestrus and estrus days (P = 0.5; **Table 1**). Consistent with normal ovarian function, levels of circulating progesterone during the follicular or luteal phases (P = 0.2 and 0.9; **Table 1**), and average ovarian weight were not different between cGαi2$^{-/-}$ and cGαi2$^{+/-}$ females (P = 0.2–0.9; **Table 1**). We measured uterus weight as a proxy for circulating estradiol, and found a weight decrease during the luteal vs. follicular phases (P < 0.001 and 0.05; **Table 1**), but no differences between genotypes (P = 0.2–0.9; **Table 1**). Finally, we compared three fertility parameters—percentage of pregnant females after 7 days, delivery latency and litter size—and found no differences between cGαi2$^{-/-}$ and cGαi2$^{+/-}$ (P = 0.2–0.3; **Table 1**). Together, these findings indicate that reproductive physiology and ovarian function are normal in cGαi2$^{-/-}$ females.

DISCUSSION

The central hypothesis of this study was that detection of environmental stimuli by the VNO modulates experience-dependent plasticity, possibly influencing the display of social behaviors in female mice. To test this hypothesis, we chose an animal model with a conditional mutation for Gαi2 gene, which harbors a partial loss of VNO function (Trouillet et al., 2019), and two experimental paradigms (pup retrieval and sexual receptivity) that are strongly dependent on social experience (repeated contact with pups or the male). We previously showed that Gαi2 is necessary for the detection of small organic pheromones by apical VSNs, and genetic ablation of these neurons severely impairs pup-directed aggression in virgin males (Trouillet et al., 2019). This is consistent with published studies that show that pup cues preferentially activate neurons located in the apical VNO and the anterior AOB in virgin males (Tachikawa et al., 2013; Nakahara et al., 2020). Our results show higher c-Fos activation in the anterior AOB after pup-exposure (**Figures 1C,D**), indicating that pups are also preferentially detected by Gαi2+ VSNs in virgin females.

In contrast to males, we found that deletion of Gαi2 in virgin females does not increase parental care (i.e., grooming) toward pups, but reduces pup retrieval (**Figures 1A,B**). Interestingly, mutant females that retrieve pups still display other types of parenting behaviors such as grooming and nesting, suggesting that different pup care behaviors are controlled independently. Importantly, Gαi2 deletion does not affect pup retrieval and maternal aggression in mothers (**Figure 2**), indicating that other neural substrates different from Gαi2^{+} VSNs control these behaviors, likely by auditory, olfactory and Gαo-dependent signals (Chamero et al., 2011; Weiss et al., 2011; Fraser and Shah, 2014; Marlin et al., 2015).

The mechanism by which social experience drives neural plasticity to modify the behaviors display is unclear. Not only centrally controlled neural changes, but also sensory organ sensitivity to olfactory stimuli have been suggested to have an influence. In particular, previous studies report a decline in VNO activity induced by pup cues in virgin males after cohabitation with a pregnant female (Tachikawa et al., 2013; Nakahara et al., 2020), suggesting the existence of a silencing mechanism at the

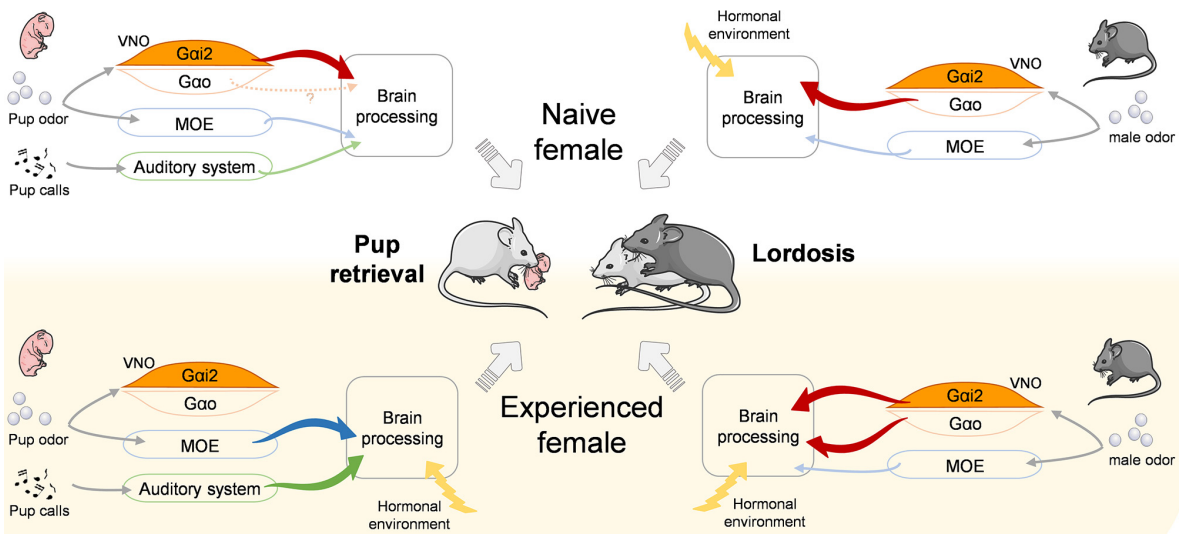

FIGURE 5 | Model for the proposed control of pup retrieval and lordosis behaviors depending on social experience. Olfactory and auditory cues relevant for pup retrieval (***left***) and lordosis (***right***) behaviors are differentially processed by the sensory systems and the brain in naïve (***top***) and experienced (***down***) females. Significantly, Gαi2+ vomeronasal neurons are activated by pup odor in naïve females to trigger retrieval but are dispensable in experienced females. Inversely, they are dispensable in naïve females to trigger the lordosis response but become necessary in experienced females to reach high lordosis levels. VNO, vomeronasal organ; MOE, main olfactory epithelium.

level of VSNs. We can thus speculate that a similar process may occur in females after parturition, either induced by hormonal changes intrinsic to gestation, or by repeated exposure to pups. Indeed, pup retrieval is improved in virgin females after co-housing with a dam and litter, even after ovariectomy (Ehret et al., 1987; Koch and Ehret, 1989; Stolzenberg and Rissman, 2011; Elyada and Mizrahi, 2015), suggesting that pup signals modulate the behavioral response. In this scenario, hormones such as oxytocin may influence experience-dependent plasticity directly at the sensory processing level (Fleming et al., 1979; Marlin et al., 2015; Nakahara et al., 2020).

Studies on Trpc2$^{-/-}$ mice suggest that sex discrimination and opposite-sex preference depend on a functional VNO because of indiscriminate mounting expressed by males and females (Leypold et al., 2002; Stowers et al., 2002; Kimchi et al., 2007). Other studies point to a significant role of testosterone levels (rather than VNO function) to explain the unusual mounting of Trpc2$^{-/-}$ females (Martel and Baum, 2009). The absence of mounting behavior in our Gαi2 mutant females (**Figure 3C**) as well as in conditional Gαo mutants (Oboti et al., 2014), suggest a minor role of the VNO in the control of sexual preference in females. Nonetheless, either the apical or basal VSN layers alone may be sufficient to enable sex preference by using redundant neural pathways (Chamero et al., 2012). Further research is required to elucidate the control of sexual preference.

Although many aspects of sexual receptivity in females may be innate, acquiring elevated levels of lordosis performance depends on the combination of adequate hormonal environment with sensory experience (Thompson and Edwards, 1971). It has been shown that lesions of the VNO and AOB reduce the lordosis quotient of sexually naïve females (Keller et al., 2006; Martel and Baum, 2009) and that acute inhibition of AOB activity reduces the lordosis quotient of sexually experienced females (McCarthy et al., 2017). Our results show that Gαi2-dependent VNO activity is dispensable for the display of basal levels of lordosis (**Figure 3**), which likely depends on Gαo signaling (Oboti et al., 2014). After mating experience, however, we demonstrate that Gαi2+ VSNs play a critical role in the acquisition of complete sexual receptivity in females, transforming weaker responses into more robust and frequent lordosis episodes (**Figure 3**). Thus, synergy between innate and experience-dependent processes may be critical for fast, efficient, and flexible display of complex behaviors.

We have screened for the expression of c-Fos, an early gene linked to neural activity, in the brain and found that the number of c-Fos+ cells was reduced in the anterior AOB and RP3V of cGαi2$^{-/-}$ females after lordosis (**Figure 4**). This reduction in c-Fos+ neurons in both regions is consistent with reduced sensory input from the VNO. However, we observe a positive correlation of the number of c-Fos+ cells in the RP3V with lordosis, also in control animals (**Figure 4E**). Further experiments are needed to establish causality, but these results suggest that neural activity in the RP3V may regulate the level of sexual receptivity integrating sensory information from Gαi2+ neurons. In particular, RP3V-kisspeptin neurons seem to be essential to trigger lordosis (Hellier et al., 2018), although activity of these cells is not lower in cGαi2$^{-/-}$ females (**Figure 4I**). This is in line with the view that the display of basal levels of lordosis is largely Gαi2-independent and suggests that the recruitment of additional RP3V-kisspeptin neurons is not required to increase lordosis performance. In accordance with this, non-kisspeptin neurons in the RP3V, such as tyrosine-hydroxylase (TH) positive neurons, are also sensitive to male odors (Bakker et al., 2010; Taziaux and Bakker, 2015). Remarkably, targeted ablation of TH neurons in the RP3V does not seem to reduce the lordosis quotient in sexually naïve females (Scott et al., 2015). Further research is needed to establish whether TH neurons in the RP3V participate in the acquisition of sexual experience.

Our findings complement recent studies of neural circuits involved in social behavior by revealing that experience-dependent improvement of ethologically important behaviors can be shaped by sensory components (**Figure 5**). This may exemplify a mechanism of neuroplasticity in which olfaction in combination with social experience improve social behavior synergistically.

DATA AVAILABILITY STATEMENT

The raw data supporting the conclusions of this article will be made available by the authors, without undue reservation.

ETHICS STATEMENT

The animal study was reviewed and approved by the CEEA Val de Loire.

AUTHOR CONTRIBUTIONS

PC, MK, LB, FZ, and TL-Z designed the research. A-CT, CM, and KP performed the research. A-CT and CM analyzed the data. PC and A-CT wrote the manuscript with edits of all authors.

FUNDING

This work was supported by the Deutsche Forschungsgemeinschaft (DFG) grants Sonderforschungsbereich-Transregio TRR 152/P10, project 239283807 (FZ and TL-Z) and Sonderforschungsbereich 894 project A17 (FZ and TL-Z), and Region Centre Val de Loire project 201900134883 (PC). LB was supported in part by the Intramural Research Program of the NIH (Project Z01-ES-101643). A-CT was supported by the grant from the University of Tours and Region Centre Val de Loire.

ACKNOWLEDGMENTS

We thank Deborah Crespin, Flora Martin, and Aurelie Gasnier for mice husbandry; Marie-Claire Blache for help with imaging experiments; the staff of the hormonal assay laboratory; and Isabelle Franceschini for the kisspeptin antibody.

REFERENCES

Bakker, J., Pierman, S., and González-Martínez, D. (2010). Effects of aromatase mutation (ArKO) on the sexual differentiation of kisspeptin neuronal numbers and their activation by same versus opposite sex urinary pheromones. *Horm. Behav.* 57, 390–395. doi: 10.1016/j.yhbeh.2009.11.005

Bonthuis, P. J., Patteson, J. K., and Rissman, E. F. (2011). Acquisition of sexual receptivity: roles of chromatin acetylation, estrogen receptor-α, and ovarian hormones. *Endocrinology* 152, 3172–3181. doi: 10.1210/en.2010-1001

Chamero, P., Katsoulidou, V., Hendrix, P., Bufe, B., Roberts, R., Matsunami, H., et al. (2011). G protein G o is essential for vomeronasal function and aggressive behavior in mice. *Proc. Natl. Acad. Sci. U.S.A.* 108, 12898–12903. doi: 10.1073/pnas.1107770108

Chamero, P., Leinders-Zufall, T., and Zufall, F. (2012). From genes to social communication: molecular sensing by the vomeronasal organ. *Trends Neurosci.* 35, 597–606. doi: 10.1016/j.tins.2012.04.011

Del Punta, K., Leinders-Zufall, T., Rodriguez, I., Jukam, D., Wysocki, C. J., Ogawa, S., et al. (2002). Deficient pheromone responses in mice lacking a cluster of vomeronasal receptor genes. *Nature* 419, 70–74. doi: 10.1038/nature00955

Ehret, G., Koch, M., Haack, B., and Markl, H. (1987). Sex and parental experience determine the onset of an instinctive behavior in mice. *Naturwissenschaften* 74, 47–47. doi: 10.1007/BF00367047

Elyada, Y. M., and Mizrahi, A. (2015). Becoming a mother—circuit plasticity underlying maternal behavior. *Curr. Opin. Neurobiol.* 35, 49–56. doi: 10.1016/j.conb.2015.06.007

Ferrero, D. M., Moeller, L. M., Osakada, T., Horio, N., Li, Q., Roy, D. S., et al. (2013). A juvenile mouse pheromone inhibits sexual behaviour through the vomeronasal system. *Nature* 502, 368–371. doi: 10.1038/nature12579

Flanagan, K. A., Webb, W., and Stowers, L. (2011). Analysis of male pheromones that accelerate female reproductive organ development. *PLoS One* 6:e16660. doi: 10.1371/journal.pone.0016660

Fleming, A., Vaccarino, F., Tambosso, L., and Chee, P. (1979). Vomeronasal and olfactory system modulation of maternal behavior in the rat. *Science (80)* 203, 372–374. doi: 10.1126/science.760196

Franceschini, I., Yeo, S. H., Beltramo, M., Desroziers, E., Okamura, H., Herbison, A. E., et al. (2013). Immunohistochemical evidence for the presence of various kisspeptin isoforms in the mammalian brain. *J. Neuroendocrinol.* 25, 839–851. doi: 10.1111/jne.12069

Fraser, E. J., and Shah, N. M. (2014). Complex chemosensory control of female reproductive behaviors. *PLoS One* 9:e90368. doi: 10.1371/journal.pone.0090368

Hasen, N. S., and Gammie, S. C. (2009). Trpc2 gene impacts on maternal aggression, accessory olfactory bulb anatomy and brain activity. *Genes Brain Behav.* 8, 639–649. doi: 10.1111/j.1601-183X.2009.00511.x

Hellier, V., Brock, O., Candlish, M., Desroziers, E., Aoki, M., Mayer, C., et al. (2018). Female sexual behavior in mice is controlled by kisspeptin neurons. *Nat. Commun.* 9:400. doi: 10.1038/s41467-017-02797-2

Inoue, S., Yang, R., Tantry, A., Davis, C., Yang, T., Knoedler, J. R., et al. (2019). Periodic remodeling in a neural circuit governs timing of female sexual behavior. *Cell* 179, 1393–1408.e16. doi: 10.1016/j.cell.2019.10.025

Ishii, K. K., and Touhara, K. (2019). Neural circuits regulating sexual behaviors via the olfactory system in mice. *Neurosci. Res.* 140, 59–76. doi: 10.1016/j.neures.2018.10.009

Isogai, Y., Wu, Z., Love, M. I., Ahn, M. H.-Y., Bambah-Mukku, D., Hua, V., et al. (2018). Multisensory logic of infant-directed aggression by males. *Cell* 175, 1827–1841.e17. doi: 10.1016/j.cell.2018.11.032

Jouhanneau, M., Cornilleau, F., and Keller, M. (2014). Peripubertal exposure to male odors influences female puberty and adult expression of male-directed odor preference in mice. *Horm. Behav.* 65, 128–133. doi: 10.1016/j.yhbeh.2013.12.006

Keller, M., Baum, M. J., Brock, O., Brennan, P. A., and Bakker, J. (2009). The main and the accessory olfactory systems interact in the control of mate recognition and sexual behavior. *Behav. Brain Res.* 200, 268–276. doi: 10.1016/j.bbr.2009.01.020

Keller, M., Pierman, S., Douhard, Q., Baum, M. J., and Bakker, J. (2006). The vomeronasal organ is required for the expression of lordosis behaviour, but not sex discrimination in female mice. *Eur. J. Neurosci.* 23, 521–530. doi: 10.1111/j.1460-9568.2005.04589.x

Kimchi, T., Xu, J., and Dulac, C. (2007). A functional circuit underlying male sexual behaviour in the female mouse brain. *Nature* 448, 1009–1014. doi: 10.1038/nature06089

Koch, M., and Ehret, G. (1989). Estradiol and parental experience, but not prolactin are necessary for ultrasound recognition and pup-retrieving in the mouse. *Physiol. Behav.* 45, 771–776. doi: 10.1016/0031-9384(89)90293-X

Kohl, J., Autry, A. E., and Dulac, C. (2017). The neurobiology of parenting: a neural circuit perspective. *BioEssays* 39, 1–11. doi: 10.1002/bies.201600159

Lévy, F., Keller, M., and Poindron, P. (2004). Olfactory regulation of maternal behavior in mammals. *Horm. Behav.* 46, 284–302. doi: 10.1016/j.yhbeh.2004.02.005

Leypold, B. G., Yu, C. R., Leinders-Zufall, T., Kim, M. M., Zufall, F., and Axel, R. (2002). Altered sexual and social behaviors in trp2 mutant mice. *Proc. Natl. Acad. Sci. U.S.A.* 99, 6376–6381. doi: 10.1073/pnas.082127599

Marlin, B. J., Mitre, M., D'Amour, J. A., Chao, M. V., and Froemke, R. C. (2015). Oxytocin enables maternal behaviour by balancing cortical inhibition. *Nature* 520, 499–504. doi: 10.1038/nature14402

Martel, K. L., and Baum, M. J. (2009). Adult testosterone treatment but not surgical disruption of vomeronasal function augments male-typical sexual behavior in female mice. *J. Neurosci.* 29, 7658–7666. doi: 10.1523/jneurosci.1311-09.2009

McCarthy, E. A., Kunkhyen, T., Korzan, W. J., Naik, A., Maqsudlu, A., Cherry, J. A., et al. (2017). A comparison of the effects of male pheromone priming and optogenetic inhibition of accessory olfactory bulb forebrain inputs on the sexual behavior of estrous female mice. *Horm. Behav.* 89, 104–112. doi: 10.1016/j.yhbeh.2016.12.011

Nakahara, T. S., Camargo, A. P., Magalhães, P. H. M., Souza, M. A. A., Ribeiro, P. G., Martins-Netto, P. H., et al. (2020). Peripheral oxytocin injection modulates vomeronasal sensory activity and reduces pup-directed aggression in male mice. *Sci. Rep.* 10:19943. doi: 10.1038/s41598-020-77061-7

Nakahara, T. S., Cardozo, L. M., Ibarra-Soria, X., Bard, A. D., Carvalho, V. M. A., Trintinalia, G. Z., et al. (2016). Detection of pup odors by non-canonical adult vomeronasal neurons expressing an odorant receptor gene is influenced by sex and parenting status. *BMC Biol.* 14:12. doi: 10.1186/s12915-016-0234-9

Norlin, E. M., Gussing, F., and Berghard, A. (2003). Vomeronasal phenotype and behavioral alterations in Gαi2 mutant mice. *Curr. Biol.* 13, 1214–1219. doi: 10.1016/S0960-9822(03)00452-4

Numan, M. (1974). Medial preoptic area and maternal behavior in the female rat. *J. Comp. Physiol. Psychol.* 87, 746–759. doi: 10.1037/h0036974

Oboti, L., Pérez-Gómez, A., Keller, M., Jacobi, E., Birnbaumer, L., Leinders-Zufall, T., et al. (2014). A wide range of pheromone-stimulated sexual and reproductive behaviors in female mice depend on G protein Gαo. *BMC Biol.* 12:31. doi: 10.1186/1741-7007-12-31

Pfaff, D. W., and Sakuma, Y. (1979). Deficit in the lordosis reflex of female rats caused by lesions in the ventromedial nucleus of the hypothalamus. *J. Physiol.* 288, 203–210. doi: 10.1113/jphysiol.1979.sp012691

Scott, N., Prigge, M., Yizhar, O., and Kimchi, T. (2015). A sexually dimorphic hypothalamic circuit controls maternal care and oxytocin secretion. *Nature* 525, 519–522. doi: 10.1038/nature15378

Simerly, R. B. (2002). Wired for reproduction: organization and development of sexually dimorphic circuits in the mammalian forebrain. *Annu. Rev. Neurosci.* 25, 507–536. doi: 10.1146/annurev.neuro.25.112701.142745

Stolzenberg, D. S., and Rissman, E. F. (2011). Oestrogen-independent, experience-induced maternal behaviour in female mice. *J. Neuroendocrinol.* 23, 345–354. doi: 10.1111/j.1365-2826.2011.02112.x

Stowers, L., Holy, T. E., Meister, M., Dulac, C., and Koentges, G. (2002). Loss of sex discrimination and male-male aggression in mice deficient for TRP2. *Science* 295, 1493–1500. doi: 10.1126/science.1069259

Stowers, L., and Kuo, T.-H. (2015). Mammalian pheromones: emerging properties and mechanisms of detection. *Curr. Opin. Neurobiol.* 34, 103–109. doi: 10.1016/j.conb.2015.02.005

Stowers, L., and Liberles, S. D. (2016). State-dependent responses to sex pheromones in mouse. *Curr. Opin. Neurobiol.* 38, 74–79. doi: 10.1016/j.conb.2016.04.001

Tachikawa, K. S., Yoshihara, Y., and Kuroda, K. O. (2013). Behavioral transition from attack to parenting in male mice: a crucial role of the vomeronasal system. *J. Neurosci.* 33, 5120–5126. doi: 10.1523/JNEUROSCI.2364-12.2013

Taziaux, M., and Bakker, J. (2015). Absence of female-typical pheromone-induced hypothalamic neural responses and kisspeptin neuronal activity in

α-fetoprotein knockout female mice. *Endocrinology* 156, 2595–2607. doi: 10.1210/en.2015-1062

Thompson, M. L., and Edwards, D. A. (1971). Experiential and strain determinants of the estrogen-progesterone induction of sexual receptivity in spayed female mice. *Horm. Behav.* 2, 299–305. doi: 10.1016/0018-506X(71)90004-3

Trouillet, A.-C., Keller, M., Weiss, J., Leinders-Zufall, T., Birnbaumer, L., Zufall, F., et al. (2019). Central role of G protein Gαi2 and Gαi2 + vomeronasal neurons in balancing territorial and infant-directed aggression of male mice. *Proc. Natl. Acad. Sci. U.S.A.* 116, 5135–5143. doi: 10.1073/pnas.1821492116

Weiss, J., Pyrski, M., Jacobi, E., Bufe, B., Willnecker, V., Schick, B., et al. (2011). Loss-of-function mutations in sodium channel Na v 1.7 cause anosmia. *Nature* 472, 186–192. doi: 10.1038/nature09975

Wu, Z., Autry, A. E., Bergan, J. F., Watabe-Uchida, M., and Dulac, C. G. (2014). Galanin neurons in the medial preoptic area govern parental behaviour. *Nature* 509, 325–330. doi: 10.1038/nature13307

Wysocki, C. J., and Lepri, J. J. (1991). Consequences of removing the vomeronasal organ. *J. Steroid Biochem. Mol. Biol.* 39, 661–669. doi: 10.1016/0960-0760(91)90265-7

Conflict of Interest: The authors declare that the research was conducted in the absence of any commercial or financial relationships that could be construed as a potential conflict of interest.

frontiers in Cellular Neuroscience

ORIGINAL RESEARCH
published: 25 February 2021
doi: 10.3389/fncel.2021.646413

Genetic Background Effects on the Expression of an Odorant Receptor Gene

*Artur Guazzelli Leme Silva, Maira Harume Nagai†, Thiago Seike Nakahara and Bettina Malnic**

Department of Biochemistry, University of São Paulo, São Paulo, Brazil

OPEN ACCESS

Edited by:
Jeremy C. McIntyre, University of Florida, United States

Reviewed by:
Timothy McClintock, University of Kentucky, United States
Simone Pifferi, International School for Advanced Studies (SISSA), Italy
Casey Trimmer, Firmenich SA, Switzerland

***Correspondence:**
Bettina Malnic
bmalnic@iq.usp.br

†Present address:
Maira Harume Nagai, Department of Molecular Genetics and Microbiology, Duke University Medical Center, Durham, NC, United States

Specialty section:
This article was submitted to Cellular Neurophysiology, a section of the journal Frontiers in Cellular Neuroscience

Received: *26 December 2020*
Accepted: *08 February 2021*
Published: *25 February 2021*

Citation:
Leme Silva AG, Nagai MH, Nakahara TS and Malnic B (2021) Genetic Background Effects on the Expression of an Odorant Receptor Gene. Front. Cell. Neurosci. 15:646413. doi: 10.3389/fncel.2021.646413

There are more than 1000 odorant receptor (OR) genes in the mouse genome. Each olfactory sensory neuron expresses only one of these genes, in a monoallelic fashion. The transcript abundance of homologous OR genes vary between distinct mouse strains. Here we analyzed the expression of the OR gene *Olfr17* (also named P2) in different genomic contexts. *Olfr17* is expressed at higher levels in the olfactory epithelium from 129 mice than from C57BL/6 (B6) mice. However, we found that in P2-IRES-tauGFP knock-in mice, the transcript levels of the 129 *Olfr17* allele are highly reduced when compared to the B6 *Olfr17* allele. To address the mechanisms involved in this variation we compared the 5′ region sequence and DNA methylation patterns of the B6 and 129 *Olfr17* alleles. Our results show that genetic variations in *cis* regulatory regions can lead to differential DNA methylation frequencies in these OR gene alleles. They also show that expression of the *Olfr17* alleles is largely affected by the genetic background, and suggest that in knock-in mice, expression can be affected by epigenetic modifications in the region of the targeted locus.

Keywords: DNA methylation, odorant receptor gene, olfactory receptor gene, genetic background, gene expression, single nucleotide polymorphism

INTRODUCTION

Odorants are detected by a large family of odorant receptors (ORs) expressed in the olfactory sensory neurons of the nose (Buck and Axel, 1991). In the mouse genome, there are more than 1000 different OR genes, which are spread over almost all chromosomes (Zhang and Firestein, 2002; Godfrey et al., 2004). A recent comprehensive analysis found that there are in total 1141 protein-coding OR genes plus 342 OR pseudogenes in the mouse genome (Barnes et al., 2020). Each olfactory sensory neuron in the olfactory epithelium expresses one single OR gene out of the complete repertoire, through a tight mechanism of gene regulation, which is not completely understood (Chess et al., 1994; Malnic et al., 1999; Monahan and Lomvardas, 2015; Nagai et al., 2016).

Different members of the OR gene family show unequal levels of gene expression in the olfactory epithelium (Young et al., 2003; Zhang et al., 2004; Rodriguez-Gil et al., 2010; Khan et al., 2011; Ibarra-Soria et al., 2017). In addition, transcript abundance of homologous OR genes vary extensively between different mouse strains (Ibarra-Soria et al., 2017). Little is known about the mechanisms involved in this variation.

Odorant receptor gene expression encompasses various levels of regulation, involving both regulatory DNA sequences and epigenetic modifications (Monahan and Lomvardas, 2015; Nagai et al., 2016; Degl'innocenti and D'errico, 2017). *Cis* acting regulatory elements like the H and P enhancers were shown to play important roles in OR gene expression (Serizawa et al., 2003; Bozza et al., 2009; Khan et al., 2011). OR gene promoter regions and enhancer sequences are enriched in binding motifs for homeodomain and O/E-like transcription factors (Vassalli et al., 2002; Rothman et al., 2005; Hoppe et al., 2006; Michaloski et al., 2006; Hirota et al., 2007; Nishizumi et al., 2007; Young et al., 2011; Cichy et al., 2019) and motifs for other types of transcription factors (Clowney et al., 2011; Michaloski et al., 2011; Markenscoff-Papadimitriou et al., 2014; Iwata et al., 2017). These motifs are thought to influence OR gene expression frequency in olfactory sensory neurons (Michaloski et al., 2006; Khan et al., 2011; Vassalli et al., 2011; Plessy et al., 2012; Zhang et al., 2016).

Genetic variations in *cis* regulatory regions were shown to affect OR gene expression in different mouse strains (Ibarra-Soria et al., 2017). Sequence variants generated by single nucleotide polymorphisms (SNPs) may influence transcription factor-binding affinities. Also, binding of transcription factors to their respective DNA binding motifs can be affected, either, negatively or positively, by cytosine methylation (Yin et al., 2017). Even though there is evidence that DNA methylation plays a role in global gene expression in the olfactory epithelium (Macdonald et al., 2005, 2010; Colquitt et al., 2013, 2014), the involvement of DNA methylation in OR gene regulation has been poorly investigated so far.

Here we show that the OR gene *Olfr17* (also named P2) is expressed at different levels depending on the genomic context. While *Olfr17* is expressed at higher levels in the olfactory epithelium from 129 mice than from B6 mice, in P2-IRES-tauGFP knock-in (P2-GFP) mice, the transcript levels of the 129 *Olfr17* allele are highly reduced when compared to the B6 *Olfr17* allele. We found that the *Olfr17* allele from the 129-mouse strain contains SNPs leading to the occurrence of two additional CpG dinucleotides in the 5′ region. As a result, the 5′ region of the 129 *Olfr17* allele shows higher levels of DNA methylation than the one from the B6 *Olfr17* allele. The levels of DNA methylation in the 129 *Olfr17* allele are not reduced in neurons expressing 129 *Olfr17*. Finally, we found that the transcript levels of other OR genes that are in *cis* and close to the targeted locus, are also reduced in the P2-GFP mice.

MATERIALS AND METHODS

Animal Procedures

The mouse strains used were 129S1/SvlmJ, C57BL/6 and the knock-in strain *Olfr17*tm7Mom/MomJ (P2-IRES-tauGFP) (Stock number: 006669, obtained from The Jackson Laboratory). As previously described (Feinstein and Mombaerts, 2004), the P2-GFP mice express the *Olfr17* gene from the 129SvJ mouse strain containing an IRES-tauGFP 3 bp after the stop codon of the gene, and were originally generated in a 129P2/OlaHsd background and bred with a mouse carrying an Ella-cre transgene, a transgene generated in FVB/N but having been backcrossed at least four generations to C57BL/6 before this cross to excise the loxP-flanked neomycin resistance sequence and having unknown pedigree prior to that. The resulting mice, lacking the neomycin resistance cassette, were intercrossed and homozygotes were selected that were devoid of the Ella-cre transgene, and homozygous males were sent to The Jackson Laboratory for cryopreservation of sperm. Upon our request, The Jackson Laboratory performed cryo-recovery of these mice using C57BL/6J (Stock# 000664) females as the oocyte donors. We obtained heterozygous mice from The Jackson Laboratory and intercrossed them to produce the P2-GFP$^{+/+}$, P2-GFP$^{+/-}$, and P2-GFP$^{-/-}$ mice analyzed in this study.

RLM-RACE

RNA ligase-mediated rapid amplification of cDNA ends (RLM-RACE) was performed using the GeneRacer Kit™ as previously described (Michaloski et al., 2006). Total olfactory mucosa RNA was purified from C57BL/6 using TRIzol (Invitrogen, Cat. No. 15596026), following the user guide workflow. The following primers were used to amplify the *Olfr17* gene 5′-UTR: P2_R: TCCTGGAGTATCAGAGTACTC and P2_R_NESTED: CAGAGCAAGAGTCAGCTGTAG.

DNA Bisulfite Sequencing

Olfactory mucosa and liver were dissected from C57BL/6 or *Olfr17*tm7Mom/MomJ knock-in mice in PBS pH 7.4 and the genomic DNA was immediately purified using DNeasy Blood and Tissue Kit (Qiagen, Cat. No. 69504). DNA bisulfite conversion was performed using EpiTect Bisulfite Kits (Qiagen, Cat. No. 59104). The regions of interest were amplified by PCR using the bisulfite converted DNA and the following primers: *Olfr17* promoter region (Forward TGTGTTATGATTGGTATTTTTG, Reverse CCATCCCATTATCTAATAAACTC); *Olfr17* CDS 1 (Forward AGATGTTGAGTATTTTGATATT, Reverse ACATAAAAACCCAAAATCAAC); *Olfr17* CDS 2 (Forward ATAGTTTTAGTTTGTGTTGATA, Reverse CAATATTTCCTTCAACATCCT).

The amplicons were synthetized by Platinum® Taq DNA Polymerase (Invitrogen) and were subcloned using the Dual promoter TA cloning® kit (Invitrogen, 45-0007LT). Individual clones were sequenced using BigDye® Terminator v3.1 Cycle Sequencing Kit (Life Technologies™, Cat. No. 4337455) on an ABI PRISM 3100 Genetic Analyzer (Hitachi). The number of sequenced clones varied from 10 to 17 clones for the experiments with whole olfactory mucosa and from 12 to 25 clones per replica in the case of the dissociated cells (FACS experiments).

FACS

Fluorescence-activated cell sorting (FACS) was performed as described (Leme Silva et al., 2018). Briefly, whole olfactory mucosa was dissected in liquid culture medium CMRL-1066 supplemented with EGTA (2.0 mM) and kept on ice and cell dissociation was carried out as follows. Dissected tissue was incubated with 5 μL DNase (1 U/μL, Invitrogen, Cat. No. 18068-015) for 5 min at room temperature. During incubation, the tissue was pipetted up and down using a glass Pasteur pipette with

polished tip, to obtain better dissociation. After DNase treatment, the tissue was incubated with 200 μL papain (100 U/mL, Sigma No. P 4762) for each 1.0 mL of dissociation solution, for 10 min at 37°C. To remove papain, cells were centrifuged at 300 × *g* for 5 min at 4°C, and the supernatant was discarded. Centrifugation was repeated one more time, the pellet was resuspended in CMRL-1066 containing EGTA (2 mM), and pipetted up and down using a glass Pasteur pipette with polished tip to release the cells. The cellular suspension was filtered in 40 μm mesh twice, and cells were sorted with a FACS Aria III in the Core Facility for Scientific Research – University of São Paulo (CEFAP-USP/FLUIR).

RT-qPCR

Olfactory epithelia were dissected from 6 to 8-week-old mice and total RNA was prepared using TRIzol reagent (Thermo Fisher Scientific). RT-qPCR was performed as described in Michaloski et al. (2011), using the Fast SYBR™ Green Master Mix (Thermo Fisher Scientific, Cat. No. 4385612) and a 7500 Fast Real-Time PCR System (Applied Biosystems). Primer sequences for *Olfr17* were: CTCTGATACTCCAGGACAAAACC (forward) and GGATCACAGATCGCCATGTAG (reverse); for *Olfr6* were: CTTTATGTCCCTTGCCTGTACTG (forward) and ACTGGATAGCGAAGAGGCCAA (reverse); for *Olfr15* were: TGCCTTTACTACCAGTTCAGTCC (forward) and ACACCCACCATAGCTGATTGT (reverse); for *Olfr566* were: CTGTCCTCAGTATCGCCTCCT (forward) and GGGTGCTGACCGACCATATC (reverse); for *Olfr1507* were: CAAATCCGAAAGTACAGATGGCT (forward) and CGGTGGTCGTGTATGATTGTTAT (reverse); for β-actin: AAGGCCAACCGTGAAAAGATG (forward) and GTGGTACGACCAGAGGCATACA (reverse).

In situ Hybridization

In situ hybridization was performed as previously described (Von Dannecker et al., 2005; Camargo et al., 2019). Sections cut through the noses of 3-week-old mice were hybridized with digoxigenin-labeled cRNA probes corresponding to the nucleotides 169–931 within the coding region of the *Olfr17* gene. For **Figure 1A**, the olfactory epithelium from three C57BL6/J and three 129S animals were cut in 16 μm sections parallel to the cribriform plate, in a posterior-anterior direction. Sections were collected in a serial fashion, discarding six 40 μm sections between the series. For each nose, eight different series were collected on 10 microscope slides, resulting in each slide representing all regions of the olfactory epithelium. Each section was imaged using a 10X objective lens and composite images were obtained using Image J Stitching plugin (Preibisch et al., 2009). The olfactory epithelium area for one half of each section was manually defined using Image J's Polygon tool and the total area was calculated in μm^2. The *Olfr17*-positive neurons were manually counted with Image J's Multi-point tool. For **Figure 1C**, the olfactory epithelium was cut as above and adjacent tissue sections were collected on microscope slides, corresponding to locations 1, 2, and 3. Images of the entire *in situ* hybridization sections in **Figure 1C** were acquired by using the TissueFAXS System and the analysis was carried out using TissueFAXS™ Cytometry. Image analysis was done by StrataQuest TissueGnostics, Austria. The number of black spots (positive *in situ* hybridization signals) per olfactory epithelium area (μm^2, shown in green) per slice was determined.

Statistical Analysis

Analysis was performed using the GraphPad Prism software. For more than two groups we employed one-way analysis of variance (ANOVA) followed by a Newman–Keuls *post hoc* test.

RESULTS

Gene Expression Levels of *Olfr17* in Different Mouse Strains

We first determined the transcript levels of *Olfr17* in the olfactory epithelium from the wild type 129 and B6 mouse strains. *In situ* hybridization experiments showed that the number of *Olfr17* expressing olfactory neurons is higher in the 129-mouse strain (7.6×10^{-5} neurons/μm^2 in 129 versus 5.8×10^{-5} neurons/μm^2 in B6; **Figure 1A**). In addition, RT-qPCR experiments, where a pair of primers matching regions that are common to both the 129 and B6 *Olfr17* alleles were used, showed that *Olfr17* transcript levels were higher in the 129 strain than in the B6 strain (**Figure 1B**). These results are in agreement with previous RNA-seq experiments, where the transcriptional profiles of the complete OR repertoire was quantified in different mouse strains (Ibarra-Soria et al., 2017).

We next compared the transcript levels of *Olfr17* in the olfactory epithelium from P2-GFP mice. In these mice, the targeted *Olfr17* is derived from the 129-mouse strain, while the untargeted *Olfr17* is from the B6 strain (Mombaerts et al., 1996; Feinstein and Mombaerts, 2004). We found a significant difference in the transcript levels of the *Olfr17* alleles when the knock-in mice are compared to the wild type mouse strains. In the olfactory epithelium from P2-GFP$^{+/+}$ mice, *Olfr17* is expressed only from 129 alleles, and the *Olfr17* transcript levels are significantly reduced when compared to the levels of the olfactory epithelium from P2-GFP$^{-/-}$ mice, where the *Olfr17* is expressed from the B6 alleles (**Figure 1B**). Accordingly, we found that P2-GFP$^{+/+}$ mice show 30% reduction in the number of *Olfr17* expressing neurons in comparison to the P2-GFP$^{-/-}$ mice (9.1×10^{-5} neurons/μm^2 and 6.3×10^{-5} neurons/μm^2, respectively) (**Figure 1C**). These results suggest that the difference observed by RT-qPCR is due to a decreased number of neurons that express *Olfr17*, which is consistent with previous observations (Walters et al., 1995; Khan et al., 2011; Ibarra-Soria et al., 2017). It is important to note, however, that in this case, while there is a 30% decrease in the number of *Olfr17* expressing neurons in the P2-GFP$^{+/+}$ mice (**Figure 1C**), there is a 64% reduction in *Olfr17* mRNA, when compared to P2-GFP$^{-/-}$ mice (**Figure 1B**). These results indicate that the reduced number of *Olfr17* expressing neurons alone does not account for the reduced levels of *Olfr17* mRNA, and raises the possibility that in the knock-in animals, the levels of *Olfr17* mRNA per neuron are lower as well.

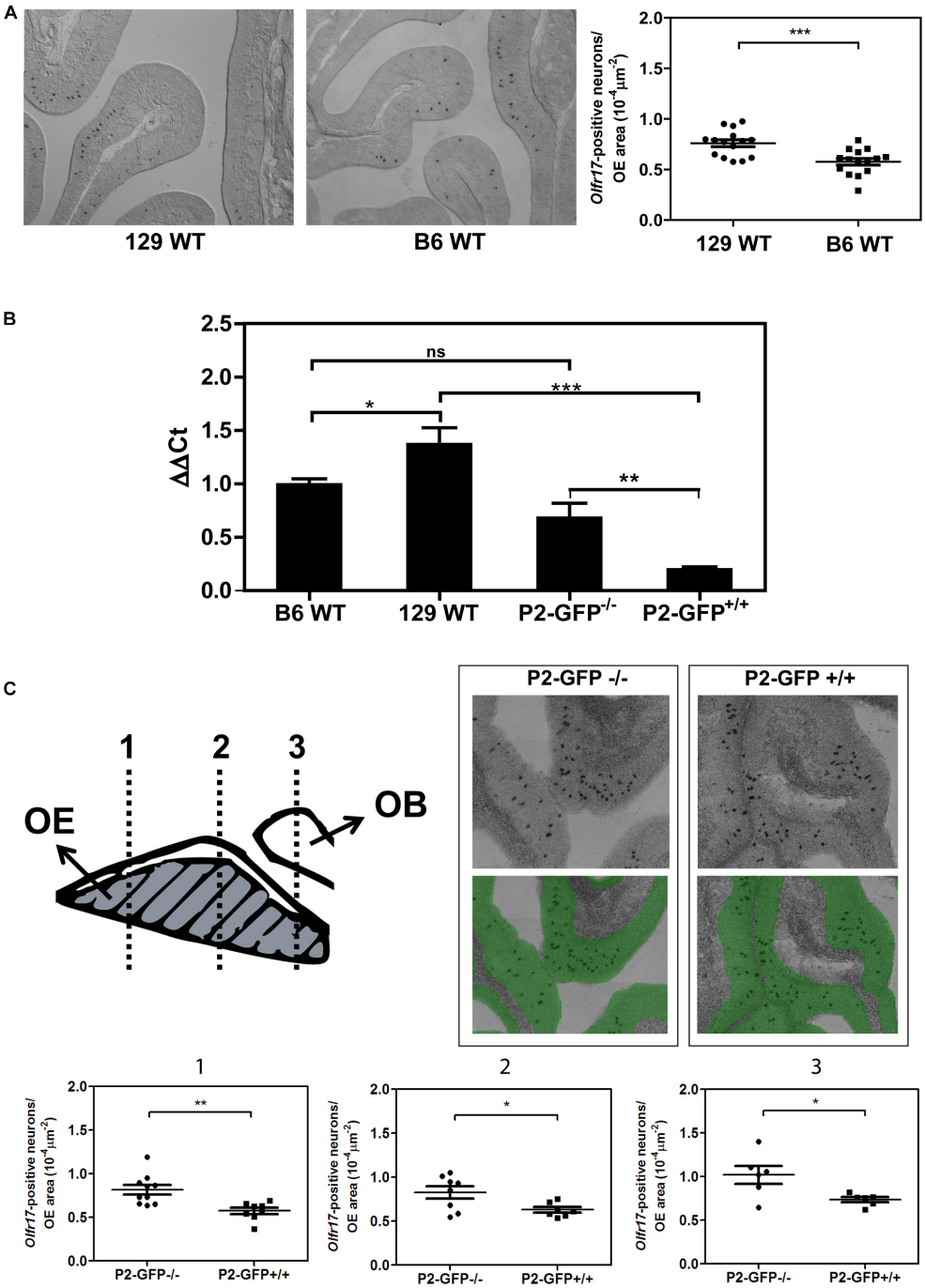

FIGURE 1 | Expression of the *Olfr17* alleles in different genetic backgrounds. **(A)** Number of olfactory sensory neurons expressing *Olfr17* in the wild type mouse strains. Coronal sections through the anterior-posterior axis of the olfactory epithelium from 129 and B6 mouse strains were hybridized with antisense digoxigenin-labeled probe specific for *Olfr17*. Representative images of the labeled sections are shown. The graph shows the number of *Olfr17*-positive neurons per olfactory epithelium area. $N = 3$ animals from each strain, five sections per animal. Student's *t*-test $^{***}P < 0.001$. **(B)** RT-qPCR was performed to determine the relative *Olfr17* gene expression levels in the olfactory epithelium from 129 and B6 wild type mouse strains, or from P2-GFP$^{-/-}$ and P2-GFP$^{+/+}$ knock-in siblings. The levels were normalized to β-actin and are shown relative to the expression in the wild type B6 olfactory epithelium. The graph shows mean +/− SEM (B6, $n = 3$; 129, $n = 4$; P2-GFP$^{-/-}$, $n = 4$; P2-GFP$^{+/+}$, $n = 4$). Not significant: ns, $^{*}P < 0.05$; $^{**}P < 0.01$ and $^{***}P < 0.001$. One-way ANOVA followed by Newman–Keuls *post hoc* test. **(C)** Coronal sections through the anterior-posterior axis of the olfactory epithelium from P2-GFP$^{-/-}$ and P2-GFP$^{+/+}$ mice were hybridized with antisense digoxigenin-labeled probe specific for *Olfr17*. Olfactory neurons that hybridized with the *Olfr17* probe were counted in 7–10 adjacent sections from each genotype from the three indicated locations using Tissue FAXS. Representative images of the labeled sections are shown on the top right. The number of labeled neurons (black dots) per olfactory epithelium area (labeled in green), was determined in each section. Student's *t*-test, $^{*}P < 0.05$ and $^{**}P < 0.01$. Dots and squares represent the number of *Olfr17*-positive neurons per olfactory epithelium area in each section.

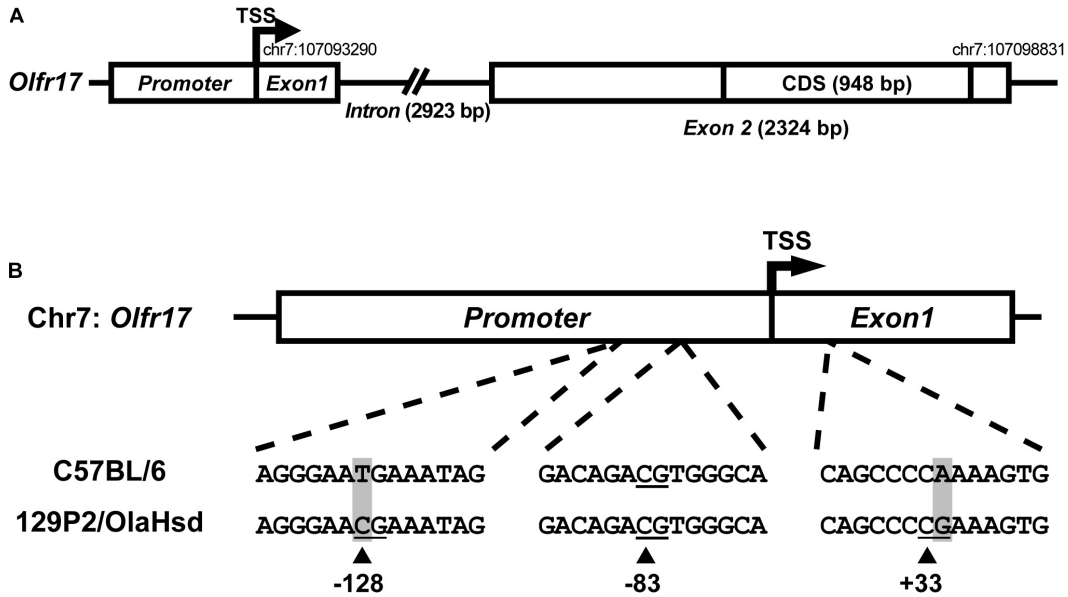

FIGURE 2 | Sequence variation in the 5′ regions of the 129 and B6 *Olfr17* alleles. **(A)** Schematic representation of the *Olfr17* gene structure. The olfactory receptor gene *Olfr17* contains two exons, and the second exon contains the complete coding sequence (CDS) of the gene. The genomic coordinates are according to the GRCm38/mm10 assembly and display the positions of the transcription start site (TSS) and of the last nucleotide within the 5′-UTR. The presumed promoter region is indicated. **(B)** Schematic representation of the 5′ region of the *Olfr17* gene of the B6 and 129 mouse strain alleles showing the positions of the CpG dinucleotides. There are two single nucleotide polymorphisms (SNPs) in this region which lead to the generation of two additional CpGs in the 129 *Olfr17* allele (at positions –128 and +33).

Altogether these results show that the 129 *Olfr17* allele is expressed at reduced levels in the P2-GFP mice (of mixed B6/129 genetic background) when compared to the wild type 129 mouse strain. In contrast, the B6 *Olfr17* allele is expressed at similar levels in both wild type B6 mice and knock-in mice.

Genetic Variation in the 5′ Region of the 129 and B6 *Olfr17* Alleles

Sequence variation in *cis* regulatory regions of the *Olfr17* alleles could account for the reduced expression levels of the 129 allele when compared to the B6 allele in the P2-GFP mice. We next determined the 5′ gene structure (exon and intron distribution) and transcription start site (TSS) of *Olfr17* by using RLM-RACE (Michaloski et al., 2006, 2011). The *Olfr17* gene shows a structure that is similar to a large number of OR genes: it is composed by two exons, which are separated by a long intron (in this case, 2923 bps long) (**Figure 2A**; Michaloski et al., 2006). The coding sequence (CDS, 948 bp long) is located within the second exon. The genomic position of the transcription start site (TSS) (chr7:107093290) is highly coincident with the one previously identified by using a microarray based high-throughput method (chr7:107093296) (Clowney et al., 2011).

Promoter sequences are typically located immediately upstream of the TSS. A previous large-scale study has shown that 88.5% of the OR gene promoters have a single well defined TSS position (Plessy et al., 2012). Different studies also showed that genomic sequences in the region −300 (upstream) of these OR gene TSSs are enriched for well-established OR *cis*-regulatory elements, such as the O/E and HD like sites (Michaloski et al., 2006, 2011; Clowney et al., 2011; Plessy et al., 2012). However, a very small number of minimal OR promoter sequences have been empirically validated to date, by showing that these short sequences (∼300 bp) located upstream the TSS are capable of driving punctate gene expression in the olfactory epithelium (Vassalli et al., 2002; Rothman et al., 2005; Zhang et al., 2007; Plessy et al., 2012). Based on these findings, we determined the presumed promoter region of the *Olfr17* gene (**Figure 2A**). Whether this sequence is able to control *Olfr17* gene transcription, still remains to be empirically determined.

By comparing the 5′ region sequences of the *Olfr17* gene derived from the 129 and B6 mouse strains, we identified the presence of two SNPs that lead to the occurrence of two additional CpG dinucleotides in the 129 *Olfr17* allele, one in the promoter region and the other one in exon 1, which are absent from the B6 *Olfr17* allele (**Figure 2B**). Since DNA methylation is usually involved in regulation of gene expression and typically occurs at the carbon 5 position of cytosine (5 mC) in CpG dinucleotides, we decided to investigate the methylation pattern of the *Olfr17* gene.

DNA Methylation in *Olfr17*

We used DNA bisulfite sequencing (DNA bis-seq) to determine the DNA methylation profile in *Olfr17*. This method allows us to identify the presence of 5 mC at single-base resolution. Since cytosine methylation may vary among cells, we sequenced a large number of clones (see "Materials and Methods") to analyze the distribution of the methylated cytosines in single molecules. To

check the efficiency of the bisulfite treatment we first analyzed the methylation frequency in six CpG dinucleotides within the Gap43 promoter, which were previously shown to be highly methylated in the mature olfactory epithelium (Macdonald et al., 2010). We obtained results that are highly similar to the previous ones (**Supplementary Figure 1**).

Methylation results obtained for the 5′ region and coding region of the *Olfr17* gene in the olfactory mucosa from B6 mice are shown in **Figure 3A**. CpGs within the coding region of the gene show high frequencies of cytosine methylation (varying from 65 to 94%). There is only one CpG in the promoter region of the *Olfr17* gene, and this CpG shows an extremely low frequency of methylation (methylation was observed in only 6% of the analyzed sequences). We next analyzed CpG methylation in the promoter regions of the two *Olfr17* alleles in the P2-GFP mice and found that the level of CpG −83 methylation in the 129 *Olfr17* promoter region in the olfactory mucosa is higher when compared to the B6 *Olfr17* promoter region (**Figure 3B**). Also, the presence of the two additional CpGs contribute to an overall higher DNA methylation level in the 129 *Olfr17* promoter region when compared to the B6 *Olfr17* promoter region (**Figure 3B**).

We also determined the *Olfr17* gene cytosine methylation frequencies in the olfactory mucosa from E15.5 mouse embryos (which is composed mainly of immature OSNs) and in liver (where ORs are not expressed). These tissues showed similar distributions of CpG methylation, with higher frequencies in the coding region (≥58%) than in the promoter region (6 to 20%) (**Figure 3A**).

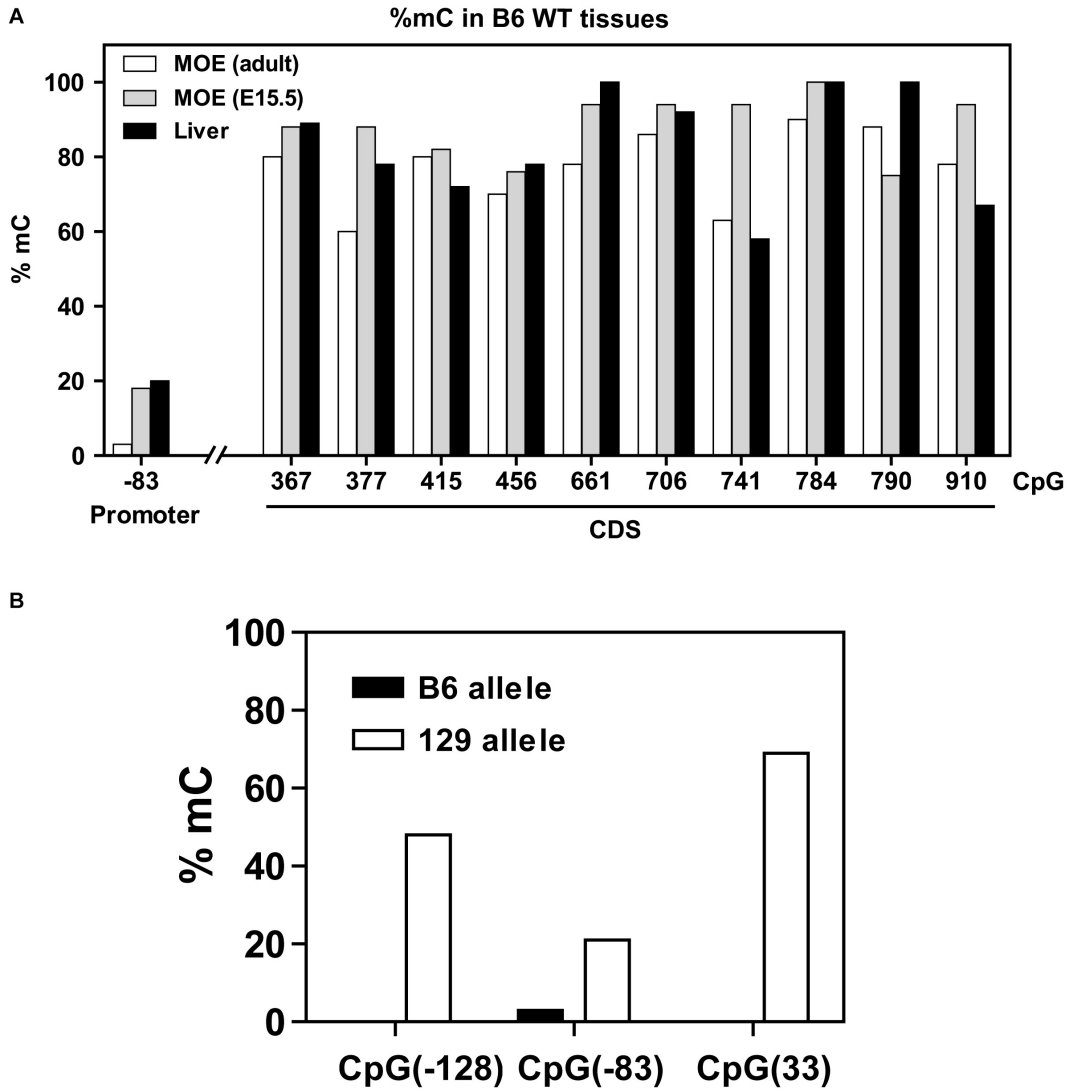

FIGURE 3 | DNA methylation in the *Olfr17* gene. **(A)** The CpG methylation frequencies in the promoter and coding regions of the *Olfr17* gene are shown. The frequencies are given by the number of clones that retain cytosine after bisulfite conversion in each position divided by the total number of clones analyzed. *Olfr17* cytosine methylation was analyzed in olfactory mucosa from adult mice (MOE, adult), olfactory mucosa from E15.5 mouse embryos (MOE, E15.5) and liver. **(B)** Comparison of the methylation frequencies of the CpGs in the *Olfr17* promoter region from the B6 and 129 alleles in the P2-GFP mice.

As mentioned above, cytosine methylation occurs in general at CpG dinucleotides, however, non-CpG methylation has been increasingly reported, although its function is not understood (Ramsahoye et al., 2000; Guo et al., 2014; Patil et al., 2014; Kinde et al., 2015). Cytosine methylation in the CpA context was previously shown to occur in an OR gene enhancer (the H region) in the olfactory mucosa (Lomvardas et al., 2006). We therefore also analyzed the distribution of CpA methylation in the *Olfr17* gene, and found that it occurs at low frequencies, both in the promoter region and coding region of the *Olfr17* gene (varying from 6 to 24%) (**Supplementary Figure 2**). Also, CpA methylation is randomly distributed throughout the sequence, that is, there are no specific CpAs which are preferentially methylated in the *Olfr17* gene.

CpG Methylation of the *Olfr17* Gene From P2-GFP^{+} Neurons

CpG methylation is usually correlated with repression of gene transcription. We next asked whether the methylation pattern observed in the 5′ region of 129 *Olfr17* is reduced when the gene is expressed. The *Olfr17* DNA methylation patterns shown in **Figure 3** were obtained by using genomic DNA extracted from the whole olfactory mucosa, which, in addition to the olfactory sensory neurons, contains other cell types such as the supporting cells and progenitor cells. Also, since each OR gene is typically expressed in a very low percentage of the olfactory sensory neurons (∼0.1% in average), this *Olfr17* DNA methylation pattern likely corresponds to that shown by the inactive gene.

To analyze DNA methylation in the active *Olfr17*, we first separated GFP positive olfactory sensory neurons from heterozygous (P2-GFP$^{+/-}$) knock-in mice by fluorescence-activated cell sorting (FACS) (**Figure 4A**). Since GFP is co-expressed only with the 129 *Olfr17* allele, these neurons must contain the active 129 *Olfr17* allele, which can be discriminated from the inactive B6 *Olfr17* allele (**Figure 4B**). Genomic DNA from the pre-sorted and sorted neurons was submitted to DNA bis-seq and the methylation profiles of the 129 *Olfr17* allele promoter region was analyzed. The SNP +34 was used to discriminate between the (GFP containing) 129 *Olfr17* allele and the B6 *Olfr17* allele during DNA bis-seq (**Figures 2B**, **4B**). We found that in the sorted neurons, the CpGs in the 129 *Olfr17* alleles show similar levels of methylation, except for CpG −83, which showed increased level of methylation when compared to pre-sorted cells (**Figure 4C**). We also found that CpGs in the coding region remain highly methylated, with CpGs showing 80–95% methylation frequencies (data not shown). The CpGs in the 129 *Olfr17* alleles from sorted cells show a random pattern of methylation, with no CpG site being preferentially methylated or unmethylated in the majority of the clones (**Figure 4D**). Thus, DNA methylation in the promoter region of *Olfr17* is not reduced in GFP positive neurons. Instead, a significant increase in the methylation frequency is observed in one of the three CpGs (CpG −83).

As shown in **Figure 2**, the B6 allele has only one CpG in the promoter region (CpG −83). One could expect that in the sorted cells, which contains only cells that express *Olfr17* from the 129 allele, the methylation frequency in the B6 allele would be higher than in the pre-sorted cells, which encompass cells expressing *Olfr17* from both the B6 and 129 alleles. Indeed, the B6 allele showed higher CpG −83 methylation levels in the sorted cells than in the pre-sorted cells, however, these methylation levels were very low (0% methylation frequency in pre-sorted cells versus 9% in sorted cells) (**Figure 4C**).

We also examined cytosine methylation in *Olfr1507* (also known as MOR28), an OR gene that is highly expressed in the B6 olfactory epithelium (11.101 fpm, as determined by Ibarra-Soria et al., 2017), and contains four CpGs in its promoter region. We found that, despite the fact that this is one of most abundantly expressed OR genes, the CpGs in the *Olfr1507* show high methylation frequencies (**Supplementary Figure 3**). Therefore, high methylation frequencies do not necessarily result in low expression levels. However, analysis of a larger number OR genes would be required to clarify this issue.

Expression of Neighboring OR Genes in the P2-GFP Mice

As shown above the B6 and 129 *Olfr17* alleles contain *cis* proximal regulatory regions which differ in sequence and methylation levels. Our RT-qPCR experiments show that in the knock-in siblings, where both *Olfr17* alleles are expressed from the same mixed genetic background (129/B6), the 129 *Olfr17* allele is expressed at lower levels than the B6 *Olfr17* allele. As shown above, the *Olfr17* transcript levels in the olfactory epithelium from homozygotes (P2-GFP$^{+/+}$), where *Olfr17* is expressed from 129 alleles, is significantly reduced when compared to the levels from wild types (P2-GFP$^{-/-}$), where the *Olfr17* is expressed from the B6 alleles (**Figure 1B**). Accordingly, heterozygotes (P2-GFP$^{+/-}$), where *Olfr17* is expressed from one B6 and one 129 allele, show intermediate levels of expression (**Figure 5A**).

The variations in the 5′ region of the two *Olfr17* alleles could account for the reduced expression levels of the 129 allele when compared to the B6 allele in the P2-GFP mice. Nevertheless, other factors could also be involved. Selection and stabilization of the expression of an OR gene type was shown to depend on the level of expression of the OR gene, so that ORs that are transcribed at higher levels are able to more efficiently suppress the expression of other OR genes than ORs that are expressed at lower levels (Abdus-Saboor et al., 2016). Therefore, it is possible that the bicistronic P2-IRES-tauGFP mRNA produced from the tagged 129 allele used in our experiments may be less stable and/or less efficiently translated than the untagged 129 *Olfr17* mRNA, leading to reduced levels of *Olfr17* mRNA and *Olfr17* protein in the cells expressing the knock-in allele (Bressel et al., 2016).

We next analyzed the transcript levels of additional OR genes in the same P2-GFP siblings. The experiments were performed with two OR genes located in *cis* to *Olfr17* (*Olfr6*, located in the *Olfr17* cluster and *Olfr566*, located 5 Mb away from *Olfr17*) and two OR genes located in other chromosomes (*Olfr15*, located in chromosome 16 and *Olfr1507*, located in chromosome 14). We found that like *Olfr17*, the OR genes that are in *cis* to *Olfr17* show reduced transcript levels in the heterozygote and homozygote mice (**Figure 5B**). On the other hand, the OR

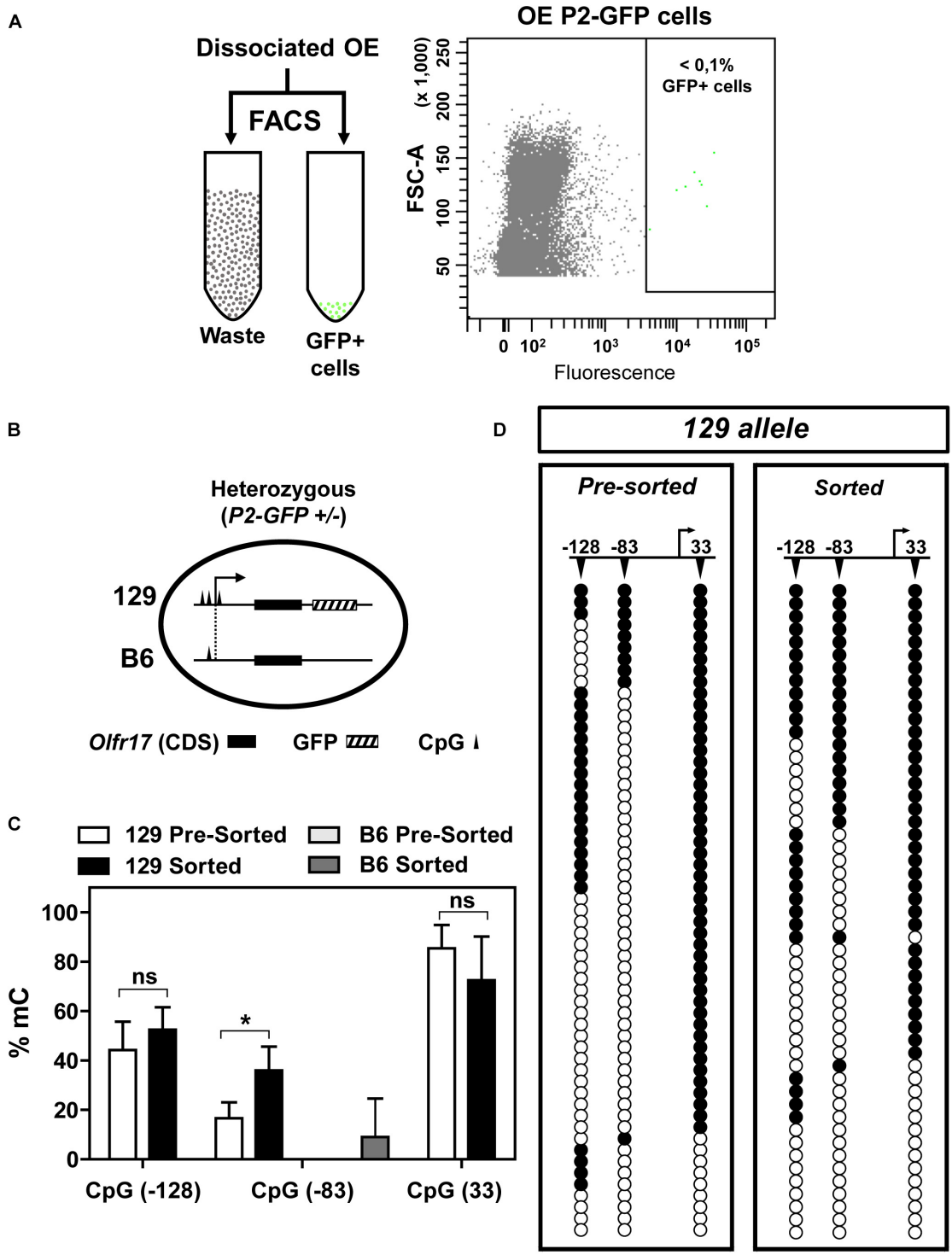

FIGURE 4 | DNA methylation in the 5′ region of *Olfr17* in GFP positive neurons. **(A)** Olfactory mucosa cells were dissociated from P2-GFP mice and submitted to fluorescence activated cell sorting (FACS) in order to isolate GFP+ neurons. The flow cytometry dot plot on the right was obtained when olfactory neurons from the P2-GFP mice were sorted, and the green dots within the square represent GFP+ neurons. **(B)** Schematic representation of the olfactory neurons sorted by FACS, showing that the cells from heterozygous knock-in mice contain one transgenic allele (129 *Olfr17* allele) and one B6 *Olfr17* allele. The vertical lines indicate the positions of the CpGs (–128, –83, and +33) in the promoter region and exon1. The 129 allele contains the three CpGs and the B6 allele contains only CpG –83. **(C)** Comparison of the *Olfr17* methylation frequencies in pre-sorted and sorted neurons in both alleles. In the pre-sorted cells, CpG-83 in the B6 allele showed 0% methylation frequency. Student's *t*-test, $n = 3$, $^*P < 0.05$. **(D)** Distribution of the methylated CpGs in each sequenced clone from the 129 allele shown in the graph in **(C)**. Open and closed circles indicate unmethylated and methylated CpGs, respectively.

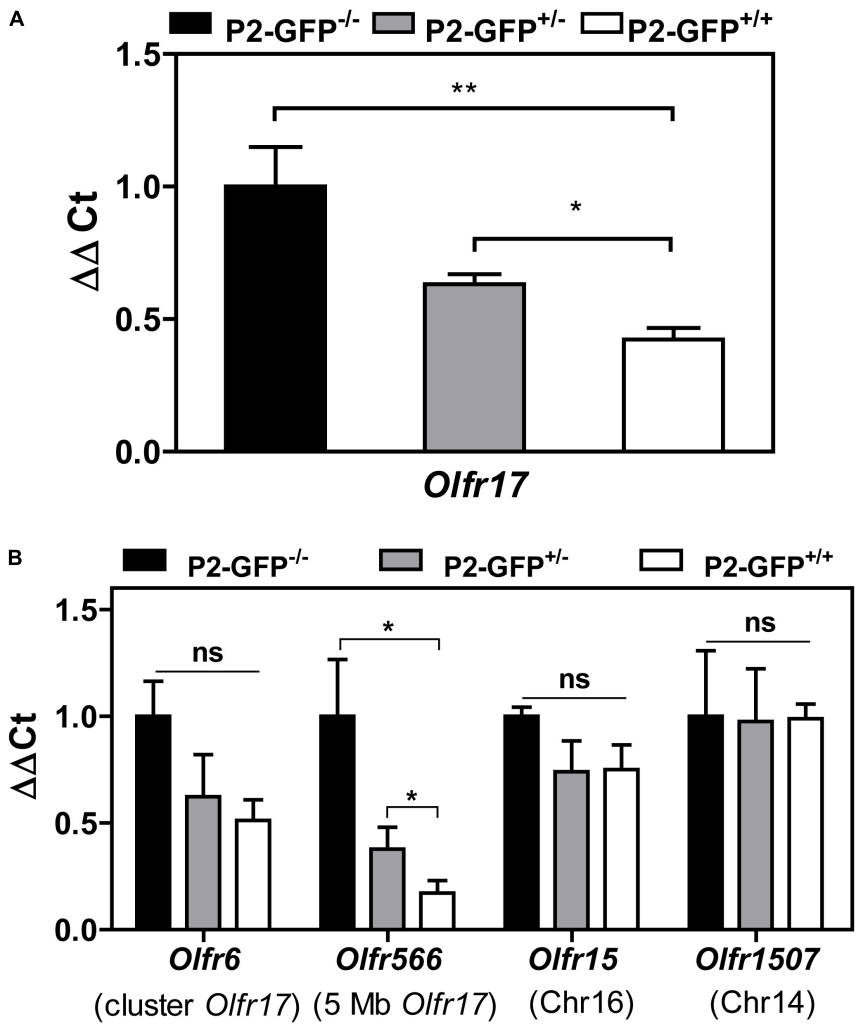

FIGURE 5 | Expression of OR genes located close to *Olfr17* or in other chromosomes in the P2-GFP mice. **(A)** RT-qPCR was performed to determine the relative *Olfr17* gene transcript levels in the olfactory epithelium from P2-GFP$^{-/-}$; P2-GFP$^{+/-}$ and P2-GFP$^{+/+}$ mice. The levels were normalized to β-actin and are shown relative to the expression in homozygous olfactory epithelium. Graph shows mean +/− SEM (P2-GFP$^{+/+}$, n = 5; P2-GFP$^{+/-}$, n = 4; P2-GFP$^{-/-}$, n = 5). *$P < 0.05$; **$P < 0.01$. One-way ANOVA followed by Newman–Keuls *post hoc* test or student's *t*-test. **(B)** RT-qPCR and the same cDNAs as in **(A)** were used to determine the relative transcript levels of *Olfr6*, *Olfr566*, *Olfr15*, and *Olfr1507*. Graph shows mean +/− SEM [P2-GFP$^{+/+}$, n = 3 (n = 4 for *Olfr6* and *Olfr15*); P2-GFP$^{+/-}$, n = 4 (n = 3 for *Olfr1507*); P2-GFP$^{-/-}$, n = 3]. Not significant: ns, *$P < 0.05$. One-way ANOVA followed by Newman–Keuls *post hoc* test.

genes that are located in different chromosomes show similar levels of expression in all three knock-in genotypes (**Figure 5B**). Therefore, not only the 129 *Olfr17* targeted allele, but other OR genes that are located in *cis* to the targeted allele also show reduced levels of expression.

DISCUSSION

DNA Methylation Pattern of *Olfr17*

Technologies that allow for genome wide analysis of DNA methylation in mammals have revealed that the genome is globally methylated at CpG sites, except for the ones which are localized within CpG islands and other regulatory gene regions, which would be bound by proteins involved in transcription and protected from methylation by DNA methyltransferases (DNMTs) (Suzuki and Bird, 2008; Laird, 2010; Jones, 2012). Consistent with these observations, we found that the coding region of the *Olfr17* gene shows high levels of CpG methylation. OR gene promoter regions are usually AT rich sequences and their CpG dinucleotides content is lower than the one observed across the mouse genome (around 1 versus 42%) (Jabbari and Bernardi, 2004; Clowney et al., 2011). Consequently, no CpG islands are present in the promoter regions of the OR genes, but only a small number of CpGs (Clowney et al., 2011). Whether methylation of one or a few CpGs in the regulatory region can affect transcription, remains unclear (Lioznova et al., 2019).

The *Olfr17* gene DNA methylation was similar in the olfactory mucosa and liver (where OR genes are not expressed), indicating that the DNA methylation pattern of this OR gene is not tissue

specific. Accordingly, a previous study showed that the CpGs in the coding region of *Ofr151* are also highly methylated, both in the olfactory mucosa and in sperm (Dias and Ressler, 2014). In addition, we found no evident differences in methylation between different developmental stages (embryonic and adult olfactory mucosa).

The role played by DNA methylation at non-CpG sites is not well understood. Genome wide non-CpG methylation was observed in the adult mouse brain (Xie et al., 2012; Guo et al., 2014). The most common type of non-CpG methylation is methylation at CpA sites. Our results show that CpA methylation in *Olfr17* occurs at low frequencies and is randomly distributed throughout the sequence, with no preferentially CpA methylated sites being observed.

Polymorphisms in the 5′ Region of *Olfr17*

We show that due to sequence variation, the 5′ region of the 129 *Olfr17* allele shows an overall higher level of DNA methylation than the one from the B6 *Olfr17* allele. In general, CpG methylation is thought to repress transcription by directly preventing the binding of transcription factors, or by recruiting histone deacetylases which promote chromatin condensation. However, we found that DNA methylation levels in the 5′ region of the 129 *Olfr17* in olfactory neurons that express *Olfr17*, are similar to the ones obtained from whole olfactory mucosa. Therefore, within the same genomic context (in the transgenic mixed B6/129 background), we observe no correlation between reduced levels of DNA methylation and *Olfr17* expression.

Even though we do not observe a difference in methylation between the active and inactive states of *Olfr17*, we cannot exclude the possibility that DNA methylation levels in regulatory regions may interfere with the probability by which an OR gene is selected for expression. A high-throughput analysis using human genome data from the 1000 Genomes Project revealed a high level of SNPs in the promoter regions of human OR genes (Ignatieva et al., 2014). Whether this high level of polymorphism contributes to differential expression of the OR types across human individuals, is an intriguing question.

Differential Expression of the 129 and B6 *Olfr17* Alleles

By comparing the expression of the B6 and 129 *Olfr17* alleles in the P2-GFP animals we found that the 129 allele is expressed at lower levels and in a smaller number of olfactory neurons than the B6 allele. These results cannot be attributed to different genomic backgrounds, since the alleles were analyzed on the same mixed B6/129 background. Different possibilities, which are not exclusive, could account for reduced expression of the 129 allele.

In the knock-in mice, the 129 *Olfr17* allele is tagged, while the B6 one is not. To what extent expression of a bicistronic mRNA affects OR gene expression, is not clear yet. One way to address this point would be to compare the expression of wild type and tagged OR alleles in the same neurons. In a previous work, expression of a wild type 129 *Olfr1507* allele and a tagged 129 *Olfr1507* allele in the olfactory epithelium from 129 MOR28-IRES-gap-GFP/129 MOR28 mice was compared. In these experiments, a slight reduction in the probability of choice was observed for the tagged allele, when compared to the wild type allele [51.1% of neurons expressed *Olfr1507* and 47.2% of the neurons expressed both *Olfr1507* and GFP (Low and Mombaerts, 2017)]. Therefore, in this case, even though the presence of the tag contributed to a reduction in the probability of OR gene choice, this effect was very small, when compared to the ones observed in our experiments: a 64% reduction in the *Olfr17* transcript levels (as measured by RT-qPCR) and a 30% reduction in the number of *Olfr17* expressing neurons in P2-GFP$^{+/+}$ mice when compared to P2-GFP$^{-/-}$.

The observations above suggest that the burden of expressing the GFP tag may not be the only reason for the reduced *Olfr17* transcript levels we observe in the knock-in mice. The results could also be explained by a competition process between the alleles, where transcription of the B6 allele would be more permissive than the transcription of the 129 allele, due to sequence/epigenetic variations in the 5′ regions of these alleles. A similar type of competition has already been observed in heterozygous cells containing both the B6 and 129 *Olfr1507* alleles. In this case, there was also a preference for the expression of the B6 allele (Low and Mombaerts, 2017). Alternatively, higher expression levels from the B6 allele in the heterozygous cells, could suppress expression of the 129 allele, through a post selection refinement (PSR) process (Abdus-Saboor et al., 2016).

We found that reduced expression is not limited to *Olfr17*, but additional OR genes that are located in *cis* to the *Olfr17* locus are also expressed at lower levels in the knock-in mice. These results suggest that *cis* effects of the integrated DNA interfere with the expression of the neighboring genes. Altered chromatin configuration and other *cis*-regulatory interactions could contribute to these effects (Olson et al., 1996). Notably, based on the work by Ibarra-Soria et al., 2017, the expression levels of the nearby *Olfr6* and *Olfr566* are lower in 129 wild type mice than in B6 wild type mice. It is not clear yet how much of the flanking regions from the targeted locus in the P2-GFP mice are still derived from the 129 background. These regions could include not only OR genes, but also enhancers and other regulatory sequences. Therefore, a comparative analysis of the whole *Olfr17* locus and its flanking regions in the wild type and knock-in mice should contribute to unveil the regulatory mechanisms responsible for the differences in *Olfr17* expression. Finally, these findings highlight the importance of considering that such *cis*-acting effects may occur when using gene-targeted animal models in the study of OR genes.

Olfr17 Expression in the Wild Type Strains

Our study raises important questions regarding differential OR gene expression between diverse wild type strains. Why is *Olfr17* expressed at higher levels in the 129-mouse strain compared to the B6 strain? Does the 129 *Olfr17* promoter region in wild type 129 mice show lower frequencies of methylation than in P2-GFP mice, as it would be expected? Our results with *Olfr1507* argue against a simple and linear correlation between promoter methylation status and expression levels of OR genes. Olfactory neurons have a characteristic form of nuclear organization, and both in *cis* and inter-chromosomal interactions are required

for the correct expression of the OR genes (Clowney et al., 2012; Armelin-Correa et al., 2014; Monahan et al., 2019). DNA methylation and/or other epigenetic factors could result in differential 3D chromatin organization in the olfactory nuclei from the different mouse strains, and produce distinct *cis* and *trans* effects that could lead to differential *Olfr17* expression levels. The understanding of how genetic variations among mouse strains contribute to differential OR gene expression, should reveal important aspects of OR gene regulation.

DATA AVAILABILITY STATEMENT

The original contributions presented in the study are included in the article/**Supplementary Material**, further inquiries can be directed to the corresponding author.

ETHICS STATEMENT

The animal study was reviewed and approved by the University of São Paulo Chemistry Institute's Animal Care and Use Committee, under the protocols number 19/2013 and 60/2017.

AUTHOR CONTRIBUTIONS

AL, MN, TN, and BM designed the experiments and analyzed the data. AL, MN, and TN performed the experiments. AL and BM wrote the manuscript. All authors contributed original ideas to the research and agreed on the final version of the manuscript.

FUNDING

This work was supported by grants from the Fundação de Amparo à Pesquisa do Estado de São Paulo [FAPESP, #2016/24471-0 (BM), #2012/15882-6 (AL), #2014/15495-8 (MN), #2018/11860-4 (TN)] and Conselho Nacional de Desenvolvimento Científico e Tecnológico (CNPq).

ACKNOWLEDGMENTS

We thank Silvânia S. P. Neves and Renata Spalutto Fontes for assistance in our animal facility, Erica Michele Bandeira and Edson Alves for technical assistance, Fernando Delgado Pretel from the Core Facility for Scientific Research- University of São Paulo (CEFAP-USP/FLUIR) for help with cell sorting, Bianca Plosnita and Rupert Ecker (from TissueGnostics) for analysis of the *in situ* hybridization images and Victor Pereira de Sá Xavier for help with microscope images. We also thank Angela Saito and Michel Vaz de Oliveira and acknowledge the animal facility of the Brazilian Biosciences National Laboratory (LNBio), CNPEM, Campinas, Brazil, for providing the 129S animals.

SUPPLEMENTARY MATERIAL

The Supplementary Material for this article can be found online at: https://www.frontiersin.org/articles/10.3389/fncel.2021.646413/full#supplementary-material

REFERENCES

Abdus-Saboor, I., Al Nufal, M. J., Agha, M. V., Ruinart De Brimont, M., Fleischmann, A., and Shykind, B. M. (2016). An expression refinement process ensures singular odorant receptor gene choice. *Curr. Biol.* 26, 1083–1090. doi: 10.1016/j.cub.2016.02.039

Armelin-Correa, L. M., Gutiyama, L. M., Brandt, D. Y., and Malnic, B. (2014). Nuclear compartmentalization of odorant receptor genes. *Proc. Natl. Acad. Sci. U S A.* 111, 2782–2787. doi: 10.1073/pnas.1317036111

Barnes, I. H. A., Ibarra-Soria, X., Fitzgerald, S., Gonzalez, J. M., Davidson, C., Hardy, M. P., et al. (2020). Expert curation of the human and mouse olfactory receptor gene repertoires identifies conserved coding regions split across two exons. *BMC Genom.* 21:196. doi: 10.1186/s12864-020-6583-3

Bozza, T., Vassalli, A., Fuss, S., Zhang, J. J., Weiland, B., Pacifico, R., et al. (2009). Mapping of class I and class II odorant receptors to glomerular domains by two distinct types of olfactory sensory neurons in the mouse. *Neuron* 61, 220–233. doi: 10.1016/j.neuron.2008.11.010

Bressel, O. C., Khan, M., and Mombaerts, P. (2016). Linear correlation between the number of olfactory sensory neurons expressing a given mouse odorant receptor gene and the total volume of the corresponding glomeruli in the olfactory bulb. *J. Comp. Neurol.* 524, 199–209. doi: 10.1002/cne.23835

Buck, L., and Axel, R. (1991). A novel multigene family may encode odorant receptors: a molecular basis for odor recognition. *Cell* 65, 175–187. doi: 10.1016/0092-8674(91)90418-x

Camargo, A. P., Nakahara, T. S., Firmino, L. E. R., Netto, P. H. M., Do Nascimento, J. B. P., Donnard, E. R., et al. (2019). Uncovering the mouse olfactory long non-coding transcriptome with a novel machine-learning model. *DNA Res.* 26, 365–378. doi: 10.1093/dnares/dsz015

Chess, A., Simon, I., Cedar, H., and Axel, R. (1994). Allelic inactivation regulates olfactory receptor gene expression. *Cell* 78, 823–834. doi: 10.1016/s0092-8674(94)90562-2

Cichy, A., Shah, A., Dewan, A., Kaye, S., and Bozza, T. (2019). Genetic depletion of class I odorant receptors impacts perception of carboxylic acids. *Curr. Biol.* 29, 2687–2697. doi: 10.1016/j.cub.2019.06.085

Clowney, E. J., Legros, M. A., Mosley, C. P., Clowney, F. G., Markenskoff-Papadimitriou, E. C., Myllys, M., et al. (2012). Nuclear aggregation of olfactory receptor genes governs their monogenic expression. *Cell* 151, 724–737. doi: 10.1016/j.cell.2012.09.043

Clowney, E. J., Magklara, A., Colquitt, B. M., Pathak, N., Lane, R. P., Lomvardas, S. et al. (2011). High-throughput mapping of the promoters of the mouse olfactory receptor genes reveals a new type of mammalian promoter and provides insight into olfactory receptor gene regulation. *Genom. Res.* 21, 1249–1259. doi: 10.1101/gr.120162.110

Colquitt, B. M., Allen, W. E., Barnea, G., and Lomvardas, S. (2013). Alteration of genic 5-hydroxymethylcytosine patterning in olfactory neurons correlates with changes in gene expression and cell identity. *Proc. Natl. Acad. Sci. U S A.* 110, 14682–14687. doi: 10.1073/pnas.1302759110

Colquitt, B. M., Markenscoff-Papadimitriou, E., Duffie, R., and Lomvardas, S. (2014). Dnmt3a regulates global gene expression in olfactory sensory neurons and enables odorant-induced transcription. *Neuron* 83, 823–838. doi: 10.1016/j.neuron.2014.07.013

Degl'innocenti, A., and D'errico, A. (2017). Regulatory features for odorant receptor genes in the mouse genome. *Front. Genet.* 8:19. doi: 10.3389/fgene.2017.00019

Dias, B. G., and Ressler, K. J. (2014). Parental olfactory experience influences behavior and neural structure in subsequent generations. *Nat. Neurosci.* 17, 89–96. doi: 10.1038/nn.3594

Feinstein, P., and Mombaerts, P. (2004). A contextual model for axonal sorting into glomeruli in the mouse olfactory system. *Cell* 117, 817–831. doi: 10.1016/j.cell.2004.05.011

Godfrey, P. A., Malnic, B., and Buck, L. B. (2004). The mouse olfactory receptor gene family. *Proc. Natl. Acad. Sci. U S A.* 101, 2156–2161. doi: 10.1073/pnas.0308051100

Guo, J. U., Su, Y., Shin, J. H., Shin, J., Li, H., Xie, B., et al. (2014). Distribution, recognition and regulation of non-CpG methylation in the adult mammalian brain. *Nat. Neurosci.* 17, 215–222. doi: 10.1038/nn.3607

Hirota, J., Omura, M., and Mombaerts, P. (2007). Differential impact of Lhx2 deficiency on expression of class I and class II odorant receptor genes in mouse. *Mol. Cell. Neurosci.* 34, 679–688. doi: 10.1016/j.mcn.2007.01.014

Hoppe, R., Breer, H., and Strotman, J. (2006). Promoter motifs of olfactory receptor genes expressed in distinct topographic patterns. *Genom. Res.* 87, 711–723. doi: 10.1016/j.ygeno.2006.02.005

Ibarra-Soria, X., Nakahara, T. S., Lilue, J., Jiang, Y., Trimmer, C., Souza, M. A., et al. (2017). Variation in olfactory neuron repertoires is genetically controlled and environmentally modulated. *Elife* 6:e21476.

Ignatieva, E. V., Levitsky, V. G., Yudin, N. S., Moshkin, M. P., and Kolchanov, N. A. (2014). Genetic basis of olfactory cognition: extremely high level of DNA sequence polymorphism in promoter regions of the human olfactory receptor genes revealed using the 1000 genomes project dataset. *Front. Psychol.* 5:247. doi: 10.3389/fpsyg.2014.00247

Iwata, T., Niimura, Y., Kobayashi, C., Shirakawa, D., Suzuki, H., Enomoto, T., et al. (2017). A long-range cis-regulatory element for class I odorant receptor genes. *Nat. Commun.* 8:885.

Jabbari, K., and Bernardi, G. (2004). Cytosine methylation and CpG, TpG (CpA) and TpA frequencies. *Gene* 333, 143–149. doi: 10.1016/j.gene.2004.02.043

Jones, P. A. (2012). Functions of DNA methylation: islands, start sites, gene bodies and beyond. *Nat. Rev. Genet.* 13, 484–492. doi: 10.1038/nrg3230

Khan, M., Vaes, E., and Mombaerts, P. (2011). Regulation of the probability of mouse odorant receptor gene choice. *Cell* 147, 907–921. doi: 10.1016/j.cell.2011.09.049

Kinde, B., Gabel, H. W., Gilbert, C. S., Griffith, E. C., and Greenberg, M. E. (2015). Reading the unique DNA methylation landscape of the brain: Non-CpG methylation, hydroxymethylation, and MeCP2. *Proc. Natl. Acad. Sci. U S A.* 112, 6800–6806. doi: 10.1073/pnas.1411269112

Laird, P. W. (2010). Principles and challenges of genomewide DNA methylation analysis. *Nat. Rev. Genet.* 11, 191–203. doi: 10.1038/nrg2732

Leme Silva, A. G., Nagai, M. H., and Malnic, B. (2018). Fluorescence-activated cell sorting of olfactory sensory neuron subpopulations. *Methods Mol. Biol.* 1820, 69–76. doi: 10.1007/978-1-4939-8609-5_6

Lioznova, A. V., Khamis, A. M., Artemov, A. V., Besedina, E., Ramensky, V., Bajic, V. B., et al. (2019). CpG traffic lights are markers of regulatory regions in human genome. *BMC Genom.* 20:102. doi: 10.1186/s12864-018-5387-1

Lomvardas, S., Barnea, G., Pisapia, D., Mendelsohn, M., Kirkland, J., and Axel, R. (2006). Interchromosomal interactions and olfactory receptor choice. *Cell* 126, 403–413. doi: 10.1016/j.cell.2006.06.035

Low, V. F., and Mombaerts, P. (2017). Odorant receptor proteins in the mouse main olfactory epithelium and olfactory bulb. *Neuroscience* 344, 167–177. doi: 10.1016/j.neuroscience.2016.12.044

Macdonald, J. L., Gin, C. S., and Roskams, A. J. (2005). Stage-specific induction of DNA methyltransferases in olfactory receptor neuron development. *Dev. Biol.* 288, 461–473. doi: 10.1016/j.ydbio.2005.09.048

Macdonald, J. L., Verster, A., Berndt, A., and Roskams, A. J. (2010). MBD2 and MeCP2 regulate distinct transitions in the stage-specific differentiation of olfactory receptor neurons. *Mol. Cell. Neurosci.* 44, 55–67. doi: 10.1016/j.mcn.2010.02.003

Malnic, B., Hirono, J., Sato, T., and Buck, L. B. (1999). Combinatorial receptor codes for odors. *Cell* 96, 713–723. doi: 10.1016/s0092-8674(00)80581-4

Markenscoff-Papadimitriou, E., Allen, W. E., Colquitt, B. M., Goh, T., Murphy, K. K., Monahan, K., et al. (2014). Enhancer interaction networks as a means for singular olfactory receptor expression. *Cell* 159, 543–557. doi: 10.1016/j.cell.2014.09.033

Michaloski, J., Galante, P., and Malnic, B. (2006). Identification of potential regulatory motifs in odorant receptor genes by analysis of promoter sequences. *Genom. Res.* 16, 1091–1098. doi: 10.1101/gr.5185406

Michaloski, J. S., Galante, P. A., Nagai, M. H., Armelin-Correa, L., Chien, M. S., Matsunami, H., et al. (2011). Common promoter elements in odorant and vomeronasal receptor genes. *PLoS One* 6:e29065. doi: 10.1371/journal.pone.0029065

Mombaerts, P., Wang, F., Dulac, C., Chao, S., Nemes, A., Mendelsohn, M., et al. (1996). Visualizing an olfactory sensory map. *Cell* 87, 675–686. doi: 10.1016/s0092-8674(00)81387-2

Monahan, K., Horta, A., and Lomvardas, S. (2019). LHX2- and LDB1-mediated trans interactions regulate olfactory receptor choice. *Nature* 565, 448–453. doi: 10.1038/s41586-018-0845-0

Monahan, K., and Lomvardas, S. (2015). Monoallelic expression of olfactory receptors. *Annu. Rev. Cell. Dev. Biol.* 31, 721–740. doi: 10.1146/annurev-cellbio-100814-125308

Nagai, M. H., Armelin-Correa, L. M., and Malnic, B. (2016). Monogenic and monoallelic expression of odorant receptors. *Mol. Pharmacol.* 90, 633–639. doi: 10.1124/mol.116.104745

Nishizumi, H., Kumasaka, K., Inoue, N., Nakashima, A., and Sakano, H. (2007). Deletion of the core-H region in mice abolishes the expression of three proximal odorant receptor genes in cis. *Proc. Natl. Acad. Sci. USA.* 104, 20067–20072. doi: 10.1073/pnas.0706544105

Olson, E. N., Arnold, H. H., Rigby, P. W., and Wold, B. J. (1996). Know your neighbors: three phenotypes in null mutants of the myogenic bHLH gene MRF4. *Cell* 85, 1–4. doi: 10.1016/s0092-8674(00)81073-9

Patil, V., Ward, R. L., and Hesson, L. B. (2014). The evidence for functional non-CpG methylation in mammalian cells. *Epigenetics* 9, 823–828. doi: 10.4161/epi.28741

Plessy, C., Pascarella, G., Bertin, N., Akalin, A., Carrieri, C., Vassalli, A., et al. (2012). Promoter architecture of mouse olfactory receptor genes. *Genom. Res.* 22, 486–497. doi: 10.1101/gr.126201.111

Preibisch, S., Saalfeld, S., and Tomancak, P. (2009). Globally optimal stitching of tiled 3D microscopic image acquisitions. *Bioinformatics* 25, 1463–1465. doi: 10.1093/bioinformatics/btp184

Ramsahoye, B. H., Biniszkiewicz, D., Lyko, F., Clark, V., Bird, A. P., Jaenisch, R. et al. (2000). Non-CpG methylation is prevalent in embryonic stem cells and may be mediated by DNA methyltransferase 3a. *Proc. Natl. Acad. Sci. U S A.* 97, 5237–5242. doi: 10.1073/pnas.97.10.5237

Rodriguez-Gil, D. J., Treloar, H. B., Zhang, X., Miller, A. M., Two, A., Iwema, C., et al. (2010). Chromosomal location-dependent nonstochastic onset of odor receptor expression. *J. Neurosci.* 30, 10067–10075. doi: 10.1523/jneurosci.1776-10.2010

Rothman, A., Feinstein, P., Hirota, J., and Mombaerts, P. (2005). The promoter of the mouse odorant receptor gene M71. *Mol. Cell. Neurosci.* 28, 535–546. doi: 10.1016/j.mcn.2004.11.006

Serizawa, S., Miyamichi, K., Nakatani, H., Suzuki, M., Saito, M., Yoshihara, S., et al. (2003). Negative feedback regulation ensures the one receptor-one olfactory neuron rule in the mouse. *Science* 302, 2088–2094. doi: 10.1126/science.1089122

Suzuki, M. M., and Bird, A. (2008). DNA methylation landscapes: provocative insights from epigenomics. *Nat. Rev. Genet.* 9, 465–476. doi: 10.1038/nrg2341

Vassalli, A., Feinstein, P., and Mombaerts, P. (2011). Homeodomain binding motifs modulate the probability of odorant receptor gene choice in transgenic mice. *Mol. Cell. Neurosci.* 46, 381–396. doi: 10.1016/j.mcn.2010.11.001

Vassalli, A., Rothman, A., Feinstein, P., Zapotocky, M., and Mombaerts, P. (2002). Minigenes impart odorant receptor-specific axon guidance in the olfactory bulb. *Neuron* 35, 681–696. doi: 10.1016/s0896-6273(02)00793-6

Von Dannecker, L., Mercadante, A., and Malnic, B. (2005). Ric-8B, an olfactory putative GTP exchange factor, amplifies signal transduction through the olfactory-specific G-protein Gαolf. *J. Neurosci.* 25, 3793–3800. doi: 10.1523/jneurosci.4595-04.2005

Walters, M. C., Fiering, S., Eidemiller, J., Magis, W., Groudine, M., Martin, D. I. et al. (1995). Enhancers increase the probability but not the level of gene expression. *Proc. Natl. Acad. Sci. U S A.* 92, 7125–7129. doi: 10.1073/pnas.92.15.7125

Xie, W., Barr, C. L., Kim, A., Yue, F., Lee, A. Y., Eubanks, J., et al. (2012). Base-resolution analyses of sequence and parent-of-origin dependent DNA methylation in the mouse genome. *Cell* 148, 816–831. doi: 10.1016/j.cell.2011.12.035

Yin, Y., Morgunova, E., Jolma, A., Kaasinen, E., Sahu, B., Khund-Sayeed, S., et al. (2017). Impact of cytosine methylation on DNA binding specificities of human transcription factors. *Science* 356:eaaj2239. doi: 10.1126/science.aaj2239

Young, J. M., Luche, R. M., and Trask, B. J. (2011). Rigorous and thorough bioinformatic analyses of olfactory receptor promoters confirm enrichment of O/E and homeodomain binding sites but reveal no new common motifs. *BMC Genom.* 12:561. doi: 10.1186/1471-2164-12-561

Young, J. M., Shykind, B. M., Lane, R. P., Tonnes-Priddy, L., Ross, E. M., Walker, M., et al. (2003). Odorant receptor expressed sequence tags demonstrate olfactory expression of over 400 genes, extensive alternate splicing and unequal expression levels. *Genom Biol.* 4:R71.

Zhang, G., Titlow, W. B., Biecker, S. M., Stromberg, A. J., and Mcclintock, T. S. (2016). Lhx2 determines odorant receptor expression frequency in mature olfactory sensory neurons. *eNeuro* 3:ENEURO.230.16.2016.

Zhang, X., and Firestein, S. (2002). The olfactory receptor gene superfamily of the mouse. *Nat. Neurosci.* 5, 124–133. doi: 10.1038/nn800

Zhang, X., Rogers, M., Tian, H., Zhang, X., Zou, D.-J., Liu, J., et al. (2004). High-throughput microarray detection of olfactory receptor gene expression in the mouse. *Proc. Natl. Acad. Sci. U S A.* 101, 14168–14173. doi: 10.1073/pnas.0405350101

Zhang, Y., Breer, H., and Strotmann, J. (2007). Promoter elements governing the clustered expression pattern of odorant receptor genes. *Mol. Cell. Neurosci.* 36, 95–107. doi: 10.1016/j.mcn.2007.06.005

Conflict of Interest: The authors declare that the research was conducted in the absence of any commercial or financial relationships that could be construed as a potential conflict of interest.

frontiers in Cellular Neuroscience

ORIGINAL RESEARCH
published: 23 March 2021
doi: 10.3389/fncel.2021.639754

Norepinephrine-Induced Calcium Signaling and Store-Operated Calcium Entry in Olfactory Bulb Astrocytes

Timo Fischer, Jessica Prey, Lena Eschholz, Natalie Rotermund and Christian Lohr**

Division of Neurophysiology, Department of Biology, Institute of Zoology, University of Hamburg, Hamburg, Germany

It is well-established that astrocytes respond to norepinephrine with cytosolic calcium rises in various brain areas, such as hippocampus or neocortex. However, less is known about the effect of norepinephrine on olfactory bulb astrocytes. In the present study, we used confocal calcium imaging and immunohistochemistry in mouse brain slices of the olfactory bulb, a brain region with a dense innervation of noradrenergic fibers, to investigate the calcium signaling evoked by norepinephrine in astrocytes. Our results show that application of norepinephrine leads to a cytosolic calcium rise in astrocytes which is independent of neuronal activity and mainly mediated by PLC/IP3-dependent internal calcium release. In addition, store-operated calcium entry (SOCE) contributes to the late phase of the response. Antagonists of both α1- and α2-adrenergic receptors, but not β-receptors, largely reduce the adrenergic calcium response, indicating that both α-receptor subtypes mediate norepinephrine-induced calcium transients in olfactory bulb astrocytes, whereas β-receptors do not contribute to the calcium transients.

Keywords: olfactory bulb, astrocytes, norepinephrine receptors, calcium signaling, store-operated calcium entry

OPEN ACCESS

Edited by:
Shaina M. Short,
The University of Utah, United States

Reviewed by:
Peter Illes,
Leipzig University, Germany
Dmitry Lim,
University of Eastern Piedmont, Italy
Matthew s. Grubb,
King's College London,
United Kingdom

****Correspondence:***
Timo Fischer
timo.fischer@uni-hamburg.de
Christian Lohr
christian.lohr@uni-hamburg.de

Specialty section:
This article was submitted to Cellular Neurophysiology, a section of the journal Frontiers in Cellular Neuroscience

Received: *09 December 2020*
Accepted: *02 March 2021*
Published: *23 March 2021*

Citation:
Fischer T, Prey J, Eschholz L, Rotermund N and Lohr C (2021) Norepinephrine-Induced Calcium Signaling and Store-Operated Calcium Entry in Olfactory Bulb Astrocytes. Front. Cell. Neurosci. 15:639754. doi: 10.3389/fncel.2021.639754

INTRODUCTION

Norepinephrine is one of the major neuromodulators in the mammalian central nervous system. It is involved in a variety of vital cognitive functions such as memory and attention (Berridge and Waterhouse, 2003; Aston-Jones and Cohen, 2005). Furthermore, it has been shown that norepinephrine plays a crucial role in sleep-wake cycle (O'Donnell et al., 2015). The locus coeruleus (LC) is the major site for the biosynthesis of norepinephrine. Its widespread neuronal projections innervate many different brain regions such as the neocortex, amygdala, hippocampus, and hypothalamus. They also reach the main olfactory bulb, where ≈40% of LC neurons project to (Shipley et al., 1985). Thus, noradrenergic input to the main olfactory bulb is part of the centrifugal innervation and plays a key role in odor learning, recognition, and recall (Linster et al., 2011). Previous studies showed that the majority of norepinephrine fibers target the external plexiform layer (EPL), the internal plexiform layer (IPL), and the granule cell layer (GCL), and to a lesser extent the mitral cell layer (ML) and the glomerular layer (GL) (McLean et al., 1989). Norepinephrine release in the main olfactory bulb regulates the strength of GABAergic inhibition of mitral cells depending on the norepinephrine receptor subtype activated (Trombley, 1992; Trombley and Shepherd, 1992; Nai et al., 2009). In accordance with the noradrenergic fiber distribution, each of the three major subtypes, α1-, α2-, and β-receptors, are expressed in multiple layers of the olfactory bulb, and distinct main olfactory bulb neurons seem to express

various norepinephrinereceptor subtypes, e.g., granule cells express α1- and α2-receptors, whereas mitral cells express all three subtypes (Nai et al., 2009, 2010). While expression and function of norepinephrine receptors are well-studied in neurons, it is unknown to date whether olfactory bulb astrocytes possess noradrenergic receptors.

An increasing number of studies has unraveled the role of astrocytes in the brain during the past two decades and it is generally accepted that astrocytes act on neurons in a manner that extends the traditional view of being solely supporting cells. Astrocytes take part in the regulation of synaptic transmission and plasticity through a wide variety of processes, developing the idea of the tripartite synapse (Araque et al., 1999a,b; Brockhaus and Deitmer, 2002; Volterra and Meldolesi, 2005; Henneberger et al., 2010). Specifically, these processes include modulation of synaptic glutamate and potassium homeostasis, activity-dependent synaptogenesis and elimination, neurotransmitter synthesis, synaptic connectivity, and vascular function (Araque et al., 2014; Lohr et al., 2014; Guerra-Gomes et al., 2017). In this context, astrocytic calcium signaling provides a fundamental mechanism to integrate synaptic function of surrounding cellular circuits and has been subject to intense research in the last decades (Deitmer et al., 1998; Verkhratsky et al., 2012; Verkhratsky and Zorec, 2019). The effect of norepinephrine on astrocytes and astrocytic calcium signaling has been extensively studied in diverse brain regions such as sensory cortex, where it has been demonstrated that astrocytes play a key role in the modulatory network of norepinephrine (Vardjan and Zorec, 2017). However, although norepinephrine innervation in the olfactory bulb is high and has a strong influence on neuronal network activity, the role of norepinephrine on olfactory bulb astrocytes remains unknown. In this study, we investigated the physiology of norepinephrine receptors in olfactory bulb astrocytes by employing the calcium indicator Fluo-8 and confocal calcium imaging in acute olfactory bulb brain slices. Our results show that olfactory bulb astrocytes respond to bath application of norepinephrine with α-receptor-mediated calcium release from internal stores. Furthermore, we demonstrate the contribution of store-operated calcium entry (SOCE) to norepinephrine-induced calcium transients.

MATERIALS AND METHODS

Animals Used for Slice Preparation

Naval Medical Research Institute (NMRI) outbred mice from postnatal day 7 (p7) to p21 were used for calcium imaging experiments. No differences in results were found within this time range. Mice were bred in the institute's animal facility at the University of Hamburg and all experiments were carried out in accordance with the recommendations of the European Union's and local animal welfare guidelines (03/2020; approved by Behörde für Gesundheit und Verbraucherschutz, Hamburg, Germany). Mice were anesthetized using isoflurane (5% mixed with 1 L/min O_2) and decapitated before using for experiments. Olfactory bulb slices were prepared as described before (Fischer et al., 2012). Brains were quickly dissected and transferred into a chilled artificial cerebrospinal fluid (ACSF, see below). Two hundred micrometer thick horizontal slices of the bulbs were cut using a vibratome (Leica VT1200S, Bensheim, Germany). Slices were stored in ACSF for 30 min at 30°C and then at room temperature until starting experiments. Artificial cerebrospinal fluid was continuously gassed with carbogen (95% O_2/5% CO_2; buffered to pH 7.4 with CO_2/bicarbonate).

Solutions and Chemicals

The standard ACSF for acute brain slices contained (in mM): NaCl 125, KCl 2.5, $CaCl_2$ 2, $MgCl_2$ 1, D-glucose 25, $NaHCO_3$ 26, $NaHPO_4$ 1.25, gassed during the entire experiment with carbogen to adjust the pH to 7.4. Phosphate buffered solution (PBS) contained (in mM): NaCl 130, Na_2HPO_4 7, NaH_2PO_4 3. Norepinephrine and 2-APB (2-aminoethyl diphenylborinate) were obtained from Sigma-Aldrich (Darmstadt, Germany). ICI 118,551 hydrochloride (ICI), MPEP, CGP55845, MRS 2179, and ZM241385 were obtained from Tocris (Bristol, UK). BTP2 (YM-58483), D-APV, NBQX, gabazine, TTX (tetrodotoxin), CPA (cyclopiazonic acid), prazosin, and rauwolscine were obtained from Abcam (Cambridge, United Kingdom). All substances were stored as stock solutions according to the manufacturers' description.

Immunohistochemistry

Immunohistochemistry on olfactory bulbs of NMRI mice (p14) was performed as described before (Klein et al., 2020). After preparation, olfactory bulb hemispheres were kept in PFA 4% for 1 h at room temperature. Hemispheres were cut into 100-μm sagittal slices using a vibratome (VT1000S, Leica, Nussloch, Germany) and then incubated for 1 h at room temperature in blocking solution (10% normal goat serum, 0.5% Triton X-100 in PBS). Subsequently, the slices were incubated with primary antibody solution, containing antibodies diluted in 1% NGS, 0.05% Triton X-100 in PBS for 48 h at 4°C. The primary antibodies chicken anti-NET (1:500, Synaptic Systems, Göttingen, Germany) and rabbit anti-GFAP (1:1,000, Dako, Hamburg, Germany) were used. Afterwards, slices were incubated in PBS with the following secondary antibodies for 24 h at 4°C: goat anti-chicken Alexa 488 (1:1,000, Abcam) and goat anti-rabbit Alexa 555 (1:1,000, Invitrogen Thermo Fisher, Darmstadt, Germany). Additionally, DAPI (5 μM, Thermo Fischer) was added to visualize nuclei. Slices were mounted on slides using a self-hardening embedding medium (Immu-Mount, Thermo Fisher). A confocal microscope (C1 Eclipse, Nikon, Düsseldorf, Germany) was used to image immunohistochemical staining. Image processing and analysis is described in Klein et al. (2020). Image stacks were obtained with an axial step size of 150 nm. Stacks were deconvolved using Huygen's software (SVI, Hilversum, Netherlands). Projections were made using Image J (NIH, Bethesda, USA), contrast and brightness were adjusted with Adobe Photoshop CS2 graphics editor.

Calcium-Imaging

Slices were incubated with the membrane-permeable form of the calcium indicator Fluo-8 (Fluo-8-AM; 2 μM in ACSF) made from a 2 mM stock solution (dissolved in DMSO and 20% pluronic) for 30 min. Brain slices were then placed in the

recording chamber and fixed with a U-shaped platinum wire with nylon strings. Brain slices were continuously perfused at a rate of 2 ml/min with ACSF that was gassed with carbogen (95 O_2/5% CO_2). Bath perfusion with ACSF was accomplished using a peristaltic pump (Vario, Ismatec, Germany). Drugs were applied via the perfusion system. If not stated otherwise, ACSF contained 1 μM TTX to suppress neuronal activity. Changes in intracellular calcium levels in olfactory bulb astrocytes were recorded by confocal microscopy (C1 Eclipse, Nikon, Düsseldorf, Germany). An excitation laser wavelength of 488 nm and a frame rate of 0.66 fps were used, and the fluorescence was collected through a 500–530 nm bandpass filter.

Data Analysis and Statistic

The data were evaluated with Nikon EZ-C1 Viewer (Nikon) and statistical tests have been applied with Origin Pro 9.1 (OriginLab Corporation, Northampton, USA). To analyze changes of the calcium level in astrocytes, all cell somata were manually marked as regions of interests (ROIs), each ROI outlining the silhouette of the soma. Cells located in the GL and EPL that showed a calcium response to bath-applied ADP and to low extracellular K^+ were identified as astrocytes (Hartel et al., 2007; Doengi et al., 2008; Fischer et al., 2020). The astrocytic calcium elevations have been observed in both GL and EPL without a significant difference in amplitude or duration, therefore the results in the present study are pooled data of both layers. To evaluate changes of calcium levels over time, Fluo-8 fluorescence intensity (F) was recorded during the course of the experiment and normalized to the basal fluorescence intensity in absence of pharmacological stimuli. Changes in calcium are given by ΔF as the percentage changes in fluorescence with respect to the basal fluorescence which was set to 100%. Since bleaching of Fluo-8 or slight movement of the tissue can lead to shifts in the baseline, the baseline was adjusted for each calcium response to the average of the last 10 data points before each calcium response. The starting time point of the response was defined as the first time point with a fluorescence value clearly higher than the baseline, which could easily be identified due to the rapid onset of the response. The peak of the calcium response was taken as the maximum value during the response. Calcium responses were assessed as amplitude (baseline to peak) and area (integral of the curve from the starting time point of the response until baseline was reached again). Duration of the response was assessed as the time span from the starting time point until the time point when the curve returned to baseline. All values are given as mean values ± standard error of the mean with "*n*" representing the sample size, given as "number of cells/number of brain slices/number of animals." Some of the data populations were not normally distributed (Kolmolgorov-Smirnov's test), hence proof of statistical significance for paired data was done by non-parametric Wilcoxon signed-rank test at an error probability p: $^*p < 0.05$; $^{**}p < 0.01$; $^{***}p < 0.001$. In case of independent data the Mann-Whitney-U test was applied. Multiple comparisons were done using Kruskal-Wallis ANOVA followed by Dunn's *post-hoc* test (all tests done using Origin Pro 9.8, OriginLab Corp., Northampton, MA). To test the effect of a drug or combination of drugs (e.g., a receptor antagonists) on norepinephrine-evoked calcium signals in a test experiment, a first application of norepinephrine in the absence of the drug was performed, followed by a second application in the presence of the drug. Drugs were pre-incubated at least for 5 min. The effect of the drug was then expressed as percentage inhibition of the norepinephrine-evoked calcium response compared to the first application. However, in a rundown experiment, the second application of norepinephrine in the absence of a drug *per se* resulted in a significantly smaller calcium response (rundown) compared to the first application. The effect of the rundown was given as percentage reduction compared to the first application. A drug was only considered effective if the inhibition in the presence of the drug (second application, test experiment) was significantly larger than the reduction in the absence of the drug (second application, rundown experiment) which served as control. Therefore, means of the second application of test experiments were tested against the mean of the second application in the rundown experiment. In the figures, data populations are represented as violin plots. The violin plots also include symbols representing single data values, the median and 25–75% percentiles as horizontal lines as well as the mean values. Mean values of different data populations within a given graph are connected by a dotted line to improve visualization.

RESULTS

Close Proximity of Noradrenergic Fibers and Astrocyte Processes

We first studied the structural relationship between noradrenergic fibers originating in the LC and olfactory bulb astrocytes. Noradrenergic fibers were visualized using an antibody against norepinephrine transporters (NET) while astrocytes were highlighted using anti-GFAP staining (**Figure 1**). Both noradrenergic fibers and astrocytes were present in all layers of the olfactory bulb except the most superficial layer, the nerve layer. Sensory information is propagated by axons of olfactory sensory neurons that project into spherical neuropilar structures called glomeruli where the axons synapse onto projection neurons, mitral, and tufted cells. Glomeruli were penetrated by a dense meshwork of noradrenergic fibers that intermingle with astrocyte processes. Frequently, astrocyte processes were in close proximity of varicosities, the release sites of centrifugal fibers (**Figures 1B,C**; **Supplementary Figure 1**). In the EPL, the density of noradrenergic fibers was lower, however, astrocyte processes adjacent to varicosities were also found in the EPL (**Figures 1D,E**; **Supplementary Figure 1**). These results suggest that astrocytes might be able to detect norepinephrine released from centrifugal fibers of the LC.

Norepinephrine Induces Calcium Transients in Olfactory Bulb Astrocytes

The present study focuses on the effect of norepinephrine on astrocytes in the GL and EPL of the olfactory bulb, the layers with the highest synaptic activity in the olfactory bulb (Rotermund et al., 2019). We used application of ADP to test the viability of the cells and to identify astrocytes in the olfactory bulb.

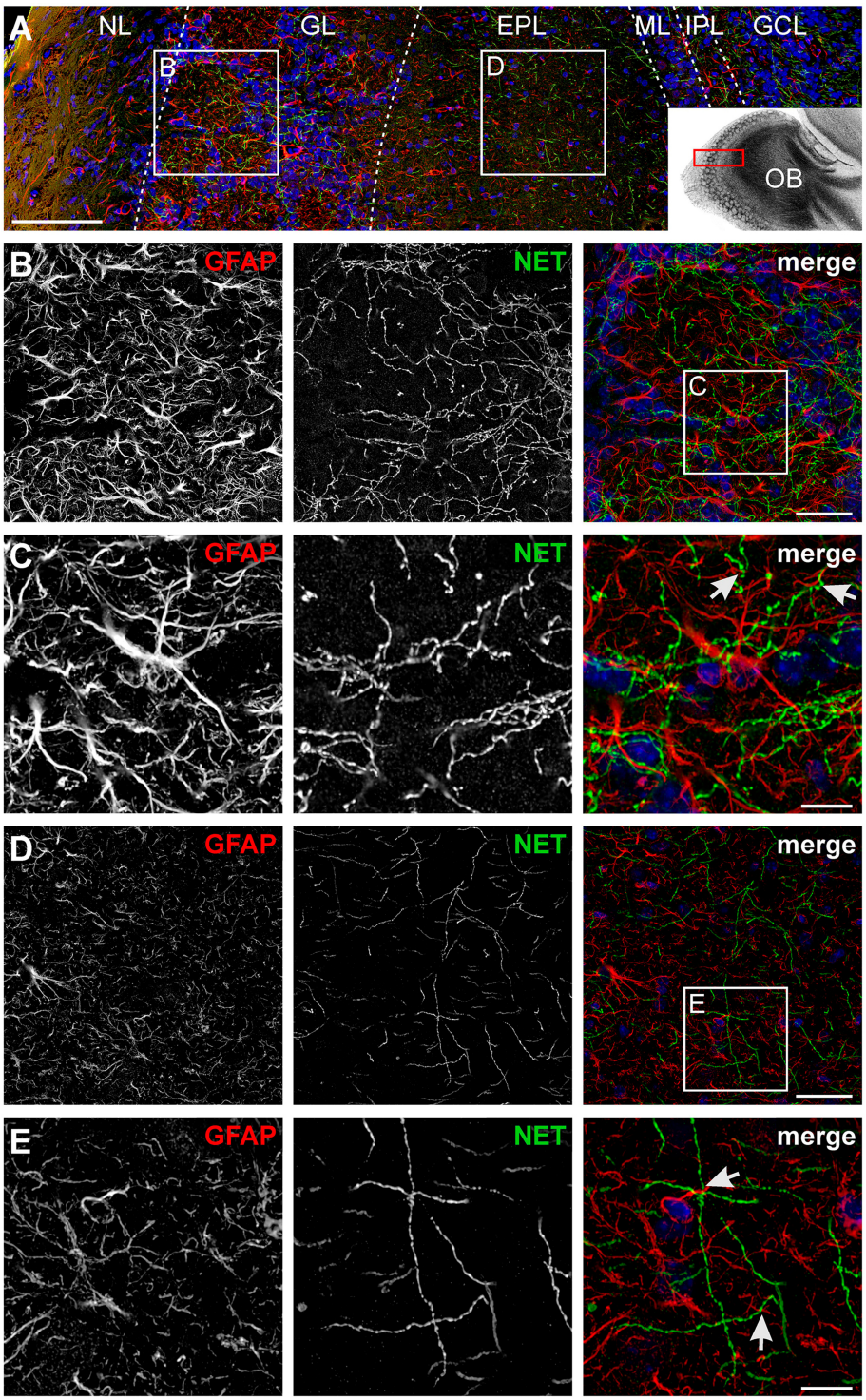

FIGURE 1 | Visualization of noradrenergic fibers and astrocytes in the olfactory bulb. **(A)** Laminar organization of the olfactory bulb. Astrocytes were labeled by GFAP immunostaining (red), noradrenergic fibers were visualized by staining of the norepinephrine transporter (NET; green). Nuclei were stained with Dapi (blue). NL, nerve layer; GL, glomerular layer; EPL, external plexiform layer; ML, mitral cell layer; IPL, internal plexiform layer; GCL, granule cell layer. Scale bar: 100 μm. The inset depicts the location of the section in the olfactory bulb. **(B)** Astrocytes and noradrenergic fibers in the GL. Scale bar: 20 μm. **(C)** Magnified view of the GL. Astrocytes and noradrenergic fibers strongly intermingle, bringing astrocytic processes, and noradrenergic varicosities closely together (arrows). Scale bar: 5 μm. See also **Supplementary Figure 1**. **(D)** Astrocytes and noradrenergic fibers in the EPL. Scale bar: 20 μm. **(E)** Magnified view of the EPL. Arrows point to astrocyte processes adjacent to varicosities. Scale bar: 5 μm. All images represent projections of image stacks spanning 8 μm in depth.

Olfactory bulb astrocytes express P2Y1-receptors and respond to ADP with calcium transients, whereas earlier studies could show that Fluo-8-loaded olfactory bulb neurons do not respond to bath application of ADP (Doengi et al., 2008, 2009; Fischer et al., 2020). The aim of our study was to find out whether norepinephrine induces calcium transients in olfactory bulb astrocytes. We recorded calcium responses in astrocytes of the GL and EPL (**Figures 2A,B**). Application of 10 μM norepinephrine led to a cytosolic calcium rise with an amplitude of 115.0 ± 4.3% ΔF and an area of 47.5 ± 2.2 ΔF*s ($n = 101/6/4$) in the EPL and an amplitude of 116.1 ± 5.9% and area of 40.1 ± 2.8 ΔF*s ($n = 49/6/4$) in the GL, showing no significant difference in response amplitude and a small yet significant difference in the area ($p = 0.025$) between the layers (**Figure 2C**). Since the differences were neglectable we pooled data of the two layers for all following experiments. To appraise the optimal dose of norepinephrine we applied various concentrations. The results show that the minimal concentration to which all astrocytes responded was 10 μM, while some astrocytes started to respond to 3 μM (**Figures 2D–F**). The response consisted of a rapid increase that peaked after a few seconds, followed by a rapid decrease that turned into a plateau-like phase that stayed elevated at least as long as the application of norepinephrine continued (**Figure 2B**). Multiple applications of 10 μM norepinephrine in the same preparation led to a signal rundown, which resulted in a significant reduction by 10.8 ± 2.2% ($n = 44/3/2$; $p < 0.001$) in the second and 26.2 ± 2.6% ($n = 44/3/2$; $p < 0.001$) in the third application (**Figure 2G**) as compared to the first application (control). We refer to this as "rundown experiment." We then compared responses evoked by norepinephrine application in the presence of a mix of GABAergic, glutamatergic, and purinergic antagonists (blockermix; GABAA: Gabazine 10 μM; GABAB: CGP55845 10 μM; AMPA-receptors: NBQX 10 μM; NMDA-receptors: D-APV 50 μM; mGluR5: MPEP 2 μM; P2Y1: MRS2179 50 μM; A2A: ZM241385 0.5 μM; sodium channels: TTX 1 μM) with the corresponding application in the absence of receptor antagonists (second application, rundown experiment) to evaluate the contribution of these receptors to the norepinephrine-evoked response and to isolate the response from indirect neuronal impact (**Figures 2H,I**). In the presence of the blockermix, no significant differences between the values of the second application in the control experiments and in experiments using the blockermix were found, indicating that the norepinephrine-evoked calcium signals were not modulated by spontaneous neuronal activity or synaptic transmission as they were not affected by application of the blockermix (**Figure 2I**). We nevertheless performed all subsequent experiments in the presence of this blockermix to suppress any indirect neuronal effect. Hence, the second application of the experiments in the presence of the blockermix served as control for the following experiments.

Norepinephrine-Induced Calcium Transients Depend on Both α1 and α2, but Not on β-receptors

Taking into account that norepinephrine-evoked calcium transients in astrocytes were not affected by blockers of neuronal voltage-gated sodium channels and neurotransmitter receptors, we assumed that astrocytes expressed noradrenergic receptors themselves. Thus, we applied norepinephrine in the presence of antagonists for the major subtypes of noradrenergic receptors to test whether the norepinephrine-induced calcium transients are affected (**Figure 3**). In the presence of the α1-receptor antagonist prazosin, norepinephrine-induced calcium transients were reduced by 65.3 ± 6.8% ($n = 35/3/3$; $p < 0.001$) in amplitude and 70.9 ± 7.1% ($n = 35/3/3$; $p < 0.001$) in area (**Figures 3A,E**). Under the influence of the α2-antagonist rauwolscine, the norepinephrine-induced calcium transients were diminished by 27.5 ± 2.6% ($n = 64/3/2$; $p < 0.001$) in amplitude and 43.1 ± 6.2% ($n = 64/3/2$; $p < 0.001$) in area (**Figures 3B,E**). To test the possible involvement of β-adrenergic receptors, we used the β-selective antagonist ICI-118,551. In the presence of ICI-118,551, norepinephrine-induced calcium transients were not significantly reduced in amplitude and in area when compared to the second application of the control experiment ($n = 71/6/3$; $p > 0.05$) (**Figures 3C,E**). In the presence of all antagonists mentioned above, the calcium transients were nearly completely abolished with a reduction of 94.6 ± 2.3% ($n = 17/1/1$; $p < 0.001$) in amplitude and 96.8 ± 1.1% ($n = 17/1/1$; $p < 0.001$) in area (**Figures 3D,E**).

Norepinephrine-Induced Calcium Transients Depend on Intracellular Calcium Stores

We next aimed to investigate whether the cytosolic calcium rise depends on intracellular calcium stores. To elucidate this, we applied norepinephrine before and after calcium stores were depleted by incubation with 20 μM cyclopiazonic acid (CPA), an inhibitor of the sarco-/endo-plasmic reticulum calcium-ATPase (SERCA). Cyclopiazonic acid entirely suppressed norepinephrine-evoked calcium responses (**Figure 4A**). The mean amplitude of norepinephrine-induced calcium transient was reduced by 95.5 ± 1.6% ($n = 42/5/3$; $p < 0.001$) in amplitude and by 97.2 ± 2.7% ($n = 42/5/3$; $p < 0.001$) in area (**Figures 4A,E**), indicating that release of calcium from the endoplasmic reticulum (ER) is required for the norepinephrine-induced cytosolic calcium rise. We also tested the contribution of extracellular calcium to norepinephrine-evoked calcium responses. Withdrawal of extracellular calcium led to a reduction by 29.2 ± 3.2% (45/5/4; $p < 0.001$) in amplitude of norepinephrine-evoked calcium responses, while the area of the response was reduced by a much larger fraction of 66.2 ± 3.9% (45/5/4; $p < 0.001$) (**Figures 4B,E**). This indicates that norepinephrine-induced calcium transients not exclusively depend on intracellular calcium, but also needs calcium influx from the extracellular space. In particular, the late plateau-like phase of the response was entirely suppressed in the absence of extracellular calcium, suggesting that the plateau was mediated by calcium influx.

To test whether the norepinephrine-induced calcium rise depends on the PLC/IP3 signaling pathway, we applied norepinephrine after incubation with the IP3 receptor antagonist 2-APB. Since concentrations above 50 μM of 2-APB activate

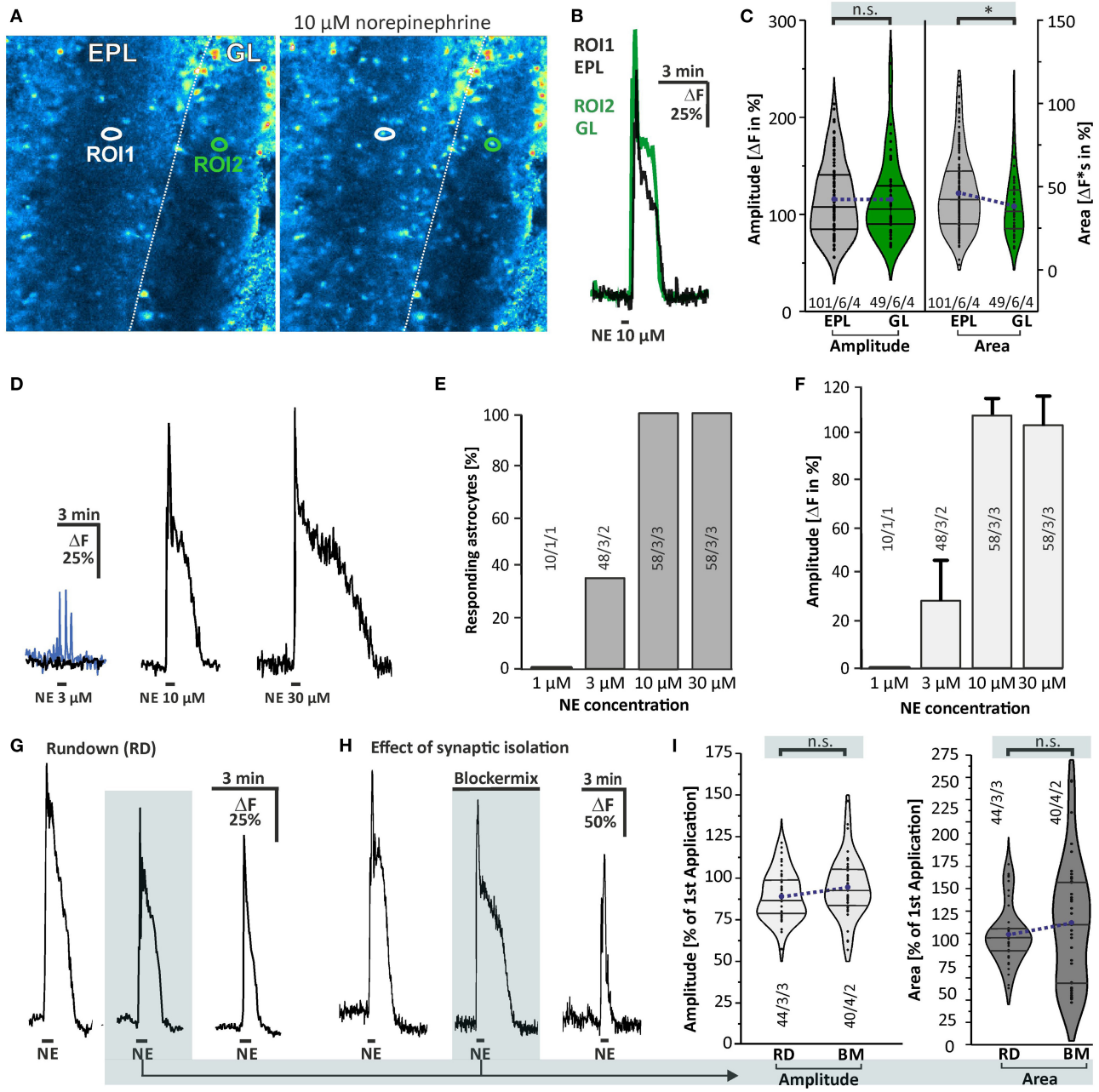

FIGURE 2 | Norepinephrine-induced calcium transients in olfactory bulb astrocytes. **(A)** Fluo-8 staining of acute olfactory bulb slices with example ROIs shown in idle state (left) and in the presence of 10 µM norepinephrine (right). **(B)** Example traces of cells located in the external plexiform layer (EPL; ROI1, black trace) and in the glomerular layer (GL; ROI2, green trace). **(C)** Violin plots of amplitude (left) and area (right) of norepinephrine-induced calcium responses in EPL (gray) and GL (green) (see section Materials and Methods for details). Sample size as specified: cells/slices/animals. n.s., not significant. *$p < 0.05$. **(D)** Dose-response relationship of calcium transients evoked by norepinephrine (NE). At 3 µM NE, most astrocytes did not respond with Ca^{2+} transients (black trace), while some astrocytes generated a small Ca^{2+} rise (blue trace). **(E)** 1 µM NE failed to trigger calcium transients in astrocytes, while 3 µM evoked a Ca^{2+} response in about one-third of the astrocytes. Ten micromolars of NE was sufficient to induce calcium transients in all astrocytes investigated, with **(F)** maximal amplitude. **(G)** Example of multiple applications of NE (10 µM) with a 10-min interval displaying a significant signal rundown. **(H)** Calcium transients were not affected in presence of tertodotoxin (TTX), GABAergic, glutamatergic, and purinergic antagonists (Blockermix contains: NBQX 10 µM, D-APV 50 µM, gabazine 10 µM, CGP55845 10 µM, MPEP 2 µM, MRS2179 50 µM, ZM241385 0.5 µM, TTX 1 µM). For statistical analyses, the second application in blockermix was compared to the second application in the rundown experiment [depicted in **(G)**]. **(I)** Ca^{2+} responses by the second application of NE were normalized to responses of the first application, set to 100%. Amplitudes (left) and area (right) of calcium responses compared between the rundown experiment, i.e., in the absence of the blockermix (RD), and in presence of the blockermix (BM). Both amplitude and area were not significantly different (n.s.).

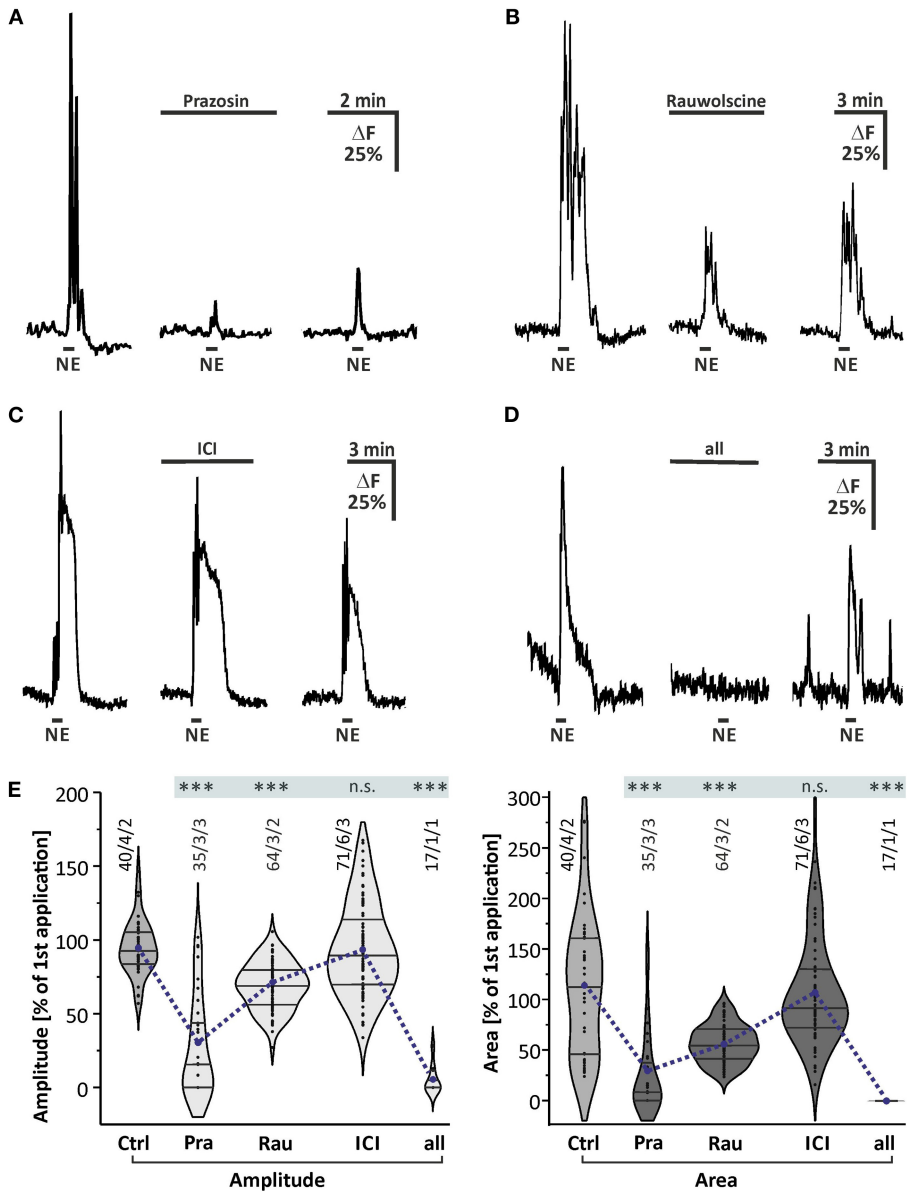

FIGURE 3 | Effect of noradrenergic receptor antagonists. **(A)** All experiments were performed in the presence of the blockermix described in **Figure 2** to isolate the direct response in astrocytes. Norepinephrine-induced calcium responses were strongly reduced in the presence of α1-antagonist prazosin (10 μM). **(B)** Calcium transients were affected in the presence of the α2-antagonist rauwolscine (0.5 μM). **(C)** Calcium transients were not significantly affected by β-receptor antagonist ICI-118,551 (15 μM). **(D)** Calcium transients were entirely abolished in the presence of a combination of all antagonists mentioned above. **(E)** Violin plots of amplitudes (light gray) and area (dark gray) of calcium responses under control conditions (i.e. second application of the blockermix experiment depicted in **Figure 2H**) and in the presence of prazosin (Pra), rauwolscine (Rau), ICI, and a combination of all. n.s. = not significant; $^{***}P < 0.001$.

transient receptor potential channels TRPV and lead to calcium oscillations in olfactory bulb astrocytes (Doengi et al., 2009), the selective TRPV4 antagonist HC-067047 (1 μM) was co-applied with 2-APB to suppress TRPV4-mediated calcium oscillations and to allow for a higher concentration of 2-APB. However, HC-067047 alone partly reduced the amplitude and area of norepinephrine-evoked calcium responses (**Figures 4C,E**). Additional application of 100 μM 2-APB almost entirely suppressed norepinephrine-induced calcium responses, on average by 83.9 ± 1.6% ($n = 57/5/3$; $p < 0.001$) in amplitude and 90.3 ± 2.5% ($n = 57/5/3$; $p < 0.001$) in area, indicating the involvement of IP3-receptors (**Figure 4E**). It must be noted, however, that 2-APB also blocks calcium channels such as Orai and some TRP channels and hence part of the effect of 2-APB is on calcium influx from the extracellular space (see below).

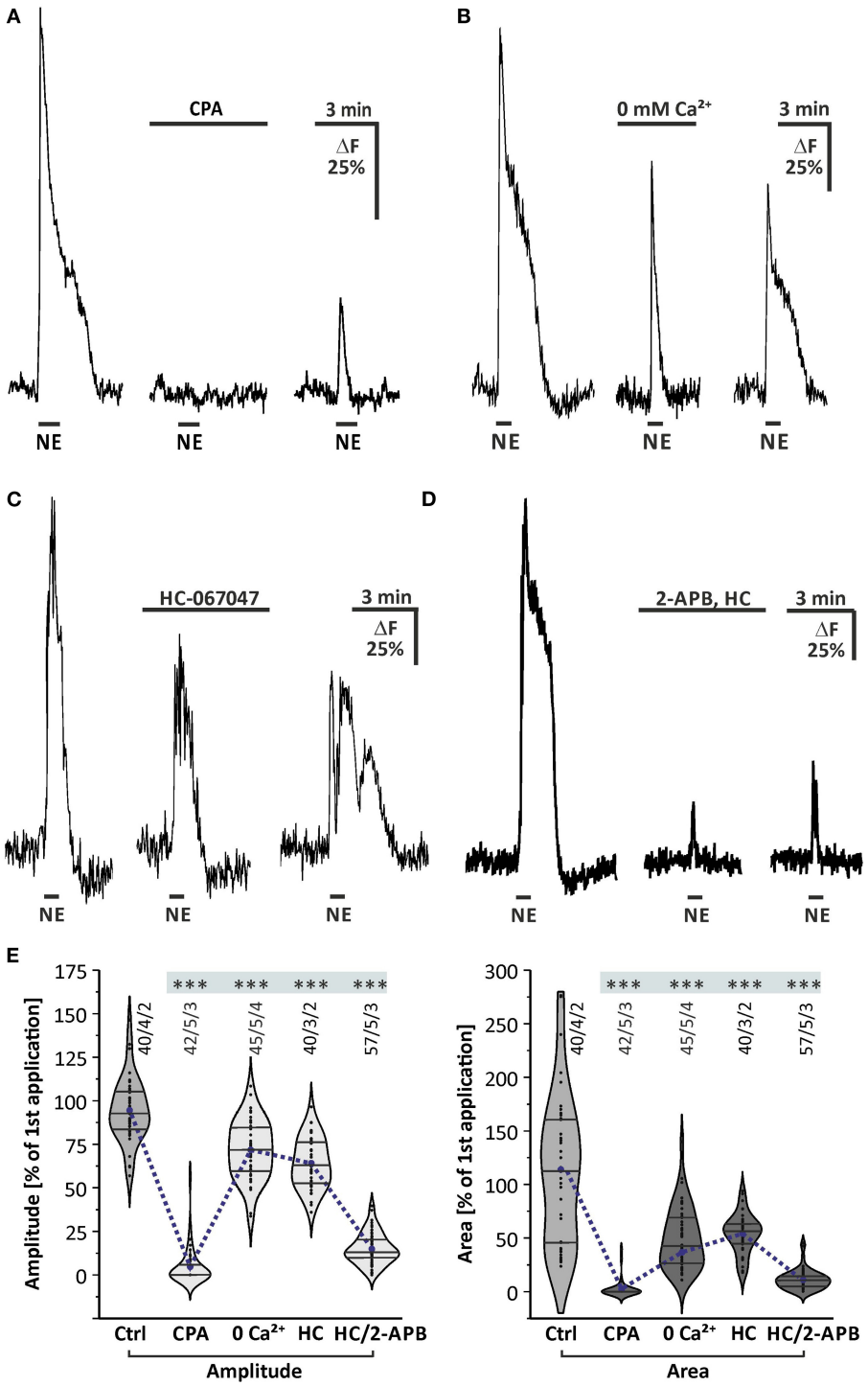

FIGURE 4 | Internal calcium release and phospholipase C mediate norepinephrine-induced calcium transients in olfactory bulb astrocytes. **(A)** Norepinephrine-induced calcium transients are entirely suppressed in the presence of SERCA inhibitor cyclopiazonic acid (CPA, 20 μM). **(B)** Calcium transients are significantly reduced in the absence of extracellular calcium (0 mM Ca^{2+}). **(C)** Norepinephrine-induced calcium transients are partly suppressed in the presence of TRPV4 inhibitor HC-067047 (1 μM). **(D)** Calcium response is entirely abolished in the presence of IP3-receptor antagonist 2-APB (100 μM) and HC-067047 (HC). **(E)** Violin plots of amplitudes (light gray) and area (dark gray) of calcium responses under control conditions (i.e., second application of the blockermix experiment depicted in **Figure 2H**) and in the presence of CPA, Ca^{2+}-free solution, HC-067047 (HC) alone and in combination with 2-APB. ***$P < 0.001$.

Store-Operated Calcium Entry in Olfactory Bulb Astrocytes

It is not yet known which mechanism is responsible for calcium influx from the extracellular space into olfactory bulb astrocytes. Since calcium is partly transported out of the cell by plasma membrane calcium transporters, glial cells accomplish calcium store refilling by employing plasma membrane calcium channels under the control of the ER calcium content, a mechanism known as SOCE (Parekh and Putney, 2005). It has been shown that SOCE plays an important role in calcium homeostasis and signaling of cerebellar glial cells (Singaravelu et al., 2006). To determine whether SOCE is relevant in olfactory bulb astrocytes, we studied SOCE as induced by CPA in olfactory bulb astrocytes regarding its sensitivity to different drugs (**Figure 5**). The CPA-induced depletion of calcium stores resulted in calcium transients during re-addition of calcium with a mean amplitude of 35.1 ± 1.9% ΔF (n = 72/6/4; $p < 0.001$). The calcium transients were significantly reduced by 45 ± 1.9% (n = 41/4/4; $p < 0.001$) in the presence of 2-APB (100 μM), an inhibitor of SOCE channels (Ma et al., 2000; Bakowski et al., 2001; Singaravelu et al., 2006). 2-Aminoethyl diphenylborinate was applied 10 min before the re-addition of calcium in the presence of CPA (**Figures 5A,B**). However, since 2-APB is also an inhibitor of PLC (see **Figure 4**), we performed experiments using BTP2, a structurally distinct blocker of SOCE channels also known as calcium release-activated channels (CRAC), but without effect on PLC (Ishikawa et al., 2003; Zitt et al., 2004). BTP2 (25 μM), pre-incubated for 10 min, significantly reduced SOCE by 62.9 ± 3.1% (n = 26/2/2; $p < 0.001$) (**Figures 5A,B**). To test whether iPLA2 plays a role in SOCE in olfactory bulb astrocytes, as it has been shown for Bergmann glia and cerebellar granule cells (Singaravelu et al., 2006, 2008), a specific inhibitor of iPLA2, AACOCF3 (25 μM) was applied. It is well-established to inhibit iPLA2 at a concentration of 15 μM and higher (Ackermann et al., 1995). The calcium transients during calcium re-addition in the presence of CPA were significantly reduced by 35.4 ± 1.0% ΔF (n = 86/9/4; $p < 0.001$) by AACOCF3 (**Figures 5A,B**). Our results show that depletion of calcium stores evokes SOCE, involving ICRAC channels and iPLA2.

Store-Operated Calcium Entry Contributes to Norepinephrine-Induced Calcium Transients

We investigated the involvement of SOCE in norepinephrine-induced calcium transients. The late plateau-like phase of the norepinephrine-evoked calcium response was abolished in calcium-free solution, indicating calcium influx (**Figure 4B**). To elucidate whether SOCE is the crucial mechanism responsible for this late phase calcium influx contributing to the norepinephrine-induced calcium response, we applied norepinephrine in the presence of the SOCE inhibitor BTP2 (25 μM). For this experiment, the duration of application was extended to 150 s to elongate the late phase of the calcium response. The data obtained were compared with a rundown experiment adapted to the modified application time of norepinephrine (**Figure 6A**). The second application of norepinephrine in the rundown experiment induced a calcium response with an amplitude of 89.0 ± 4.0% (n = 44/4/1) and area of 63.3 ± 2.9% (n = 44/4/1) compared to the first application (**Figure 6A**). Addition of BTP2 had no significant effect on the amplitude of the calcium response (n = 38/3/2), indicating that the initial Ca^{2+} peak is not mediated by BTP2-sensitive Ca^{2+} influx (**Figures 6B,C**). In contrast, the area of the second response was significantly reduced by BTP2 (n = 38/3/2; $p < 0.001$), indicating a prominent role of SOCE in the late phase of norepinephrine-induced calcium transients in olfactory bulb astrocytes. In addition, the Ca^{2+} trace returned

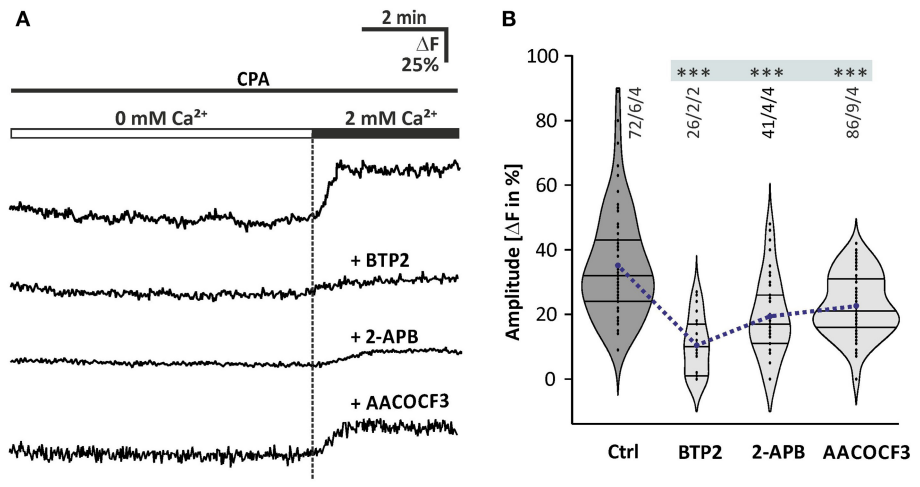

FIGURE 5 | Store-operated calcium entry in olfactory bulb astrocytes. **(A)** Original recordings of the cytosolic calcium concentration in somata of astrocytes of four different experiments. Acute brain slices were exposed to 20 μM CPA for 10 min in calcium-free solution (0 mM Ca^{2+}) before 2 mM calcium was re-added, and the resulting cytosolic calcium rise was indicative of SOCE. Traces show astrocytes that had been treated with CPA alone as a control, and with CPA in combination with the SOCE channel inhibitors 2-APB (100 μM) and BTP2 (25 μM) as well as the iPLA2 inhibitor AACOCF3 (25 μM). **(B)** Violin plots of amplitudes of calcium responses after calcium re-addition under control conditions (only CPA) and in the presence of 2-APB, BTP2, and AACOCF3. ***$P < 0.001$.

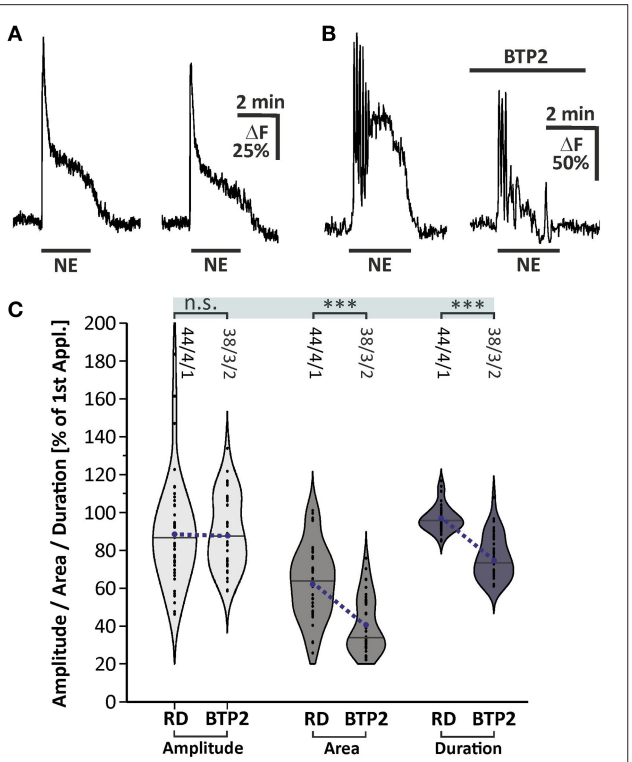

FIGURE 6 | Store-operated calcium entry contributes to norepinephrine-induced calcium transients in olfactory bulb astrocytes. **(A)** Example of two consecutive applications of norepinephrine (NE, 10 μM) for 150 s with a 10-min interval. **(B)** Calcium transients were affected in area and duration by BTP2. **(C)** Violin plots of amplitudes (light gray), area (mid gray) and duration (dark gray) of calcium responses under control conditions [i.e. second application of the rundown experiment depicted in **(A)**] and in the presence of BTP2. n.s. = not significant, ***$P < 0.001$.

to baseline even in the presence of norepinephrine (**Figure 6B**) and thus the duration of the calcium response was significantly shortened by BTP2 ($n = 38/3/2$; $p < 0.001$) (**Figure 6C**). In summary, norepinephrine evokes a biphasic calcium response in olfactory bulb astrocytes, consisting of an initial and transient calcium peak reflecting internal calcium release, followed by a sustained plateau phase established by calcium influx via SOCE channels.

DISCUSSION

Norepinephrine Induces Calcium Transients in Olfactory Bulb Astrocytes

In the present study, we showed that norepinephrine induced a rise in cytosolic calcium concentration in mouse olfactory bulb astrocytes *in situ*. The study was performed on brain slices obtained from animals at an age of 1–3 weeks and we cannot exclude changes in adrenergic calcium signaling in olfactory bulb astrocytes during adolescent development and aging. Ten micromolars of norepinephrine were needed to reliably trigger calcium responses, which appears to be rather high. However, norepinephrine is rapidly taken up by NET that are abundant in the olfactory bulb according to our immunhistological stainings. In addition, extracellular norepinephrine is degraded by catechol-O-methyltransferase (COMT), an enzyme with particular high expression and efficacy in the olfactory bulb (Eisenhofer et al., 2004; Cockerham et al., 2016). Hence, the effective concentration of norepinephrine at the receptor most likely was drastically less than adjusted in the perfusion solution. We demonstrated that the norepinephrine-induced calcium rise was entirely blocked in the presence of the SERCA inhibitor CPA, indicating that norepinephrine triggers calcium release from internal stores such as the ER. In the absence of extracellular calcium, on the contrary, the norepinephrine-induced calcium transients were only slightly reduced in amplitude, but to a larger extend in area and duration, indicating an involvement of extracellular calcium at least in the late plateau-like phase of the calcium response. The most common mechanism to liberate calcium from the ER is the phospholipase C (PLC)/IP3 signaling pathway, which has previously been shown for olfactory bulb astrocytes to be activated by P2Y1, A2A, mGluR5, and dopamine receptors and has been confirmed in the present study (Doengi et al., 2008; Otsu et al., 2015; Fischer et al., 2020). Calcium withdrawal suppressed only the late plateau phase of the calcium response with little effect on the initial calcium peak, whereas suppression of internal calcium release by CPA entirely blocked norepinephrine-mediated calcium responses. This suggests that calcium influx is downstream to calcium release, in line with SOCE which is only activated after calcium store depletion (Lopez et al., 2020). Indeed, the late calcium influx could be blocked by the SOCE channel blockers BTP2 and 2-APB (Somasundaram et al., 2014). Involvement of SOCE in norepinephrine-induced calcium transients has also been shown for hippocampal and cortical astrocytes (Gaidin et al., 2020; Okubo et al., 2020). Furthermore, we demonstrate that SOCE is dependent of iPLA2 by suppressing iPLA2 activity with AACOCF3, as shown in cerebellar astrocytes and granule cells as well as olfactory bulb ensheathing cells (Singaravelu et al., 2006, 2008; Thyssen et al., 2013).

α1 and α2-Adrenergic Receptors Mediate Calcium Signaling in Olfactory Bulb Astrocytes

The different subtypes of norepinephrine receptors are known to be linked to different signaling cascades. For α1-receptors the Gq-coupling was shown early on (Schwinn, 1993). α2-receptors, on the contrary, are mainly known to be negatively coupled to adenylate cyclase activity via Gi-proteins, but recent studies revealed a α2-receptor-mediated and Gq-coupled calcium response in hippocampal astrocytes (Gaidin et al., 2020). The norepinephrine-induced cytosolic calcium rise was decreased by α1- and α2-receptor antagonists, but not by a β-antagonist, indicating that both α-receptor subtypes contribute to norepinephrine-evoked calcium transients. There is a large amount of studies that have investigated adrenoceptor expression and function in astrocytes. Early electron microscopic studies on cortex first demonstrated both α- and β-adrenergic receptors

in astrocytic membranes (Aoki, 1992; Aoki et al., 1998) and, moreover, a close proximity of astrocytic processes with LC-noradrenergic varicosities and terminals (Cohen et al., 1997; Aoki et al., 1998), suggesting that astrocytes are well-positioned as a target for norepinephrine release from LC fibers. Our immunohistological results suggest that in the olfactory bulb astrocytic processes and noradrenergic varicosities are in close proximity. Astrocytes have also been shown to respond to norepinephrine *in situ* with calcium transients in hippocampal brain slices, mediated primarily by α1-adrenergic receptors (Duffy and MacVicar, 1995). More recently, α1-receptors have been highlighted as important participants in astrocytic calcium signaling in many different brain regions, such as cerebellum, ventrolateral medulla, and visual cortex (Ding et al., 2013; Paukert et al., 2014; Schnell et al., 2016). Furthermore, it has been demonstrated in awake behaving mice that α1-receptors of layer 2/3 neocortical astrocytes are very sensitive to norepinephrine and can induce gliotransmission of ATP and D-serine. Gliotransmission is followed by ATP receptor-mediated currents in adjacent pyramidal neurons which contributes to neocortical synaptic plasticity (Pankratov and Lalo, 2015). Another recently discovered example of norepinephrine-induced gliotransmission is mediated by α1-receptors (Gaidin et al., 2020). However, there are also results suggesting that β-receptors may also be involved in astrocytic calcium signaling in the cortex (Bekar et al., 2008).

Astrocytes as Neuromodulatory Elements in the Olfactory Bulb

In olfactory bulb neurons, the distribution of noradrenergic receptors has been extensively studied (Jahr and Nicoll, 1982; Trombley and Shepherd, 1992; Jiang et al., 1996; Matsutani and Yamamoto, 2008). Studies of the last decades on norepinephrine focused on the modulation of dendro-dendritic inhibition at the mitral cell–granule cell synapse with steadily increasing details (Nai et al., 2009, 2010; Linster et al., 2011; Li et al., 2015; Manella et al., 2017). For olfactory bulb astrocytes, the current work provides the first evidence for adrenergic receptors. However, norepinephrine is not the only neuromodulator that evokes calcium signaling in olfactory bulb astrocytes, yet it is the first "top down" neuromodulator released from centrifugal fibers described so far to act on astrocytes in the olfactory bulb. Dopamine is a neuromodulator that is released by local interneurons in the olfactory bulb and induced calcium responses in astrocytes similar to those evoked by norepinephrine (Fischer et al., 2020). In addition, ATP is released from nerve terminals of olfactory sensory neurons in the GL and is degraded by ectoenzymes to adenosine, another neuromodulator inducing calcium signaling in olfactory bulb astrocytes (Doengi et al., 2008; Thyssen et al., 2010; Thyssen et al., 2010). Interestingly, many of the neuromodulator receptors in astrocytes such as α2 adrenergic receptors, D1- and D2-like dopamine receptors and A_{2A} adenosine receptors that typically mediate stimulation or inhibition of adenylate cyclase are linked to IP_3 receptor-dependent release of calcium from internal stores in olfactory bulb astrocytes. Such calcium signaling may have a significant impact on neuronal performance in the olfactory bulb on different levels. Upon mechanical stimulation, e.g., rat olfactory bulb astrocytes release GABA and glutamate to evoke ionic currents in mitral and granule cells (Kozlov et al., 2006). Another gliotransmitter released by olfactory bulb astrocytes is ATP that is degraded to adenosine, a potent neuromodulator in the olfactory bulb (Roux et al., 2015; Schulz et al., 2017; Rotermund et al., 2018). Besides gliotransmission, astrocytes contribute to the blood brain barrier, mediate neurovascular coupling, and hence adjust local blood flow (Petzold et al., 2008; Doengi et al., 2009; Otsu et al., 2015; Beiersdorfer et al., 2020). Olfactory bulb astrocytes not only transmit information to neurons and blood vessels, but also to olfactory ensheathing cells, another type of glial cell that is coupled to astrocytes in a panglial network (Beiersdorfer et al., 2019). Considering the increasing evidence for functional contribution of astrocytes to neuromodulation and neurovascular coupling in the olfactory bulb, it is likely that noradrenergic fibers not only affect neuronal performance by directly stimulating neuronal adrenoceptors, but also employ astrocytes as active components of neural circuits.

DATA AVAILABILITY STATEMENT

The raw data supporting the conclusions of this article will be made available by the authors, without undue reservation.

ETHICS STATEMENT

The animal study was reviewed and approved by Behörde für Gesundheit und Verbraucherschutz, Hamburg, Germany.

AUTHOR CONTRIBUTIONS

TF, NR, and CL designed the study. TF, JP, and LE performed the experiments and analyzed the data. TF and CL wrote the manuscript. All authors contributed to the article and approved the submitted version.

FUNDING

This work was supported by funding from the Deutsche Forschungsgemeinschaft (LO 779/11-1 and SFB 1328 TP-A07).

ACKNOWLEDGMENTS

We thank A. C. Rakete, M. Fink, and P. Scheffler for excellent technical assistance.

SUPPLEMENTARY MATERIAL

The Supplementary Material for this article can be found online at: https://www.frontiersin.org/articles/10.3389/fncel.2021.639754/full#supplementary-material

REFERENCES

Ackermann, E. J., Conde-Frieboes, K., and Dennis, E. A. (1995). Inhibition of macrophage $Ca^{(2+)}$-independent phospholipase A2 by bromoenol lactone and trifluoromethyl ketones. *J. Biol. Chem.* 270, 445–450. doi: 10.1074/jbc.270.1.445

Aoki, C. (1992). Beta-adrenergic receptors: astrocytic localization in the adult visual cortex and their relation to catecholamine axon terminals as revealed by electron microscopic immunocytochemistry. *J. Neurosci.* 12, 781–792. doi: 10.1523/JNEUROSCI.12-03-00781.1992

Aoki, C., Venkatesan, C., Go, C. G., Forman, R., and Kurose, H. (1998). Cellular and subcellular sites for noradrenergic action in the monkey dorsolateral prefrontal cortex as revealed by the immunocytochemical localization of noradrenergic receptors and axons. *Cereb. Cortex* 8, 269–277. doi: 10.1093/cercor/8.3.269

Araque, A., Carmignoto, G., Haydon, P. G., Oliet, S. H., Robitaille, R., and Volterra, A. (2014). Gliotransmitters travel in time and space. *Neuron* 81, 728–739. doi: 10.1016/j.neuron.2014.02.007

Araque, A., Parpura, V., Sanzgiri, R. P., and Haydon, P. G. (1999a). Tripartite synapses: glia, the unacknowledged partner. *Trends Neurosci.* 22, 208–215. doi: 10.1016/s0166-2236(98)01349-6

Araque, A., Sanzgiri, R. P., Parpura, V., and Haydon, P. G. (1999b). Astrocyte-induced modulation of synaptic transmission. *Can. J. Physiol. Pharmacol.* 77, 699–706.

Aston-Jones, G., and Cohen, J. D. (2005). An integrative theory of locus coeruleus-norepinephrine function: adaptive gain and optimal performance. *Annu. Rev. Neurosci.* 28, 403–450. doi: 10.1146/annurev.neuro.28.061604.135709

Bakowski, D., Glitsch, M. D., and Parekh, A. B. (2001). An examination of the secretion-like coupling model for the activation of the Ca^{2+} release-activated Ca^{2+} current I(CRAC) in RBL-1 cells. *J Physiol.* 532(Pt 1), 55–71. doi: 10.1111/j.1469-7793.2001.0055g.x

Beiersdorfer, A., Scheller, A., Kirchhoff, F., and Lohr, C. (2019). Panglial gap junctions between astrocytes and olfactory ensheathing cells mediate transmission of $Ca^{(2+)}$ transients and neurovascular coupling. *Glia* 67, 1385–1400. doi: 10.1002/glia.23613

Beiersdorfer, A., Wolburg, H., Grawe, J., Scheller, A., Kirchhoff, F., and Lohr, C. (2020). Sublamina-specific organization of the blood brain barrier in the mouse olfactory nerve layer. *Glia* 68, 631–645. doi: 10.1002/glia.23744

Bekar, L. K., He, W., and Nedergaard, M. (2008). Locus coeruleus alpha-adrenergic-mediated activation of cortical astrocytes *in vivo*. *Cereb. Cortex* 18, 2789–2795. doi: 10.1093/cercor/bhn040

Berridge, C. W., and Waterhouse, B. D. (2003). The locus coeruleus-noradrenergic system: modulation of behavioral state and state-dependent cognitive processes. *Brain Res. Brain Res. Rev.* 42, 33–84. doi: 10.1016/s0165-0173(03)00143-7

Brockhaus, J., and Deitmer, J. W. (2002). Long-lasting modulation of synaptic input to Purkinje neurons by Bergmann glia stimulation in rat brain slices. *J. Physiol. (Lond.).* 545, 581–593. doi: 10.1113/jphysiol.2002.028423

Cockerham, R., Liu, S., Cachope, R., Kiyokage, E., Cheer, J. F., Shipley, M. T., et al. (2016). Subsecond regulation of synaptically released dopamine by COMT in the olfactory bulb. *J. Neurosci.* 36, 7779–7785. doi: 10.1523/JNEUROSCI.0658-16.2016

Cohen, Z., Molinatti, G., and Hamel, E. (1997). Astroglial and vascular interactions of noradrenaline terminals in the rat cerebral cortex. *J. Cereb. Blood Flow Metab.* 17, 894–904. doi: 10.1097/00004647-199708000-00008

Deitmer, J. W., Verkhratsky, A. J., and Lohr, C. (1998). Calcium signalling in glial cells. *Cell Calcium* 24, 405–416. doi: 10.1016/s0143-4160(98)90063-x

Ding, F., O'Donnell, J., Thrane, A. S., Zeppenfeld, D., Kang, H., Xie, L., et al. (2013). α1-Adrenergic receptors mediate coordinated Ca^{2+} signaling of cortical astrocytes in awake, behaving mice. *Cell Calcium* 54, 387–394. doi: 10.1016/j.ceca.2013.09.001

Doengi, M., Deitmer, J. W., and Lohr, C. (2008). New evidence for purinergic signaling in the olfactory bulb: A2A and P2Y1 receptors mediate intracellular calcium release in astrocytes. *FASEB J.* 22, 2368–2378. doi: 10.1096/fj.07-101782

Doengi, M., Hirnet, D., Coulon, P., Pape, H. C., Deitmer, J. W., and Lohr, C. (2009). GABA uptake-dependent $Ca^{(2+)}$ signaling in developing olfactory bulb astrocytes. *Proc. Natl. Acad. Sci. U.S.A.* 106, 17570–17575. doi: 10.1073/pnas.0809513106

Duffy, S., and MacVicar, B. A. (1995). Adrenergic calcium signaling in astrocyte networks within the hippocampal slice. *J. Neurosci.* 15, 5535–5550. doi: 10.1523/JNEUROSCI.15-08-05535.1995

Eisenhofer, G., Kopin, I. J., and Goldstein, D. S. (2004). Catecholamine metabolism: a contemporary view with implications for physiology and medicine. *Pharmacol. Rev.* 56, 331–349. doi: 10.1124/pr.56.3.1

Fischer, T., Rotermund, N., Lohr, C., and Hirnet, D. (2012). P2Y1 receptor activation by photolysis of caged ATP enhances neuronal network activity in the developing olfactory bulb. *Purinergic Signal.* 8, 191–198. doi: 10.1007/s11302-011-9286-z

Fischer, T., Scheffler, P., and Lohr, C. (2020). Dopamine-induced calcium signaling in olfactory bulb astrocytes. *Sci. Rep.* 10:631. doi: 10.1038/s41598-020-57462-4

Gaidin, S. G., Zinchenko, V. P., Sergeev, A. I., Teplov, I. Y., Mal'tseva, V. N., and Kosenkov, A. M. (2020). Activation of alpha-2 adrenergic receptors stimulates GABA release by astrocytes. *Glia* 68, 1114–1130. doi: 10.1002/glia.23763

Guerra-Gomes, S., Sousa, N., Pinto, L., and Oliveira, J. F. (2017). Functional roles of astrocyte calcium elevations: from synapses to behavior. *Front. Cell. Neurosci.* 11:427. doi: 10.3389/fncel.2017.00427

Hartel, K., Singaravelu, K., Kaiser, M., Neusch, C., Hulsmann, S., and Deitmer, J. W. (2007). Calcium influx mediated by the inwardly rectifying K+ channel Kir4.1 (KCNJ10) at low external K+ concentration. *Cell Calcium* 42, 271–280. doi: 10.1016/j.ceca.2006.12.004

Henneberger, C., Papouin, T., Oliet, S. H., and Rusakov, D. A. (2010). Long-term potentiation depends on release of D-serine from astrocytes. *Nature* 463, 232–236. doi: 10.1038/nature08673

Ishikawa, J., Ohga, K., Yoshino, T., Takezawa, R., Ichikawa, A., Kubota, H., et al. (2003). A pyrazole derivative, YM-58483, potently inhibits store-operated sustained Ca^{2+} influx and IL-2 production in T lymphocytes. *J. Immunol.* 170, 4441–4449. doi: 10.4049/jimmunol.170.9.4441

Jahr, C. E., and Nicoll, R. A. (1982). Noradrenergic modulation of dendrodendritic inhibition in the olfactory bulb. *Nature* 297, 227–229. doi: 10.1038/297227a0

Jiang, M., Griff, E. R., Ennis, M., Zimmer, L. A., and Shipley, M. T. (1996). Activation of locus coeruleus enhances the responses of olfactory bulb mitral cells to weak olfactory nerve input. *J. Neurosci.* 16, 6319–6329. doi: 10.1523/JNEUROSCI.16-19-06319.1996

Klein, M., Lohr, C., and Droste, D. (2020). Age-dependent heterogeneity of murine olfactory bulb astrocytes. *Front. Aging Neurosci.* 12:172. doi: 10.3389/fnagi.2020.00172

Kozlov, A. S., Angulo, M. C., Audinat, E., and Charpak, S. (2006). Target cell-specific modulation of neuronal activity by astrocytes. *Proc. Natl. Acad. Sci. U.S.A.* 103, 10058–10063. doi: 10.1073/pnas.0603741103

Li, G., Linster, C., and Cleland, T. A. (2015). Functional differentiation of cholinergic and noradrenergic modulation in a biophysical model of olfactory bulb granule cells. *J. Neurophysiol.* 114, 3177–3200. doi: 10.1152/jn.00324.2015

Linster, C., Nai, Q., and Ennis, M. (2011). Nonlinear effects of noradrenergic modulation of olfactory bulb function in adult rodents. *J. Neurophysiol.* 105, 1432–1443. doi: 10.1152/jn.00960.2010

Lohr, C., Grosche, A., Reichenbach, A., and Hirnet, D. (2014). Purinergic neuron-glia interactions in sensory systems. *Pflugers Arch.* 466, 1859–1872. doi: 10.1007/s00424-014-1510-6

Lopez, J. J., Jardin, I., Albarran, L., Sanchez-Collado, J., Cantonero, C., Salido, G. M., et al. (2020). Molecular basis and regulation of store-operated calcium entry. *Adv. Exp. Med. Biol.* 1131, 445–469. doi: 10.1007/978-3-030-12457-1_17

Ma, H. T., Patterson, R. L., van Rossum, D. B., Birnbaumer, L., Mikoshiba, K., and Gill, D. L. (2000). Requirement of the inositol trisphosphate receptor for activation of store-operated Ca^{2+} channels. *Science* 287, 1647–1651. doi: 10.1126/science.287.5458.1647

Manella, L. C., Petersen, N., and Linster, C. (2017). Stimulation of the locus ceruleus modulates signal-to-noise ratio in the olfactory bulb. *J. Neurosci.* 37, 11605–11615. doi: 10.1523/JNEUROSCI.2026-17.2017

Matsutani, S., and Yamamoto, N. (2008). Centrifugal innervation of the mammalian olfactory bulb. *Anat. Sci. Int.* 83, 218–227. doi: 10.1111/j.1447-073X.2007.00223.x

McLean, J. H., Shipley, M. T., Nickell, W. T., Aston-Jones, G., and Reyher, C. K. (1989). Chemoanatomical organization of the noradrenergic input from locus coeruleus to the olfactory bulb of the adult rat. *J. Comp. Neurol.* 285, 339–349. doi: 10.1002/cne.902850305

Nai, Q., Dong, H. W., Hayar, A., Linster, C., and Ennis, M. (2009). Noradrenergic regulation of GABAergic inhibition of main olfactory bulb mitral cells varies as a function of concentration and receptor subtype. *J. Neurophysiol.* 101, 2472–2484. doi: 10.1152/jn.91187.2008

Nai, Q., Dong, H. W., Linster, C., and Ennis, M. (2010). Activation of α1 and α2 noradrenergic receptors exert opposing effects on excitability of main olfactory bulb granule cells. *Neuroscience* 169, 882–892. doi: 10.1016/j.neuroscience.2010.05.010

O'Donnell, J., Ding, F., and Nedergaard, M. (2015). Distinct functional states of astrocytes during sleep and wakefulness: is norepinephrine the master regulator? *Curr Sleep Med Rep.* 1, 1–8. doi: 10.1007/s40675-014-0004-6

Okubo, Y., Iino, M., and Hirose, K. (2020). Store-operated $Ca^{(2+)}$ entry-dependent $Ca^{(2+)}$ refilling in the endoplasmic reticulum in astrocytes. *Biochem. Biophys. Res. Commun.* 522, 1003–1008. doi: 10.1016/j.bbrc.2019.12.006

Otsu, Y., Couchman, K., Lyons, D. G., Collot, M., Agarwal, A., Mallet, J. M., et al. (2015). Calcium dynamics in astrocyte processes during neurovascular coupling. *Nat. Neurosci.* 18, 210–218. doi: 10.1038/nn.3906

Pankratov, Y., and Lalo, U. (2015). Role for astroglial α1-adrenoreceptors in gliotransmission and control of synaptic plasticity in the neocortex. *Front. Cell. Neurosci.* 9, 230. doi: 10.3389/fncel.2015.00230

Parekh, A. B., and Putney, J. W. Jr. (2005). Store-operated calcium channels. *Physiol. Rev.* 85, 757–810. doi: 10.1152/physrev.00057.2003

Paukert, M., Agarwal, A., Cha, J., Doze, V. A., Kang, J. U., and Bergles, D. E. (2014). Norepinephrine controls astroglial responsiveness to local circuit activity. *Neuron* 82, 1263–1270. doi: 10.1016/j.neuron.2014.04.038

Petzold, G. C., Albeanu, D. F., Sato, T. F., and Murthy, V. N. (2008). Coupling of neural activity to blood flow in olfactory glomeruli is mediated by astrocytic pathways. *Neuron* 58, 897–910. doi: 10.1016/j.neuron.2008.04.029

Rotermund, N., Schulz, K., Hirnet, D., and Lohr, C. (2019). Purinergic signaling in the vertebrate olfactory system. *Front. Cell. Neurosci.* 13:112. doi: 10.3389/fncel.2019.00112

Rotermund, N., Winandy, S., Fischer, T., Schulz, K., Fregin, T., Alstedt, N., et al. (2018). Adenosine A1 receptor activates background potassium channels and modulates information processing in olfactory bulb mitral cells. *J. Physiol. (Lond.).* 596, 717–733. doi: 10.1113/JP275503

Roux, L., Madar, A., Lacroix, M. M., Yi, C., Benchenane, K., and Giaume, C. (2015). Astroglial connexin 43 hemichannels modulate olfactory bulb slow oscillations. *J. Neurosci.* 35, 15339–15352. doi: 10.1523/JNEUROSCI.0861-15.2015

Schnell, C., Negm, M., Driehaus, J., Scheller, A., and Hulsmann, S. (2016). Norepinephrine-induced calcium signaling in astrocytes in the respiratory network of the ventrolateral medulla. *Respir. Physiol. Neurobiol.* 226, 18–23. doi: 10.1016/j.resp.2015.10.008

Schulz, K., Rotermund, N., Grzelka, K., Benz, J., Lohr, C., and Hirnet, D. (2017). Adenosine A1 receptor-mediated attenuation of reciprocal dendro-dendritic inhibition in the mouse olfactory bulb. *Front. Cell. Neurosci.* 11:435. doi: 10.3389/fncel.2017.00435

Schwinn, D. A. (1993). Adrenoceptors as models for G protein-coupled receptors: structure, function and regulation. *Br. J. Anaesth.* 71, 77–85. doi: 10.1093/bja/71.1.77

Shipley, M. T., Halloran, F. J., and de la Torre, J. (1985). Surprisingly rich projection from locus coeruleus to the olfactory bulb in the rat. *Brain Res.* 329, 294–299. doi: 10.1016/0006-8993(85)90537-2

Singaravelu, K., Lohr, C., and Deitmer, J. W. (2006). Regulation of store-operated calcium entry by calcium-independent phospholipase A2 in rat cerebellar astrocytes. *J. Neurosci.* 26, 9579–9592. doi: 10.1523/JNEUROSCI.2604-06.2006

Singaravelu, K., Lohr, C., and Deitmer, J. W. (2008). Calcium-independent phospholipase A2 mediates store-operated calcium entry in rat cerebellar granule cells. *Cerebellum* 7, 467–481. doi: 10.1007/s12311-008-0050-z

Somasundaram, A., Shum, A. K., McBride, H. J., Kessler, J. A., Feske, S., Miller, R. J., et al. (2014). Store-operated CRAC channels regulate gene expression and proliferation in neural progenitor cells. *J. Neurosci.* 34, 9107–9123. doi: 10.1523/JNEUROSCI.0263-14.2014

Thyssen, A., Hirnet, D., Wolburg, H., Schmalzing, G., Deitmer, J. W., and Lohr, C. (2010). Ectopic vesicular neurotransmitter release along sensory axons mediates neurovascular coupling via glial calcium signaling. *Proc. Natl. Acad. Sci. U.S.A.* 107, 15258–15263. doi: 10.1073/pnas.1003501107

Thyssen, A., Stavermann, M., Buddrus, K., Doengi, M., Ekberg, J. A., St John, J. A., et al. (2013). Spatial and developmental heterogeneity of calcium signaling in olfactory ensheathing cells. *Glia* 61, 327–337. doi: 10.1002/glia.22434

Trombley, P. Q. (1992). Norepinephrine inhibits calcium currents and EPSPs via a G-protein-coupled mechanism in olfactory bulb neurons. *J. Neurosci.* 12, 3992–3998. doi: 10.1523/JNEUROSCI.12-10-03992.1992

Trombley, P. Q., and Shepherd, G. M. (1992). Noradrenergic inhibition of synaptic transmission between mitral and granule cells in mammalian olfactory bulb cultures. *J. Neurosci.* 12, 3985–3991. doi: 10.1523/JNEUROSCI.12-10-03985.1992

Vardjan, N., and Zorec, R. (2017). *Noradrenergic Signaling and Astroglia.* London: Elsevier Academic Press.

Verkhratsky, A., Rodriguez, J. J., and Parpura, V. (2012). Calcium signalling in astroglia. *Mol. Cell. Endocrinol.* 353, 45–56. doi: 10.1016/j.mce.2011.08.039

Verkhratsky, A., and Zorec, R. (2019). Astroglial signalling in health and disease. *Neurosci. Lett.* 689, 1–4. doi: 10.1016/j.neulet.2018.07.026

Volterra, A., and Meldolesi, J. (2005). Astrocytes, from brain glue to communication elements: the revolution continues. *Nat. Rev. Neurosci.* 6, 626–640. doi: 10.1038/nrn1722

Zitt, C., Strauss, B., Schwarz, E. C., Spaeth, N., Rast, G., Hatzelmann, A., et al. (2004). Potent inhibition of Ca^{2+} release-activated Ca^{2+} channels and T-lymphocyte activation by the pyrazole derivative BTP2. *J. Biol. Chem.* 279, 12427–12437. doi: 10.1074/jbc.M309297200

Conflict of Interest: The authors declare that the research was conducted in the absence of any commercial or financial relationships that could be construed as a potential conflict of interest.

frontiers in Cellular Neuroscience

ORIGINAL RESEARCH
published: 30 April 2021
doi: 10.3389/fncel.2021.633757

Plume Dynamics Structure the Spatiotemporal Activity of Mitral/Tufted Cell Networks in the Mouse Olfactory Bulb

Suzanne M. Lewis[1], Lai Xu[1], Nicola Rigolli[2,3], Mohammad F. Tariq[4], Lucas M. Suarez[1], Merav Stern[5], Agnese Seminara[3] and David H. Gire[1]**

[1] Department of Psychology, University of Washington, Seattle, WA, United States, [2] Dipartimento di Fisica, Istituto Nazionale Fisica Nucleare (INFN) Genova, Universitá di Genova, Genova, Italy, [3] CNRS, Institut de Physique de Nice, Université Côte d'Azur, Nice, France, [4] Graduate Program in Neuroscience, University of Washington, Seattle, WA, United States, [5] Department of Applied Mathematics, University of Washington, Seattle, WA, United States

Although mice locate resources using turbulent airborne odor plumes, the stochasticity and intermittency of fluctuating plumes create challenges for interpreting odor cues in natural environments. Population activity within the olfactory bulb (OB) is thought to process this complex spatial and temporal information, but how plume dynamics impact odor representation in this early stage of the mouse olfactory system is unknown. Limitations in odor detection technology have made it difficult to measure plume fluctuations while simultaneously recording from the mouse's brain. Thus, previous studies have measured OB activity following controlled odor pulses of varying profiles or frequencies, but this approach only captures a subset of features found within olfactory plumes. Adequately sampling this feature space is difficult given a lack of knowledge regarding which features the brain extracts during exposure to natural olfactory scenes. Here we measured OB responses to naturally fluctuating odor plumes using a miniature, adapted odor sensor combined with wide-field GCaMP6f signaling from the dendrites of mitral and tufted (MT) cells imaged in olfactory glomeruli of head-fixed mice. We precisely tracked plume dynamics and imaged glomerular responses to this fluctuating input, while varying flow conditions across a range of ethologically-relevant values. We found that a consistent portion of MT activity in glomeruli follows odor concentration dynamics, and the strongest responding glomeruli are the best at following fluctuations within odor plumes. Further, the reliability and average response magnitude of glomerular populations of MT cells are affected by the flow condition in which the animal samples the plume, with the fidelity of plume following by MT cells increasing in conditions of higher flow velocity where odor dynamics result in intermittent whiffs of stronger concentration. Thus, the flow environment in which an animal encounters an odor has a large-scale impact on the temporal representation of an odor plume in the OB. Additionally, across flow conditions odor dynamics are a major driver of activity in many glomerular networks. Taken together, these data demonstrate that plume dynamics structure olfactory representations in the first stage of odor processing in the mouse olfactory system.

Keywords: olfaction, olfactory navigation, plume dynamics, sensory processing, natural sensing, population dynamics

OPEN ACCESS

Edited by:
Shaina M. Short, The University of Utah, United States

Reviewed by:
Andreas Schaefer, Francis Crick Institute and University College London, London, United Kingdom
Shawn Denver Burton, Lehigh University, United States

****Correspondence:***
David H. Gire
dhgire@uw.edu
Suzanne M. Lewis
slewis4@uw.edu

Specialty section:
This article was submitted to Cellular Neurophysiology, a section of the journal Frontiers in Cellular Neuroscience

Received: *26 November 2020*
Accepted: *15 March 2021*
Published: *30 April 2021*

Citation:
Lewis SM, Xu L, Rigolli N, Tariq MF, Suarez LM, Stern M, Seminara A and Gire DH (2021) Plume Dynamics Structure the Spatiotemporal Activity of Mitral/Tufted Cell Networks in the Mouse Olfactory Bulb. Front. Cell. Neurosci. 15:633757. doi: 10.3389/fncel.2021.633757

1. INTRODUCTION

Mice are adept at localizing odor sources (Gire et al., 2016; Baker et al., 2018; Liu et al., 2019; Gumaste et al., 2020), but the spatiotemporal information in olfactory environments that aids this search behavior is largely unknown. Odors travel in plumes which pull odor away from its source in filaments that are broken and distorted as they travel in air, creating complex odor environments. From the perspective of an olfactory searcher, these intermittent filaments create stochastic odor encounters, or whiffs, such that odor concentration dynamics fluctuate rapidly from moment to moment. Features of these complex plume dynamics contain information regarding odor source location (Murlis et al., 2000; Celani et al., 2014). For example, as a searcher encounters odors, the frequency, strength, and timing of encounters provide complex cues about an odor source (Atema, 1996; Vergassola et al., 2007; Ache et al., 2016; Michaelis et al., 2020).

A simple strategy, such as averaging odor concentration across whiffs could eliminate the complexity of an odor plume, allowing an animal to simply follow an increasing odor concentration gradient to the odor source. However, an animal dependent on this search strategy would operate at a timescale far slower than that observed in mice engaged in olfactory-guided search (Gumaste et al., 2020). This suggests that rodents most likely extract information from the complex spatiotemporal dynamics of olfactory environments to support their efficient odor-guided search behavior.

The extraction of information from fluctuating odor plumes will necessarily be impacted by the physics of odor transport. Factors such as wind speed and the Reynolds number of the plume could impact early olfactory processing in mammals. Precise olfactometers have been used to model certain features found in natural odor environments, such as fluctuating and intermittent odor concentration dynamics. Although this work provides important insights, olfactometers do not capture the full complexity of the odor environment. One problem is a lack of knowledge regarding which features of the plume are relevant to olfactory search, constraining which features olfactometers have been used to mimic. In addition, olfactometers create artificial plumes that decouple odor concentration from features present in olfactory environments. This omits correlations between concentration fluctuations and the surrounding air flow as well as small scale details of odor transport like diffusion. Decoupling these factors creates challenges for interpretation because it implicitly disrupts processing moderated by these features, such as the impact of wind speed on the vibrissal system (Yu et al., 2016) or feedback regarding bilateral nasal sampling (Markopoulos et al., 2012; Esquivelzeta Rabell et al., 2017). Directly observing how MT activity is impacted by the plume dynamics of natural olfactory scenes will thus constrain hypotheses regarding which spatiotemporal features of natural odor stimuli are conveyed by the brain.

We studied the response of MT cells in the OB to odor concentration dynamics in awake mice as they processed natural olfactory scenes, i.e., odor plumes. We used wide-field calcium imaging to measure MT activity, allowing us to study MT activity contributing to OB output at the level of glomerular complexes on the dorsal surface of the OB. Simultaneous recordings of the OB and plume dynamics show glomerular population activity follows fluctuations of odor concentration during plume encounters. The reliability and following behavior of glomerular responses were moderated by wind speed and the resulting changes in plume structure. The fidelity of odor concentration tracking increased when concentration dynamics were skewed, creating intermittent odor encounters across the plume presentation. In addition, as the strength and reliability of odor-evoked activity in MT cells increased, this activity more accurately followed plume dynamics. Together, these data demonstrate for the first time that the rapid fluctuations present in natural olfactory scenes significantly structure the activity of glomerular MT cell populations in the mouse OB.

2. MATERIALS AND METHODS

2.1. Olfactory Stimuli

Olfactory stimuli were released by an automated odor port within a 40 × 40 × 80 cm acrylic wind tunnel where airspeed was controlled by a vacuum at the rear of the wind tunnel, posterior to the animal's location (**Figure 1A**). Concentration dynamics of olfactory stimuli varied stochastically from trial to trial creating plumes with unique concentration dynamics on each trial. Adjusting the velocity of wind flow allowed for variation in the Reynolds number, resulting in characteristic changes of plume dynamics for different flow levels (**Supplementary Figure 1**). Reynolds numbers were calculated using the mean flow of each condition and the half height of the tunnel (20 cm) as the head-fix setup is placed on a stage such that it is elevated ∼20 cm from the tunnel floor (**Figure 1B**). Low, medium, and high flow Reynolds numbers were 2,400 ± 1,000, 8,800 ± 400, and 9,800 ± 200, respectively (mean ± st. dev), hence the medium and high flow conditions are fully turbulent, while the low flow is in the chaotic mixing regime. Across all flow conditions, plume presentations are stochastic and plume dynamics do not correlate across time within trials (**Supplementary Figure 2A**) or across trials (**Supplementary Figure 2B**). Odor statistics confirm that high and medium conditions are fully turbulent (as seen from large skewness levels implying intermittency (**Figures 1E–G**) and spectra close to the expectation for turbulent flows, see **Supplementary Figure 1D**). The low flow condition is not yet fully turbulent [as seen from the low values of skewness and symmetric odor distribution (**Figures 1E,G**) and flatter spectrum (**Supplementary Figure 1D**)]. Absolute velocities of low, medium and high flow conditions were 0.40 ± 0.16, 1.31 ± 0.05, and 1.81 ± 0.17 fpm and velocity fluctuations were 14 ± 3, 6 ± 2, and 5.3 ± 1.5 fpm, respectively.

A single session consisted of forty trials of odor presentation. Odor ports were located upwind ∼ 13 cm anterior to the animal's nose (**Figure 1B**), and each plume presentation had a duration of 10 s. Odor release began ∼10 s into the trial. In order to avoid responses predicting the beginning of the plume, the exact time of odor release was randomized by adjusting the duration of the 5 s intertrial interval by a length of time (s) drawn randomly from a uniform distribution, $U(-2, 2)$. Random clicking noise

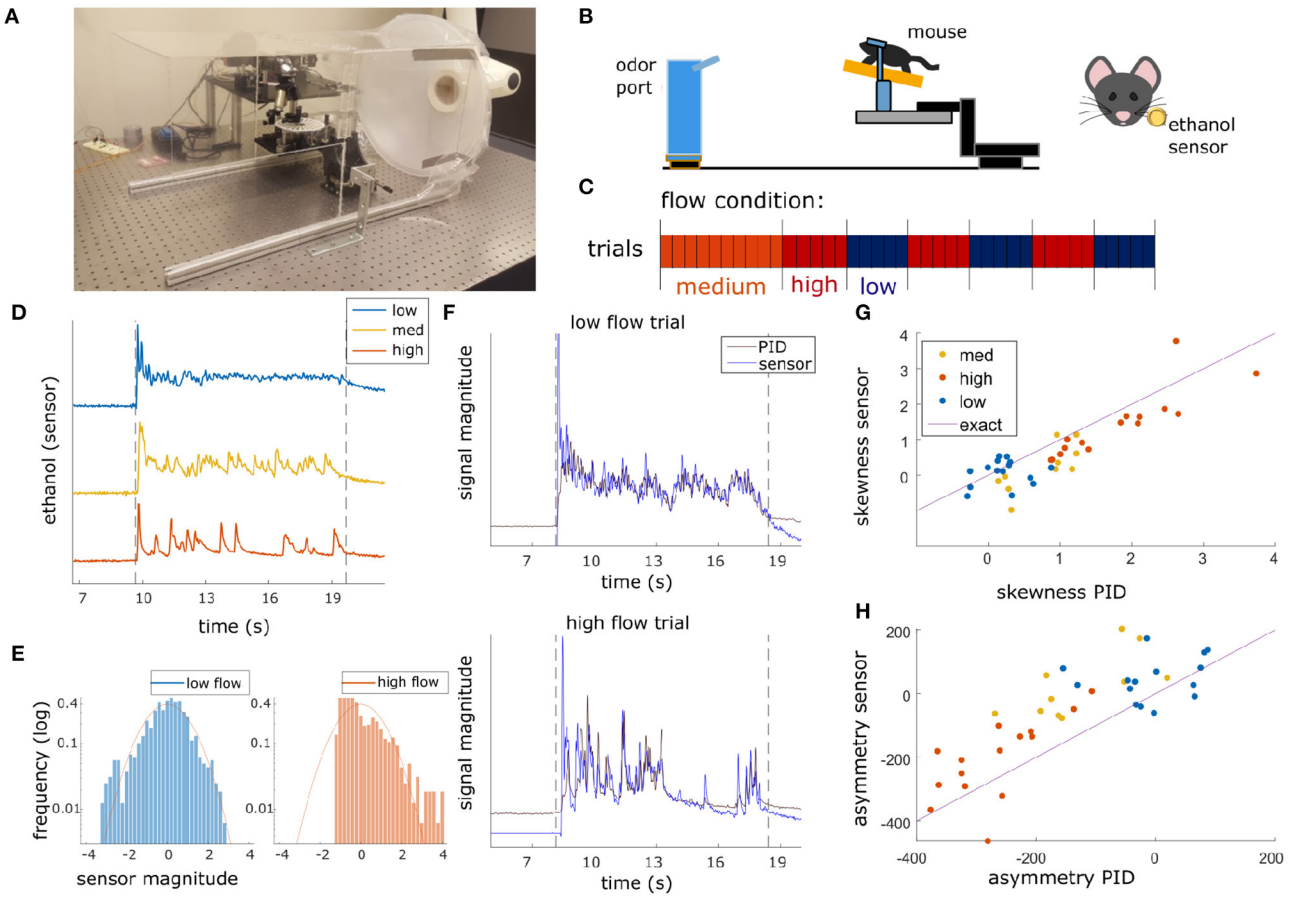

FIGURE 1 | Plume presentations and head-fix setup for *in-vivo* recording experiments. **(A)** All experiments conducted in a 40 × 40 × 80 cm wind tunnel for quick clearing of odor presentations. The odor port (not pictured) was located ∼ 13 cms upwind of the animal's nose. **(B)** (Left) Graphic detailing experimental setup. (Right) Ethanol odor concentration measured using a modified, commercially available ethanol sensor placed ∼ 4 mm from the outer edge of the mouse's nostril. **(C)** Diagram depicting flow conditions (high, medium, or low) of the 40 trials within a single session. **(D)** Example odor traces are depicted for each flow condition. **(E)** Histograms of the odor concentration magnitude sampled across two examples trials show a change in skewness between low flow (left, blue) and high flow (right, red), with skewness increasing with increased airflow during plume presentations. **(F)** Comparisons between the deconvolved sensor signal and a PID signal during a set of paired recordings show odor concentration dynamics of the deconvolution can recover dynamics observed in the PID recordings ($r = 0.61$, $p < 0.001$). An example from low flow (top) and high flow (bottom) are shown. **(G,H)** Skewness **(G)** and asymmetry **(H)** of the deconvolved ethanol signal vs. the PID traces for each trial. All points lie close to the bisector (Purple line, labeled "exact") showing that the deconvolution preserves measures of skewness and asymmetry consistent to the PID trace. High flow trials (orange) are separable from low flow trials (blue) and are substantially different from 0 (the expectation for any symmetric distribution, e.g., a Gaussian).

was used to control for the clicking sound of the port serving as a cue for plume onset. Starting 5 s prior to plume onset, a number was drawn from a uniform distribution, $U(0, 1)$, for each camera frame, and if the number exceeded 0.95 a clicking sound was produced.

Ethanol concentration throughout each trial was measured by a modified, commercially available ethanol sensor placed within 3.5–4 mm from the mouse's right nostril (**Figure 1B**). For the experimental flow sessions, a benzaldehyde and ethanol odor solution (0.6% benzaldehyde, 85.7% 200 proof ethanol, and 13.7% distilled water) was used as the plume source for all trials. Odor solutions were stored in odor reservoirs (centrifuge tubes) with air-tight, customized tops. Tops had two openings connected to tubing. One tube was connected to a Clippard electric valve (part no. EV-2-12) to create airflow and the other was attached to a 3D printed odor port. For each plume presentation, the valve was opened to allow airflow into the tube such that odor vapors exited the odor reservoir and traveled through cylindrical tubing (1/16″ inner diameter) to the release point at the odor port. The odor port mounted the end of the tubing so that it was suspended at roughly nose height and located ∼13 cm directly upwind of the animal's nose (**Figure 1B**).

One set of experiments consisted of an odor panel during which 3 odors were released across forty trials. For these sessions, wind speed was held constant and only odor changed. For all trials plumes were presented at high flow. For the first ten trials, ethanol was presented (solution for plume source 86.3% 200 proof ethanol and 13.7% distilled water), for trials 11–25 a

benzaldehyde-ethanol mixture was presented (solution same as flow experiments), and for trials 26–40 a isoamyl acetate- ethanol mixture was presented (solution for plume source consisted of 0.6% isoamyl acetate, 85.7% 200 proof ethanol, and 13.7% distilled water). Solutions were stored in three separate reservoirs, each with its own separate value and tubing. To change between odors during a session, the tubing running into the odor port was switched out manually during the appropriate intertrial intervals dividing odor conditions.

2.2. Implantation of Cranial Window

Implantation of the cranial window was adapted from methodology detailed in Batista-Brito et al. (2017). Mice (n = 3 flow panel, n = 2 odor panel) were anesthetized with isoflurane for surgery. 2 × 2.5 or 2 × 3 mm craniotomies were performed above the olfactory bulbs and custom cut double windows were implanted. A customized stainless steel head plate was glued directly on the skull posterior to the window, and two stainless steel screws (Neuroscience *Invivo* Research Components) were placed posterior to the head plate. Metabond was then added to cover all exposed skull and a thin layer built to cover the screws and the central surface of the headplate. The position of the craniotomy was biased toward either the left or right bulb.

2.3. *In vivo* Imaging

Widefield fluorescent microscopy was used for awake, head-fixed imaging in Thy1-GCaMP6f-GP 5.11 (IMSR Cat# JAX:024339, RRID:IMSR_JAX:024339) mice to view neural activity in the dorsal OB. Mice were between 11 weeks and 13 months old when imaged. 488 nm LED stimulation was used for the duration of the trial (∼30 s), but was absent during intertrial intervals (∼ 5 s) to avoid excessive bleaching. All mice were imaged at 30 Hz with 4× 0.13 NA objective (Nikon). Neural activity was recorded using a Teledyne Photometrics Prime 95B sCMOS camera. For each session, mice were head-fixed above a freely rotating, circular track, allowing mice to run at will during imaging sessions.

2.4. *In vitro* OB Slice Imaging

To establish patterns of expression and signals obtained from the OB of Thy1- GCaMP6f- GP 5.11 animals, imaging experiments were conducted in OB slices. These animals show GCaMP6f expression in the main olfactory bulb as well as other areas of olfactory cortex, including but not limited to piriform and anterior olfactory cortex (Dana et al., 2014). Slice work verified strong expression in MT somas and dendrites (**Figure 2A**). Although we believe MT cells to drive the signal imaged in the OB, it is possible centrifugal feedback could contribute to some of the observed responses.

Horizontal OB slices (300–400 μm) were made following isoflurane anesthesia and decapitation. Olfactory bulbs were rapidly removed and placed in oxygenated (95% O_2, 5% CO_2) ice-cold solution containing the following (in mM): 83 NaCl, 2.5 KCl, 3.3 $MgSO_4$, 1 NaH_2PO_4, 26.2 $NaHCO_3$, 22 glucose, 72 sucrose, and 0.5 $CaCl_2$. Olfactory bulbs were separated into hemispheres with a razor blade and attached to a stage using adhesive glue applied to the ventral surface of the tissue. Slices were cut using a vibrating microslicer (Leica VT1000S) and were incubated in a holding chamber for 30 min at 32°C. Subsequently, the slices were stored at room temperature.

Slices were placed on a Scientifica SliceScope Pro 6000, using near infrared imaging for slice placement and 488 nm LED illumination for imaging activity and a QI825 Scientific CCD Camera (Q Imaging) for image acquisition. Imaging was performed at 32–35°C. The base extracellular solution contained the following: 125 mM NaCl, 25 mM $NaHCO_3$, 1.25 mM $NaHPO_4$, 25 mM glucose, 3 mM KCl, 1 mM $MgCl_2$, and 2 mM $CaCl_2$ (pH 7.3 and adjusted to 295 mOsm), and was oxygenated (95% O_2, 5% CO_2). An elevated KCl solution (equimolar replacement of 50 mM NaCl with KCl in the extracellular solution) locally applied through a borosilicate pipette using a picospritzer 2 (Parker Instrumentation) was used to stimulate cells.

2.5. Data Pre-processing

ImageJ was used to crop fields of view (FOVs) for data analysis. It was also used to extract pixel averaged signal for hand-drawn region of interest (ROI) analysis.

Matlab 2019b was used to analyze data and plot figures. Data was aligned using NoRMCorre software to perform piecewise rigid and non-rigid motion correction (Pnevmatikakis and Giovannucci, 2017). This alignment corrected for both global frame movement due to head jitter (rigid) and localized distortion due to brain movement (non-rigid).

2.6. Precise Tracking of Plume Dynamics

In the past it has been difficult to simultaneously record neural responses and plume dynamics without disrupting plume structure. Photoionization detectors (PIDs) are used to detect odorants, but PIDs sample via an active process, redirecting airflow into the sensor to detect odorants. In these experiments we used a miniaturized ethanol sensor modified from a commercially available metal oxide (MOX) sensor (Tariq et al., 2021). The sensor was placed within 4 mm of the lateral edge of the mouse's right nostril to capture the odor concentration signal across plume presentations for each trial. The sensor, a Figaro TGS 2620 Organic Solvent Vapor Sensor, was adapted similar to described in Tariq et al. (2021) by removing most of the metal head cap, including both a mesh covering and a solid metal covering. The resulting sensor was open to make direct contact with the airflow. In this adapted design, the sensor is mounted only to a circular base plate with a shortened metal cylindrical wall surrounding it. A single odor, a benzaldehyde-ethanol mixture, was used for each trial in the flow experiments. Odors released together travel together within plumes at sufficiently small scales because dispersion dominates over diffusion (Yeung and Pope, 1993; Celani et al., 2014). In this way, the ethanol sensor measured the odor concentration of the benzaldehyde-ethanol mixture. The plume for each trial was released by an automated odor port at the upwind end of the wind tunnel, and the ethanol sensor measured the odor concentration of the ethanol across each trial. During plume presentations, the odor released from the odor port traveled in stochastic plumes through the wind tunnel. Therefore, plume onset time varied on each

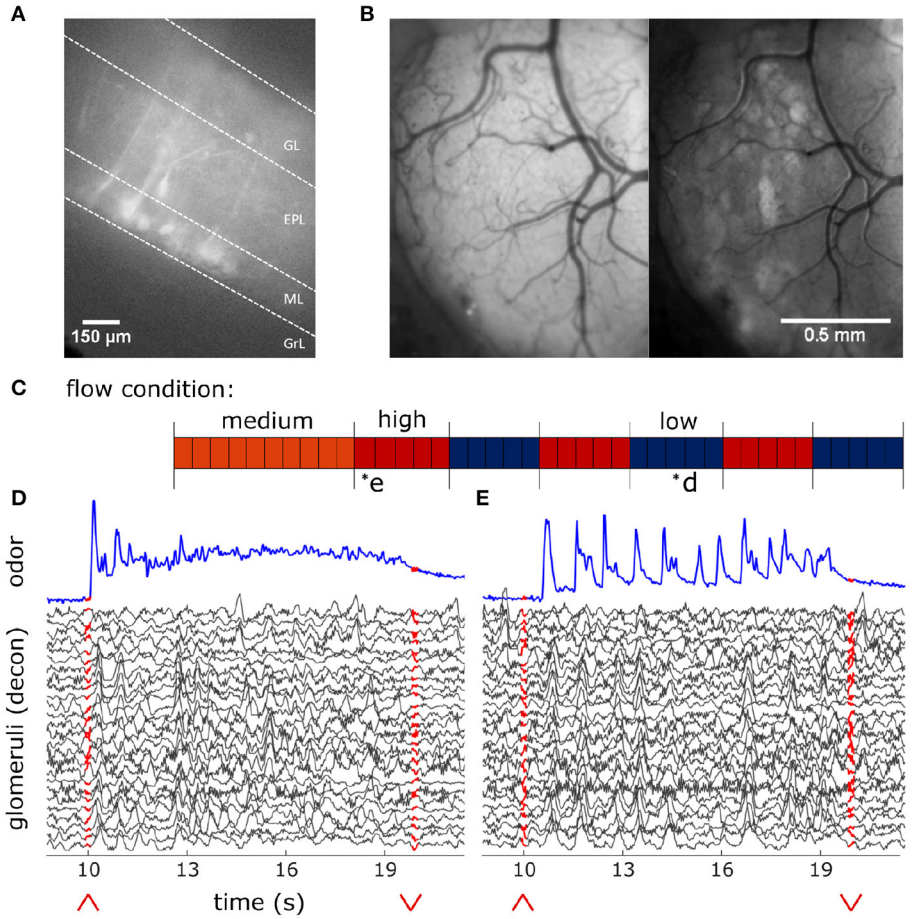

FIGURE 2 | *In-vivo* recording of glomerular population response. **(A)** Change in fluorescence of MT cells in an acute *in vitro* OB slice preparation averaged over 3 s following a puff of high K+ solution. **(B)** *In vivo* view of the dorsal olfactory bulb through an implanted cranial window. (Left) Window activity averaged across a single trial. (Right) Projected standard deviation for the same trial shows MT activity in the dorsal OB responsive to the odor presentation. **(C)** Diagram depicting flow conditions (high, medium, or low) of the 40 trials within a single session. **(D)** The deconvolved ethanol trace (blue) compared to the deconvolved response of each glomeruli (black) within the recorded FOV during a single low flow trial depicted by asterisk in **(C)**. Red arrows indicate onset and offset of plume presentation. **(E)** Same as **(D)** but for a single high flow trial from the same session also depicted by asterisk in **(C)**.

trial dependent on when the first filament made contact with the plume sensor. Reynold's numbers calculated within each flow condition (see Olfactory Stimuli above) show that plume dynamics are highly unsteady and dynamic, and fully turbulent at both medium and high flow. The odor was released 10 s after the trial began for a duration of 10 s. Each indicated flow condition was maintained throughout the entire trial. Flow condition was set for each trial block (**Figure 1C**) by adjusting the strength of a vacuum exhaust at the downwind side of the wind tunnel to one of three levels, low, medium, and high. Plumes were presented at medium level flow for the first 10 trials, after which flow alternated between high and low flow in blocks of five trials. Some sessions transitioned from medium to low flow initially and others transitioned from medium to high flow.

2.7. Ethanol Deconvolution

Recent characterization of MOX sensors comparing their deconvolved signals to simultaneously recorded PID (200B: mini photo-ionization dectector) signals have validated the use of MOX sensors in capturing turbulent plume dynamics despite their slower recording dynamics (Martinez et al., 2019; Tariq et al., 2021). Tariq et al. show resolution of frequencies up to 15 Hz and high correlations between deconvolved MOX sensor and PID recordings at distances extending to >1 m in a turbulent airflow setting. For our experiments, ethanol concentration throughout each trial was measured by a modified, commercially available ethanol sensor placed within 3.5–4 mm from the mouse's right nostril (**Figure 1B**). A single session consisted of 40 trials of odor presentation (plumes).

Sensor signal was acquired at 100 Hz and then low pass filtered at 30 Hz using a Kaiser window. The signal, *e*, was then normalized within each trial using the mean and standard deviation of the signal during the plume presentation. The signal was deconvolved by adapting the deconvolution specified in Tariq et al. (2021). The kernel was defined in the same manner, but instead of normalizing the range of the kernel, the integral

of the kernel is normalized. Thus, the kernel, k, is calculated as follows:

$$k_0(t) = e^{-t/\tau_{decay}} - e^{-t/\tau_{rise}} \quad (1)$$

$$k(t) = k_0(t) / \int_0^T k_0(s)ds \quad (2)$$

where t is an array with evenly spaced timestamps at the proper sampling rate for the length of a single trial (T), $\tau_{decay} = 0.4629$, and $\tau_{rise} = 0.0001$. Both signals, e and k, are then transformed into Fourier space using the Matlab Fourier transform function, and the ethanol signal is deconvolved in Fourier space by dividing $\hat{e}$ by $\hat{k}$. The inverse Fourier transform of the resulting deconvolution is taken to obtain d such that $d = F^{-1}(\hat{e}/\hat{k})$. The deconvolved signal, d, is then normalized within each trial using the mean and standard deviation during the plume presentation, $d = (d - < d >)/std(d)$. The deconvolution optimizes the preservation of odor concentration dynamics across trials, but does not preserve the absolute value of odor concentration.

To optimize the parameters for the deconvolution, a complete session of 40 plume presentations was recorded with the usual ordering of flow condition blocks (**Figure 1C**). No mice were recorded during this session. Instead, a PID was placed 4 mm from the ethanol sensor in the same position where the animal is usually head-fixed.

To optimize parameters, the PID signal, p, was first downsampled to 100 Hz to match the sensor sampling rate. Next, the signal was normalized within each trial using the mean and standard deviation of the signal during plume presentation, $p = (p - < p >)/std(p)$. This normalized signal was then Fourier transformed, convolved with the kernel and back-transformed to obtain the convolved signal $c = \mathcal{F}^{-1}(\hat{p} \cdot \hat{k})$. It was then normalized and compared to the raw ethanol across a range of τ_{decay} and τ_{rise} parameter values. The Kernel parameters were chosen by minimizing mean squared error between the e and normalized c signals averaged across all trials within the paired recording session: $\min_{\tau_{rise}, \tau_{decay}} < ||e - (c - < c >)/std(c)||^2 >$. This optimized kernel is used to deconvolve the raw ethanol signal in the recording sessions. The deconvolved ethanol sensor signal allows for the recovery of plume dynamics unique to each trial (**Supplementary Figure 2**). It is significantly correlated with the PID signal as measured during plume presentations ($r = 0.61$, $p < 0.001$, both sampled at 100 Hz), which is a 0.22 improvement from the correlation between the raw ethanol sensor and PID signal ($r = 0.39$, $p < 0.001$, both sampled at 100 Hz).

Finally, with the exception of **Supplementary Figure 1**, the deconvolved trace was downsampled for figures and analyses to match the calcium trace (30 Hz) by averaging all samples taken across each camera frame. Deconvolution of the sensor signal during paired recordings is plotted and compared to both the raw sensor signal and to the PID reading from the paired recordings (**Supplementary Figure 1**). An initial inflection of signal at plume onset can be observed in the deconvolved ethanol signal for some trials (**Figure 1D**, **Supplementary Figure 1B**). This peak at plume onset is not reported by the raw sensor signal (**Supplementary Figure 1A**) or by the PID signal (**Supplementary Figure 1C**) and is likely an artifact of the deconvolution. Since these experiments focus on how well MT activity follows odor concentration dynamics during plume encounters, the first and last seconds of the 10 s plume are omitted when analyzing neural responses to plume dynamics. The only exception is for the analysis of responsivity, which is based on the percentage of timepoints for which a significant response is observed and so this thresholded measure does not directly consider signal magnitude. Therefore, any artifact of plume onset dynamics in the sensor signal due to the deconvolution of its slower dynamics do not affect correlations reported between stimulus and response.

2.8. Defining Dynamic Flow

Dynamic flow was calculated within each session. In the experimental setup, flow condition is defined by wind speed. Intermittency was measured within a trial during the middle 8 s of the 10 s plume presentation by calculating asymmetry or by using the 3rd moment of the sampled distribution (the distribution odor concentration magnitude as measured for each time point across the window) (**Figure 1E**). Low and high flow trials were separable using either of these measures. As determined by these measures, intermittency increased with airflow moving from low to high flow conditions. The PID signal from the paired odor recording session shows this difference in dynamics as the concentration plotted across high flow trials exhibits increased intermittency as compared to that for low flow trials (**Supplementary Figure 1C**).

To see if there was a main effect of flow condition on these stimulus properties, skewness and asymmetry, a one-way analysis of variance (ANOVA) test was conducted for each parameter. For each ANOVA, multiple comparisons using a Tukey's test were performed to look for significant differences of the parameter between flow where comparisons were considered significant for $p < 0.01$. These tests indicated that both skewness and asymmetry vary significantly across flow condition [$F_{(2, 155)} = 52.7$, $p < 0.001$ and $F_{(2, 155)} = 54.9$, $p < 0.001$, respectively]. Multiple comparison tests examining the differential effect of flow on these parameters showed that, for both, there was a significant difference between low and medium flow and a significant difference between low and high flow. No significant difference was found between medium and high flow. Therefore, only low and high flow conditions were selected when examining the effect of air flow on neural parameters.

2.9. Measuring Glomerular Responses to Plume Dynamics

Widefield imaging of the dorsal surface of the OB in Thy1-GCaMP6f-GP5.11 mice was used to capture MT cell activity at the glomerular level (**Figure 2B**). Thy1 mice exhibit fast kinetics and strong expression in MT cells within the OB (Dana et al., 2014). Global MT activity is clustered into dendritic complexes known as glomeruli. Widespread activity of secondary dendrites in the external plexiform layer (EPL) of the dorsal OB causes diffuse fluorescence across the imaging field. Therefore, CaImAn, a constrained non-negative matrix factorization (CNMF) algorithm, was used on each FOV to find regions of interest (ROIs) (FOV 1, FOV 2, and FOV 3 from mouse 1,

n = 27, 17, and 6 glomeruli, respectively; FOV 4 from mouse 2, n = 35; FOV 5 from mouse 3, n = 26) and their activity traces (Pnevmatikakis et al., 2016). Thus, the spatial decomposition of CNMF provided the ROI for each glomerulus, and the temporal decomposition provided its corresponding denoised activity trace. The denoising of the CNMF temporal decomposition helps to remove correlated signals between neighboring glomeruli, accounts for calcium drift within recording sessions, and separates glomeruli overlapping in the dorsal-ventral dimension. The change in the distribution of correlation coefficients between ROIs before and after denoising (**Supplementary Figure 3**) shows a decorrelation of glomerular signals. A two-sample Kolmogorov-Smirnoff test shows the distributions of correlation coefficients between the pixel averaged ROI traces, 0.87 ± 0.07 (mean ± st. dev), and the CNMF ROI traces, 0.36 ± 0.28 (mean ± st. dev), are significantly different ($D = 0.86, p < 0.001$).

To protect against over-segmenting a single glomerulus into multiple ROIs, neighboring ROIs whose baseline CNMF activity was correlated above 0.75 were selected as candidates for ROI merging (**Supplementary Figure 4**). The baseline period was examined as criteria for possible merging since glomeruli might have similar response profiles to the stimulus dynamics during plume presentations. The baseline activity of the neighboring ROIs was then binarized using a threshold of ±1 st. dev. If the correlation of the binarized activity between neighboring ROIs exceeded 0.75, the ROI with the lower mean activity (presumably encompassing less of the glomerulus) was dropped from the analysis.

To validate the use of CNMF for ROI selection, results were compared to a hand-drawn ROI analysis conducted on one of the fields of view (FOV 5) in ImageJ (**Supplementary Figure 5**). Using this standard, manual ROI selection, we show CNMF decomposition and denoising does not qualitatively change the interpretation of the data. Rather, CNMF recovers spatial and temporal resolution of MT activity by increasing the number of ROIs detected per field and decreasing pairwise correlation between ROIs. This decrease in pairwise correlation between ROIs suggests CNMF reduces common global signal, such as that from neuropil activity where secondary dendrites and global centrifugal feedback in the OB produce diffuse excitation across the dorsal surface of the OB. Hand-drawn ROIs were selected after viewing footage and reviewing standard deviation and maximum value projections of activity from the FOV within each trial. The activity averaged from within hand-drawn ROIs has higher pairwise correlations than denoised CNMF activity traces. This mirrors what is seen when pixel-averaged activity from within CNMF ROIs (without denoising) is compared to the denoised traces. Thus, the denoising of CNMF recovers the spatiotemporal resolution of glomerular activity observed in the dorsal OB recordings in both types of analyses. A two-sample Kolmogorov-Smirnoff test shows the distributions of correlation coefficients between the deconvoled hand-drawn ROIs, 0.81 ± 0.08 (mean ± st. dev), and the deconvolved CNMF traces, 0.1935 ± 0.3471 (mean ± st. dev), are significantly different ($D = 0.86$, $p < 0.001$). Results of the hand-drawn ROI analysis (power and correlation analyses, **Supplementary Figures 5D,E**, respectively) were qualitatively similar to those found using CNMF corroborating the ability of glomerular networks to resolve odor concentration dynamics. Cross-correlations show a relation between glomerular and ethanol signals during odor presentation with all glomeruli having significant correlation with the plume during odor presentation as compared to their respective null distributions from trial shuffled correlation analyses. In addition, a strong correlation between glomerular response power (0–5 Hz) and ability to track odor concentration dynamics is also present in the hand-drawn ROIs ($r = 0.80$, $p =< 0.001$). Thus, we find that CNMF captures the relationship between glomeruli and plume dynamics while improving the resolution of glomerular network activity and inter-glomerular temporal dynamics.

The CNMF activity traces from the identified glomeruli were baseline normalized using the mean and standard deviation of a 5 s baseline activity period prior to stimulus onset. Traces for each glomerulus were then deconvolved in the style of Stern et al. (2020) to recover the average activity rate of each glomerulus. To find the optimal penalty parameter, λ, for deconvolution, λ was optimized within each glomerulus. Then the median of this optimized distribution was used as the λ in the deconvolution for all glomeruli. After deconvolution, traces were standardized using the standard deviation of the glomerulus's entire trace. Deconvolved signals were standardized in this way since the florescence range of a glomerulus's response depends on the number of expressing MT cells, the depth of the glomerulus from the dorsal surface, and other methodological factors unrelated to the magnitude of the response.

2.10. Testing for Responsive Glomeruli

A glomerulus was considered to be responsive to odor if its deconvolved trace exceeded threshold more time points than expected by chance during plume presentations as compared to its activity level during odorless baseline periods (**Figure 6**). Since this preliminary measure does not rely on stimulus dynamics, it captures glomeruli that respond to the plume even if their response is unrelated to odor concentration dynamics or only present for part of the plume.

First, the deconvolved trace of a single glomerulus was split into two periods: baseline activity and odor response. The baseline period is a 5 s period at the beginning of each trial prior to plume onset. The odor response period is the time during which the plume is present as well as 1 s immediately following the plume since inhibition has been shown to induce excitatory rebound responses in tufted cells (Cavarretta et al., 2018). The signal is first baseline normalized by subtracting the mean and dividing by the st. dev of the baseline activity within each trial. Next, it is binarized, thresholding for time points where activity exceeded the 95% confidence interval of the glomerulus's original baseline activity (thresholded at ±1.96 baseline mean). In this way, each time point that crossed the threshold was considered an event. Within each trial's plume presentation, if the number of events exceeded the null expectation (5% of the total number of time points during plume presentation rounded up to the nearest integer), the glomerulus was considered to be responsive to the plume during that trial. The proportion of trials to which the glomerulus responded was

calculated within three sets of flow conditions (all flows, low flow, and high flow). To illustrate responsivity scores within and between glomeruli simultaneously, scores are plotted as a stacked bar graph (**Figure 6A**, cumulative scores are not used for analytic purposes).

2.11. Cross-Correlation Between Plume Dynamics and Corresponding Neural Responses

To understand the relation between stimulus and response time series, a preliminary analysis was conducted by calculating the correlation coefficients between the two signals for each glomerulus. In the future, more sophisticated techniques will be used to establish how much of the neural representations can be explained by high-fidelity odor concentration encoding.

Due to the stochastic nature of plume onset and offset times, the correlation is only calculated for the middle 8 s of the 10 s plume so that onset and offset dynamics are not included and the correlation measure represents the magnitude of plume tracking during plume encounters. The cross-correlation coefficient of a glomerulus r_g is calculated between the ethanol e and calcium c deconvolutions during plume presentations. For a single glomerulus, the correlation coefficient between the two deconvolutions within a single trial n is calculated at all possible lags l. Using the xcorr() function in Matlab to compute the coefficients, both signals are mean subtracted prior to calculating the cross-correlations such that the correlation coefficients are synonymous with calculating the Pearson correlation coefficient between the two signals at each respective lag value.

$$r_{g,n,l} = corr(e_{n,l}, c_{n,l}) \tag{3}$$

The mean coefficient for each glomerulus, $\bar{r}_{g,l}$, is calculated by averaging across all trials within the session (n = 40 for 3 FOVs, and n = 39 for 2 FOVs) at each possible lag. The maximum coefficient mean is selected from all lags within a 500 ms window w of the neural activity following the ethanol signal.

$$r_g = \max_{0<l\leq w} \bar{r}_{g,l} \tag{4}$$

This is considered to be a window of sufficient size to account for variable delays in glomerular processing. The average time lag of r_g was 130 ms ± 100 (mean ± st. dev).

Within flow cross-correlations are calculated in the same manner but averaged only across trials within the specified flow condition.

For plotting of tracking ability (**Figures 5A,B**), r_g is compared to a single trial shuffled analysis using the same method as detailed above. The difference between the matched and shuffled coefficients suggest correlations are not solely a result of plume structure, but are driven by the temporal dynamics unique to each trial. Trials were shuffled within each glomerulus by calculating the correlations between e_n and $c_{\neq n}$. In this way, any relation dependent on the dynamics of the stochastic fluctuations within each plume presentation is lost, but other statistical features of the plume presentation are preserved, yielding a baseline value for the cross-correlation. Glomeruli are plotted in **Figures 5A,B** if their correlation coefficient from the matched analysis exceeds ±2 standard deviations (st. dev of the coefficient distribution from the shuffled analysis) of the shuffled mean coefficient. Since correlation varies significantly within a glomerulus across flow conditions, a glomerulus is considered to exceed the shuffled mean if it does so in at least one of the three defined conditions, all flows, low flow, or high flow.

Using the same shuffled correlation, a bootstrap analysis was conducted (10,000 iterations) creating a null distribution of the shuffled mean correlation coefficients to test for significance (**Supplementary Figure 7C**). The mean correlations are compared to their respective 95% confidence interval for the null distribution. Glomeruli are considered to respond significantly to plume dynamics when their mean coefficients exceed their null expectation. Non-significantly responding glomeruli are depicted in stacked bar graphs using gray hues (**Figures 5C**, **6A**).

Comparison of correlation coefficients in the matched vs. shuffled cross-correlations does not naturally divide the glomeruli into two subpopulations, but rather the strength of this relationship varies continuously across glomeruli. Therefore, instead of dividing glomeruli into subpopulations of tracking vs. non-tracking, our analyses consider how the strength of odor concentration tracking compares to other properties of the glomerulus and its response.

3. RESULTS

3.1. Measuring Glomerular Responses to Plume Dynamics

Using a modified, commercially available odor sensor combined with widefield calcium imaging techniques in head-fixed mice, we reliably tracked plume dynamics and investigated glomerular responses to this fluctuating input. Imaging was conducted in Thy1-GCaMP6f-GP5.11 mice which have fast kinetics and expression in mitral and tufted (MT) cells within the olfactory bulb (OB) (Dana et al., 2014) (**Figure 2A**). Widefield imaging of the dorsal surface of the OB allows for glomerular level resolution of the neural response (**Figure 2B**) (Fletcher et al., 2009). To explore a range of plume dynamics an animal may encounter in its natural environment, we changed the airspeed in the wind tunnel to create stochastic plumes with different odor concentration dynamics (**Figures 1D–H**). Odor identity, concentration and volume released from the odor port remained constant across all flow conditions, making the plume dynamics the only source of variation (**Figures 2C–E**).

3.2. Mitral and Tufted Population Activity Correlates With Plume Dynamics

At the bulbar level, imaging of MT cell activity shows activation of glomerular networks during odor exposure (**Figure 3A**). The global MT activity for a given field of view (FOV) was subjected to principal component analysis (PCA) and compared to the simultaneously recorded plume dynamics (**Figure 3B**). The FOV's were aligned prior to PCA, but no segmentation

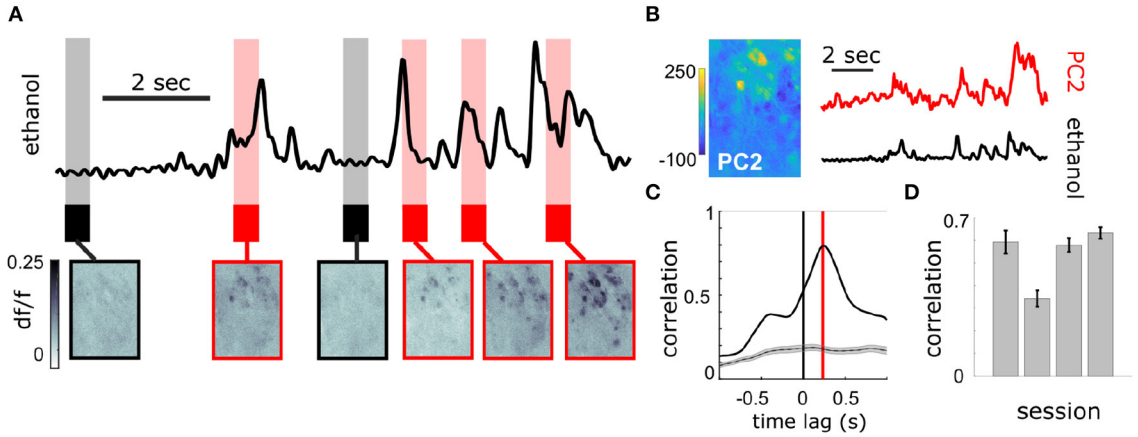

FIGURE 3 | Population response of MT cells in dorsal OB respond to changes in odor concentration during plume presentations. **(A)** Simultaneously recorded deconvolved ethanol plume (top) and imaging of calcium signals from MT cell activity in an example FOV of a Thy1-GCaMP6f (GP5.11) mouse (bottom). Baseline and odorless periods (black) and odor plume input (red) are shown from the indicated time points. Fluctuations in the odor plume elicit repeatable activation of specific glomerular networks in response to whiffs of odor during plume presentations. **(B)** (Left) An image of the principal component loadings corresponding to the odor-evoked activity [principal component 2 (PC2)]. (Right) Time series of PC2 (top, red) aligned to the simultaneous ethanol signal (bottom, black). Scale bar indicates 2 s. **(C)** Cross-correlogram between the two signals in **(B)**. Red line indicates a slight offset from 0 for the peak correlation (~ 250 ms mean lag across FOVs from sensor to OB response). Gray plots average the null correlation ± SEM (correlation of neural activity from the example trial with odor signal from all non-matched trials in session). **(D)** Cross-correlations (mean ± SEM) between odor evoked population activity (principal component) and ethanol sensor signal are strong across 3 Thy1-GCaMP6f (GP5.11) mice ($r = 0.54 \pm 0.07$).

or denoising was performed. To search for component activity responsive to plume dynamics, the correlation between each principal component and the odor concentration dynamics was calculated. There exists a high ranking component for each mouse that correlates strongly with plume dynamics (**Figures 3C,D**). Plotting the loading weights of the maximally correlated component shows dense clusters of high variance resembling partial spatial maps of glomerular activity. These findings demonstrate that MT population activity recorded in the first relay of olfactory processing is correlated to odor concentration dynamics during plume presentations. In order to establish whether individual glomeruli are correlated to odor cues, we sought to segment the MT activity into glomerular units to determine their respective contributions to the observed tracking of plume fluctuations by population activity.

3.3. Neural Activity of Glomeruli

CNMF decomposition provided locations of glomeruli and their corresponding denoised traces (**Figure 4**). To recover the average activity of synaptic complexes of MT activity known as glomeruli, CNMF traces were deconvolved in the style of Stern et al. (2020) (see methods). The mean deconvolved trace across trials was calculated for each glomerulus during plume presentations (**Figure 4E**). The mean response of a deconvolved trace (**Figure 4F**) was only considered during the middle 8 s of the 10 s odor plume to concentrate on glomerular responses to odor concentration dynamics during plume presentations and avoid responses to onset or offset plume dynamics.

For each glomerulus, the mean response across plumes was also calculated within low and high flow conditions. A paired samples *t*-test found that glomerular response means varied significantly across low and high flow conditions [$t_{(110)} = 9.71$, $p < 0.001$]. Mean responses were higher in low flow conditions, during which lower airspeed resulted in plume dynamics that were less intermittent, as shown by lower skewness and asymmetry in the deconvolved odor signals of low flow trials as compared to high flow trials [$F_{(2, 155)} = 52.7$, $p < 0.001$ and $F_{(2, 155)} = 54.9$, $p < 0.001$, respectively] (**Figures 1E–H**). In high flow conditions, increased intermittency produced more brief, high concentration fluctuations followed by blanks, or periods without odor signal. This decreased response observed across high flow conditions could be due to a decrease in odor concentration means as plumes had lower concentration means in high flow. PID recordings from the paired recording experiment show a significant 50% decrease of the mean concentration in high flow as compared to low flow ($z = 6.65$, $p < 0.001$). Thus, the mean MT activity increased in low flow trials following the increase in stimulus mean, but activity became less correlated with plume dynamics, suggesting the response of glomerular populations are moderated by plume dynamics.

3.4. Correlation Between Stimulus and Glomerular Activity

To determine if plume dynamics could be moderating the glomerular population response, cross-correlation was used to quantify the relation between odor concentration dynamics and simultaneously recorded glomerular activity (**Figure 5**). Most glomeruli significantly followed plume dynamics when correlation between neural activity and odor activity was calculated across all trials (100/111), across low flow (97/111) trials, or across high flow (100/111) trials. Significant tracking of the stochastic changes in odor concentration across plume presentations is determined by comparing mean correlation

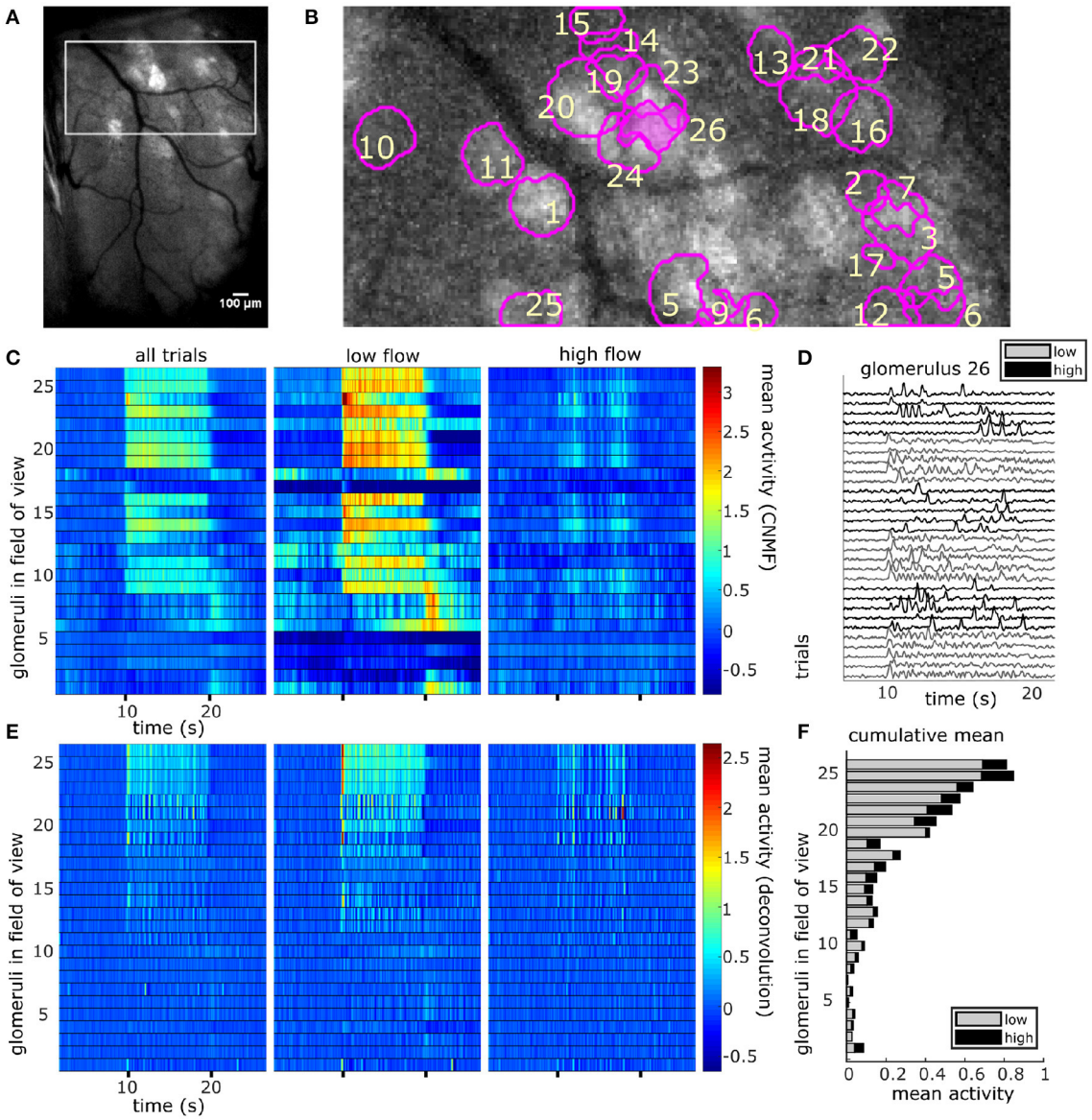

FIGURE 4 | The spatial and temporal decomposition of CNMF identifies glomeruli and denoises their traces. **(A)** The white box outlines the FOV used for analysis as it relates to the larger recording window. The image shows the standard deviation projection of the aligned recording during a single odor presentation. **(B)** Mean subtracted maximum projection of the same trial overlaid with ROIs from CNMF spatial decomposition shows segmentation of glomeruli for a single FOV using CNMF spatial decomposition. The spatial decomposition of the FOV results in 26 glomeruli (four dropped units after merge analysis not pictured) as outlined and numbered. **(C)** Shows the mean traces of each glomerulus's CNMF temporal decomposition within each flow condition (left to right : all trials, low flow, high flow). Trials sorted by magnitude of normalized mean deconvolved response **(E)** during odor exposure. **(D)** The deconvolved CNMF response of a single glomerulus [pink fill **(B)**] to all low (gray) and high (black) flow trials across the recording session shows glomerular responses vary due to the unique odor concentration dynamics of each plume. **(E)** Deconvolution accelerates dynamics of glomerular responses as shown by the mean deconvolved traces of the corresponding glomeruli depicted in **(C)**. **(F)** The cumulative mean, a sum of the mean responses for each glomerulus in low and high flow, are plotted as a stacked bar graph so that comparisons between mean responses can be made within and across glomeruli simultaneously. Mean responses are calculated for the deconvolution **(E)** within each flow condition during the plume release and vary significantly between conditions [$t_{(110)} = 11.43$, $p < 0.001$] with higher average responses in low flow.

coefficients to a null distribution created using a trial shuffled bootstrap analysis (see methods) (**Supplementary Figure 7C**). Within glomeruli that significantly responded to plume dynamics, the degree of tracking (the strength of the correlation between plume dynamics and a glomerulus's response) varied along a continuum such that some glomeruli were more responsive to fluctuations in odor concentration than others (**Figures 5C,D**). Higher correlation coefficients are not observed when glomerular responses are trial shuffled and ethanol recordings are no longer compared to the glomerular responses they elicited (**Figures 5A,B**, **Supplementary Figure 7C**). This shows that it is not the statistics of stimulus presentations that

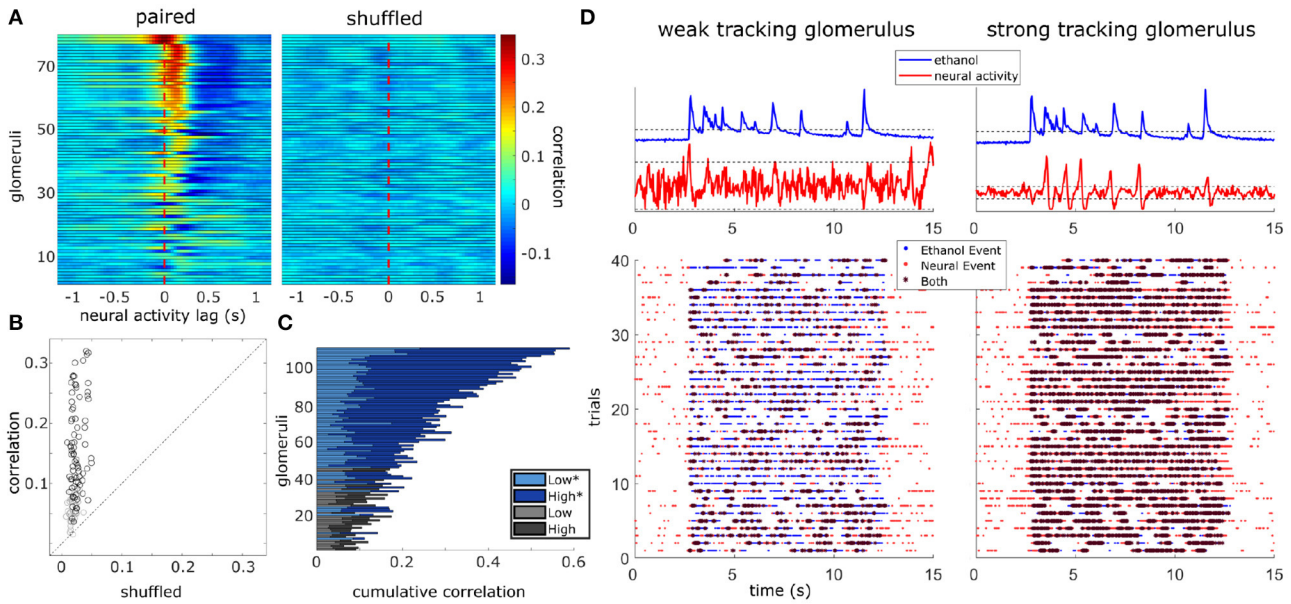

FIGURE 5 | Glomerular population activity follows odor concentration dynamics across plume encounters. (Left) The cross-correlation between the deconvolved ethanol trace and each glomerulus's deconvolved activity trace is calculated within each trial and then averaged across trials. Each row is a glomeruli and each time point represents the cross-correlation at the indicated lag. Glomeruli are sorted in order of decreasing magnitude of correlation coefficient (see methods). (Right) Same as left but glomerular responses are trial shuffled so that the signals compared are not from the same trial. Glomeruli are sorted to match their corresponding unshuffled cross-correlation in the right panel. **(B)** Scatterplot of the correlation coefficient of all glomeruli if compared to their respective shuffled coefficient. Glomeruli plotted in **(A)** are marked in black if their coefficient exceeds their shuffled coefficient from a single trial shuffled comparison by 2 standard deviations. **(C)** The cumulative correlation, a sum of correlation coefficients for each glomerulus in low and high flow, are plotted as a stacked bar graph so that comparisons between mean responses can be made within and across glomeruli simultaneously. The cumulative plotting shows variation in ability to detect changes in odor concentration dynamics across glomeruli both within and across flow conditions. On average, a glomerulus's tracking ability varies significantly between conditions [$t_{(110)} = 12.81$, $p < 0.001$], with most glomeruli having stronger correlation coefficients in high flow trials. Glomeruli that significantly correlate with plume dynamics in at least one condition are plotted in blues (*) while those that do not are plotted in grays. **(D)** Binary cross-correlation. Top: Simultaneously recorded signals shown for two example glomeruli responding to the same example trial's odor plume. Odor and glomerular activity traces plotted with their respective thresholds (dotted, odor threshold: mean during plume presentation, neural threshold: ±2 st. dev of baseline). Bottom: Resulting binarized traces plotted for each trial illustrate the magnitude of concurrent activity as events (stars) between the plume and the response of each glomerulus across the experimental session.

drive this correlation, but rather the plume's temporal dynamics unique to each trial.

Correlation coefficients (tracking) increased from the null expectations by 0.13 ± 0.08 (mean ± st. dev) across all flow conditions, 0.08 ± 0.07 within low flow, and 0.16 ± 0.11 within high flow. Glomeruli were significantly better at tracking plume dynamics in high flow than they were in low [$t_{(110)} = 12.81$, $p < 0.001$] (**Figure 5C**) with average correlation coefficients increasing by 0.11 ± 0.09 (mean ± st. dev). We wondered if this increase in correlation could result from increased sparsity. Indeed correlation between two signals where the values are constant or zero for most of the time is automatically high, even if the peaks are entirely uncorrelated. If this was the case, the shuffled correlations in high flow should be significantly higher than in low flow, but this is not observed when looking at the confidence intervals for the null correlation coefficients computed within flow conditions (**Supplementary Figure 7C**). Thus, a large fraction of the glomerular population follows fluctuations during plume encounters, and the degree of dynamic tracking is moderated by plume dynamics, becoming stronger on average during plumes with higher levels of intermittency (as measured by increased skewness in high flow trials).

A second set of experiments, an odor panel, was used to assess whether the tracking behavior seen in the flow experiments is generalizable beyond the benzaldehyde mixture used. We recorded MT activity as it responded to plumes of three different odors within a single session. Plumes consisted of either ethanol (without a mixed odorant), benzaldehyde, or isoamyl acetate. For all trials, flow stayed constant and was set to the high flow condition. Results corroborated the ability of MT activity to respond to odor concentration dynamics and show tracking behavior generalizes beyond the benzaldehyde mixture used in the flow experiments. Glomeruli that significantly responded to odor concentration dynamics were found in the ethanol only condition (41/59 glomeruli), the benzaldehyde/ethanol condition (38/59), and the isoamyl acetate/ethanol condition (41/59) (**Supplementary Figure 8A**), and the majority of glomeruli reached significance in at least one odor condition (54/59).

3.5. Plume Fluctuations Structure Glomerular Network Dynamics

We measured glomerular responsivity and response power to see the effect of flow condition on these measures and whether

these measures were related to how well a glomerulus followed plume dynamics.

We found that there was a significant effect of flow condition on glomerular responsivity. Responsivity is defined as the proportion of trials to which a glomerulus responded to the odor (see methods). Glomeruli had significantly higher responsivity during low flow trials ($t = 12.1$, $p < 0.001$), with responsivity scores increasing by 0.21 ± 0.18 (mean $\pm$ st. dev) as compared to high flow (**Figure 6**). Therefore, glomeruli responded to low flow trials more reliably than they responded to high flow trials. As noted previously, the average correlation between plume dynamics and MT activity increased in high flow conditions, so although glomerular responses became less reliable as airflow increased, they became more correlated with plume dynamics (**Figure 6B**).

Responsivity is a thresholded measure that determines if a glomerulus is more active than expected by chance during a plume presentation and does not capture the dynamics present in the response. The strength of the dynamic activity of glomeruli was determined by measuring the change in cumulative response power between baseline periods and plume presentations (see methods) (**Supplementary Figure 6**). Fast Fourier transform was used to measure response power within 0–5 Hz, a frequency range relative to the stimulus dynamics (**Figure 7**). Response power (0–5 Hz) increased significantly from baseline during plume presentations [$t_{(110)} = 20$, $p < 0.001$] by 5.7 ± 3.0 a.u. (mean $\pm$ st. dev), a 448% increase (**Figure 7**). On average $86.7 \pm 4.9\%$ (mean $\pm$ st. dev) of cumulative stimulus power for each session was within 0–5 Hz. Stimulus power was measured using the deconvolved odor signal of the plumes to which MT cell responses were recorded (experimental flow sessions only). The majority of cumulative response power for each glomerulus, $88.5 \pm 7.9\%$ (mean $\pm$ st. dev), was also found to be within this range. Thus, the majority of response power for each glomerulus was measured to be within a relative frequency range of the stimulus (**Figures 7A,B**). Across all glomeruli recorded, response power was not significantly different between flow conditions. To examine the effect of flow conditions on the response power of cells that most strongly responded to the odor, we next analyzed only glomeruli whose mean response was above the 75th percentile. Within this group of glomeruli, response power did change significantly between flow [$t_{(27)} = 5.52$, $p < 0.001$], with stronger response power during high flow conditions (**Figures 7D,E**). This increase reflects the significant increase in stimulus power (0–5 Hz) observed in high flow as compared to low flow trials [$t_{(116)} = 31$, $p < 0.001$] (**Figure 7C**). Thus, the response power of glomeruli with the strongest signals was significantly affected by flow condition.

There exists a relationship between each of these two response features, responsivity and response power, and how well a glomerulus follows plume dynamics. Across all trials, glomeruli with higher responsivity to plume presentations were better at following changes in odor concentration ($r = 0.76$, $p < 0.001$). Thus, the more reliably a glomerulus responded to plume presentations, the more likely it was to better follow changes in odor concentration (**Figure 6C**). These findings were reflected in the supplementary odor panel study, where glomeruli with higher responsivity to plumes had responses that were more correlated with plume dynamics [$F_{(2,116)} = 8.06$, $p < 0.001$] (**Supplementary Figure 8E** sorted bottom to top by increasing correlation magnitude). This is not a perfect relationship as glomeruli that are responsive to the plume but not its dynamics exist (**Figure 6A**), but a glomerulus with higher responsivity is more likely to be correlated to plume dynamics than one with lower responsivity. As mentioned previously, a glomerulus's average responsivity level is also moderated by flow condition. Thus, a glomerulus's responsivity predicts its ability to track plume dynamics and is moderated by changes in dynamic regimes.

As for the second response feature, response power was also correlated with how well the glomerulus followed changes in odor concentration, when averaged across all trials glomeruli with higher response power were significantly better at following plume dynamics ($r = 0.74$, $p < 0.001$) (**Figure 7E**). When this relationship was examined within flow conditions (**Figure 7C**), high flow was significantly correlated ($r = 0.73$, $p < 0.001$), but low flow was no longer significantly correlated ($r = 0.19$, $p = 0.05$). This significant correlation in high flow was driven by a subset of the strongest responding glomeruli (75th percentile) whose response power was significantly moderated by flow condition. This relationship between response power and tracking ability (correlation with plume dynamics) was also observed in the supplementary odor panel study where higher average response power predicted higher correlations between that response and plume dynamics [$F_{(2,116)} = 29.2$, $p < 0.001$] (**Supplementary Figure 8C**). Thus, a glomerulus's response power predicts its ability to track plume dynamics and for stronger responders, this relationship is moderated by changes in dynamic regimes.

These results suggest that both the reliability and the temporal pattern of MT activity is significantly moderated by the odor concentration dynamics of the incoming stimuli. Thus, the spatiotemporal dynamics of plumes play a role in structuring activity in the first olfactory relay of the mouse's brain during natural olfactory processing.

4. DISCUSSION

Mice are adept at olfactory guided search despite the stochasticity and complexity of odor plumes used in navigation. Spatiotemporal cues present in natural odor scenes are thought to drive decision-making in olfactory search (Mafra-Neto and Cardé, 1994; Vickers, 2006; Pang et al., 2018), but how they moderate population activity in the olfactory bulb (OB) is unknown. Releasing odor within a custom-built wind tunnel, we were able to hold constant all properties of the odor stimulus and the animal's position relative to the source and vary only the air velocity through which the plume traveled. By using this approach we altered the Reynolds number of the flow and created plumes with varying statistical structures and odor concentration dynamics. In this way, the effect of plume dynamics on MT population activity could be examined using naturally evolving odor plumes. Recording

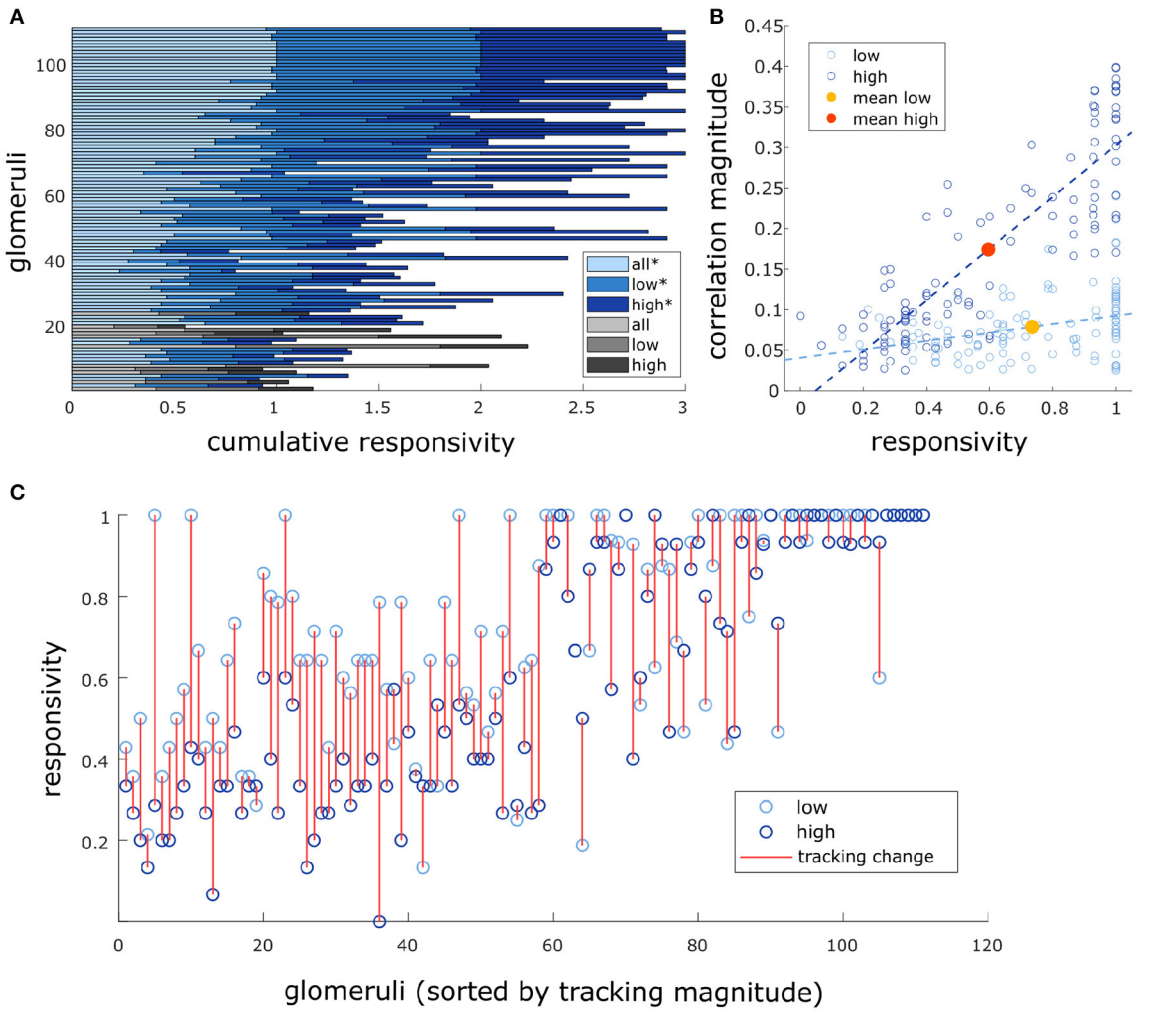

FIGURE 6 | Glomeruli that respond more reliably to plumes are more correlated with their dynamics. **(A)** Responsivity scores plotted as a cumulative bar graph to illustrate differences within and across glomeruli when responsivity is calculated across all conditions (lightest blue) or is calculated exclusively within low flow (medium blue) or high flow (dark blue). Glomeruli are sorted top to bottom by decreasing average tracking ability (correlation magnitude) and glomeruli that significantly track plume dynamics (as defined in methods) are plotted in blue hues(*) while those that do not are plotted in gray hues. The graph shows magnitude of odor concentration tracking is correlated with ($r = 0.76$, $p < 0.001$), but is not strictly defined by response reliability as glomeruli exist that respond strongly to odor presence but not to concentration dynamics. In addition, within flow comparisons show responsivity is significantly higher in low flow than high flow [$t_{(110)} = 12.1263$, $p < 0.001$]. **(B)** Within flow condition, responsivity is plotted against tracking ability (correlation magnitude) for each glomerulus (circle). To represent the population response, the average responsivity across all glomeruli (low average = yellow dot, high average = red dot) is plotted against average correlation with plume dynamics within low (light blue) and high (dark blue) flow conditions illustrating how flow moderates these relationships. Across glomeruli, responsivity is positively correlated with tracking ability as is illustrated by the lines of best fit. On average, higher flow predicts a decrease in average responsivity level but also predicts an increase in tracking ability. **(C)** Average responsivity in low and high flow is plotted for each glomerulus, and the change in mean responsivity between flows shown in **(A)** is explicitly plotted for each glomerulus (red line) as well. Glomeruli are sorted by increasing tracking ability (from left to right) showing glomeruli with higher response reliability are more sensitive to plume dynamics.

MT activity in mice expressing GCaMP6f, we show that a significant fraction of glomerular populations of MT cells follow odor plume dynamics. Additionally, the strength with which they do so is moderated by airflow, such that increased flow velocity and turbulence (Reynolds number) results in increased correlation of MT cell activity with plume dynamics. This work shows that plume dynamics structure the activity of the OB, the first relay of olfactory coding in the mouse's brain.

The recent history of an odor stimulus has been shown to be present in olfactory encoding in both serial sampling of odor concentration in mice (Parabucki et al., 2019) and tracking of odor concentration in invertebrates (Geffen et al., 2009), showing odor concentration changes influence olfactory encoding. Although inter-sniff comparisons in mice show that MT cells can detect the sign and magnitude of changes in odor concentration (Parabucki et al., 2019), it is unknown whether they are able to resolve the dynamics of natural plumes, which

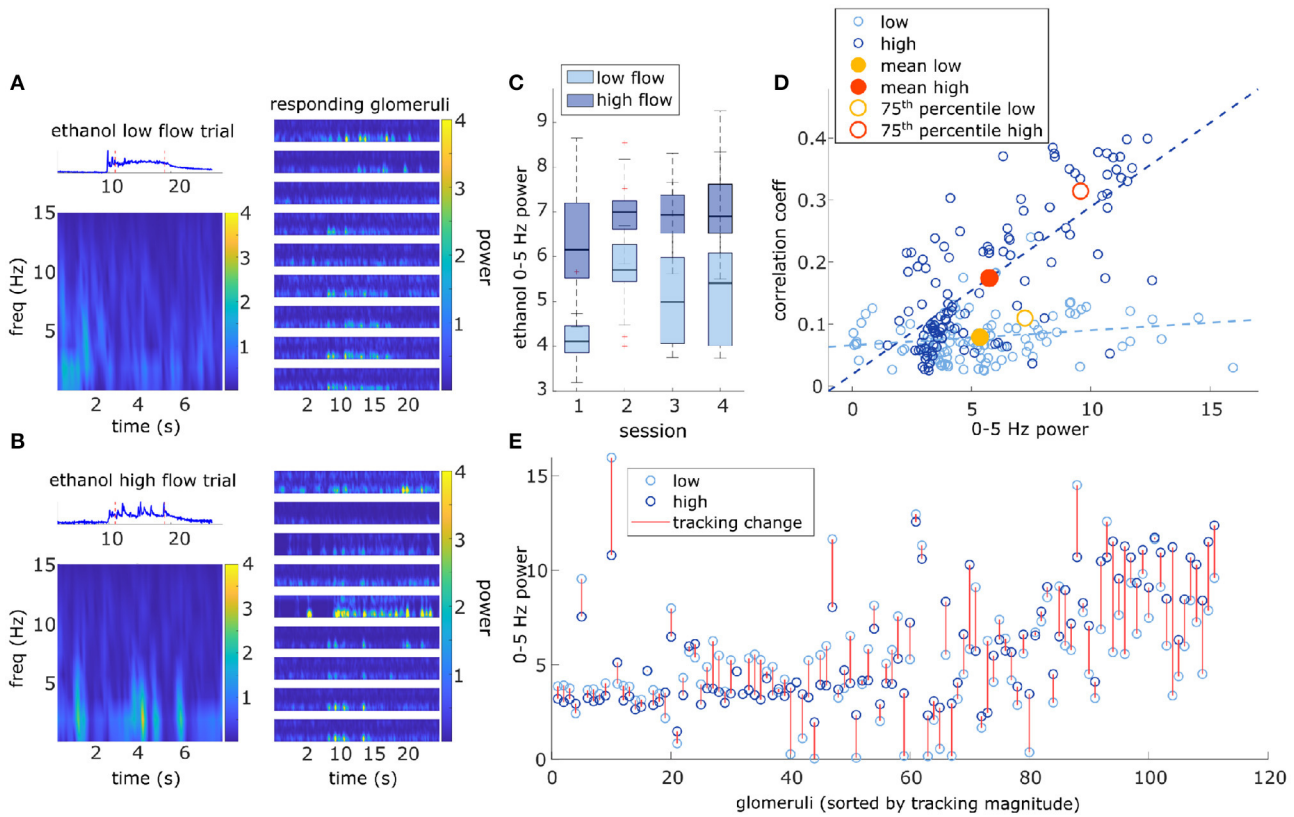

FIGURE 7 | Higher magnitude of glomerular response power (0–5 Hz) is associated with higher correlation with plume dynamics. **(A)** Ethanol signal from a single low flow trial is plotted (top-left) and a corresponding Short-time Fourier transform (STFT) of the plume (time between red dotted lines) is shown below (bottom-left). STFTs are also shown for a sample of glomeruli responding to the plume (right). STFTs show most response power of the glomeruli and odor signal is concentrated between 0 and 5 Hz. Glomeruli STFTs are sorted (top to bottom) by increasing correlation with plume dynamics. **(B)** Same as **(A)** but for a single high flow trial from another example FOV. **(C)** Box plots for the distributions of stimulus power (0–5 Hz) for all trials within the demarcated flow condition are plotted for each session. On average, high flow distribution means (dark blue) significantly exceeded low flow distribution means (light blue) [$t_{(116)} = 31, p < 0.001$]. **(D)** Within both high and low flow conditions, tracking (correlation magnitude of glomerular responses with plume dynamics) is plotted against response power (0–5 Hz power spectrum change between "odor off" and "odor on" periods) for each glomerulus (blue hues, circles). Glomeruli with stronger tracking have a greater increase in response power during plume presentations ($r = 0.74$, $p < 0.001$). When calculated within flow, this relationship is significant within high flow ($r = 0.73$, $p < 0.001$), but not within low flow ($r = 0.19$, $p = 0.05$). The average response across all glomeruli is plotted (low average = yellow dot, high average = red dot) to represent the population response. Mean response power of the glomerular population is not significantly different between low and high flow, except for when calculated with glomeruli whose mean activity is in the 75th percentile (low average = yellow circle, high average = red circle). **(E)** Response power of each glomerulus is again plotted, but the change within a glomerulus between low flow (light blue) and high flow (dark blue) is signified by the red line. Glomeruli are plotted sequentially along the x-axis and are sorted left to right by increasing tracking ability. As tracking ability increases, so does the change in response power between flow conditions. This is consistent with the significant change in mean response between flow condition observed in the 75th percentile [plotted as red/yellow circles in **(D)**].

span across a range of temporal scales. If odor concentration dynamics are resolved, computational work has shown that they are informative for olfactory search (Baker et al., 2018; Gumaste et al., 2020). To avoid the complexity of stochastic odor plumes, the averaging of odor concentration dynamics could be an alternative strategy to navigate olfactory environments. Mean odor concentration levels are moderated both by the distance from an odor source and by how close an animal is to the central stream of the plume (Crimaldi and Koseff, 2001). While this measure is potentially informative, it does not by itself sufficiently inform decision-making on the timescale observed in rodents (Gumaste et al., 2020). Therefore, it is likely that the mouse relies upon spatiotemporal features of the plume for olfactory search as information can be extracted from odor concentration dynamics (Baker et al., 2018).

Our study found a correlation between MT activity and odor concentration dynamics during plume presentations. The temporal information conveyed by MT cells could support a variety of navigation algorithms. For instance, two important dynamic features are the length of odor encounters, whiffs, and the timing between odor encounters, blanks. Whiff and blank duration are moderated by the distance between an animal and the odor source. As an animal approaches an odor source, plume encounters become shorter and more frequent (Wright and Thomson, 2005; Celani et al., 2014). Blank duration has been shown to be particularly informative even when olfactory

environments change. Computational modeling of olfactory search in invertebrates (Park et al., 2016; Rapp and Nawrot, 2020) as well as fluid dynamics modeling (Celani et al., 2014) shows that the time between odor encounters, blank duration, is less sensitive to environmental conditions, such as plume velocity or potency of the odor source that are known to affect interpretation of odor concentration dynamics (Webster and Weissburg, 2001; Connor et al., 2018). Specifically, Park et al., found blank duration to be a more efficient source of information for olfactory search than instantaneous tracking of odor concentration. In our study, we observed that MT activity was more correlated with plume dynamics in high flow trials than low flow trials. Odor concentration in low flow trials was less skewed, meaning that these trials had lower intermittency and odor concentration tended to fluctuate around a central value. Alternatively, high flow trials were more skewed and were characterized by a whiff and blank structure. The fact that correlations are higher in high flow suggests MT activity may be more responsive to whiff and blank features as opposed to tracking fine fluctuations in odor concentration across more constant plume encounters. One limitation of this study is that medium flow was not statistically distinguishable from high flow, therefore, we were unable to include intermediary intermittency levels between low and high flow conditions in our analysis. Future studies exploring the effect of a broader range of intermittency levels on MT activity during plume encounters could help determine which spatiotemporal features of intermittency are moderating MT responses to plume dynamics.

A network where the majority of glomerular activity responds to concentration dynamics could be considered to be inefficient when the OB has to perform other tasks, such as odor identification and segmentation. Glomerular spatial maps, i.e., glomerular ensembles consistently responding to an odor, are thought to be one of the primary means of odor identification (Wachowiak and Shipley, 2006). Odors maps vary with concentration (Xu et al., 2000; Wachowiak and Cohen, 2001), but are stable enough to reliably encode odor identity (Belluscio and Katz, 2001). Although pulsed odors can be rapidly discriminated (<200 ms, or a single sniff, Uchida and Mainen, 2003), in a natural olfactory environment where odors are intermittent (Murlis et al., 2000; Celani et al., 2014) and mixed, identification becomes a much more complicated task especially for identification of mixtures. Glomerular ensembles reliably responding across odor encounters could aid odor discrimination in mixed odor environments. Spatial maps of odor identification will overlap in natural olfactory scenes where an animal encounters signals from multiple odor sources as it navigates a plume. Odors co-released travel together (Celani et al., 2014), and therefore a mixture of odors emanating from the same source will have correlated temporal dynamics in the plume and will thus be experienced by a searcher as having correlated encounters across whiffs. This means the probability of the signal from separate sources arriving together reliably across whiffs would be low if odors are released from spatially separated sources. Grouping and demixing these odor representations using the correlation, or lack thereof, in the odor concentration dynamics could aid odor discrimination in complex environments (Hopfield, 1991).

Since our studies are not recorded at the individual cell level, the potential degree of heterogeneous tuning to different features among MT cells within a single glomerulus was not examined. It could be that observed correlations of glomerular MT populations were a product of the collective activity of heterogeneously tuned MT cells within a glomerulus, but MT responses have been shown to linearly sum odor inputs (Gupta et al., 2015), which contradict the idea that they are directly tuned to different features of plume dynamics. At the same time, this does not infer MT activity responding to plume dynamics is homogeneous as the responsiveness (Adam et al., 2014) and the response (Geramita and Urban, 2017) varies between MT cells across concentration levels (Cleland and Borthakur, 2020). Future research across a variety of odor concentration dynamic regimes and odor mixtures at both the cellular and population level are needed to further investigate the degree to which bulbar responses are tuned to features of odor concentration dynamics and how this tuning may impact optimal encoding of odor information.

Sniff frequencies are known to influence bulbar oscillations, and thus if sniffing behavior varied significantly between flow conditions, this may have contributed to some of the observed differences in tracking behavior between low and high flow trials. For example, it could be that faster stimulus dynamics in high flow may cause the mouse to miss features of the dynamics due to an inability to resolve them with sufficient sampling speed. However, recent work suggests sniff frequency does not necessarily limit the resolution of plume frequencies in such a manner (Dasgupta et al., 2020). Dasgupta et al. (2020) found subthreshold MT activity was able to couple with frequencies of odor pulsed at supra-sniff frequencies. Thus, if sniff frequency was moderated significantly between flow conditions, it would not necessarily set an absolute bound on the resolution of plume dynamics. We believe it is important to monitor sniff frequency in the future to observe how it affects inter-sniff and intra-sniff activity, and consequently how these changes relate to tracking behavior observed in MT populations across flow conditions.

Our data show that MT activity in the OB of mice follows the temporal dynamics of odor plumes. Additionally, we demonstrate that this effect is stronger under conditions that generate larger Reynolds numbers. Following odor concentration dynamics within plumes could enable MT cells to convey information useful for olfactory search. Following the temporal dynamics of odor plumes may also be an efficient form of multiplexing odor identity and source location for the first olfactory relay in mice. Although MT activity responds to changes in odor concentration, the observed correlations do not suggest perfect tracking at the level of individual glomeruli and indicate inter-individual differences in the degree to which glomeruli follow plume dynamics. Future research focusing on location encoding across a wide range of both intermittency regimes and odor panels is needed to clarify the degree to which bulbar activity is tuned to features of plume dynamics and how

a balance between identity coding and concentration coding is instrumental in supporting the wide variety of behaviors enabled by olfaction.

DATA AVAILABILITY STATEMENT

The data supporting the conclusions of this article will be made available by the authors, without undue reservation.

ETHICS STATEMENT

The animal study was reviewed and approved by Institutional Animal Care and Use Committee (IACUC) of the University of Washington.

AUTHOR CONTRIBUTIONS

DG, AS, and SL initiated the study and designed the experiments. DG and SL built the head-fixed imaging setup, built the plume delivery setup, and wrote the acquisition software. SL and LX performed the cranial window surgeries. SL, LX, and LS performed the experiments. DG, MS, and SL performed the analysis of neural data. DG, AS, SL, and NR performed the analysis of plume dynamics, developed the deconvolution based on Tariq et al. (2021) (MT) and MT assisted with sensor characterization. DG, AS, SL, and NR generated the figures reporting data with input from MS. All authors helped with the text.

FUNDING

This work was supported by grants R00 DC013305 (DG), R01 DC018789 (DG), and a Thomas Jefferson Award from the FACE Foundation (AS and DG). This material was based upon work supported by the Air Force Office of Scientific Research under award number FA8655-20-1-7028.

ACKNOWLEDGMENTS

We would like to thank Michael Grybko for *in vitro* characterization of GCaMP6f expression in MT cells, Katie Ferguson (Post-doctoral Fellow, Neuroscience, Yale University) for consultation regarding calcium imaging data acquisition and analysis, Kelly Chang (Graduate Student, Psychology, University of Washington) for advice on data analysis and figure design, and Jin Young Park for assisting in data collection.

SUPPLEMENTARY MATERIAL

The Supplementary Material for this article can be found online at: https://www.frontiersin.org/articles/10.3389/fncel.2021.633757/full#supplementary-material

REFERENCES

Ache, B. W., Hein, A. M., Bobkov, Y. V., and Principe, J. C. (2016). Smelling time: a neural basis for olfactory scene analysis. *Trends Neurosci.* 39, 649–655. doi: 10.1016/j.tins.2016.08.002

Adam, Y., Livneh, Y., Miyamichi, K., Groysman, M., Luo, L., and Mizrahi, A. (2014). Functional transformations of odor inputs in the mouse olfactory bulb. *Front. Neural Circuits* 8:129. doi: 10.3389/fncir.2014.00129

Atema, J. (1996). Eddy chemotaxis and odor landscapes: exploration of nature with animal sensors. *Biol. Bull.* 191, 129–138. doi: 10.2307/1543074

Baker, K. L., Dickinson, M., Findley, T. M., Gire, D. H., Louis, M., Suver, M. P., et al. (2018). Algorithms for olfactory search across species. *J. Neurosci.* 38, 9383–9389. doi: 10.1523/JNEUROSCI.1668-18.2018

Batista-Brito, R., Vinck, M., Ferguson, K. A., Chang, J., Laubender, D., Lur, G., et al. (2017). Developmental dysfunction of VIP interneurons impairs cortical circuits. *Neuron* 95, 884–895.e9. doi: 10.1016/j.neuron.2017.07.034

Belluscio, L., and Katz, L. C. (2001). Symmetry, stereotypy, and topography of odorant representations in mouse olfactory bulbs. *J. Neurosci.* 21, 2113–2122. doi: 10.1523/JNEUROSCI.21-06-02113.2001

Cavarretta, F., Burton, S. D., Igarashi, K. M., Shepherd, G. M., Hines, M. L., and Migliore, M. (2018). Parallel odor processing by mitral and middle tufted cells in the olfactory bulb. *Sci. Rep.* 8:7625. doi: 10.1038/s41598-018-25740-x

Celani, A., Villermaux, E., and Vergassola, M. (2014). Odor landscapes in turbulent environments. *Phys. Rev. X* 4:041015. doi: 10.1103/PhysRevX.4.041015

Cleland, T. A., and Borthakur, A. (2020). A systematic framework for olfactory bulb signal transformations. *Front. Comput. Neurosci.* 14:579143. doi: 10.3389/fncom.2020.579143

Connor, E. G., McHugh, M. K., and Crimaldi, J. P. (2018). Quantification of airborne odor plumes using planar laser-induced fluorescence. *Exp. Fluids* 59:137. doi: 10.1007/s00348-018-2591-3

Crimaldi, J. P., and Koseff, J. R. (2001). High-resolution measurements of the spatial and temporal scalar structure of a turbulent plume. *Exp. Fluids* 31, 90–102. doi: 10.1007/s003480000263

Dana, H., Chen, T. W., Hu, A., Shields, B. C., Guo, C., Looger, L. L., et al. (2014). Thy1-GCaMP6 transgenic mice for neuronal population imaging *in vivo*. *PLoS ONE* 9:e108697. doi: 10.1371/journal.pone.0108697

Dasgupta, D., Warner, T. P. A., Erskine, A., and Schaefer, A. T. (2020). Coupling of mouse olfactory bulb projection neurons to fluctuating odour pulses. *bioRxiv* 2020.11.29.402610. doi: 10.1101/2020.11.29.402610

Esquivelzeta Rabell, J. F., Mutlu, K., Noutel, J., Olmo, P., and Haesler, S. (2017). Spontaneous rapid odor source localization behavior requires interhemispheric communication. *Curr. Biol.* 27, 1542–1548.e4. doi: 10.1016/j.cub.2017.04.027

Fletcher, M. L., Masurkar, A. V., Xing, J., Imamura, F., Xiong, W., Nagayama, S., et al. (2009). Optical imaging of postsynaptic odor representation in the glomerular layer of the mouse olfactory bulb. *J. Neurophysiol.* 102, 817–830. doi: 10.1152/jn.00020.2009

Geffen, M. N., Broome, B. M., Laurent, G., and Meister, M. (2009). Neural encoding of rapidly fluctuating odors. *Neuron* 61, 570–586. doi: 10.1016/j.neuron.2009.01.021

Geramita, M., and Urban, N. N. (2017). Differences in glomerular-layer-mediated feedforward inhibition onto mitral and tufted cells lead to distinct modes of intensity coding. *J. Neurosci.* 37, 1428–1438. doi: 10.1523/JNEUROSCI.2245-16.2016

Gire, D. H., Kapoor, V., Arrighi-Allisan, A., Seminara, A., and Murthy, V. N. (2016). Mice develop efficient strategies for foraging and navigation using complex natural stimuli. *Curr. Biol.* 26, 1261–1273. doi: 10.1016/j.cub.2016.03.040

Gumaste, A., Coronas-Samano, G., Hengenius, J., Axman, R., Connor, E. G., Baker, K. L., et al. (2020). A comparison between mouse, *in silico*, and robot odor plume navigation reveals advantages of mouse odor tracking. *eNeuro* 7:ENEURO.0212–19.2019. doi: 10.1523/ENEURO.0212-19.2019

Gupta, P., Albeanu, D. F., and Bhalla, U. S. (2015). Olfactory bulb coding of odors, mixtures and sniffs is a linear sum of odor time profiles. *Nat. Neurosci.* 18, 272–281. doi: 10.1038/nn.3913

Hopfield, J. J. (1991). Olfactory computation and object perception. *Proc. Natl. Acad. Sci. U.S.A.* 88, 6462–6466. doi: 10.1073/pnas.88.15.6462

Liu, A., Papale, A., Hengenius, J., Patel, K., Ermentrout, B., and Urban, N. (2019). Mouse navigation strategies for odor source localization. *bioRxiv* 558643. doi: 10.1101/558643

Mafra-Neto, A., and Cardé, R. T. (1994). Fine-scale structure of pheromone plumes modulates upwind orientation of flying moths. *Nature* 369, 142–144. doi: 10.1038/369142a0

Markopoulos, F., Rokni, D., Gire, D. H., and Murthy, V. N. (2012). Functional properties of cortical feedback projections to the olfactory bulb. *Neuron* 76, 1175–1188. doi: 10.1016/j.neuron.2012.10.028

Martinez, D., Burgués, J., and Marco, S. (2019). Fast measurements with MOX sensors: a least-squares approach to blind deconvolution. *Sensors* 19:4029. doi: 10.3390/s19184029

Michaelis, B. T., Leathers, K. W., Bobkov, Y. V., Ache, B. W., Principe, J. C., Baharloo, R., et al. (2020). Odor tracking in aquatic organisms: the importance of temporal and spatial intermittency of the turbulent plume. *Sci. Rep*. 10:7961. doi: 10.1038/s41598-020-64766-y

Murlis, J., Willis, M. A., and Carde, R. T. (2000). Spatial and temporal structures of pheromone plumes in fields and forests. *Physiol. Entomol*. 25, 211–222. doi: 10.1046/j.1365-3032.2000.00176.x

Pang, R., Breugel, F., Dickinson, M., Riffell, J. A., and Fairhall, A. (2018). History dependence in insect flight decisions during odor tracking. *PLoS Comput. Biol*. 14:e1005969. doi: 10.1371/journal.pcbi.1005969

Parabucki, A., Bizer, A., Morris, G., Munoz, A. E., Bala, A. D. S., Smear, M., et al. (2019). Odor concentration change coding in the olfactory bulb. *eNeuro* 6:ENEURO.0396-18.2019. doi: 10.1523/ENEURO.0396-18.2019

Park, I. J., Hein, A. M., Bobkov, Y. V., Reidenbach, M. A., Ache, B. W., and Principe, J. C. (2016). Neurally encoding time for olfactory navigation. *PLoS Comput. Biol*. 12:e1004682. doi: 10.1371/journal.pcbi.1004682

Pnevmatikakis, E. A., and Giovannucci, A. (2017). NoRMCorre: an online algorithm for piecewise rigid motion correction of calcium imaging data. *J. Neurosci. Methods* 291, 83–94. doi: 10.1016/j.jneumeth.2017.07.031

Pnevmatikakis, E. A., Soudry, D., Gao, Y., Machado, T. A., Merel, J., Pfau, D., et al. (2016). Simultaneous denoising, deconvolution, and demixing of calcium imaging data. *Neuron* 89, 285–299. doi: 10.1016/j.neuron.2015.11.037

Rapp, H., and Nawrot, M. P. (2020). A spiking neural program for sensorimotor control during foraging in flying insects. *Proc. Natl. Acad. Sci. U.S.A*. 117, 28412–28421. doi: 10.1073/pnas.2009821117

Stern, M., Shea-Brown, E., and Witten, D. (2020). Inferring the spiking rate of a population of neurons from wide-field calcium imaging. *bioRxiv*. doi: 10.1101/2020.02.01.930040

Tariq, M. F., Lewis, S. M., Lowell, A., Moore, S., Miles, J. T., Perkel, D. J., et al. (2021). Using head-mounted ethanol sensors to monitor olfactory information and determine behavioral changes associated with ethanol-plume contact during mouse odor-guided navigation. *eNeuro* 8:ENEURO.0285–20.2020. doi: 10.1523/ENEURO.0285-20.2020

Uchida, N., and Mainen, Z. F. (2003). Speed and accuracy of olfactory discrimination in the rat. *Nat. Neurosci*. 6, 1224–1229. doi: 10.1038/nn1142

Vergassola, M., Villermaux, E., and Shraiman, B. I. (2007). 'Infotaxis' as a strategy for searching without gradients. *Nature* 445, 406–409. doi: 10.1038/nature05464

Vickers, N. J. (2006). Winging it: Moth flight behavior and responses of olfactory neurons are shaped by pheromone plume dynamics. *Chem. Senses* 31, 155–166. doi: 10.1093/chemse/bjj011

Wachowiak, M., and Cohen, L. B. (2001). Representation of odorants by receptor neuron input to the mouse olfactory bulb. *Neuron* 32, 723–735. doi: 10.1016/S0896-6273(01)00506-2

Wachowiak, M., and Shipley, M. T. (2006). Coding and synaptic processing of sensory information in the glomerular layer of the olfactory bulb. *Semin. Cell Dev. Biol*. 17, 411–423. doi: 10.1016/j.semcdb.2006.04.007

Webster, D. R., and Weissburg, M. J. (2001). Chemosensory guidance cues in a turbulent chemical odor plume. *Limnol. Oceanogr*. 46, 1034–1047. doi: 10.4319/lo.2001.46.5.1034

Wright, G. A., and Thomson, M. G. A. (2005). Odor perception and the variabilityin natural odor scenes. *Recent Adv. Phytochem*. 39, 191–226. doi: 10.1016/S0079-9920(05)80009-7

Xu, F., Greer, C. A., and Shepherd, G. M. (2000). Odor maps in the olfactory bulb. *J. Compar. Neurol*. 422, 489–495. doi: 10.1002/1096-9861(20000710)422:4<489::AID-CNE1>3.0.CO;2-#

Yeung, P. K., and Pope, S. B. (1993). Differential diffusion of passive scalars in isotropic turbulence. *Phys. Fluids A Fluid Dyn*. 5, 2467–2478. doi: 10.1063/1.858760

Yu, Y. S. W., Graff, M. M., Bresee, C. S., Man, Y. B., and Hartmann, M. J. Z. (2016). Whiskers aid anemotaxis in rats. *Sci. Adv*. 2:e1600716. doi: 10.1126/sciadv.1600716

Conflict of Interest: The authors declare that the research was conducted in the absence of any commercial or financial relationships that could be construed as a potential conflict of interest.

Advantages of publishing in Frontiers

OPEN ACCESS
Articles are free to read for greatest visibility and readership

FAST PUBLICATION
Around 90 days from submission to decision

HIGH QUALITY PEER-REVIEW
Rigorous, collaborative, and constructive peer-review

TRANSPARENT PEER-REVIEW
Editors and reviewers acknowledged by name on published articles

Frontiers
Avenue du Tribunal-Fédéral 34
1005 Lausanne | Switzerland

Visit us: www.frontiersin.org
Contact us: frontiersin.org/about/contact

REPRODUCIBILITY OF RESEARCH
Support open data and methods to enhance research reproducibility

DIGITAL PUBLISHING
Articles designed for optimal readership across devices

FOLLOW US
@frontiersin

IMPACT METRICS
Advanced article metrics track visibility across digital media

EXTENSIVE PROMOTION
Marketing and promotion of impactful research

LOOP RESEARCH NETWORK
Our network increases your article's readership